Assessing the mechanistic synergy between cancer virotherapy and external beam radiation

Dr Tzveta Pokrovska

Lady Margaret Hall, University of Oxford



A thesis submitted for the degree of Doctor of Philosophy to the Department of Oncology, University of Oxford

Michaelmas Term 2020

Supervisors: Prof Len Seymour, Prof Geoff Higgins,

Dr Janet Lei-Rossmann

ABSTRACT

One of the core radiobiological features determining response to fractionated treatment is repair of ionising radiation-mediated damage. Adenoviruses are shown to inhibit the DNA damage response (DDR), in particular the pathways involved in repairing double-strand DNA breaks. Combination treatment with radiation and oncolytic adenoviruses therefore offers the potential for tumour-targeted radiosensitisation, and even synergy.

Oncolytic adenovirus treatment is frequently limited to intratumoural delivery, restricting treatment to directly-accessible cancers. Enadenotucirev (EnAd), a Group B chimeric oncolytic adenovirus, has been shown to localise to a number of different tumour types following intravenous delivery. EnAd may therefore allow treatment of patients with visceral and widespread metastatic disease. We hypothesised that combination therapy with EnAd and radiation may lead to synergistic cytotoxicity, and aimed to explore potential underlying mechanisms.

We demonstrated EnAd- and adenovirus serotype 5 (Ad5)-mediated inhibition of the DDR at multiple points along the pathway. Adenovirus infection resulted in decreased 53BP1 and RAD51 foci formation following irradiation, and reduced DNA ligase IV levels. Interestingly, EnAd and Ad11p, but not Ad5, caused phosphorylation of 53BP1 even in the absence of irradiation. Irradiation enhanced infectious particle production of EnAd, but not Ad5 or Ad11p, *in vitro*, and likewise caused increased EnAd production and transgene expression *in vivo*. We propose that these results are at least partially due to radiation-mediated enhanced expression of viral E1A. Treatment synergy was indeed seen *in vitro* in cells irradiated prior to EnAd infection, and irradiation of xenografts following EnAd treatment *in vivo* resulted in significant tumour growth delay when compared to animals receiving PBS prior to radiation.

Our results were consistent with synergistic cytotoxicity *in vitro*, and radiosensitisation *in vivo*, using EnAd and radiation combination therapy. This is likely due to a combination of enhanced oncolytic virus production and increased radiation-induced cytotoxicity following DNA damage repair inhibition. Our findings provide further support for the phase 1 Chemoradiation with Enadenotucirev as a Radiosensitiser in locally Advanced Rectal cancer (CEDAR) trial, which is now recruiting.

PUBLICATION NOTE

Portions of the work presented in chapter 1 have been accepted for publication in Frontiers in Oncology (O'Cathail *et al*., 2017):

Sean M. O'Cathail, **Tzveta D. Pokrovska**, Timothy S. Maughan, Kerry D. Fisher, Leonard W. Seymour, and Maria A. Hawkins

Combining Oncolytic Adenovirus with Radiation—A Paradigm for the Future of Radiosensitization

Doi: 10.3389/fonc.2017.00153

The work presented in chapters 3, 4, 5, and 6 has been accepted for publication in Cancers (Pokrovska *et al*., 2020):

Tzveta D. Pokrovska, Egon J. Jacobus, Rathi Puliyadi, Remko Prevo, Sally Frost, Arthur Dyer, Richard Baugh, Gonzalo Rodriguez-Berriguete, Kerry Fisher, Giovanna Granata, Katharine Herbert, William K. Taverner, Brian R. Champion, Geoff S. Higgins, Len W. Seymour, and Janet Lei-Rossmann

External Beam Radiation Therapy and Enadenotucirev: Inhibition of the DDR and Mechanisms of Radiation-Mediated Virus Increase

Doi: 10.3390/cancers12040798

За мама,

баба,

& Janet

“This I choose to do” – Tiffany Aching

Sir Terry Pratchett

ACKNOWLEDGEMENTS

I have been lucky in the number of people who have helped me along the 18-year long road to submitting a DPhil in Oncology. First and foremost, I am very grateful to my supervisors, Professor Len Seymour, Professor Geoff Higgins, and Dr Janet Lei-Rossmann, for giving me the opportunity to conduct this research project, and for the ideas, discussions, and support.

In my lab groups I undoubtedly did not have colleagues, but family. I am very grateful to the Higgins group for all the help with the radiation side of this project. Remko, whose patience is frankly awe-inspiring, and who was calm and helpful throughout. Gonzalo who continuously provided ideas, support, and laughter, and without whom my western blots would not be what they are today. Rathi for all the help with the mice, and even the occasional hug. Katie who was always helpful and kind, for your help with protocols and for the rainbows and unicorns. Karen for the chats on statistics and generally everything. To James, for our many conversations and late evening lab takeaway. And of course to Giovanna, I was lucky to have you alongside me and you made it so much more fun (and stylish). I would also very much like to thank Professor Gillies McKenna for his insight and helpful comments throughout the duration of this project.

To Len's angels and the Theoangels, who made every failed experiment worth it, and who know that there aren't words for how grateful and happy I was to be part of our group. Sally, there at the start and at the finishing line, we went through it all together and thank heavens for that. Thank you also for kindly assisting with the density analysis of the western blots. Thank you Arthur, for taking care of us, for the science, the chats, all the time you gave up helping me understand viruses, and for helping us settle in after the shock of moving away. You were the best lab husband anyone could have hoped for. El, thank you for your time, for your help with the thesis, and for being you. Will, for the help with the viruses and with walking 100km alongside me. Hena, for being our lab mum and looking after us all. Brian, for always being ready to help with the HPLC or pretty much any help I needed. Sophie for being kind, helpful, and basically perfect. Iris for being my lab sister. Egon, my unofficial supervisor, who gave up so much of his time to teach me how to be a better scientist, and who I was glad to have alongside me working, and sometimes dancing, at all hours. Richard, I couldn't have asked for a happier, better next desk over buddy, who always knew how to make things a bit better, in particular the figures in this thesis and chapter 5. Flurin, our time working together was not long enough but even after I left you brightened my life with songs that I couldn't get out of my head. Mags for teaching me how to do plaque assays and for being so inspirational to us gals. To Josh, for making me feel so welcome and who is both an excellent scientist and a kind friend. To Claudia for being such a great scientist and friend, and Matt for making everything brighter. To Kerry, whose ideas were brilliant and mad at the same time, thank you in particular for thinking up the modified plaque assay which formed the basis of so much of this work. Mandy who helps us all in every way she can think of. To Su for all the help with the viruses and for your brilliant attitude. To Abishek for the advice on the DDR. To Vivian for the chats about science, academia, life and brunch. Sarah, I really appreciated your advice on thesesing. To Alex and Mahnoor, I didn't get as much time as I would have liked to work with you, but I wish you both the best of luck with your projects. And finally to Clara, for your many messages of support that got me through some of the hardest times.

I am particularly grateful to Professor Tim Humphrey, for providing advice and help with the development of this project at multiple stages along the way. Thank you also to Dr Andrew Blackford for meeting to discuss the DDR aspect of the results and providing his background knowledge which helped in optimising directions taken in the final few months.

A big thank you to Dr Rhodri Wilson for all his work and help with the Celigo experiments. I am grateful also to Dr Scott Cribbes for assisting me in optimising the analysis settings for the later Celigo experiments.

For their support with planning and conducting the *in vivo* work I am grateful to Dr Ana Gil-Bernabe, Karla Watson, and Magda Hutchins. Thank you also to Dr Brian Champion and Dr Sam Illingworth for their helpful input into understanding the scientific landscape of EnAd *in vivo* research.

For starting all of this off and teaching me how to be a scientist, I am particularly thankful to Professor Peter Amlot, as well as Fari and Eira. I am grateful to Professor Chris Norbury for giving me the opportunity and the support that has allowed me to achieve what I initially told him I wanted to do 18 years ago. And of course to Professor Grant Churchill, Sri and Parv, who were so monumental in helping me decide to continue working in science alongside my clinical career.

The last four years have by no means been easy, I am therefore particularly thankful to my brilliant, ominous friends and to the OULES for helping me sing and dance through the many failed experiments. And of course, thank you Nina, Steph, Jen, Sean, Catherine and Lucy.

I am so grateful to my wonderful family for their support and help, my mum and grandmother to whom this thesis is dedicated, my dad Mark who has been the best father I could have hoped for, my grandfather, my uncle, aunt and cousin, and my godfather.

And finally, to Dave, who has read (and probably changed) every comma in this thesis, for everything that you do, and everything that you are.

Table of Contents

ABSTRACT i
PUBLICATION NOTE ii
ACKNOWLEDGEMENTS iv
LIST OF ABBREVIATIONS ix
Chapter 1: Introduction 1
1.1 Introduction to radiation-induced DNA damage 1
1.1.1 Homologous recombination repair 3
1.1.2 Classical non-homologous end joining 4
1.2 The concept of virotherapy 5
1.3 Adenoviruses 8
1.4 Oncolytic adenoviruses and the DNA damage response 10
1.4.1 The effect of virus proteins on the MRN complex 11
1.4.2 The effects of virus proteins on phosphatidylinositol-3-kinase-related kinase (PIKK) family 15
1.4.3 The effects of virus proteins on p53 19
1.4.4 Effects of adenovirus on DNA repair proteins 21
1.5 Combination therapy between radiation and oncolytic adenovirus 22
1.6 Enadenotucirev 24
1.7 Central hypothesis and aims 25
Chapter 2: Materials and Methods 27
2.1 Tissue culture 27
2.1.1 Cell culture 27
2.1.2 Mycoplasma testing 28
2.1.3 Cryopreservation 28
2.1.4 Cell seeding 28
2.1.5 In vitro irradiation 29
2.1.6 RNA interference (RNAi) by reverse transfection 29
2.1.7 xCELLigence 30
2.2 Virological methods 30
2.2.1 Adenovirus propagation 30
2.2.2 Adenovirus purification 30
2.2.3 PicoGreen assay 32
2.2.4 Absolute quantification of genome copies 33
2.2.5 $TCID_{50}$ assay 34
2.2.6 Virus infection 34
2.2.7 Plaque assay 35

2.2.8 Assessment of endotoxin levels prior to in vivo use of virus 35
2.2.9 High performance liquid chromatography (HPLC) titration of virus concentration 36
2.3 Protein assays 37
2.3.1 Quantification of protein content 37
2.3.2 SDS-PAGE and western blot 37
2.3.3 Luciferase assays 40
2.3.4 Flow cytometry 41
2.3.5 Immunocytochemistry 42
2.4 Animal experiments 43
2.4.1 Housing and regulations 43
2.4.2 General anaesthesia 44
2.4.3 Xenograft implantation 44
2.4.4 Injection of substances 44
2.4.5 Tumour growth monitoring 44
2.4.6 In vivo irradiation 44
2.4.7 Bioluminescence imaging in vivo 45
2.4.8 Tumour homogenisation 45
2.5 Statistical analysis 45
Chapter 3: Interaction between oncolytic adenovirus and the DNA damage response 47
3.1 Introduction: Hypothesis and chapter aims 47
3.2 Results 50
3.2.1 Use of a GFP-expressing virus allows selective analysis of DDR foci formation in infected cells 50
3.2.2 Adenovirus infection is associated with increased γH2AX formation 56
3.2.3 Adenovirus infection reduces 53BP1 foci formation in irradiated cells 61
3.2.4 53BP1 is phosphorylated in EnAd-infected cells 65
3.2.5 Adenovirus infection reduces the formation of RAD51 foci following irradiation 69
3.2.6 Adenovirus infection is associated with decreased DNA ligase IV levels 77
3.3 Chapter main findings 81
3.4 Chapter discussion 81
Chapter 4: The impact of external beam radiation on virus production 90
4.1 Introduction: Hypothesis and chapter aims 90
4.2 Results 93
4.2.1 Irradiation causes an increase in EnAd viral genome production and infectious particle production in A549 cells in vitro 93
4.2.2 Irradiation leads to an increase in EnAd genome production and infectious particle production in vivo 102

4.2.3 Irradiation leads to a cell line-dependent increase in EnAd receptor levels 107
4.2.4 Irradiation does not lead to immediate or delayed increase in virus attachment and entry 115
4.2.5 Pre-irradiation leads to increased EnAd E1A expression 118
4.3 Chapter main findings 123
4.4 Chapter discussion 123
Chapter 5: Synergistic cytotoxicity using combination treatment Enadenotucirev and radiation . 129
5.1 Introduction: Hypothesis and chapter aims 129
5.2 Results 132
5.2.1 Development of a modified plaque assay to monitor virus spread 132
5.2.2 Pre-irradiation of cells increases EnAd spread through a cell monolayer 138
5.2.3 In vitro cytotoxicity of EnAd and radiation combination treatment 149
5.2.4 Early cytotoxicity in infected, irradiated cells in vitro suggests synergy between EnAd and radiation 151
5.2.5 Intravenous Enadenotucirev administration results in tumour growth delay and increased survival in mice receiving a single dose of radiation 153
5.3 Chapter main findings 156
5.4 Chapter discussion 156
Chapter 6: Discussion 161
6.1 Summary of findings 161
6.2 General discussion and future directions 161
6.3 Concluding remarks 167
BIBLIOGRAPHY 168

LIST OF ABBREVIATIONS

3’	3 prime end of DNA
5’	5 prime end of DNA
53BP1	p53-binding protein 1
#	fractions
/	per
°C	degrees Celsius
γH2AX	phosphorylated histone 2AX
µg	micrograms
µL	microlitres
µm	micrometres
A	area
Ad	adenovirus serotype
Alt-NHEJ	alternative non-homologous end joining
ANOVA	analysis of variance
ATM	ataxia-telangiectasia mutated
ATR	ATM- and RAD3-related
ATRIP	ATR-interacting protein
bp	base pair
BCA	Bicinchoninic Acid
BRCA	breast cancer gene
BSA	bovine serum albumin
CAR	coxsackie and adenovirus receptor
Cdc25	cell division cycle 25
CEDAR	Chemoradiation with Enadenotucirev as a Radiosensitiser in locally Advanced Rectal cancer
cGAS	cyclic GMP-AMP synthase
Chk1	Checkpoint kinase 1
Chk2	Checkpoint kinase 2
CI	confidence interval
CMV	cytomegalovirus immediate-early promoter
c-NHEJ	classical non-homologous end joining
CO_2	carbon dioxide
CPE	cytopathic effect
CsCl	caesium chloride
D	days
DAPI	6-diamidino-2-phenylindole
DBP	DNA binding protein
DDR	DNA damage response
DEPC	Diethylpyrocarbonate
DMEM	Dulbecco’s Modified Eagle Medium
DMSO	dimethyl sulphoxide
DNA	deoxyribonucleic acid
DNA-PKcs	DNA-dependent protein kinase catalytic subunit
ds	double-strand
DSG2	Desmoglein 2
E1b-AP5	E1b55K-associated protein 5
EDTA	Ethylenediaminetetraacetic Acid

EnAd	Enadenotucirev
ERK	extracellular signal-regulated kinase
EXO1	human exonuclease 1
FBS	foetal bovine serum
Fluc	Firefly Luciferase
FSC	forward scatter
g	gram
GFP	green fluorescent protein
g_n	gravitational force
Gy	Gray
H	height
h	hours
H_2O	water
HPLC	High performance liquid chromatography
HR	homologous recombination
HSV	Herpes Simplex Virus
IgG	Immunoglobulin G
i.v.	intravenous
IL-24	interleukin-24
IR	ionising radiation
IVIS	In Vivo Imaging System
kb	kilobase
kg	kilogram
kV	kilovolts
lacZ	β-galactosidase
LAL	Limulus Amebocyte Lysate
Ln	natural logarithm
Lum	luminescence
M	molar
mA	milliamperes
MAPK	mitogen-activated protein kinase
MDA-7	melanoma differentiation associated gene-7
MDC1	mediator of DNA damage checkpoint protein 1
mg	milligrams
min	minutes
mL	millilitres
MLP	major late promoter
mm	millimetres
MMEJ	microhomology-mediated end joining
MOI	multiplicity of infection
MRN	MRE11-Rad50-Nbs1
mRNA	messenger RNA
MTT	thiazolyl blue tetrazolium bromide
MW	molecular weight
NaCl	sodium chloride
n	nano
NHEJ	non-homologous end joining
NIS	sodium iodide symporter
no.	number
ns	not significant

OV	oncolytic virus
p53BP1	phosphorylated 53BP1
PAXX	paralog of XRCC4 and XLF
PBS	Phosphate buffered saline
PCR	polymerase chain reaction
PE	phycoerythrin
pen-strep	penicillin-streptomycin
PFU	plaque forming units
p.i.	post-infection
PI3K	phosphatidylinositol-3-kinase
PIKK	phosphatidylinositol-3-kinase-related kinase
PLK1	polo-like kinase-1
PML	promyelocytic leukaemia protein
pmol	picomole
PP2A	protein phosphatase 2A
p.t.	post-transfection
qPCR	quantitative PCR
RIF1	Rap1-interacting factor 1
RIPA	radioimmunoprecipitation assay
RNA	ribonucleic acid
RNAi	RNA interference
RNF	RING finger
RPA	replication protein A
rpm	revolutions per minute
s	second
SA	splice acceptor
s.c.	subcutaneous
SCID	severe combined immunodeficiency disease
SDS	Sodium dodecyl sulfate
SEM	standard error of the mean
Ser	serine
siRNA	short interfering RNA
SOC	standard of care
ss	single-strand
SSC	side scatter
STING	stimulator of IFN genes
TBI	total body irradiation
TBS	Tris-buffered saline
$TCID_{50}$	Tissue culture infectious dose
TE	Tris-EDTA
TOPBP1	topoisomerase-IIβ-binding protein 1
TREX1	three prime repair exonuclease 1
T-vec	Talimogene laherparepvec
UV	ultraviolet
V	volts
VP	virus particle(s)
VRC	viral replication centre
WT	wild-type
XLF	XRCC4-like factor
XRCC4	X-ray repair cross-complementing group 4

Chapter 1: Introduction

1.1 Introduction to radiation-induced DNA damage

Radiotherapy is one of the major forms of anti-cancer treatment, used alongside chemotherapy, surgical resection, immunotherapy, and targeted therapy to treat a range of tumour types. Cytotoxicity is thought to be predominantly due to ionising radiation (IR)-induced DNA damage, in particular unrepaired double-strand DNA (dsDNA) breaks [1]. The majority of radiotherapy treatment is with photons; damage occurs when energy from these is absorbed by cellular electrons, causing them to be ejected from molecules (ionisation) [2]. A cascade of events is put into motion as these electrons interact with surrounding structures, forming further highly unstable ions with the potential for the breakage of chemical bonds. Damage can occur due to direct action of these electrons on the molecules comprising DNA, or via the formation of free radicals (indirect action) [3] (Figure 1.1). The damage is not specific to DNA, however DNA comprises a comparatively large target which, for the majority of the cell cycle, is available in only two carefully maintained complementary copies. Double-strand DNA break formation as a result of ionising radiation can occur directly or through the combination of unrepaired single-strand breaks and may result in cell senescence, apoptosis, or mitotic catastrophe [4].

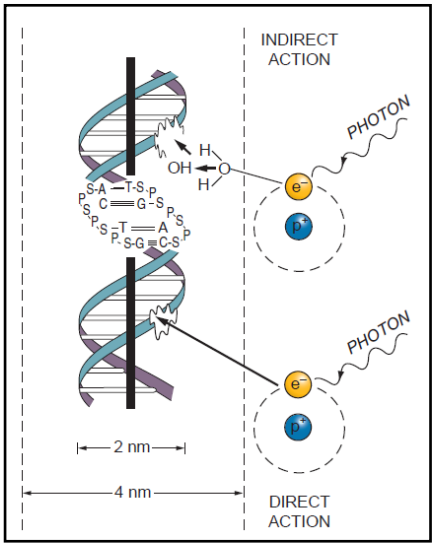


Figure 1.1 Direct and indirect action causing DNA damage. Figure taken from Hall and Giaccia [3]. Energy from a photon is absorbed into a cellular electron leading to ionisation. Indirect action (above) results from the electron interacting with cellular molecules (example shown here is water), resulting in the formation of free radicals which further act on DNA to cause damage. Direct action (below) results from direct action of the free electron on DNA. OH = hydroxyl radical; S = sugar; P = phosphorus; A = adenine; T = thymine; G = guanine; C = cytosine.

The inability to restrict IR-induced injury to the target area remains the great limitation of radiotherapy. Though current techniques allow greater precision in the delivery of the desired treatment dose to the tumour, avoidance of normal tissue toxicity whilst achieving adequate tumour control continues to be an ongoing challenge for radiation oncologists. Standard radical radiotherapy treatments use fractionated regimes to exploit the innate differences between normal and tumour tissue, allowing for treatment with doses high enough to eradicate the cancer, without exceeding pre-set targets for normal tissue tolerance above which unacceptable long-term toxicity effects are likely to occur. Five factors, known as the "5 Rs of Radiobiology", are proposed to determine the likely response to treatment with a fractionated regime [5, 6]. Four of these – repair of sub-lethal damage between fractions, tumour re-oxygenation, regeneration of surviving cells between doses, and redistribution through the cell cycle – were initially proposed by Withers in 1975 [5]. These however did not take into account the observation that some tumour types appear to be intrinsically more radiosensitive than others, thus the 5th R of Radiobiology was added in 1989 [6]. Repair of IR-induced damage is the radiobiological factor which is of particular relevance to the work in this thesis.

Repair can be through homologous recombination (HR) [7], classical non-homologous end joining (c-NHEJ) [8], alternative non-homologous end joining (alt-NHEJ) also known as microhomology-mediated end joining (MMEJ) [9], or single-strand annealing [10]. There is remarkable evolutionary conservation of key aspects of NHEJ and HR, such as the Mre11-Rad50 complex which acts as a sensor of dsDNA breaks, and homologs of Ku protein, a central component of NHEJ [8, 11-16], highlighting the importance of these pathways in cell survival.

The choice of repair pathway is highly dependent on cell cycle phase and the type of DNA lesion present. It is regulated by an interplay of different cellular proteins, however one of

the key steps is dsDNA break resection [17, 18]. This is necessary for HR, but not NHEJ. Thus, if the cell is in the S or G2 phase, cyclin-dependent kinases phosphorylate CtIP which enables resection alongside MRN, promoting HR over NHEJ [18]. The main mechanisms involved in repair of dsDNA breaks will be briefly discussed below.

1.1.1 Homologous recombination repair

HR is utilised when a sister chromatid is available to act as a template in the S and G2 phases of the cell cycle [19]. Though relatively slow, this is a more accurate repair mechanism than NHEJ. As discussed above, HR is initiated through sensing and binding of the MRE11-Rad50-Nbs1 (MRN) complex to the dsDNA break and phosphorylation of CtIP, promoting 5' – 3' end resection and processing through the action of MRN, CtIP, BLM Helicase, and EXO1 nuclease [17, 18]. MRN further recruits ataxia-telangiectasia mutated (ATM) protein, a member of the phosphatidylinositol-3-kinase-related kinase (PIKK) family which is key in mediating the cellular signaling response to dsDNA breaks. The 3' single-stranded DNA (ssDNA) overhangs are coated with replication protein A (RPA) in a CtIP- and MRN-dependent manner. RPA is displaced by RAD51, a step mediated by breast cancer gene 2 (BRCA2) and Rad52 [20]. BRCA2 localisation to dsDNA damage sites is promoted by BRCA1 in association with PALB2 [21]. RAD51 is key in mediating nucleoprotein filament strand invasion of a homologous DNA sequence from the sister chromatid, generating a D-loop intermediate. New DNA is synthesised from the 3' end along the sister chromatid, forming a double Holliday junction. The process ends with resolution of the junction, resulting in crossover or non-crossover products, and finally annealing of the resulting DNA ends (Figure 1.2A). Though we have discussed the key members of this pathway, a number of other proteins play important roles in HR, including Rad54, and the Fanconi anaemia genes. Mutations in the BRCA and Fanconi anaemia genes in particular result in a predisposition to the development of cancer [2, 10, 22, 23].

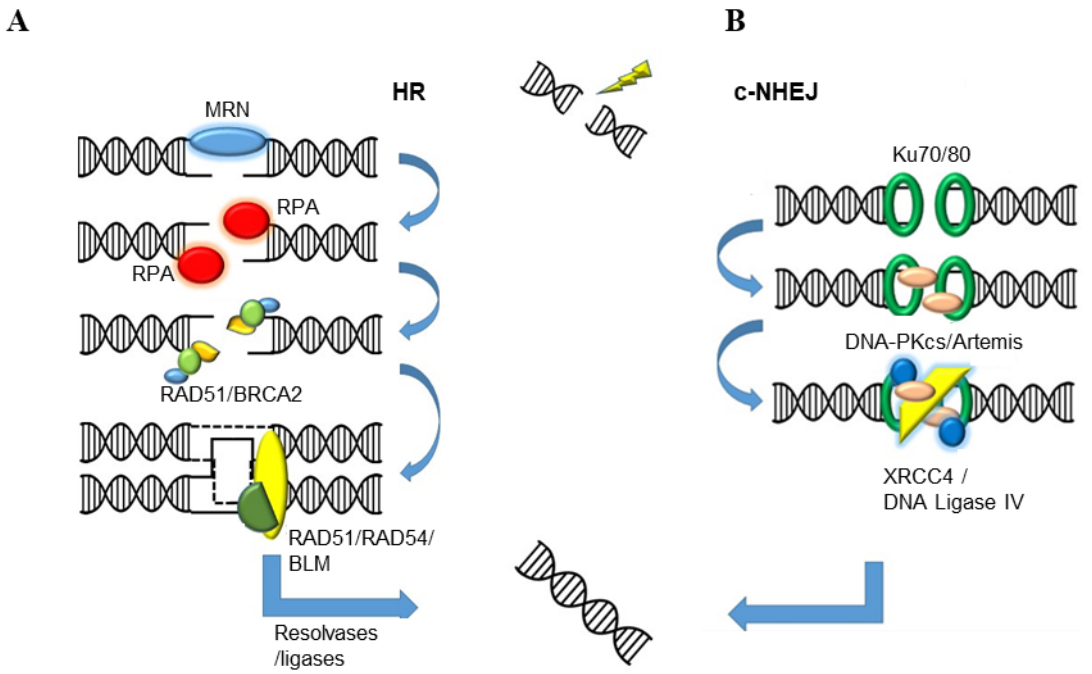


Figure 1.2 The homologous recombination (HR) and classical non-homologous end joining (c-NHEJ) pathways. Figure adapted from O'Cathail *et al*. [94] (**A)** MRN binds to the dsDNA break and processes DNA into 3' single-stranded overhangs which are subsequently coated by RPA. This is displaced by RAD51, which mediates strand invasion of a homologous sequence from the sister chromatid, generating a D-loop intermediate. DNA synthesis along the sister chromatid results in a double Holliday junction. Resolution of the junction and the ligation of the resulting DNA ends can result in crossover or non-crossover products. **(B)** The Ku heterodimer composed of Ku70/Ku80 binds DNA ends and recruits DNA-PKcs. This autophosphorylates and phosphorylates Artemis, which processes DNA ends prior to ligation. Polymerases may further add nucleotides. DNA Ligase IV and XRCC4 complex ligate the DNA ends. MRN = MRE11-Rad50-Nbs1; RPA = replication protein A; BRCA2 = breast cancer gene 2; DNA PKcs = DNA-dependent protein kinase catalytic subunit; XRCC4 = X-ray repair cross-complementing group 4.

1.1.2 Classical non-homologous end joining

C-NHEJ is the primary mechanism of dsDNA repair used in mammalian cells as it can occur at any point in the cell cycle. It is also responsible for processing dsDNA breaks that occur during V(D)J recombination [24]. It is relatively rapid, but more prone to inaccurate repair than HR as it does not utilise a template.

During G1 phase, c-NHEJ is promoted over HR by p53-binding protein 1 (53BP1) binding to damaged chromatin and preventing DNA end resection via recruitment of RIF1 [25, 26]. BRCA1 acts to counteract this [27]; pathway choice following dsDNA breaks is therefore

partially mediated through the antagonistic function of these two proteins. Isono *et al.* have demonstrated that ATM-mediated phosphorylation of 53BP1, and subsequent recruitment of RIF1, occurs in S/G2 as well as G1 phase, however BRCA1 acts to enhance PP4C-dependent dephosphorylation of 53BP1, thus favouring HR repair [28]. 53BP1 has a number of other functions alongside regulating dsDNA break repair pathway choice, including as a 'scaffold' involved in recruiting other DDR proteins to the damaged chromatin, and to amplify ATM activity [25].

Repair by c-NHEJ is initiated through binding of the Ku heterodimer consisting of Ku70 and Ku80 to DNA ends, which stabilises them and prevents resection. DNA-dependent protein kinase catalytic subunit (DNA-PKcs) is subsequently recruited, acting to form a bridge between the ends and acts to phosphorylate a number of targets, including itself and Artemis. Artemis acts to process DNA ends through its nuclease activity. Unlike HR however, extensive end resection does not occur. Nucleotide addition by members of the Pol X family is one further potential method of DNA end processing during NHEJ, also contributing to the possible variation in outcome when using this repair mechanism. The DNA ligase complex enables ligation of the DNA ends. This comprises primarily DNA ligase IV and X-ray repair cross-complementing group 4 protein (XRCC4). XRCC4-like factor (XLF) and paralog of XRCC4 and XLF (PAXX) are also thought to support ligation by this complex (Figure 1.2B). Crucially, this process is not linear: some steps may not occur at all during an NHEJ repair event, whereas others may occur multiple times. Overall, this results in a number of potential outcomes from one single dsDNA break [2, 10, 24, 29, 30].

1.2 The concept of virotherapy

Oncolytic virotherapy uses lytic viruses that replicate selectively within cancer cells. This approach combines targeted cytotoxicity with amplification of the therapeutic agent actually

within tumour cells. With the first Federal Drugs Administration approval of an oncolytic virus (OV), Talimogene laherparepvec (T-vec) in 2015 [31], interest in oncolytic virotherapy is rapidly expanding. This is, however, a field which has been developing for many years [32] and a wealth of information is now available on the ways in which these viruses can be incorporated in the current anti-cancer therapeutic paradigms [33].

A range of oncolytic viruses are currently undergoing clinical trials, including adenovirus, vaccinia virus, herpes simplex virus (HSV), reovirus, poxvirus, coxsackievirus, Newcastle disease virus, measles virus, parvovirus, Seneca Valley Virus, poliovirus and vesicular stomatitis virus [34]. Table 1.1, taken from Kaufman *et al.*, provides detail on the individual oncolytic viruses used in clinical trials, alongside the cancer types targeted and any modifications which have been made in comparison to wild-type (WT) [34].

Table 1.1 Key oncolytic viruses in clinical trials

Virus	Manufacturer	Modification	Number of clinical trials			Cancers
			Phase I	Phase II	Phase III	
Adenovirus						
Onyx-015	Onyx Pharmaceuticals	Type 2/5 chimaera, E1B deletion	6	6	0	Head and neck cancer, pancreatic cancer, ovarian cancer, colorectal cancer, gliomas, lung metastases, and liver metastases
H101	Shanghai Sunwaybio	E1B deletion, partial E3 deletion	1	2	1	Squamous cell carcinoma and head and neck cancer
DNX-2401	DNAtrix	Δ24-RGD insertion	4	0	0	Glioblastoma, ovarian cancer
VCN-01	VCN Biosciences	PH20 hyaluronidase insertion	2	0	0	Pancreatic cancer
Colo-Ad1	PsiOxus Therapeutics	Chimeric Ad11/3 group B	1	2	0	Colon cancer, NSCLC, renal cancer, bladder cancer, and ovarian cancer
ProstAtak	Advantagene	TK insertion	4	1	1	Pancreatic cancer, lung cancer, breast cancer, mesothelioma, and prostate cancer
Oncos-102	Oncos Therapeutics	Δ24-RGD-GM-CSF insertion	1	0	0	Solid cancers
CG0070	Cold Genesys	GM-CSF and E3 deletion	1	1	1	Bladder cancer
Vaccinia virus						
Pexa-vac (JX-594)	Jennerex Biotherapeutics	GM-CSF insertion, TK disruption	7	6	0	Melanoma, liver cancer, colorectal cancer, breast cancer, and hepatocellular carcinoma
GL-ONC1	Genelux	TK disruption, haemagglutin disruption, F14.5L disruption	4	1	0	Lung cancer, head and neck cancer, and mesothelioma
Herpesvirus						
T-VEC	Amgen	ICP34.5 deletion, US11 deletion, GM-CSF insertion	2	3	2	Melanoma, head and neck cancer, and pancreatic cancer
G207	Medigene	ICP34.5 deletion, UL39 disruption	3	0	0	Glioblastoma
HF10	Takara Bio	UL56 deletion, selected for single partial copy of UL52	2	1	0	Breast cancer, melanoma, and pancreatic cancer
SEPREHVIR (HSV1716)	Virttu Biologics	ICP34.5 deletion	5	1	0	Hepatocellular carcinoma, glioblastoma, mesothelioma, neuroblastoma
OrienX010	OrienGene Biotechnology	ICP34.5 deletion, ICP47 deletion, GM-CSF insertion	1	0	0	Glioblastoma
Reovirus						
Reolysin	Oncolytics Biotech	None	15	9	0	Glioma, sarcomas, colorectal cancer, NSCLC, ovarian cancer, melanoma, pancreatic cancer, multiple myeloma, head and neck cancer
Seneca Valley Virus						
SVV-001	Neotropix	None	3	1	0	Neuroendocrine-featured tumours, neuroblastoma, and lung cancer
Coxsackievirus						
Cavatak (CVA21)	Viralytics	None	3	1	0	Melanoma, breast cancer, and prostate cancer

Taken from Kaufman *et al.* [34]. GM-CSF = granulocyte-macrophage colony-stimulating factor; NSCLC = non-small-cell lung cancer; RGD = Arg-Gly-Asp motif; TK = thymidine kinase; US11 = unique short 11 glycoprotein.

The mechanism through which oncolytic viruses lead to tumour cell death varies between types, however it is the ability of certain oncolytic viruses to interact with and inhibit the DNA damage response which is of particular interest with regards to combining treatment with radiotherapy [35]. Nuclear-resident DNA viruses might be particularly sensitive to cellular DNA repair mechanisms, and therefore could have developed strategies to interact with these cellular factors to protect viral DNA from unwanted repair [36].

1.3 Adenoviruses

Adenoviruses, named for the tissue type in which they were originally discovered, were first isolated in 1953 [37, 38]. Different strains have since been found to cause acute respiratory infections, infantile gastroenteritis and conjunctivitis, as well as severe infections in immunocompromised individuals [39].

There are now 51 human serotypes which have been identified based on haemagglutination properties, and over sixty human adenoviruses in total, classified according to genotyping and subdivided into seven subgroups (A-G) [39-42]. All adenoviruses are nonenveloped and composed of an icosahedral protein shell containing a linear dsDNA genome. The protein capsid is primarily composed of hexon capsomers, with a penton capsomer and fiber shaft and knob at each vertex [43, 44].

A great deal of the information available on adenovirus properties stems from studies on adenovirus serotypes 2 and 5 (Ad2 and Ad5), both of which belong to group C. The virus genome has been shown to contain five early transcription units, three delayed early transcription units, and a late transcription unit [39]. The early transcription units, so named as they are primarily transcribed at the early stage of the virus life cycle, are E1A, E1B, E2, E3, and E4. Briefly, the E1A transcriptional unit is responsible for two principal proteins which act to induce transcription and host cell entry into S phase [45]. E1B produces two proteins which are involved in blocking apoptosis. The three proteins produced from the E2 unit function in DNA replication, E3 products modulate the host antiviral immune response, and finally the E4 proteins have a number of interesting disparate functions, the most relevant of which to this thesis is inhibition of the cellular DNA damage response [39, 44, 46].

The delayed early transcription units and late transcription unit, as the names suggest, come into play later on in the virus life cycle (approximately 5-6 hours after the start of infection) [44]. The early delayed transcription units (IX, IVa2 and E2 late) are used in the production and assembly of the capsid components [41]. The late transcription unit, under control of the major late promoter (MLP), is processed to generate five families of late mRNA [39].

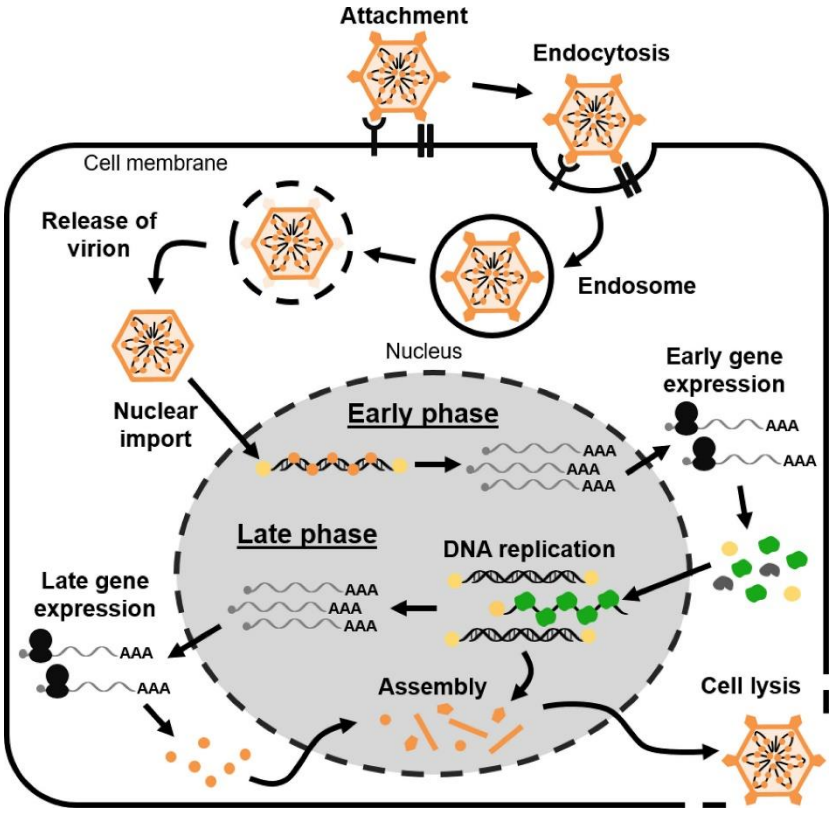


Figure 1.3 The adenovirus replication cycle. Figure taken from Charman *et al.* [41]. Adenovirus utilises cellular receptors such as coxsackie and adenovirus receptor (CAR, groups A, C, D, E, F) or Desmoglein 2/CD46 (group B). Endocytosis into early endosomes, viral disassembly and escape from the endosome occur prior to transport to the nuclear pore complex where viral DNA enters the nucleus. Early transcription units are primarily transcribed during the early phase, the late phase begins at DNA replication. Progeny virions are assembled and released through cell lysis.

The adenovirus replication cycle (illustrated in Figure 1.3, taken from Charman *et al.* [41]) begins with binding of virus to cellular receptors. The coxsackie and adenovirus receptor (CAR) was initially identified as the receptor utilised by group C adenoviruses such as Ad2/Ad5 [47]; and has since been shown to also be recognised and utilised by members of

groups A, C, D, E, and F [48]. Group B adenoviruses such as Ad11 and Ad3, however, bind via CD46 and Desmoglein 2 (DSG2) [49, 50]. Binding is followed by internalisation into early endosomes via clathrin-mediated endocytosis and virus particle disassembly. Viral nucleocapsids escape the endosome and undergo cytoplasmic transport to the nuclear pore complex via microtubules; there, viral DNA is imported into the nucleus [41, 51]. Viral gene expression occurs as discussed above; once early viral gene expression has taken place, viral DNA replication and the late phase begins, resulting in the production of the components of new virus particles. Infectious cycle length in HeLa cells lasts approximately 24-36 hours [39].

1.4 Oncolytic adenoviruses and the DNA damage response

Inhibition of the cellular DDR appears to be a key part of the normal adenovirus replication cycle (Figure 1.4) [52]. It is hypothesised that this is to prevent the linear double-stranded DNA viral genome from being recognised by the cell as a double-strand DNA break, potentially leading to concatemerisation of virus genomes [53, 54]. This was first observed using a range of mutant adenovirus type 5 and type 2 on KB cells, a human epidermoid cell line. The mutations were all located in the E4 region of the genome and, when both E4orf3 and E4orf6 regions were mutated, concatemerisation of the viral genome was noted [55].

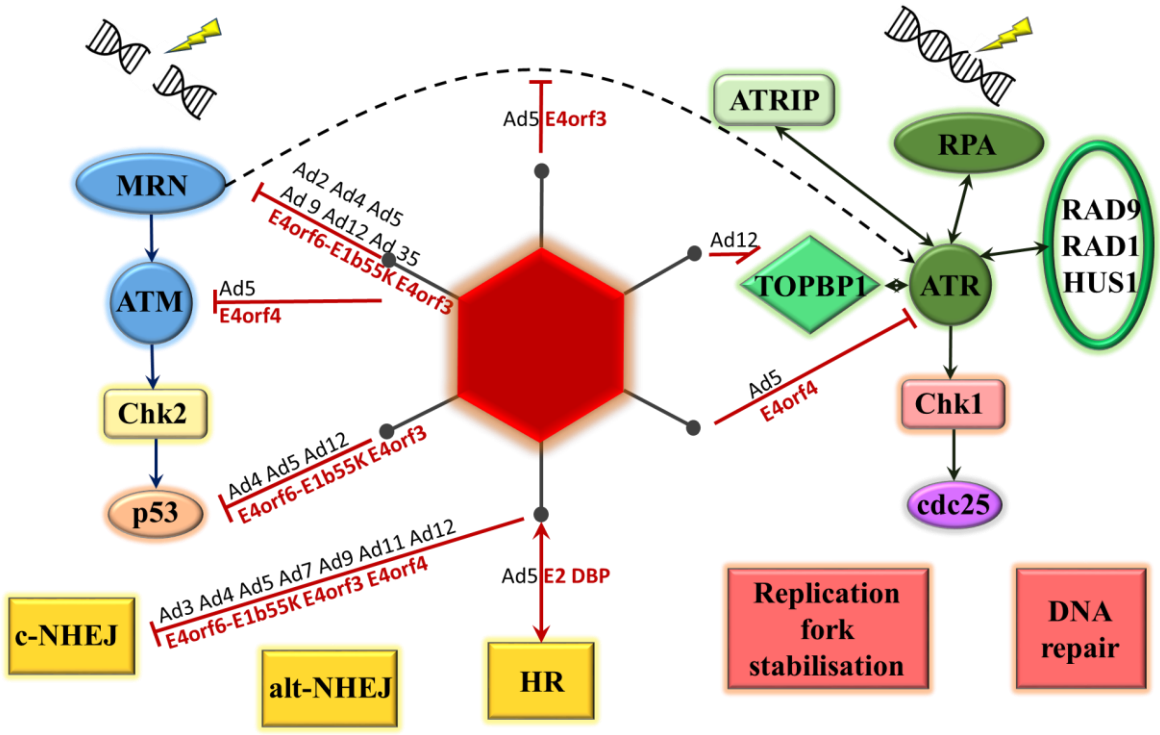


Figure 1.4 Interactions between DDR and adenovirus. Adapted from O'Cathail *et al.*[94]. Adenovirus proteins interact with the DNA damage response to double-strand DNA breaks (shown on the left) as well as recognition of single-stranded DNA (shown on the right) at multiple levels along the pathway. Adenovirus serotypes known to demonstrate interaction with the protein/complex of interest are denoted in black; Ad5 protein mediating the interaction is denoted in red. MRN = MRE11–Rad50–Nbs1; ATM = ataxia-telangiectasia mutated; Chk2 = checkpoint kinase 2; c-NHEJ = classical non-homologous end joining; alt-NHEJ = alternative non-homologous end joining; HR = homologous recombination; RPA = replication protein A; ATR = ATM- and RAD3-related; ATRIP = ATR-interacting protein; TOPBP1 = topoisomerase-IIβ-binding protein 1; Chk1 = checkpoint kinase 1; cdc25 = cell division cycle 25.

1.4.1 The effect of virus proteins on the MRN complex

As described above, the key cellular factor involved in sensing dsDNA damage is the MRN complex. The majority of the evidence relating to the interaction between adenoviral proteins and the DNA damage response is consistent with an effect on this complex. This was initially demonstrated by Stracker *et al.* [56]. Adenoviral genome concatemers formed in cells infected with Ad5 lacking the E4 region, but not with WT virus. However, no concatemers formed following infection with this mutant virus in cell lines containing any of mutant DNA ligase IV, DNA-PKcs, Nbs1 or Mre11, suggesting these cellular proteins are all required for recognition and concatemerisation of the adenoviral genome. In addition,

in cells infected with the E4 mutant virus, the MRN complex could be seen to form foci surrounding viral replication centres (VRCs). This paper was the first to provide evidence for MRN degradation mediated by the Ad5 E4orf6-E1b55K complex and MRN mislocalisation mediated by Ad5 E4orf3 [56]. These two mechanisms of MRN inhibition will be briefly explored below.

1.4.1.1 Degradation of the MRN complex

Stracker *et al.* initially demonstrated that intracellular levels of Mre11, Rad50, and Nbs1 decreased following infection with wild-type Ad5. This was due to enhanced protein turnover and was not seen following infection with E4-deficient Ad5. Infection with Ad5 mutants lacking different E4 genes demonstrated there was no degradation of Mre11 and Rad50 when cells were infected with Ad5 specifically lacking E4orf6-E1b55K. Furthermore, transfection of 293 cells with an E4orf6 expression vector resulted in Mre11 and Rad50 degradation, but not transfection with an expression vector containing mutant E4orf6 unable to form a complex with E1b55K. These therefore demonstrated that MRN degradation following infection with Ad5 is mediated by the E4orf6-E1b55K complex [56]. Karen *et al*. further showed that this MRN degradation occurs prior to viral DNA accumulation [54].

The majority of evidence available is on the function of Ad5 proteins. Stracker *et al.* compared effects on MRN following infection with Ad5, Ad4, and Ad12. Infection of HeLa cells with all three serotypes led to decreased levels of Mre11 and Rad50. Likewise, transfection of 293 cells, which stably express Ad5 E1b55K, with plasmids encoding E4orf6 from these serotypes led to degradation of all MRN components as well as p53. These results suggest that the ability of the E1b55K-E4orf6 complex to cause MRN degradation is conserved between these serotypes [57]. MRN degradation has now been demonstrated

following infection with Ad2, Ad4, Ad5, and Ad12, but not following infection with Ad3, Ad7, Ad9, and Ad11 [58, 59]. Infection with Ad35 interestingly appears to cause degradation of Rad50, without an effect on Mre11 or Nbs1 [59]. Therefore, although MRN degradation does appear to be targeted by a range of adenovirus serotypes, this is not conserved across all serotypes.

1.4.1.2 Relocalisation of the MRN complex

Stracker *et al*. demonstrated that early after infection by Ad5 there appears to be relocalisation of the MRN complex to areas of nuclear speckles partially overlapping with promyelocytic leukaemia protein (PML) [56]. In uninfected cells, PML is found in oncogenic domains (PODs/ND10), however Ad5 E4orf3 causes relocalisation of PML into nuclear tracks [56, 60, 61]. This function appears to be conserved across serotypes and has been demonstrated for Ad2, Ad4, and Ad12 E4orf3 [57, 61].

Stracker *et al*. further showed that this MRN relocalisation does not occur following infection with Ad5 lacking E4orf1 to E4orf3. Transfection of 293 cells with different expression vectors showed that expression of E4orf3 is sufficient for relocalisation of the MRN complex to occur. The relocalisation of MRN can therefore be linked directly to expression of Ad5 E4orf3 [56].

It has since been demonstrated that, at later time points of infection, Ad5 E4orf3 causes redistribution of the MRN complex to large single juxtanuclear cytoplasmic accumulations suggestive of aggresomes. These contain both E4orf3 and E1b55K, but seem to be able to form in the absence of the latter [62, 63]. Aggresomes are areas of ubiquitin-rich cytoplasmic inclusions containing aggregated misfolded proteins and surrounded by a cage of the intermediate filament protein vimentin. They are proposed to be a cellular response to undegraded, aggregated protein [64] and their formation has been linked to a number of

degenerative diseases [65]. Infection of A549 cells with an E4orf6/E4orf3 mutant Ad5 has been shown to greatly delay both aggresome formation and Mre11 localisation to these areas, but not infection with Ad5 lacking only one of these viral proteins. Therefore, both Ad5 E4orf3 and E4orf6 can be seen to be key proteins involved in Mre11 relocalisation during adenovirus infection, and appear to be functionally redundant [63]. This relocalisation to the cytoplasm accelerates degradation, thereby acting to protect the viral genome from recognition by the MRN complex and subsequent concatemerisation [63].

Evidence provided by Liu *et al*. suggests E1b55K also plays an important role in the formation of MRN-containing cytoplasmic aggresomes. They utilised leptomycin B to inhibit an exportin interacting with an E1b55K nuclear export signal. In cells infected with an Ad5 E4orf6 deletion mutant, which allows visualisation of MRN without its degradation, leptomycin B caused inhibition of Mre11 relocalisation from the nucleus to juxtanuclear aggresomes. Furthermore, addition of leptomycin B to wild-type Ad5 infected cells resulted in a decreased rate of Mre11 depletion. Finally, there was minimal exportation of Mre11 out of the nucleus following infection of cells with either an E1b55K deletion mutant Ad5 or Ad5 containing mutant E1b55K unable to bind MRN. These results suggest E1b55K plays an important role in the relocalisation and degradation of the MRN complex following infection with Ad5 [63].

Interestingly, when comparing the effects of Ad5 E4orf3 with that of Ad4 and Ad12, belonging to Groups E and A, respectively, Stracker *et al*. found that, though Nbs1 appeared to be relocated away from VRCs following infection with Ad5, Ad4 and Ad12 did not have the same effect. These results would suggest there are some differing effects on the relocalisation of MRN components by different viral serotypes [57], a finding which has since been confirmed using a range of adenoviruses [58, 59]. Forrester *et al*. demonstrated that Ad5, Ad9, and Ad4 infection caused Mre11 relocalisation to PML tracks, whereas

infection with Ad3, Ad7, Ad11, and Ad12 resulted in relocalisation of Mre11 to VRCs, as demonstrated by areas of RPA32 staining [58]. Pancholi and Weitzman focused on co-localisation of MRN members with VRCs and confirmed that Mre11 was sequestered away from VRCs in cells infected with Ad2, Ad4, Ad9, and Ad5, but not following infection with Ad12 and Ad35 [59].

The evidence therefore suggests that different virus serotypes have varying effects on the MRN complex. Surprisingly however, this does not appear to directly correlate to the impact of functional MRN on virus replication [59]. Pancholi and Weitzman utilised matched cells with or without functional Nbs1 to assess the effect of MRN deficiency on the replication of a range of Ad5 constructs, Ad2, Ad4, Ad9, Ad12, and Ad35. The addition of functional Nbs1 had no impact on the replication of Ad5 expressing either E4orf3 or E4orf6, or on Ad2 or Ad4, all serotypes causing MRN degradation and mislocalisation as part of their life cycle. Nonetheless, Ad12, which is also known to cause degradation of MRN, demonstrated enhanced replication in Nbs1 deficient cells, as did Ad9 which induces MRN mislocalisation. Further, Ad35 replication was decreased in the presence of functional MRN, despite the finding that this serotype is associated with degradation of Rad50 [59]. A number of complex interactions between different virus serotypes and components of the DDR are therefore likely to contribute to the spectrum of effects seen following adenovirus infection.

1.4.2 The effects of virus proteins on phosphatidylinositol-3-kinase-related kinase (PIKK) family

ATM and ATM- and RAD3-related (ATR), both members of the PIKK family of protein kinases, play pivotal roles in the cellular response to DNA damage. Brestovitsky *et al*. presented some data on the role of Ad5 E4orf4 in inhibiting the DNA damage response through effects on these proteins and their substrates [66]. Comparison of the

phosphorylation status between cells infected with an Ad5 E4 deletion mutant and an Ad5 E4 deletion mutant expressing only E4orf4 was carried out. Addition of E4orf4 significantly decreased the levels of phosphorylation of all ATM and ATR pathway proteins tested. This was shown to be dependent on E4orf4 interaction with the cellular protein phosphatase 2A (PP2A), which is known to dephosphorylate a number of proteins involved in the DDR including ATR, ATM, DNA-PK and a range of their substrates. Both the cytopathic effect of E4orf4 and viral replication were significantly enhanced in cells lacking wild-type ATM and treated with an ATR inhibitor. Lack of wild-type ATM appeared to be beneficial during the early part of the virus life cycle and ATR inhibition during the late part of the virus life cycle. Moreover, expression of E4orf4 alone in cells was sufficient to inhibit DNA damage repair and to sensitise cells to the effects of genotoxic drugs even out with the context of infection. These results suggest inhibition of ATM and ATR is beneficial for the Ad5 viral life cycle and is mediated via an interaction between E4orf4 and PP2A.

1.4.2.1 *The effects of virus proteins on ATM*

It has been suggested that, in the context of infection with Ad5 mutant viruses lacking E4 and unable to interfere with the MRN complex, ATM plays an important role in viral inhibition [67]. Given this and the results presented by Brestovitsky *et al*. [66] it is perhaps somewhat surprising that Forrester *et al*. demonstrated that infection of HeLa cells with Ad3, Ad4, Ad5, Ad7, Ad9, Ad11, and Ad12 all resulted in an increase in KAP1 phosphorylation, a marker of ATM activation [58]. Pancholi and Weitzman further showed that infection with Ad2, Ad4, Ad9, Ad12, and Ad35, but not with Ad5, resulted in increased ATM autophosphorylation and localisation to VRCs [59]. These results suggest all viral serotypes investigated caused activation of ATM, however the kinetics of this varied between different serotypes.

Two different mechanisms of ATM activation secondary to Ad5 infection have previously been proposed. The first is thought to be localised MRN-mediated ATM activation associated with blocking of viral genome replication at the earliest stages of the viral life cycle, prior to MRN inhibition by viral proteins. The second is an MRN-independent, global ATM activation which occurs subsequent to viral genome replication and does not impact on the viral replication cycle [68]. Thus, the increase in KAP1 phosphorylation representative of increased ATM activity following Ad5 infection would not be necessarily associated with a direct impact on viral replication.

1.4.2.2 *The effects of virus proteins on ATR*

ATR is traditionally associated with recognition of single-stranded DNA [69]. It would initially seem counter-intuitive for DNA viruses to have developed mechanisms of ATR interaction, nonetheless there is evidence that this is the case with adenovirus [66, 70, 71]. It is frequently seen that infection with Ad5 leads to widespread histone 2AX phosphorylation (γH2AX) [72, 73]. γH2AX is usually a marker for double-strand DNA breaks, however following infection it can be seen throughout the nucleus. Nichols *et al*. demonstrated that, in adenovirus-infected cells, the greatest decrease in phosphorylation of H2AX following inhibition of ATM, ATR or DNA-PK was seen following ATR inhibition, suggesting that ATR is the primary mediator of adenovirus-induced H2AX phosphorylation. Large amounts of diffuse nuclear-wide γH2AX phosphorylation were seen after the onset of viral genome replication, and some γH2AX forming distinct nuclear foci was seen following input of viral DNA at high multiplicities [72]. This suggests there is a cell response to the presence of viral DNA and potentially a mechanism by which there is ATR stimulation in response to viral replication. As ATR is known to respond to a wide range of cellular stresses [74] it may be that viral replication is a sufficient cell stressor to cause this. Alternatively, it has been demonstrated that a significant number of single-stranded DNA sequences are

generated during viral replication [75]. The virus may therefore have developed a mechanism to interact with ATR to prevent this stage of the viral replication cycle from causing cell cycle arrest.

E1b-AP5 (E1b55K-associated protein 5) is a cellular protein which binds E1b55K in both Ad5-infected and Ad5-transformed cells [76]. Blackford *et al*. have demonstrated that, in non-infected cells, this protein is localised to the nucleus, but excluded from nucleoli. In cells infected with Ad5 and Ad12, however, E1b-AP5 levels increase and it is redistributed to VRCs where is co-localises with RPA32. Moreover, infection with these virus serotypes also seemed to lead to relocalisation of ATR-interacting protein (ATRIP) to viral replication centres and co-localisation with RPA. The two different viral serotypes appeared to have different effects on ATR kinase substrates. Whereas Ad12 infection was associated with marked E1b-AP5 and ATR-dependent hyperphosphorylation of RPA32 as well as hyperphosphorylation of Rad9, Ad5 infection did not have this effect, adding evidence that different virus serotypes have varying effects on the cell's DNA damage response pathway [77]. Forrester *et al*. have provided further evidence in support of this. The effect on Checkpoint kinase 1 (Chk1) phosphorylation, an ATR substrate, in response to infection with different virus serotypes was investigated. The authors demonstrated that the overall effect on phosphorylation levels, as well as the timeline over which changes took place, differed markedly between serotypes [58]. In addition, the ATR-activator protein topoisomerase-IIβ-binding protein 1 (TOPBP1) was degraded following infection with Ad12, but not with other viral serotypes investigated [58, 71].

Carson *et al*. provide evidence that the inhibition of ATR function by Ad5 is through effects on MRN. Cell lines with hypomorphic mutations in either Nbs1 or Mre11 were infected with either wild-type or E4-deleted Ad5. Results were compared when these cell lines were transduced with Nbs1 or Mre11 wild-type cDNA. There was decreased phosphorylation of

the ATR substrates Chk1 and RPA32, suggesting decreased ATR function, when cells infected with E4-deleted Ad5 did not express wild-type Nbs1 or Mre11. Furthermore, infection of HeLa cells with an E4-deleted Ad5 mutant virus lead to phosphorylation of Chk1 and RPA32. This was markedly decreased in cells infected with Ad5 expressing E4orf3, but not in cells infected with Ad5 expressing E4orf6 or E1b55K. The authors did not find this effect on ATM signalling. Interestingly, when HeLa cells were infected with Ad5 mutants lacking E4, transfection with an Ad5 E4orf3 expression vector was sufficient to lead to a decrease in phosphorylation of Chk1 and RPA32. This was not however the case following transfection with an Ad12 E4orf3 expression vector or with an Ad5 E4orf3 expression vector mutated to abrogate the protein's ability to mislocalise MRN. Ultimately the authors provided evidence that MRN is key in the hyperphosphorylation of ATR substrates following infection with Ad5 lacking E4, and that this can abrogated through expression of Ad5 E4orf3 and subsequent mislocalisation of the MRN complex [70].

1.4.3 The effects of virus proteins on p53

The full range of p53's effects within the cell are still being elucidated, however it is clear that p53 has an inherent role in the cell's response to stressors and DNA damage [78, 79]. It is therefore perhaps no surprise that its function is targeted by adenoviruses, though the exact effects of this targeting appear to vary between serotypes. Ad5 E4orf3 and E4orf6 are known to have an effect on p53 through interaction with the E1b55K protein [80, 81]. Liu *et al*. have demonstrated that Ad5 E1b55K co-localises with p53 to aggresomes. Following transfection of 293 cells with E4orf6, the majority of cells demonstrated p53 depletion, and in those cells where p53 was visible it was associated with E4orf6 in aggresomes [63]. Harada *et al*. used a proteomics-based approach to demonstrate that the E1b55K-E4orf6 complex interacts with a number of cellular proteins to lead to the polyubiquitination of p53

in vitro [82]. It is thought that E1b55K-E4orf6 therefore leads to p53 depletion through ubiquitin-dependent proteasome-mediated destruction.

The degradation of p53 does not appear to be conserved across all virus serotypes tested. Forrester *et al*. have demonstrated that, though infection with Ad4, Ad5, and Ad12 (belonging to Groups E, C, and A respectively) leads to p53 degradation, this does not occur following infection with the group B members Ad3, Ad7, and Ad11, or with the group D serotype Ad9. Interestingly, there appeared to in fact be a marked increase in p53 levels in cells infected with Ad3, Ad7, and Ad11. The authors present evidence that this is, however, not transcriptionally active. It was shown that MDM2 levels were decreased following infection with all virus serotypes investigated, including those associated with increasing levels of p53. Furthermore, following Ad3 and Ad7 infection of cells containing a p53 plasmid and a luciferase reporter construct, though there was a significant increase in p53 levels, there was only a minor increase in reporter transcription. Cells infected with these virus serotypes demonstrated decreased protein levels of p21, a p53-regulated gene, secondary to decreased levels of p21 mRNA [58].

It remains to be seen how this variable interaction between p53 and the different adenovirus serotypes will impact on a potential synergistic effect with radiotherapy. The role of p53 within the cell is a complex and far-reaching one, hence its moniker “the guardian of the genome” [83]. In particular, p53 inactivation is key in oncogenesis and it is mutated in approximately 50% of all cancers [84]. Its function as a key modulator of apoptosis is therefore in balance with that of a DNA damage responder. Wild-type p53 is associated with enhanced chemosensitivity and radiosensitivity, but the exact p53-mediated cellular response to these stressors appears to be reliant on a range of cellular factors [85]. As such, given the complex interactions between adenovirus infection and the cellular stress

response, it is difficult to predict which p53 transcriptional pathway will ultimately be most affected by combination therapy.

1.4.4 Effects of adenovirus on DNA repair proteins

1.4.4.1 Effects of virus proteins on NHEJ

A physical interaction between an oncolytic viral protein and a protein heavily involved in the DNA damage response was first demonstrated by Boyer *et al*. [86]. Glioma cells with or without DNA-PK were infected with either wild-type Ad5 or a mutant lacking E4. Concatemers formed in cells expressing DNA-PK when these were infected by mutant virus, but not wild-type. Interestingly, no concatemerisation was seen in cells lacking DNA-PK, and following plasmid transfection of 293 cells with plasmids expressing DNA-PK and either E4orf6 or E4orf3, there appeared to be co-immunoprecipitation of DNA-PK and these viral proteins. More recently, an interaction has also been demonstrated between E4orf4 and DNA-PKcs [87]. This was shown to be biphasic in nature, with DNA-PKcs appearing to be beneficial to E4orf4-mediated inhibition of ATR and ATM function during the early part of the virus replication cycle, but to be inhibited itself at later stages.

The major effect of multiple virus serotypes on NHEJ has now been demonstrated to be through degradation of DNA ligase IV. This was initially shown in Ad5 by Baker *et al*., who demonstrated that degradation was dependent on expression of the E1b55K-E4orf6 complex and was likely mediated by ubiquitination and subsequent targeting by the proteasome [88].

Degradation of DNA ligase IV has also been observed post infection with Adenovirus serotypes 3, 4, 5, 7, 9, 11, and 12 [58, 71]. Crucially, it was the only cellular protein degraded by all adenoviral serotypes tested by Forrester *et al*., suggesting it plays a key role in the inhibition of the DNA damage response pathway by human adenoviruses [58].

1.4.4.2 *Effects of virus proteins on HR*

There is currently limited evidence on the effect of oncolytic viruses on HR. Tookman *et al.* investigated the impact of HR status in ovarian cancer on Adenovirus infection. Two cell lines were utilised, both from the same ovarian cancer patient. The first was obtained during a platinum-sensitive relapse, contained a deleterious BRCA2 mutation and was therefore HR defective, the second was obtained during a subsequent platinum-resistant relapse following development of a secondary BRCA2 mutation which restored the open reading frame and had therefore regained HR function. Cells were infected with wild-type Ad5, Ad11 or Ad35 or one of two Ad5 mutants, both containing an E3b region deletion, one of these also containing a deletion in the region of E1A CR2. Interestingly, the authors found that the cell line with functional HR demonstrated a significant decrease in cell survival following infection by all three Ad5 viruses when compared to the cell line with defective HR. Confocal microscopy showed co-localisation between VRCs and BRCA2. Surprisingly, the authors also noted co-localisation of VRCs and RAD51 foci in both the presence and absence of BRCA2, and this was confirmed in a number of other cell lines. This is the first demonstration of recruitment of HR proteins to the adenovirus VRC. Co-immunoprecipitation was consistent with an interaction between RAD51 and Ad5 E2 DNA binding protein. Furthermore, depletion of RAD51 resulted in reduced cytotoxicity and viral replication following infection with the abovementioned Ad5 mutants, BRCA2 depletion likewise lead to reduced cytotoxicity [89]. This data suggests these HR proteins are utilised by Ad5 to improve viral replication and cytotoxicity.

1.5 Combination therapy between radiation and oncolytic adenovirus

The concept of combination adenovirus and radiation treatment is an attractive one for a number of reasons. First and foremost, the ability of adenoviruses to both inhibit and – as

seems increasingly likely – commandeer members of the DDR pathway for their own use, suggests the potential for potent radiosensitisation. Further, OVs can be modified to enhance tumour tropism or limit replication to cancer cells alone [90], allowing the potential for improved targeted treatment. Adenoviruses are frequently used as vectors for transgene delivery, they can therefore be "armed" to allow a potential tri-modality treatment, for example by augmenting the immune response [91-93].

Indeed, a number of pre-clinical and clinical studies support the use of combination treatment with radiotherapy and oncolytic adenoviruses expressing a range of transgene products [94], the vast majority of these utilising Ad5-based viral constructs. This has been discussed in greater detail in chapter 5. Briefly, i*n vitro* and *in vivo*, enhanced cytotoxicity or tumour growth suppression has been demonstrated in lung [95], anaplastic thyroid [96], and glioma [97, 98] tumour models. Improvement in cytotoxicity has also been found *in vitro* in hepatocellular [95] cancer cells, whilst *in vivo,* a significant increase in mean survival has been seen using combination treatment versus monotherapy when treating mice harbouring head and neck tumour xenografts [99]. Finally, synergy has been observed when treating prostate tumour cell lines and xenografts with combined radiotherapy and oncolytic adenovirus [100, 101].

When comparing the effect of combination treatment on tumour versus normal tissue, radiosensitisation was seen in lung cancer cells, but not normal lung fibroblasts, *in vitro*, and enhanced lung tumour xenograft growth suppression was shown *in vivo* [102]. Likewise, increased apoptosis was seen in ovarian cancer cell lines, but not in normal human mesothelial cells [103], when assessing combination treatment in this tumour model.

Clinical trials assessing the safety of combining oncolytic adenovirus treatment with radiotherapy suggest this approach results in an acceptable toxicity profile, and that the

common side effects are not consistent with exacerbation of radiation toxicity [94]. Some early trials have also shown clinical benefit, for example a prospective randomised phase 2 trial in patients with intermediate-risk prostate cancer, which compared intensity modulated radiation therapy with or without a single intraprostatic injection of Ad5-yCD/mutTK$_{SR39}$*rep*-ADP (a replication-competent oncolytic adenovirus expressing a yeast cytosine deaminase / mutant HSV thymidine kinase fusion gene and the adenovirus death protein gene), given prior to 5-fluorocytosine and valganciclovir treatment. 37 patients were biopsied at two years post-treatment, with 33% positivity in patients who had received combination treatment versus 58% in patients treated with radiotherapy alone ($p = 0.13$) [104]. Promising results were further seen in a phase 2 trial comparing safety and efficacy in patients with malignant glioma receiving standard of care (SOC) (surgery followed by radiation and temozolamide), versus SOC with aglatimagene besadenovec (an adenoviral vector expressing the HSV thymidine kinase gene) administered at surgery, and followed by valacyclovir [105]. The authors reported a significant increase in median overall survival in the 48 patients receiving combination treatment (17.1 months) versus the 134 patients in the matched control group receiving SOC (13.5 months), as well as a significant increase in progression-free survival (8.1 versus 6.5 months, respectively). The biggest improvement in outcomes was seen in patients with minimum residual disease post-surgical resection.

1.6 Enadenotucirev

A key limitation of using Ad5-based constructs in oncolytic virotherapy is that most patients are likely to have been previously exposed to this relatively common serotype, and therefore to produce neutralising antibodies [106, 107]. This limits treatment to lesions which can be directly accessed, rendering it unable to be utilised in targeting multiple metastases. Studies show the seroprevalence of neutralising antibodies to group B adenoviruses such as Ad11

and Ad35 is markedly lower [107-109], which provides a possible strategy of dealing with this challenge.

This thesis focuses predominantly on EnAd (previously known as ColoAd1), a group B adenovirus comprised primarily of the Ad11p genome, but with a nearly complete deletion of E3, a partial deletion of E4 putatively mapping to E4orf4, and a chimeric Ad11p and Ad3 E2B region [110]. EnAd was developed through bioselection for oncolytic activity in the colon tumour cell line HT-29. The mechanisms behind preferential EnAd targeting of colon tumour over normal tissue have yet to be fully determined, though high levels of CD46, one of the receptors for EnAd, on cancer cells may play a role [110].

There are significantly higher levels of inhibition of Ad5 compared to EnAd in both pooled human serum and undiluted whole blood [111]. In addition, EnAd is able to localise to tumour cells following intravenous administration [112, 113], subsequently inducing a form of pro-inflammatory cell death [114]. This makes it a promising candidate for combination with radiation treatment and a phase I clinical trial combining EnAd with chemoradiation in patients with locally advanced rectal cancer (CEDAR) has now commenced recruitment [115].

1.7 Central hypothesis and aims

The core of our hypothesis is that targeted inhibition of dsDNA repair in cancer using oncolytic virotherapy has the potential to result in tumour-targeted radiosensitisation, and perhaps even synergy. Different adenovirus serotypes have been shown to interact with proteins at every level of the DDR pathway, from sensing to repair. Further, the ability of oncolytic adenoviruses to target tumour cells over normal tissue makes them particularly attractive candidates for combination treatment with radiotherapy, offering the possibility of increased target cytotoxicity without a concomitant rise in normal tissue effects. A greater

understanding of the underlying mechanisms driving the effects seen in combination therapy may help guide the interpretation and optimisation of studies such as the CEDAR trial, which is now recruiting patients.

The aims of this thesis are:

1. Explore the impact of adenovirus infection on the DDR, with a particular focus on mechanisms of double-strand DNA break repair.

2. Determine the effect of radiation on adenovirus replication and production.

3. Assess whether combination treatment with Enadenotucirev and external beam radiation results in synergistic cytotoxicity.

Chapter 2: Materials and Methods

2.1 Tissue culture

2.1.1 Cell culture

Cells were cultured in DMEM (Sigma-Aldrich) containing 10% foetal bovine serum (FBS, Gibco) in a humidity-controlled incubator at 37°C, 5% CO_2. Cells were split approximately every 3 days once 80-95% confluence was reached, using sterile techniques in a class II laminar-flow cabinet. Briefly, supernatant was removed, cells were washed with calcium- and magnesium-free phosphate buffered saline (PBS, Gibco) and incubated in trypsin-EDTA (Sigma-Aldrich) until detachment was observed. Tryptic activity was halted by adding DMEM containing 10% FBS (complete medium). Cells were typically split at a ratio of 1:10. Cell lines and culture conditions are summarised in Table 2.1.

Table 2.1 List of cell lines used

Cell line	Description	Growth medium	Source
A549	Lung carcinoma	DMEM, 10% FBS	EACC
HEK293A	Ad-Human embryonic kidney	DMEM, 10% FBS	Agilent
DLD1	Dukes' type C colorectal adenocarcinoma	DMEM, 10% FBS	ATCC
HCT116	Colorectal carcinoma	DMEM, 10% FBS	Gift from McKenna Lab (University of Oxford)
HeLa	Cervical adenocarcinoma	DMEM, 10% FBS	Gift from McKenna Lab (University of Oxford)
HT-29	Colorectal adenocarcinoma	DMEM, 10% FBS	ATCC

2.1.2 Mycoplasma testing

Mycoplasma testing was routinely carried out after thawing cell lines and repeated approximately once every ten passages. All cell lines were tested for mycoplasma prior to freezing for storage. Testing was performed as per manufacturer's instructions using the Lonza MycoAlert® Mycoplasma Detection Kit.

2.1.3 Cryopreservation

Cells were trypsinised as described above and resuspended in freezing solution comprising 10% dimethyl sulphoxide (DMSO, Sigma-Aldrich) and 90% FBS. The cell suspension was transferred into cryogenic vials (Corning) in 1 mL aliquots, frozen overnight using a Mr Frosty container (Nalgene) and transferred into -80°C storage the following day.

Cells were thawed by brief incubation at 37°C followed by resuspension of pellet in 13 mL of warmed complete medium. Cells were pelleted for 5 minutes (min) at 192 g_n, supernatant was removed, and the pellet was resuspended in fresh culture medium and transferred to a flask. The medium was refreshed the following day.

2.1.4 Cell seeding

Cells were dissociated by washing monolayers with PBS and incubating with non-enzymatic (experiments involving pre-irradiated cells) or enzymatic (all other experiments) dissociation buffers. Complete medium was added to discontinue detachment and the suspension centrifuged at 350 g_n for 5 min. Trypan blue (Sigma-Aldrich) was added to an aliquot of cells in a 1:1 ratio for cell counting only when the experiment included pre-irradiated cells. Cells were counted using a Neubauer haemocytometer or LUNA-II automated cell counter and seeded in complete medium at a density appropriate to each experimental time course and cell line. E-plates (16-well, # 05469830001, ACEA) were used

for xCELLigence experiments. All other experiments were performed in Corning Costar plates.

2.1.5 In vitro irradiation

Cells were treated in T-75 tissue culture flasks (Greiner Bio-One) or Corning Costar plates according to experimental protocol using a caesium-137 irradiator.

2.1.6 RNA interference (RNAi) by reverse transfection

Dilutions of 40 pmol siRNA and 160 µL Optimem (#31985-062, Gibco) were made alongside 18 µL Optimem and 2 µL Lipofectamine RNAiMax 0.2% (#56532, Thermo Fisher) and incubated for 2 min at room temperature. Dilutions were mixed and incubated for 30 min before being pipetted into a 6-well plate. A549 cells at 1 x 10^5 cells/well were added to this mix and allowed to adhere. Medium was changed to complete medium either 6 (RAD51 experiment) or 20 (DNA ligase IV experiment) hours (h) later. Time course of subsequent infection and lysate harvesting is detailed in the appropriate experimental results section. All siRNA was ordered from Ambion (Table 2.2 for a complete list of siRNA sequences used). Silencer Select Negative Control No. 1 siRNA (Ambion) was used as a negative control.

Table 2.2 Details of siRNA sequences used

Target gene	Sense (5'-3')	Anti-sense (5'-3')
RAD51	GGUAGAAUCUAGGUAUGCAtt	UGCAUACCUAGAUUCUACCat
DNA ligase IV	CCGUGAAUAUGAUUGCUAUtt	AUAGCAAUCAUAUUCACGGgc
PLK1	CCAUUAACGAGCUGCUUAAtt	UUAAGCAGCUCGUUAAUGGtt

2.1.7 xCELLigence

A549 cells in T-75 culture flasks were irradiated or mock-irradiated. At 8 h post-irradiation, 50 µL complete medium was added to 16-well E-plates (# 05469830001, ACEA Biosciences). A baseline reading was performed using an xCELLigence RTCA DP instrument (ACEA Biosciences), followed by seeding of 2 x 10^4 cells in 50 µL of complete medium per well. Cells were allowed to adhere overnight and 24 h post-irradiation 50 µL complete medium with or without Enadenotucirev (EnAd) was added. Electrical impedance was recorded every 15 min for 7-10 days.

2.2 Virological methods

2.2.1 Adenovirus propagation

Large-scale virus propagation was carried out on HEK293A cells. For each adenovirus propagated, a single Hyperflask (Corning) was seeded from a confluent T-175 with DMEM containing 10% FBS and 1% penicillin-streptomycin (pen-strep, Gibco). Cells were allowed to adhere and replicate for 72 h before replacing the culture medium with DMEM containing 2% FBS, 1% pen-strep and 100 virus particles (VP)/cell. Flasks were monitored until cytopathic effect (CPE) was apparent throughout the cell monolayer. The flask was gently agitated to detach cells and the flask contents were spun in 250 mL conical tubes (Corning) at 931 g_n for 10 min. Residual cells were rinsed from the Hyperflask and pooled with the cell pellet. A repeat spin of 931 g_n for 10 min was conducted, the supernatant discarded, and the cell pellet resuspended in 7 mL of complete medium.

2.2.2 Adenovirus purification

To release virus from the harvested cells, three freeze-thaw cycles were carried out. The tube containing cell suspension was alternately heated in a water bath at 37°C, followed by immersion into liquid nitrogen. After the last freeze-thaw cycle, a 1:100 volume of water

saturated n-butanol was added to the lysate and the suspension continually mixed at 4°C for 1 h. Cell lysates were then centrifuged at 500 g_n for 10 min and the supernatant utilised for further processing.

Virus particle purification was performed using a caesium chloride (CsCl) gradient. Briefly, 3 mL of 1:32ρ caesium chloride (192 g CsCl, 40.8 mL of 0.5 M Tris-HCl, 367.2 mL dH_2O) were carefully underlaid with 2mL of 1:45ρ caesium chloride (307.5 g CsCl, 43.5 mL of 0.5 M Tris-HCl, 387 mL dH_2O) in a 14 mL ultra-clear centrifuge tube (#344059, Beckman). The CsCl layers were overlaid with 2 mL of 40% glycerol. Virus-containing supernatant was gently overlaid onto the glycerol and the filled tubes placed in a SW40Ti rotor for centrifugation in an Optima XE-90 Ultracentrifuge (Beckman Coulter) for 90 min at 10°C, 25000 rpm.

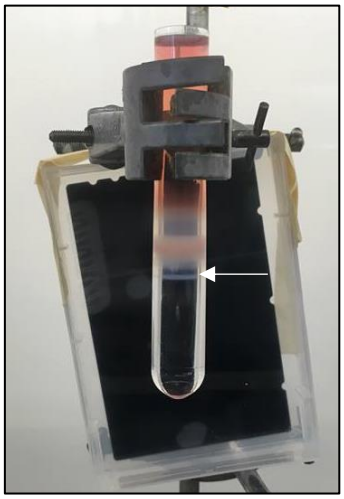


Figure 2.1: Virus band aspirated during purification

Post-centrifugation, tubes were suspended over a waste container and a 5 mL syringe (Terumo) and 21-gauge needle (Terumo) used to carefully extract the lower white band (Figure 2.1, arrow), which corresponds to mature virus particles. This was added to a pre-soaked Slide-A-Lyzer dialysis cassette (10,000 MW cut-off, Thermo Fisher) and dialysed in 500 mL of PBS for 20 min at 4°C. Dialysis medium was changed and this step was repeated twice more before dialysing overnight. The subsequent day, the dialysed solution

was aspirated and supplemented with 1 µL benzonase (#70664, Merck Millipore) per mL of virus solution and magnesium chloride to a final concentration of 2 mM. This was incubated under continuous mixing for 1 h at room temperature before the solution was added to a new CsCl gradient and centrifuged as described above. The virus band corresponding to mature particles was aspirated and placed in a pre-soaked dialysis cassette. The solution was dialysed three times using fresh PBS each time. Dialysis was carried out at 4°C for 20 min. A final dialysis step was carried out for 30 min in PBS supplemented with 5 mM of HEPES. Purified virus solution was aspirated from the dialysis cassette and supplemented with 20% glycerol. This virus stock was aliquoted at 100 µL/aliquot, snap-frozen and maintained at -80°C until required for use.

2.2.3 PicoGreen assay

Virus particle concentration in purified adenovirus solution was estimated by using the Quant-iT PicoGreen® assay (#10398702, Invitrogen) to quantify virus DNA concentration. A standard curve ranging from 0.00775 µg/mL to 0.5 µg/mL was made using seven two-fold serial dilutions of bacteriophage λ DNA into Tris-EDTA (TE) buffer containing 0.05% SDS. The virus solution of interest was diluted in TE buffer containing 0.05% SDS and heated at 56°C for 30 min. Once dilutions had been prepared, 50 µl of virus sample or standard curve solution was pipetted in duplicate into a black 96-half well microplate (Costar), and 50 µl of a 1:200 PicoGreen® reagent: TE buffer dilution subsequently added. PicoGreen® is a dye which fluoresces intensely on binding dsDNA [116]. Fluorescence intensity was measured on a Wallac 1420 Victor^2 multi-label counter (Perkin Elmer) using excitation and emission settings of 485 nm and 535 nm respectively. Mean fluorescence values were used to calculate virus dsDNA concentration. Fluorescence was converted to virus particle count by calculating 1 µg/mL of DNA to be equivalent to 2.7 x 10^{10} VP/mL, as per the methodology described by Murakami and McCaman [117].

2.2.4 Absolute quantification of genome copies

Extraction of viral DNA from fresh frozen tissue or cell lysate/supernatant was carried out as per manufacturer's instructions using the PureLink genomic DNA extraction kit (Invitrogen). Mouse tumour samples were homogenised in 10 µl PBS (containing 1% pen-strep)/mg tissue. A total of 10 mg of tissue was incubated at 55°C overnight with genomic digestion buffer and proteinase K prior to proceeding with the extraction protocol. With all samples, DNA was eluted into 200 µl DEPC-treated H_2O (Thermo Fisher) and quantified on a Nanodrop One (Thermo Fisher). For quantification of viral genome copies, a master mix containing 2 x qPCRBIO probe mix Hi-Rox (PCR Biosystems) alongside appropriate forward primer, reverse primer, and probe (see Tables 2.3 and 2.4) was plated into a 96-well PCR plate (Applied Biosystems). A standard curve of logarithmic EnAd-SA-GFP dilutions ranging from 1 x 10^3 VP/well to 1 x 10^9 VP/well was added in triplicate, alongside samples of interest and blank controls, to a total volume of 20 µl/well. Reactions were performed using a StepOnePlus Real-Time PCR system (Applied Biosystems). The amplification cycle utilised began with 2 min of denaturing at 95°C, followed by 40 cycles of alternate denaturing for 5 seconds at 95°C and annealing and extension at 60°C for 20 seconds. Sample DNA content was calculated using StepOne v2.3 software.

Table 2.3 Primers and probes used to quantify EnAd and Ad11p

Probe	**[6FAM]-CCGGACTCAGGTACTCCGAAGCATCCT-[TAM]**
Forward primer	TACATGCACATCGCCGGA
Reverse primer	CGGGCGAACTGCACCA

Table 2.4 Primers and probes used to quantify Ad5

Probe	**[6FAM]TCCAATATCTGGAACAGTTCAAAGTGCTCATCT[TAM]**
Forward primer	TGGCTGTTAAAGGCAGTTTGG
Reverse primer	GCACTCCATTTTCGTCAAATCTT

2.2.5 $TCID_{50}$ assay

The concentration of virus particles able to cause CPE was determined by using the $TCID_{50}$ assay. A549 cells were seeded in 96-well plates (Costar) at a density of $1x10^4$ cells/well and allowed to reach confluence for 1-2 days. At this point, virus-containing supernatants were serially diluted 1:10 in complete medium and applied to cells. CPE was assessed 7 days post-infection and plaque-forming units calculated using the Kärber formula [118]. When assessing $TCID_{50}$/mL in homogenised fresh frozen tissue from animals receiving treatment with Enadenotucirev-SA-Firefly Luciferase (EnAd-SA-FLuc), the luciferase assay was carried out on rows containing only a few CPE-positive wells post-scoring to confirm that plaque-positive wells also demonstrated luminescence.

2.2.6 Virus infection

Unless otherwise specified, infection of cells was conducted by replacing cell supernatant with DMEM containing 2% FBS and the virus amount required for the experiment. At 2 h post-infection (p.i.), medium was replaced with complete medium. In experiments assessing quantification of short-term virus uptake, cell monolayer was washed twice at 2 h p.i. with PBS before harvesting. In western blotting experiments, cell monolayers were washed with PBS and lysed *in situ* using an appropriate volume of Pierce RIPA buffer (Thermo Fisher)

containing Halt protease and phosphatase inhibitor (Thermo Fisher) and incubating the plate on ice for 10 min prior to harvesting.

2.2.7 Plaque assay

Cells were seeded in 6-well plates according to the seeding density appropriate for each experiment and cell line. Infection was carried out from 6 h to 2 days post-seeding, as required, by replacing medium with 500 µl DMEM containing 2% FBS with or without virus at varying dilutions. Plates were incubated for 3 h and medium replaced with DMEM containing 2% FBS and 1% agarose (Invitrogen). To assess virus spread wells were imaged on alternate days using a Celigo Imaging Cytometer (Nexcelom Bioscience). Alternatively, wells were incubated with a 1:10 dilution of 5 mg/mL thiazolyl blue tetrazolium bromide (MTT, Sigma) and imaged using a GelCount tumour colony counter (Oxford Optronix).

Tracking of individual plaque size over time was accomplished by analysing wells with Celigo software version 4.1.1.5, exporting object level data and manually matching the coordinates given for each plaque over the experimental time course. Only plaques available for analysis throughout the experimental timeline were included in analysis.

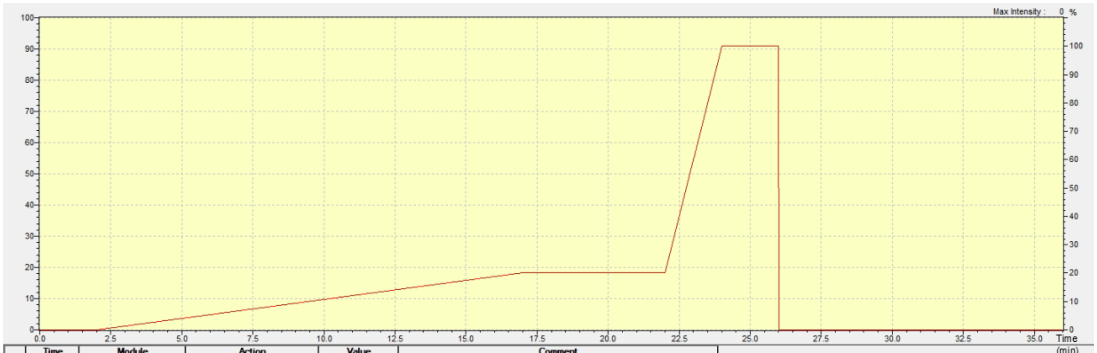
2.2.8 Assessment of endotoxin levels prior to in vivo use of virus

EnAd-SA-Fluc was tested for endotoxin levels prior to intravenous use in mouse models to ensure this was below the safe threshold. The ToxinSensor Chromogenic LAL Endotoxin Assay Kit was utilised (#ABIN491526, antibodies-online) as per manufacturer's instructions. Briefly, virus was diluted 1:50 in LAL (Limulus Amebocyte Lysate) reagent water and standard curve dilutions made by preparing a 1 EU/mL endotoxin solution and performing three 1:2 dilutions in LAL reagent water. Two blank solutions were also prepared, one of distilled water and one comprising distilled water with 1:50 PBS/glycerol dilution to match the volume used in virus suspension. In duplicate, samples, standards, and

blanks were dispensed into endotoxin-free vials at 100 µl/vial, followed by 100 µl of reconstituted LAL. As the expected concentration was in the range of 0.1-1 EU/mL, vials were incubated at 37°C for 7 min. Reconstituted chromogenic substrate solution was added to each vial (100 µl); solution was then mixed and incubated for a further 6 min at 37°C. Finally, 500 µl each of three different colour-stabilising solutions were sequentially added and the absorbance of each reaction read at 545 nm.

2.2.9 High performance liquid chromatography (HPLC) titration of virus concentration

Anion exchange HPLC quantification of virus capsid concentration was kindly carried out by Dr Brian Lyons (Department of Oncology, University of Oxford) prior to use of viruses *in vivo*. Briefly, a known concentration of GMP-grade EnAd (kindly provided by PsiOxus Therapeutics) was used to generate a standard curve. Virus samples were diluted 1:10 and transferred to HPLC vials, ensuring no bubbles were present in the solution. A robotic autosampler was used to add samples to a Shimadzu Prominence HPLC pre-fitted with a Resource Q anion exchange column. Virus was eluted using a NaCl gradient (Figure 2.2, image provided by Dr Brian Lyons). UV detection at 260 nm was used to establish viral content, at 280 nm to estimate protein content and at excitation and emission of 275 nm and 303 nm, respectively, when the sample concentration was low.



	Time	Module	Action	Value	Comment
1	0.01	Pumps	Pump B Conc.	0	
2	2.00	Pumps	Pump B Conc.	0	
3	2.01	Pumps	Pump B Conc.	0	
4	17.00	Pumps	Pump B Conc.	20	
5	22.00	Pumps	Pump B Conc.	20	
6	24.00	Pumps	Pump B Conc.	100	
7	26.00	Pumps	Pump B Conc.	100	
8	26.01	Pumps	Pump B Conc.	0	
9	36.00	Pumps	Pump B Conc.	0	
10	36.00	Controller	Stop		

Figure 2.2 NaCl gradient used to elute virus. Sample is added to column pre-equilibrated with buffer A (50 mM HEPES, 300 mM NaCl, pH 7.4). Sequential injection of buffer B (50 mM HEPES, 1.5 M NaCl, pH 7.4) at set time points results in differential elution of adenovirus serotypes.

2.3 Protein assays

2.3.1 Quantification of protein content

Protein concentration was determined using a BCA kit as per manufacturer's instructions (Sigma-Aldrich). Samples of interest were incubated with 0.25 µl of benzonase for 30 min at room temperature and centrifuged for 10 min at 10 000 g_n, 4°C. Meanwhile, a known concentration of protein standard (1 mg/mL, #P0914 Sigma-Aldrich) was diluted with DEPC-treated water to create an 11-point standard curve ranging from a protein concentration of 50 µg/mL to 1 mg/mL. A blank control was also used (DEPC-treated water only). Samples were diluted 1:10 or 1:20 as appropriate, and plated in triplicate into a 96-well plate at 5 µl/well. Standard curve was plated in duplicate at 5 µl/well and BCA assay kit reagents added to wells containing protein or control at 50 µl/well. Plate was incubated for 30 min at 60°C in the dark before measuring absorbance at 450 nm.

2.3.2 SDS-PAGE and western blot

Protein separation and transfer

Proteins were visualised by western blot using 10-70 µg of protein per lane. Cell lysates were added to Laemmli buffer (Alfa Aesar) and water and denatured for 15 min at 95°C. Samples were loaded alongside a protein ladder. PageRuler Plus Prestained Protein Ladder (#26619, Thermo Fisher) was used in all experiments except when visualisation of p53BP1 or 53BP1 was required, where a high molecular weight ladder (#LC5699, Invitrogen) was used. Samples were loaded onto pre-cast 10% Tris-glycine gels (BioRad) for experiments visualising EnAd-E1A-FLAGtag and 4-20% pre-cast Tris-glycine gels (BioRad) for all other experiments. Proteins were run at 80-120 V for 90 min in SDS running buffer (Table 2.5). Transfer was adapted based on experimental requirements. For visualisation of p53BP1 or 53BP1, proteins were transferred to a 0.45 µm nitrocellulose membrane (BioRad) for 120

min at 4°C at 300 mA in western transfer buffer (Table 2.5). For experiments visualising E1A protein production, semi-dry transfer was carried out onto 0.2 µm nitrocellulose membrane (BioRad) using a Trans-Blot Turbo Transfer System (Bio-Rad) and the pre-set mixed molecular weight protein programme (1.3 A for 7 min). For all other experiments, proteins were transferred to a 0.2 µm nitrocellulose membrane (BioRad) for 90 min at 4°C at 300 mA in western transfer buffer (Table 2.5). Successful protein transfer was confirmed using Ponceau S stain (Sigma-Aldrich).

Table 2.5. Buffers used in SDS-page and western blotting.

Running buffer (10x)	**Transfer buffer (10x)**	**Stripping buffer**
Tris-base – 30 g	Tris-base – 30 g	Tween-20 – 2 mL
Glycine – 144 g	Glycine – 144 g	Glycine – 3 g
SDS – 10 g		SDS – 200 mg
	10% methanol added for 1x	Adjust to pH 2.2
Deionised H_2O – to 1 L	Deionised H_2O – to 1 L	Deionised H_2O – to 200 mL

Staining and development

Solutions to block non-specific binding were adjusted according to experimental requirements. Experiments visualising p53BP1 and 53BP1 required blocking in 5% bovine serum albumin (BSA, Sigma-Aldrich) in 0.1% TBS-Tween (Fisher Bioreagents) for 45 min at room temperature. All other experiments were blocked in 5% milk in 0.1% PBS-T (PBS, Gibco) for 45 min at room temperature. Membranes were incubated with primary antibody either overnight at 4°C or for 1 h at room temperature in 5% BSA in TBS-T (p53BP1, 53BP1) or 5% milk PBS-T (all other antibodies). Membranes were washed three times in TBS-T (p53BP1, 53BP1) or PBS-T before incubation with conjugated secondary antibody

in 5% milk TBS-T (p53BP1, 53BP1) or PBS-T (all other experiments) either overnight or for 3 h at room temperature. Membranes were then washed three times in TBS-T or PBS-T. SuperSignal WestDura Extended Duration Substrate (Thermo Fisher) was applied to the membrane for 1 min before exposure to X-ray film (GE Life Sciences) and development in an automatic developer (CP1000, Agfa) or scanning using a ChemiDoc MP Imaging System (Bio-Rad). Membrane-bound antibodies were stripped away by incubating the membrane with stripping buffer (Table 2.5) twice for 10 min, followed by two washes with PBS and two washes with PBS-T. Membranes were then blocked again in 5% milk PBS-T for 45 min. Housekeeping proteins were detected by incubating with conjugated antibody overnight at 4°C or for 3 h at room temperature and washing three times with PBS-T before proceeding to development. Band density was determined using Image Lab (Bio-Rad) or ImageJ software. A list of all antibodies used is provided in Table 2.6.

Table 2.6 Antibodies used in western blotting.

Target	Conjugate	Source	Dilution	Company
DNA ligase IV	-	Rabbit	1:500	Cell Signaling Technologies (#14649)
p53BP1 (Ser1778)	-	Rabbit	1:1000	Cell Signaling Technologies (#2675)
53BP1	-	Rabbit	1:1000	Cell Signaling Technologies (#4937)
RAD51	-	Rabbit	1:1000	Santa Cruz (#sc-8349)
Adenovirus structural proteins	-	Goat	1:20000	Abcam (#ab36851)
Ad-2/5 E1A	-	Rabbit	1:2000	Santa Cruz (#sc-430)
FLAGtag	Horseradish peroxidase	Rat	1:5000	BioLegend (#637311)
β-actin	Horseradish peroxidase	Mouse	1:400000	Sigma-Aldrich (A3854)
Rabbit	Horseradish peroxidase	Goat	1:3000	Cell Signaling Technologies (#7074S)
Mouse	Horseradish peroxidase	Horse	1:3000	Cell Signaling Technologies (#7076)
Goat	Horseradish peroxidase	Mouse	1:10000	Santa Cruz (#sc-2354)

2.3.3 Luciferase assays

EnAd-SA-Fluc was used in all *in vivo* experiments and allowed quantification of luciferase concentration in fresh frozen tumour samples as a way of assessing virus proliferation *in*

vivo. Fresh frozen mouse tumour tissue was initially prepared by homogenisation in 10 µl PBS + 1% pen-strep/mg tissue. Of this, 50 µl was diluted 1:20 into PBS and added to 25 µl reporter lysis buffer (Promega). One freeze-thaw cycle was carried out before centrifuging samples for 10 min at 10 000 g_n. The supernatant was retained for further processing. Per sample, 20 µl was plated in triplicate into alternate wells of a white bottom 96-well plate (Costar). The plate was placed into a POLARstar Omega (BMG LABTECH) and 20 µl of a luciferase assay reagent (Promega) was injected into each sample-containing well. Luminescence was measured 1 min post luciferin injection. Concurrently, protein concentration of the supernatant was established using the BCA assay as described above, enabling a calculation of mean luminescence per µg of protein.

2.3.4 Flow cytometry

Cell supernatant was harvested from sample wells into 96-well v-bottom plates (Costar) and spun for 5 min at 400 g_n. PBS was used to wash the cell monolayer then transferred to the 96-well plates. A repeat spin was performed and fresh PBS added. Concurrently, non-enzymatic cell dissociation solution (Sigma-Aldrich) was added to each sample well and incubated at 37°C until detachment was apparent. DMEM containing 2% FBS was added to discontinue dissociation and cells were transferred to the appropriate wells in the 96-well plates, centrifuged, and washed with PBS. For each cell line investigated, two samples were used as live/dead stain positive controls. Half of these samples were boiled at 95°C for 5 min and re-added to the live cells. All experimental samples were stained with 1:5000 LIVE/DEAD Fixable Near IR stain (#L34975, Invitrogen) prior to fixing. Staining with a PE-conjugated antibody and isotype control was carried out either before or after fixing. Table 2.7 lists the antibodies used. Staining was performed in 50 µl MACS buffer (0.5% BSA, 2 mM EDTA in PBS) for 15 min at room temperature, in the dark, and under constant agitation. Cells were washed in PBS after staining. Cells were fixed by adding 100 µl 2%

formalin (Sigma-Aldrich) to each well containing sample and incubating for 10 min at room temperature, in the dark, under constant agitation. Cells were subsequently washed twice with PBS and finally resuspended in MACS buffer. Data was acquired on an Attune NxT acoustic focusing cytometer (Life Technologies) and analysis conducted using FlowJo analysis software (Becton & Dickinson).

Table 2.7 Antibodies used in flow cytometry

Target	Conjugate	Isotype	Dilution	Clone	Company
Desmoglein 2 (DSG2)	PE	Mouse IgG2b kappa	1:20	CSTEM28	#12-9159-42, Invitrogen
CD46	PE	Mouse IgG1 kappa	1:200	Tra-2-10	#352401, BioLegend
DSG2 Isotype control	PE	Mouse IgG2b kappa	1:160	eBMG2b	#12-4732-81, Invitrogen
CD46 Isotype control	PE	Mouse IgG1 kappa	1:200	MOPC-21	#400114, BioLegend

2.3.5 Immunocytochemistry

A549 cells were seeded in 96-well plates at 8 x 10^3 cells/well and the subsequent day were infected with adenovirus at an appropriate dilution. At 24 h p.i., plates were left non-irradiated or irradiated at 6 Gy. Over the next 24 hours, cells were washed with PBS and fixed by incubating for 10 min at room temperature with either 3% formalin or 3% paraformaldehyde (Thermo Fisher). Formalin/paraformaldehyde was removed and cells maintained in PBS at 4°C until proceeding to blocking and staining.

To block, cells were incubated in 100 µl PBS with 1% BSA (Sigma Aldrich), 0.1% Triton X100 (Sigma Aldrich) and 1% goat serum (Sigma Aldrich) for 1 h at room temperature. Blocking buffer was removed and cells were incubated overnight at 4°C in 50 µl PBS

containing 1% BSA and primary antibody. The next day, cells were washed three times with PBS and incubated in 50 µl per well of PBS containing 1% BSA, 1:2000 6-diamidino-2-phenylindole (DAPI, 2 mg/mL stock solution, Sigma Aldrich) and appropriate secondary antibody for 1 h at room temperature in the dark. Cells were washed with PBS and scanned on an IN Cell Analyzer 1000 (GE Healthcare). Analysis was conducted using IN Cell Investigator High-content image analysis software (GE Healthcare). Table 2.8 lists all antibodies used in immunocytochemistry.

Table 2.8 Antibodies used in immunocytochemistry

Target	Conjugate	Source	Dilution	Company
53BP1	-	Mouse	1:1000	#612523, BD Transduction
RAD51	-	Rabbit	1:1500	#sc-8349, Santa Cruz
γH2AX [pSer139]	-	Rabbit	1:2000	#nb100-2280, Novus
Rabbit	Alexa488	Goat	1:1200	#A11070, Invitrogen
Mouse	Alexa594	Goat	1:1200	#A11020, Invitrogen
Rabbit	Alexa594	Goat	1:1200	#A11072, Invitrogen

2.4 Animal experiments

2.4.1 Housing and regulations

All experiments were performed in accordance with Home Office regulations under the Project License number 30/3391, personal license IAA28099F. Mice were housed in

individually ventilated cages, in humidity and temperature-controlled conditions at the Radiobiology Research Institute, Churchill Hospital, Oxford, UK. A maximum of six animals were housed per cage.

2.4.2 General anaesthesia

Animals were anaesthetised using isoflurane inhalational anaesthetic for the duration of tumour implantation, irradiation, and imaging on the In Vivo Imaging System (IVIS). Duration of anaesthesia did not exceed 30 minutes at any time.

2.4.3 Xenograft implantation

Mice were injected with 100 µl of PBS containing 2 x 10^6 HCT116 cells into the right flank under inhalational anaesthesia. A 27-gauge size needle (Terumo) and 1 mL syringe were used for injections.

2.4.4 Injection of substances

Intravenous injection of 50 µl PBS or PBS containing 0.5 x 10^{10} virus particles of EnAd-SA-Fluc was given into the lateral tail vein in three doses, 48 h apart, using an insulin needle and syringe (BD Micro-Fine). Prior to IVIS imaging, 150 mg/kg D-Luciferin (Promega) dissolved in 100 µl sterile PBS was administered subcutaneously using a 27-gauge size needle and 1 mL syringe.

2.4.5 Tumour growth monitoring

Tumour size was monitored 3-4 times per week. Volume was determined by using digital electronic calipers and the formula 1/6 x π x height x width x length.

2.4.6 In vivo irradiation

Irradiation of xenografts was performed under inhalational anaesthesia (isoflurane). Tumours were irradiated with 10 Gy using a Gulmay 320 kV irradiator.

2.4.7 Bioluminescence imaging in vivo

Imaging was conducted under isoflurane inhalational anaesthesia. D-luciferin was administered as described above, and imaging of luminescence performed at 1 min intervals using an IVIS Spectrum 100 system (Xenogen). Imaging was discontinued once luminescence peak had been reached, or if 30 min of anaesthesia were due to elapse, whichever was soonest. Luminescence was analysed using Living Image Software (Xenogen).

2.4.8 Tumour homogenisation

Immediately post tumour harvesting, half of all tumours were frozen at -80°C and maintained until further processing. Prior to use in further experimental techniques, tumours were homogenised in 10 µl PBS containing 1% pen-strep per mg of tissue. Samples to be used in qPCR were immediately aliquoted and frozen, 1:200 Halt protease and phosphatase inhibitor was added to the remainder.

2.5 Statistical analysis

Data processing and statistical analysis were conducted using Microsoft Excel 2013 or GraphPad Prism version 5. For all analyses requiring comparison of mean or median between two groups, a two-way unpaired t-test was used to analyse parametric data, and Mann-Whitney test was used to analyse non-parametric data, respectively, unless normalisation could be achieved through transformation. For all analyses requiring comparison between more than two groups, ANOVA was used to analyse parametric data and Kruskall-Wallis to analyse non-parametric data. Two-way ANOVA was utilised to account for the impact of two different variables, such as time and radiation dose, on any changes seen in the value being measured. Test for linear regression was used to assess for

linear trend, and survival analysis conducted using log-rank test. Bliss independence analysis [119] was used to assess for synergistic cytotoxicity.

Chapter 3: Interaction between oncolytic adenovirus and the DNA damage response

3.1 Introduction: Hypothesis and chapter aims

There is a considerable amount of evidence that adenoviruses are able to interact with, and inhibit, the cellular DNA damage response [35, 36]. Induction of DNA damage, particularly dsDNA breaks, is the primary mechanism for IR-mediated cell death [120]. Further, the ability to repair sublethal damage is one of the key radiobiological properties underpinning response to fractionated radiotherapy treatment [5]. Inhibiting radiation-induced DNA damage repair specifically in tumour cells may therefore increase the probability of reaching a level of damage sufficient to induce cell death, resulting in treatment synergy. Thus, an important step in exploring the potential synergy between radiation and oncolytic virus therapy is elucidating the impact of adenovirus infection on the DDR pathways involved in repairing IR-induced DNA damage.

The vast majority of the published data on adenovirus interactions with the DDR stem from experiments using Ad5-based constructs, though some information is also available on other serotypes. Adenoviral proteins have been shown to interact with members of the DDR at multiple steps along the pathway, both at the level of DNA damage recognition and mechanisms of repair [94]. In particular, prevention of recognition of viral DNA as double-strand DNA breaks is thought to be a crucial step in the adenovirus replication cycle [54]. This may prevent the DDR machinery from attempting to “repair” the viral genomes, ligating them into concatemers [53, 54].

Sensing of double-strand DNA breaks is mediated by the MRN complex. Components of MRN are known to be targeted both for degradation [54, 56-58] and relocalisation [56-58, 62, 63] by adenoviral proteins, but this is not conserved across all serotypes. Of particular

relevance to this thesis, Forrester *et al.* found there was no MRE11 degradation following infection with Ad3 or Ad11, and that MRE11 relocalisation following infection with these viruses was to VRCs, not to PML tracks as was the case with Ad5, Ad9, and Ad4 [58]. The oncolytic adenovirus Enadenotucirev (EnAd) originated from Ad3 and Ad11p, and one would therefore expect it to behave similarly in its interactions with MRN.

MRN normally activates the ATM complex, the key mediator of the cellular response to double-strand DNA breaks. The interaction between adenovirus and ATR/ATM is a particularly interesting one, if problematic with regards to the prevalent methodology used to monitor IR-induced double-strand DNA breaks. Widespread γH2AX formation can be seen following Ad5 infection [72, 73]. Nichols *et al.* provide data suggesting this is primarily mediated by ATR, with some involvement from ATM and DNA-PK [72], whereas Blackford *et al.* found that the Ad5- and Ad12- mediated phosphorylation of H2AX is severely impaired by the ablation of ATM expression and partially reduced following the knockdown of ATR [77]. A number of interactions between the ATR pathway and adenovirus proteins have otherwise been demonstrated, and the effects on ATR substrates have been shown to differ between adenovirus serotypes [58, 77]. Though expression of Ad5 protein E4orf4 has been linked to decreased phosphorylation of ATM pathway proteins [66], all adenoviral serotypes, including Ad5, have been shown to increase ATM activation in HeLa cells [58]. This is hypothesised to be a consequence of two different mechanisms of ATM activation: a global mechanism which does not influence viral replication but is detectable by standard assays, and a localised, MRN-dependent, anti-viral mechanism which is inhibited as part of the viral replication cycle. Thus, though viral replication results in localised inhibition of the MRN-ATM pathway, there is net overall ATM phosphorylation [68].

The protein p53, a central player in the cellular response to DNA damage and stress, appears to also be differentially targeted by different serotypes. Effects of adenovirus infection range from degradation to an apparent increase in p53 levels, though this increase does not result in a corresponding increase in p53 transcriptional activity [58]. Instead, the majority of serotypes demonstrating an increase in p53 levels appear to cause p53 sequestration to VRCs [58] and viral E1A and p53 interaction is thought to be involved in major late promoter function [121]. Thus, though p53 protein levels increase following infection with specific adenoviral serotypes, normal p53 function may be subverted to aid the virus.

Repair of double-strand DNA breaks can occur via classical or alternative NHEJ or HR. Adenoviral proteins have been shown to interact with proteins involved in NHEJ [86]. Observed in several serotypes, adenoviruses appear to primarily interact with the classical NHEJ pathway through E1B55k/E4orf6-mediated DNA ligase IV degradation [58, 88]. The link between adenoviruses and HR is significantly less well established, though data suggests HR proteins seem to be recruited to Ad5 viral replication centres, reportedly improving viral replication and cytotoxicity in cells with functional HR [89].

The evidence available indicates a range and complexity in the ways different adenovirus serotypes interact with the DDR, with many aspects of this yet to be fully explored. The impact of group C adenovirus infection on the sensing of DNA double-strand breaks is well established, but the data on group B viruses are more limited. Likewise, though the data on adenovirus interaction with NHEJ are plentiful, the mechanism behind this has only been thoroughly investigated using Ad5-based vectors. Similarly, the only interaction shown between adenovirus and HR relates to Ad5 [89]. Studies into other adenovirus serotypes, particularly group B oncolytic adenoviruses such as EnAd, are warranted to guide the future development of alternative OV-based therapeutics as the widespread presence of Ad5-neutralising antibodies in the general population may limit its therapeutic activity. We

hypothesise that EnAd infection may be associated with inhibition of the DDR pathway at least through the degradation of DNA ligase IV, with a potential impact on other DDR members.

The primary aims of this chapter are:

1. Establish an alternate method to γH2AX detection to assess the impact of adenovirus infection on ionising radiation-induced DNA damage sensing.

2. Determine the impact of infection with Ad5 versus EnAd on homologous recombination.

3. Explore the interaction between the chimeric adenovirus EnAd and DNA ligase IV.

3.2 Results

3.2.1 Use of a GFP-expressing virus allows selective analysis of DDR foci formation in infected cells

As discussed in the introduction, the detection and assessment of IR-induced DNA damage in the presence of adenovirus is challenging due to widespread formation of γH2AX with the addition of virus alone [72, 73]. We therefore investigated the formation of 53BP1 foci, another key protein involved in the early stages of the DDR [122], and RAD51, a key marker of homologous recombination repair [123]. 53BP1 foci formation has previously been shown to be inhibited in Ad5-, Ad11p-, and EnAd-infected cells by another member of our group (Jorien Koelen, PhD thesis, 2015).

The timeline of all experiments investigating the formation of DDR foci in the presence of virus and/or radiation is shown in Figure 3.1. We elected to perform irradiation 24 hours post-infection (h p.i.) to allow the impact of early and late viral gene expression on foci formation to be assessed, as by this time point a full viral replication cycle is anticipated to

have taken place [39]. Cells were fixed at varying time points up to 24 h post-irradiation to determine the impact both on peak foci formation and on recovery.

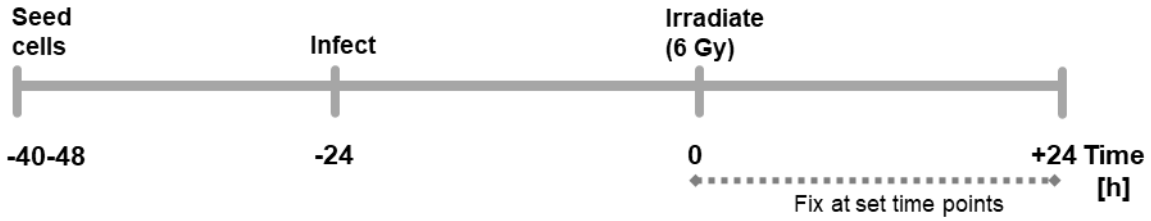


Figure 3.1 Timeline of foci experiments. A549 cells were seeded into 96-well plates and the next day mock-infected or infected with Enadenotucirev (EnAd) or Adenovirus serotype 5 (Ad5). At 24 hours post-infection (h p.i.) cells were either irradiated at 6 Gray (Gy) or left non-irradiated, and subsequently fixed at different time points up until 24 h post-irradiation.

An initial pilot experiment was conducted to determine the feasibility of utilising the IN Cell cellular imaging system, which allows automatic detection of intracellular foci. Cells were mock-infected or infected at 200 VP/cell with either Ad5 or EnAd, and at 24 h p.i. left non-irradiated or irradiated at 6 Gy. Cells were fixed with formalin at baseline, 30 min post-irradiation (irradiated cells only), and 8 and 24 h post-irradiation (both irradiated and non-irradiated). Analysis compared 53BP1 and RAD51 foci formation in mock- versus virus-infected cells. There was a significant increase in the mean number of 53BP1 foci/cell in EnAd-infected, non-irradiated cultures at all time points, and in Ad5-infected cultures at the 8 h time point (Figure 3.2D), with no difference in the percentage of non-irradiated cells containing more than ten foci (Figure 3.2B). In irradiated plates, there was a significant decrease in the mean number of 53BP1 foci/cell in Ad5-infected cultures at 8 h and 24 h post-irradiation (Figure 3.2C), as well as a significant decrease in the percentage of cells containing more than ten 53BP1 foci in Ad5-infected cultures at 8 h post-irradiation (Figure 3.2A), when compared to mock-infected samples. Analysis of RAD51 results was consistent with a marginal decrease in the mean number of foci/cell in Ad5-infected cultures at 8 h post-irradiation (Figure 3.3C).

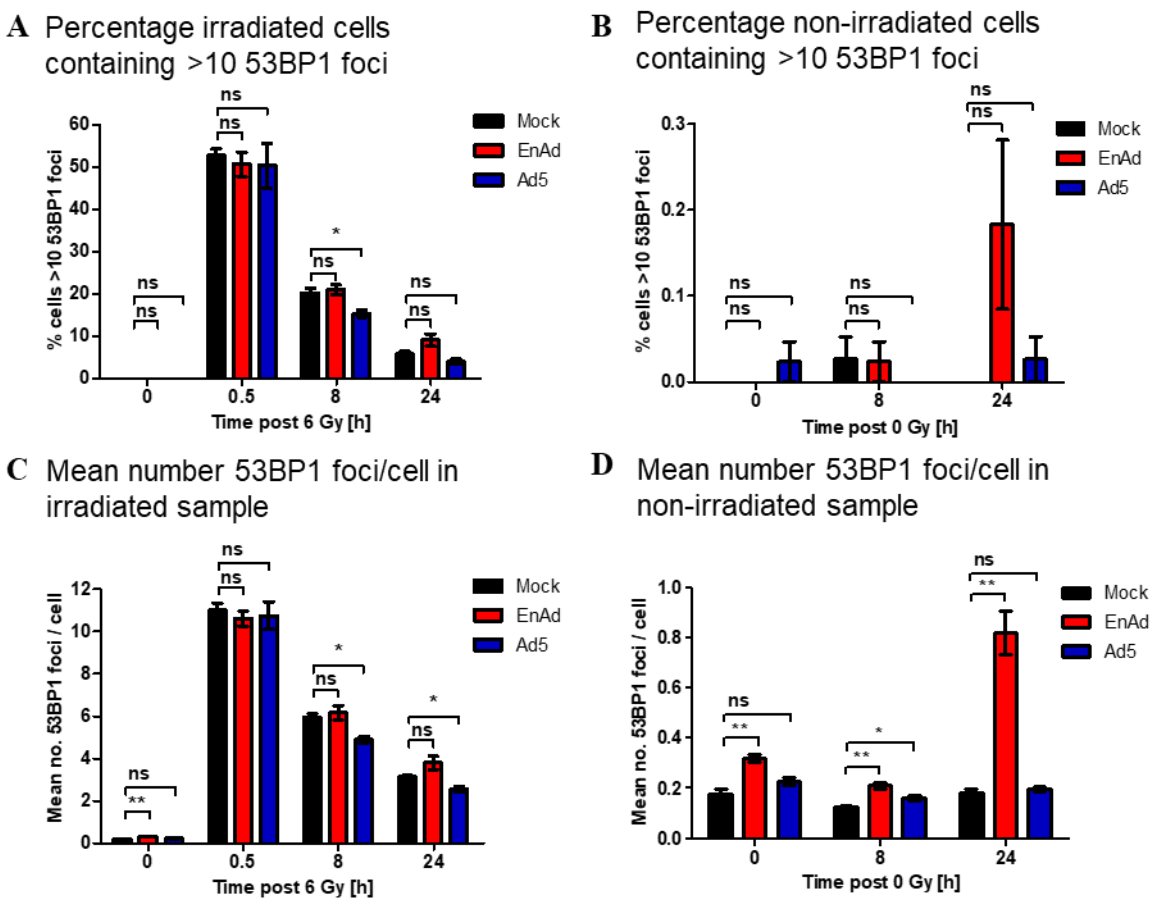


Figure 3.2 IN Cell software can be used to assess p53-binding protein 1 (53BP1) foci in adenovirus-infected cells. A549 cells were seeded into 96-well plates and the next day mock-infected or infected with EnAd or Ad5 at 200 virus particles (VP)/cell. At 24 h p.i. cells were either irradiated at 6 Gy **(A, C)** or left non-irradiated **(B, D)**. Cells were fixed at different time points following irradiation and subsequently blocked and stained for DAPI, 53BP1, and RAD51. Data was acquired and analysed using IN Cell software. Figure shows results for 53BP1. **(A-B)** Percentage of cells containing more than ten foci. **(C-D)** Mean number (no.) foci/cell. Figures show mean ± SEM of a single experiment containing three biological replicates. Significance was assessed using unpaired t-test against results for mock-infected cells. ns, not significant; $p < 0.05$, *; $p < 0.01$, **.

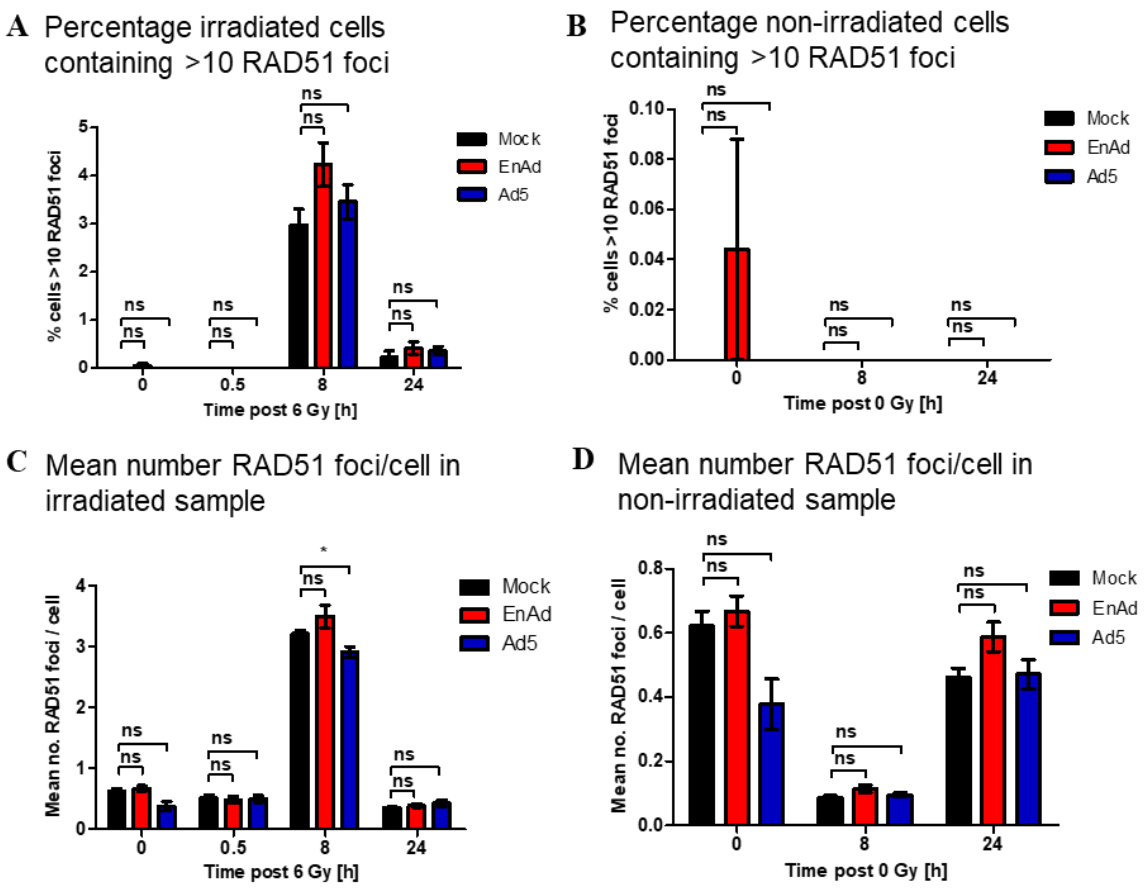


Figure 3.3 IN Cell software can be used to assess RAD51 foci in adenovirus-infected cells. A549 cells were seeded into 96-well plates and the next day mock-infected or infected with EnAd or Ad5 at 200 VP/cell. At 24 h p.i. cells were either irradiated at 6 Gy **(A, C)** or left non-irradiated **(B, D)**. Cells were fixed at different time points following irradiation and subsequently blocked and stained for DAPI, 53BP1, and RAD51. Data was acquired and analysed using IN Cell software. Figure shows results for RAD51. **(A-B)** Percentage of cells containing more than ten foci. **(C-D)** Mean number (no.) foci/cell. Figures show mean ± SEM of a single experiment containing three biological replicates. Significance was assessed using unpaired t-test against results for mock-infected cells. ns, not significant; $p < 0.05$, *; $p < 0.01$, **.

The finding of decreased 53BP1 foci formation in irradiated, Ad5-infected cultures was consistent with previous findings by our group (Jorien Koelen, PhD thesis, 2015), supporting the further use of this method to assess changes in DDR foci formation. There was, however, no way to differentiate infected and non-infected cells in wells containing adenovirus. This may in part have contributed to the results seen for EnAd, which conflicted with previous and predicted findings.

We therefore designed a pilot experiment to explore the possibility of using GFP-expressing viruses to assess changes in DDR foci formation in infected cells only, excluding any "noise" from non-infected cells within the well. As before, A549 cells were mock-infected or infected with EnAd and Ad5 at 200 VP/cell, however this time using viruses expressing GFP under the CMV promoter, which allows constitutive expression of the GFP transgene upon virus entry into the nucleus [124]. Plates were left non-irradiated or irradiated 24 h p.i. and analysed at 6 or 8 h post-irradiation for RAD51, and at 0, 30 min, 2, and 24 h post-irradiation for 53BP1. These time points were selected to allow assessment of DDR foci at the anticipated peak for RAD51 and 53BP1 foci formation, respectively. Though it was not possible to determine the percentage of GFP-positive cells containing more than ten foci, the mean number of foci/GFP-positive cell could be measured. As seen in Figure 3.4, the mean number of 53BP1 and RAD51 foci in irradiated, GFP-positive (therefore infected) cells decreased at all time points post-irradiation. Decrease of mean 53BP1 foci/cell was approximately four- to six-fold in EnAd-infected cells and two- to five-fold following Ad5 infection (Figure 3.4A). The results for RAD51 were even more striking, with a three- to nine-fold and ten- to fourteen-fold decrease in EnAd- and Ad5-infected cells, respectively (Figure 3.4C). In infected, non-irradiated cells, there was a decrease in the mean number of RAD51 foci/cell (Figure 3.4D), and an increase in mean 53BP1 foci/cell in Ad5-infected cells at the baseline and 2 h time points (Figure 3.4B), similar to findings seen in Figure 3.2. These results were in keeping with focused analysis of GFP-positive cells as a way to detect the impact of infection on intracellular DDR foci formation without interference from non-infected cells within the culture, and with potential inhibition of these two different parts of the DDR pathway by both adenoviruses studied.

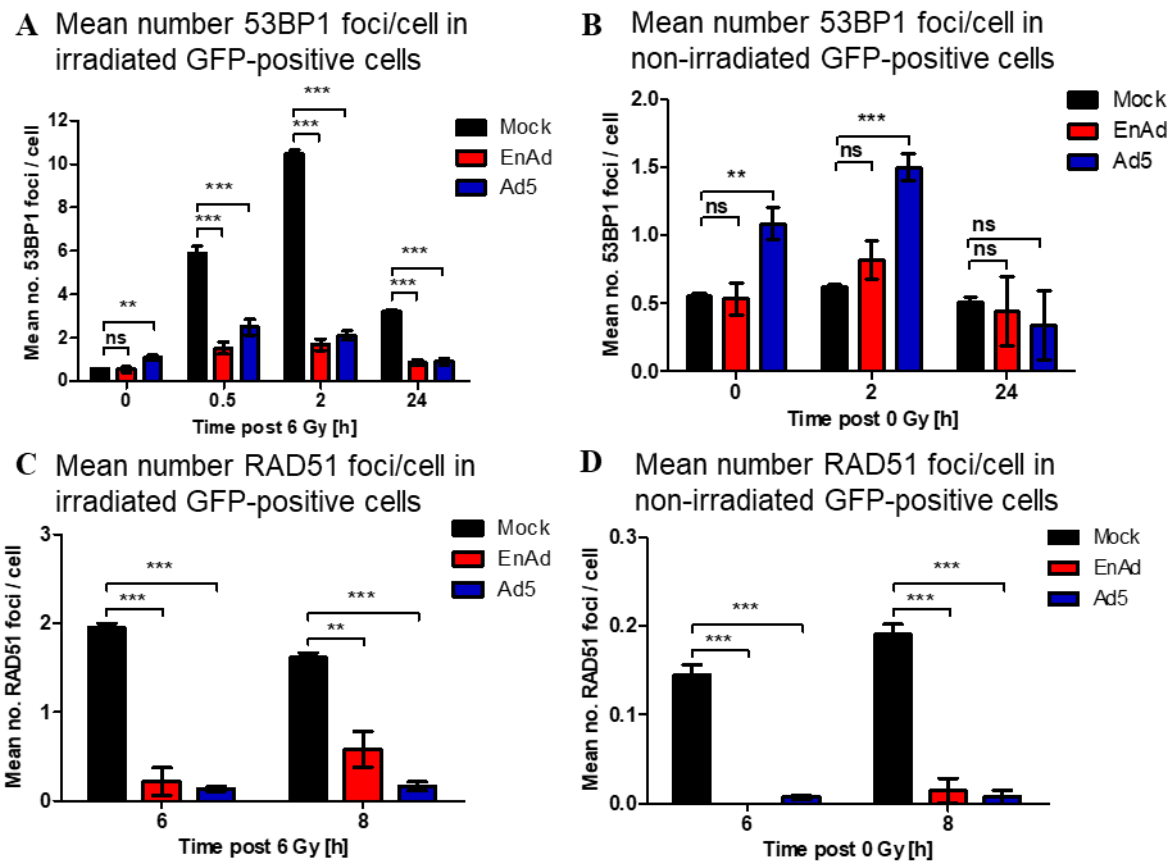


Figure 3.4 GFP-expressing viruses allow focused analysis of DNA damage response (DDR) foci formation in infected cells. A549 cells were seeded into 96-well plates and the next day mock-infected or infected with EnAd-CMV-GFP or Ad5-CMV-GFP at 200 VP/cell. At 24 h p.i. cells were either irradiated at 6 Gy **(A, C)** or left non-irradiated **(B, D**). Cells were fixed at different time points following irradiation and subsequently blocked and stained for DAPI and 53BP1 **(A-B)** or RAD51 **(C-D)**. Data was acquired and analysed using IN Cell software. Graphs demonstrate mean no. foci/cell given as mean ± SEM of a single experiment containing five biological replicates. Significance was assessed using unpaired t-test against results for mock-infected cells. ns, not significant; p <0.01, **; p <0.001, ***.

Having established that we are able to focus solely on infected cells in determining DDR foci formation, we optimised the viral dose of EnAd needed to result in adequate infection and GFP expression without causing excess cell death throughout the experimental timeline (24 – 48 h p.i., results not shown). Increasing the virus dose to 500 VP/cell ensured a sufficient number of GFP-expressing cells at each time point to allow analysis and detection of any virus effects on DDR foci formation. These optimised virus levels were used to conduct a time course experiment assessing foci formation at multiple points over the 24

hour period following irradiation (results not shown). Based on our findings, further experiments assessing the impact of IR were conducted at 2, 6, and 24 h post-irradiation, whilst foci formation in non-irradiated cells was assessed at the 0, 6, and 24 h time points (corresponding to 24, 30, and 48 h p.i.) to allow evaluation over a range of times post-infection as opposed to focusing on an expected peak and recovery as would be anticipated in irradiated cells.

Overall, these preliminary results supported the use of GFP-expressing adenovirus as a way to assess the impact of infection on DDR foci formation, and allowed the development of an optimised experimental set-up.

3.2.2 Adenovirus infection is associated with increased γH2AX formation

The finding that adenovirus infection causes γH2AX formation in the absence of irradiation has been well established [72, 73]. Staining for γH2AX was therefore selected as a control to ensure the decrease in RAD51 and 53BP1 foci seen in infected, irradiated cells was due to a true effect, as opposed to decreased detection resulting from GFP interference with analysis. A549 cells were mock-infected or infected with EnAd-CMV-GFP or Ad5-CMV-GFP at 500 VP/cell. At 24 h p.i., cells were left non-irradiated or irradiated at 6 Gy and analysed at baseline, at 2 h post-irradiation (6 Gy only) and at 6 and 24 h post-irradiation (0 Gy and 6 Gy) for γH2AX, 53BP1, or RAD51 foci formation.

Whilst establishing appropriate analysis parameters to distinguish GFP-positive cells it was noted that, though the majority of cells were clearly GFP-positive, a small number were detected by the software but not immediately noticed by visual assessment alone. Analysis settings were therefore adjusted to differentiate between strongly and weakly GFP-positive cells, to allow assessment of whether DDR foci formation differed between the two. It was

hypothesised that strongly GFP-positive cells may represent a later stage or higher level of infection.

Figure 3.5 shows representative images at 2 h post-irradiation for 6 Gy samples, at which time γH2AX foci number is expected to peak (Figures 3.5A, C, E), and at the 24 h time point for 0 Gy samples, corresponding to 48 h p.i. (Figures 3.5B, D, F). GFP expression can be clearly seen in infected, but not mock-infected, wells (Figures 3.5C-F). Though γH2AX foci (represented by red staining in the merged images) are present throughout in irradiated cells, they are much more prominent in the GFP-positive cells in non-irradiated wells (Figures 3.5D, F), in keeping with the expected result of adenovirus-induced γH2AX foci formation in the absence of radiation.

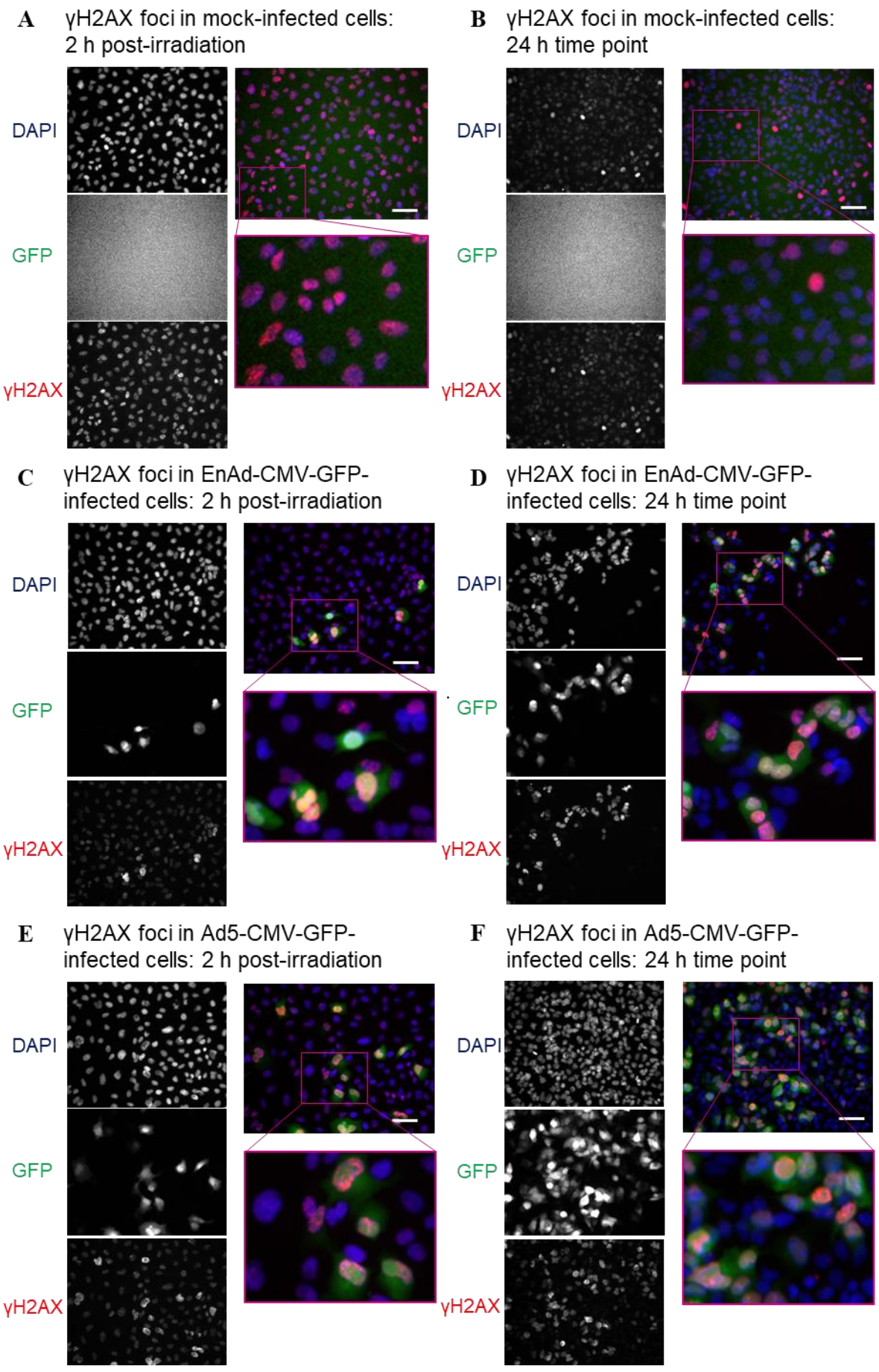
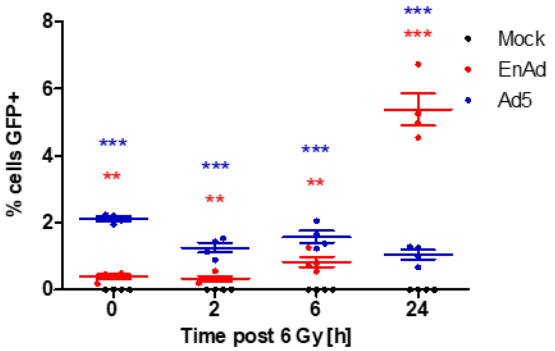

A
γH2AX foci in mock-infected cells: 2 h post-irradiation
B
γH2AX foci in mock-infected cells: 24 h time point
C
γH2AX foci in EnAd-CMV-GFP-infected cells: 2 h post-irradiation
D
γH2AX foci in EnAd-CMV-GFP-infected cells: 24 h time point
E
γH2AX foci in Ad5-CMV-GFP-infected cells: 2 h post-irradiation
F
γH2AX foci in Ad5-CMV-GFP-infected cells: 24 h time point
DAPI
GFP
γH2AX

Figure 3.5 GFP expression does not abrogate detection of DDR foci. A549 cells were seeded into 96-well plates and the next day mock-infected **(A-B)** or infected with EnAd-CMV-GFP **(C-D)** or Ad5-CMV-GFP **(E-F)** at 500 VP/cell. At 24 h p.i. cells were either irradiated at 6 Gy **(A, C, E)** or left non-irradiated **(B, D, F**). Cells were fixed at different time points following irradiation, blocked, and stained for DAPI and γH2AX. Images demonstrate typical staining pattern seen in cells 2 h post-irradiation **(A, C, E)** or at the 24 h time point in non-irradiated plates (48 h post-infection) **(B, D, F).** Separate and merged images are shown, in merged image DAPI is represented by blue, GFP by green, and γH2AX by red. Scale bar = 50 μm.

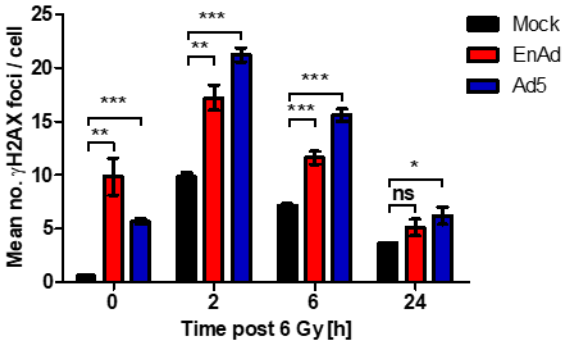
The pattern discussed above is confirmed by quantitative image analysis. Figure 3.6 shows the mean number of foci/cell in weakly and strongly GFP-positive cells (Figures 3.6B, D, F, H) alongside graphs demonstrating the percentage of cells identified as being weakly or strongly GFP-positive in the fields scanned (Figures 3.6A, C, E, G). Consistently, the mean number of γH2AX foci/cell was higher in infected cells compared to mock wells, in both the presence and absence of radiation. As anticipated, in irradiated cells foci count peaked 2 h post-irradiation (Figures 3.6B, D).

These results support the theory that foci detection using this methodology is unimpeded by GFP expression, and confirm previously published findings that adenovirus infection results in γH2AX foci formation even in the absence of radiation.

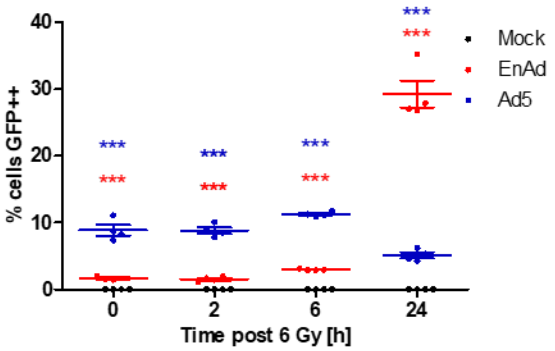
A Percentage weakly GFP-positive cells in irradiated sample



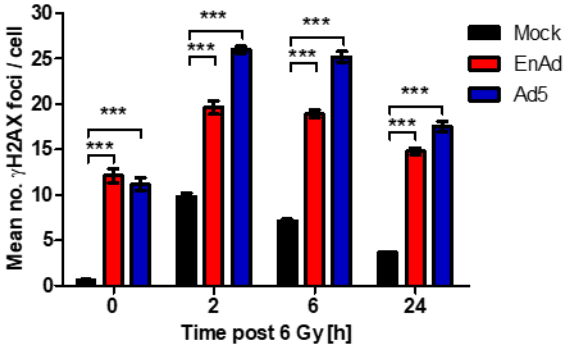
B Mean number γH2AX foci/cell in irradiated, weakly GFP-positive cells



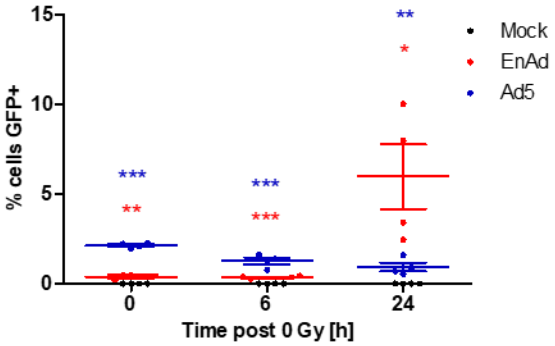
C Percentage strongly GFP-positive cells in irradiated sample



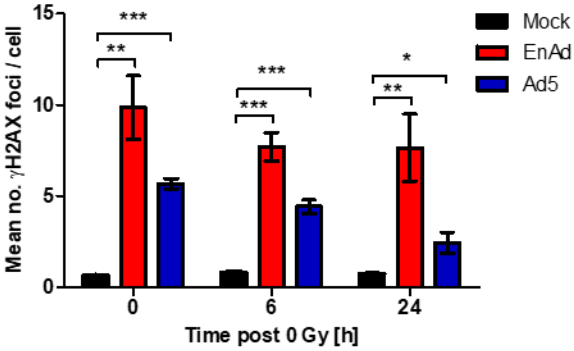
D Mean number γH2AX foci/cell in irradiated, strongly GFP-positive cells



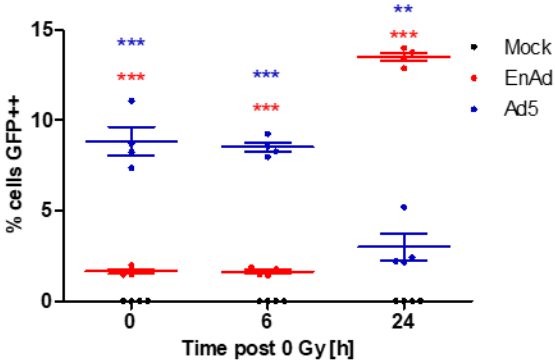
E Percentage weakly GFP-positive cells in non-irradiated sample



F Mean number γH2AX foci/cell in non-irradiated, weakly GFP-positive cells



G Percentage strongly GFP-positive cells in non-irradiated sample



H Mean number γH2AX foci/cell in non-irradiated, strongly GFP-positive cells

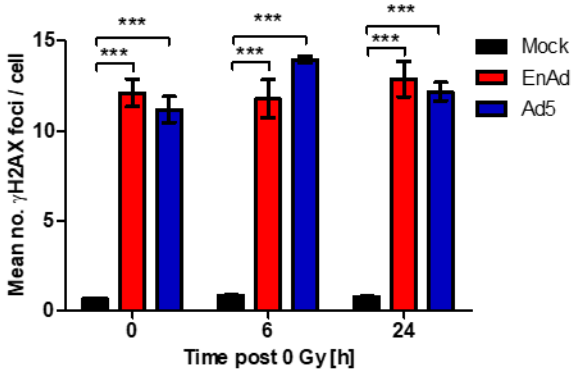


Figure 3.6 γH2AX foci formation in irradiated and non-irradiated adenovirus-infected cells. A549 cells were seeded into 96-well plates and the next day mock-infected or infected with EnAd-CMV-GFP or Ad5-CMV-GFP at 500 VP/cell. At 24 h p.i. samples were either irradiated at 6 Gy **(A-D)** or left non-irradiated **(E-H)**. Cells were fixed at different time points following irradiation and subsequently blocked and stained for DAPI and γH2AX. Data was acquired and analysed using IN Cell software to determine the percentage of weakly GFP-positive cells **(A, E)** and the percentage of strongly GFP-positive cells **(C, G)**. Gating allowed analysis of mean number of foci/cell specifically in weakly GFP-positive cells **(B, F)** and strongly GFP-positive cells **(D, H)**. Data shown is mean ± SEM of four biological replicates from a single experiment representative of three experiments. Significance was assessed using unpaired t-test against results for mock-infected cells. ns, not significant; $p < 0.05$, *; $p < 0.01$, **; $p < 0.001$, ***.

3.2.3 Adenovirus infection reduces 53BP1 foci formation in irradiated cells

The experiment described in 3.2.2., as well as evaluating γH2AX foci formation, also included wells stained with DAPI and antibody to 53BP1 to assess the impact of adenovirus infection on this key member of the DDR pathway. The typical staining pattern observed in these samples can be seen in Figure 3.7, which shows representative images for mock-infected and adenovirus-infected cells at 2 h (6 Gy condition – Figures 3.7A, C, E) and at the 24 h time point (0 Gy condition – Figures 3.7B, D, F). Though 53BP1 foci can clearly be seen 2 h post-irradiation in mock-infected cells (Figure 3.7A), the majority of GFP-positive irradiated cells do not exhibit this pattern (Figures 3.7C, E). In the non-irradiated cells there are far fewer foci visible (Figure 3.7B), but a greater number can be observed in the EnAd-infected, strongly GFP-positive cells (Figure 3.7D).

The data in Figure 3.8 support the trends described above. Irradiation-associated 53BP1 foci formation was found to be decreased in strongly GFP-positive adenovirus-infected cells compared to mock-infected wells (Figure 3.8D). A decrease in foci/cell was also seen at some, but not all, time points post-irradiation in weakly GFP-positive EnAd-infected cells compared to mock-infected wells (Figure 3.8B). Of note, the percentage of weakly GFP-positive cells in infected wells was much lower than strongly GFP-positive cells (Figures 3.8A, C, E, G).

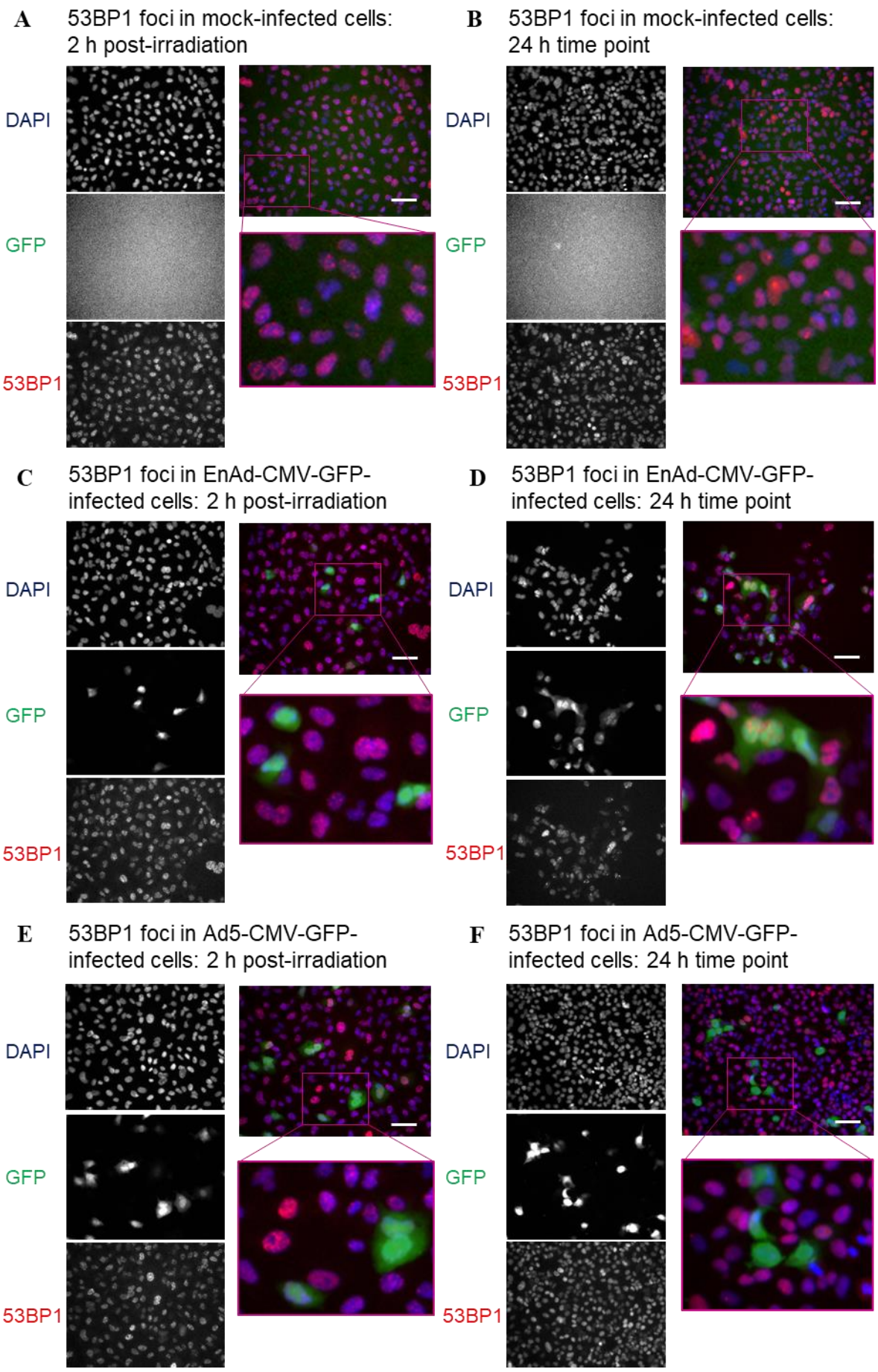

A
53BP1 foci in mock-infected cells: 2 h post-irradiation
DAPI
GFP
53BP1
B
53BP1 foci in mock-infected cells: 24 h time point
DAPI
GFP
53BP1
C
53BP1 foci in EnAd-CMV-GFP-infected cells: 2 h post-irradiation
DAPI
GFP
53BP1
D
53BP1 foci in EnAd-CMV-GFP-infected cells: 24 h time point
DAPI
GFP
53BP1
E
53BP1 foci in Ad5-CMV-GFP-infected cells: 2 h post-irradiation
DAPI
GFP
53BP1
F
53BP1 foci in Ad5-CMV-GFP-infected cells: 24 h time point
DAPI
GFP
53BP1

Figure 3.7 Adenovirus infection decreases irradiation-induced 53BP1 foci formation. A549 cells were seeded into 96-well plates and the next day mock-infected **(A-B)** or infected with EnAd-CMV-GFP **(C-D)** or Ad5-CMV-GFP **(E-F)** at 500 VP/cell. At 24 h p.i. cells were either irradiated at 6 Gy **(A, C, E)** or left non-irradiated **(B, D, F**). Cells were fixed at different time points following irradiation and subsequently blocked and stained for DAPI and 53BP1. Images demonstrate typical staining pattern seen in cells 2 h post-irradiation **(A, C, E)** or at the 24 h time point in non-irradiated plates (48 h post-infection) **(B, D, F).** Separate and merged images are shown, in merged image DAPI is represented by blue, GFP by green, and 53BP1 by red. Scale bar = 50 μm.

As shown in Figure 3.8F, though the mean number of 53BP1 foci/cell in non-irradiated samples remained low compared to the levels seen in irradiated cells, there was a significant increase in the mean number of 53BP1 foci/cell in weakly GFP-positive Ad5-infected cells (0.5-1 foci/cell) when compared to mock-infected samples (0.3 foci/cell). There was likewise a trend towards increased mean number of foci/cell in EnAd-infected weakly GFP-positive cells (0.7 foci/cell). Further, an increase in the number of mean foci/cell was seen in strongly GFP-positive Ad5- and EnAd- infected non-irradiated cells (0.3-0.9 foci/cell and 0.3-1.2 foci/cell respectively) compared to mock-infected wells (0.3 foci/cell) (Figure 3.8H).

These findings are consistent with a marked reduction in IR-induced 53BP1 foci formation in cells infected with Ad5 and EnAd compared to mock-infected cells, but also interestingly with a small yet significant increase in 53BP1 foci number in infected, non-irradiated cells.

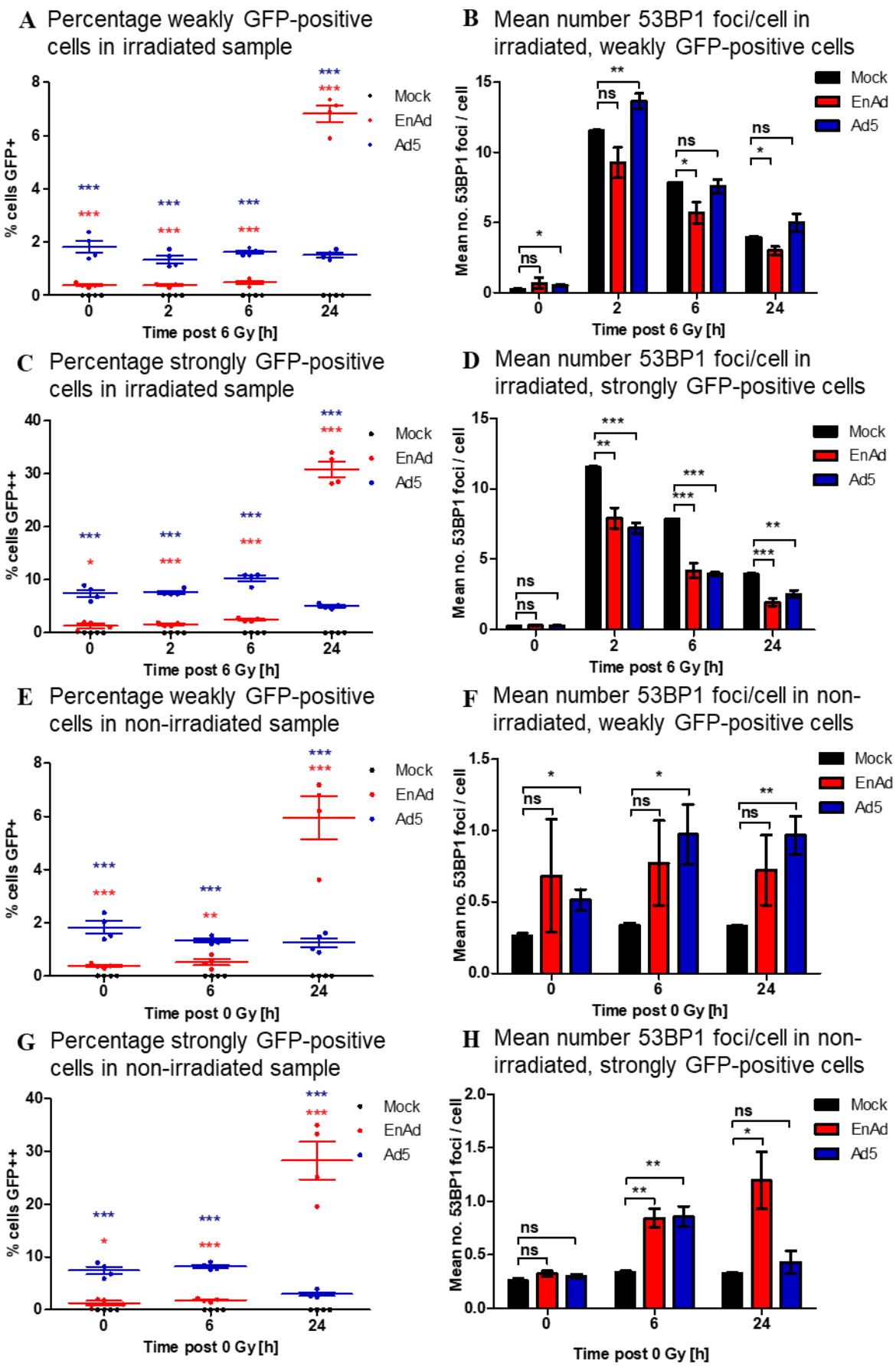

A Percentage weakly GFP-positive cells in irradiated sample
% cells GFP+
Time post 6 Gy [h]
Mock
EnAd
Ad5
B Mean number 53BP1 foci/cell in irradiated, weakly GFP-positive cells
Mean no. 53BP1 foci / cell
Time post 6 Gy [h]
C Percentage strongly GFP-positive cells in irradiated sample
% cells GFP++
Time post 6 Gy [h]
D Mean number 53BP1 foci/cell in irradiated, strongly GFP-positive cells
Mean no. 53BP1 foci / cell
Time post 6 Gy [h]
E Percentage weakly GFP-positive cells in non-irradiated sample
% cells GFP+
Time post 0 Gy [h]
F Mean number 53BP1 foci/cell in non-irradiated, weakly GFP-positive cells
Mean no. 53BP1 foci / cell
Time post 0 Gy [h]
G Percentage strongly GFP-positive cells in non-irradiated sample
% cells GFP++
Time post 0 Gy [h]
H Mean number 53BP1 foci/cell in non-irradiated, strongly GFP-positive cells
Mean no. 53BP1 foci / cell
Time post 0 Gy [h]

Figure 3.8 Adenovirus infection reduces the number of 53BP1 foci in irradiated cells. A549 cells were seeded into 96-well plates and the next day mock-infected or infected with EnAd-CMV-GFP or Ad5-CMV-GFP at 500 VP/cell. At 24 h p.i. cells were either irradiated at 6 Gy **(A-D)** or left non-irradiated **(E-H**). Cells were fixed at different time points following irradiation and subsequently blocked and stained for DAPI and 53BP1. Data was acquired and analysed using IN Cell software to determine the percentage of weakly GFP-positive cells **(A, E)** and the percentage of strongly GFP-positive cells **(C, G)**. Gating allowed analysis of mean number of foci/cell specifically in weakly GFP-positive cells **(B, F)** and strongly GFP-positive cells **(D, H)**. Data shown is mean ± SEM of four biological replicates from a single experiment representative of three experiments. Significance was assessed using unpaired t-test against results for mock-infected cells. ns, not significant; $p < 0.05$, *; $p < 0.01$, **; $p < 0.001$, ***.

3.2.4 53BP1 is phosphorylated in EnAd-infected cells

One of the ways in which Ad5 interacts with the DDR is through E4orf4-mediated inhibition of the phosphorylation of ATM and ATR substrates, including 53BP1. Interestingly, when HeLa cells were infected with an Ad5 mutant lacking *E4orf4*, foci of 53BP1 phosphorylated at Ser1778 formed around nuclear viral compartments in infected cells [66]. One of the changes that took place during the directed evolution of EnAd was the loss of E4orf4 through a 26 bp deletion near the 5'-end of the gene, causing a nonsense mutation. We therefore performed western blots on lysates of cells infected with Ad5 and EnAd in the presence and absence of irradiation to compare the impact of infection on 53BP1 phosphorylation status. A549 or HCT116 cells were mock-infected or infected with Ad5 or EnAd-SA-GFP at multiplicity of infection (MOI) 100. This viral dose was selected to ensure a sufficient level of infection after 24 h to detect any virus-mediated changes in phosphorylated and total 53BP1 levels. Use of EnAd-SA-GFP allowed a secondary method of confirming infection and virus replication were taking place, alongside checking for plaque formation. Baseline samples were harvested into RIPA buffer 2 h p.i. At 22 h p.i., half of the samples were irradiated at 6 Gy. All samples were harvested into RIPA buffer 2 h later. Blotting was performed for total 53BP1 and 53BP1 phosphorylated at Ser1778.

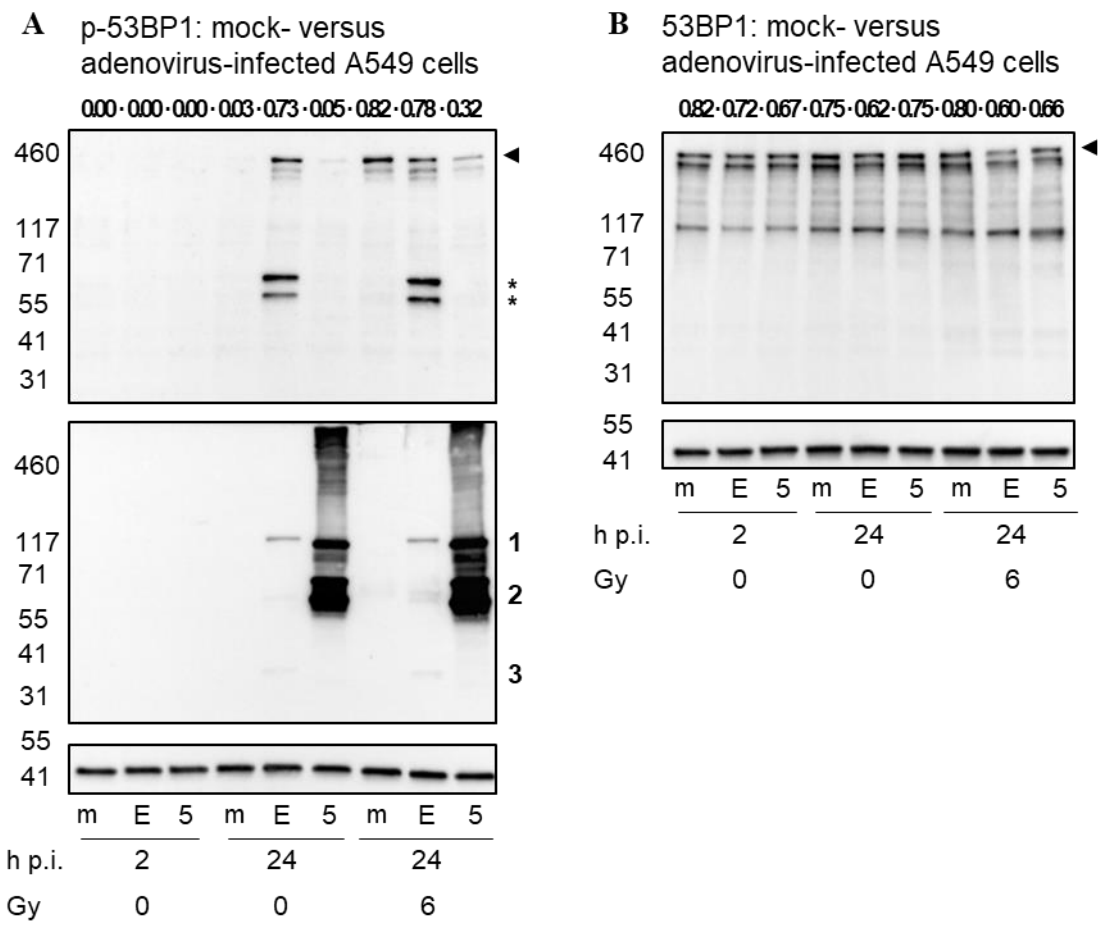


Figure 3.9 EnAd infection of A549 cells is associated with phosphorylation of 53BP1 in the absence of irradiation. A549 cells were seeded into 6-well plates and the next day mock-infected or infected with EnAd-SA-GFP or Ad5 at 100 MOI. Cell lysate was harvested 2 h p.i. and 24 h p.i. into RIPA buffer. Two hours prior to the 24 h time point, half of the samples were irradiated at 6 Gy and the other half mock-irradiated. Each lane contains 20 µg of protein. **(A)** Top panel shows results for antibody to 53BP1 phosphorylated at serine 1778 (labelled with arrow, non-specific bands labelled with *). Middle panel shows results for polyclonal antibody to late adenovirus structural proteins (labelled as 1, adenovirus hexon (105.3 kDa); 2, penton (62.3 kDa); and 3, fibre (36.1 kDa)). Bottom panel shows staining for β-actin. **(B)** Top panel shows staining for antibody to total 53BP1 (labelled with arrow) and bottom panel shows staining for β-actin. Density for each band is given above the corresponding lane as a β-actin-corrected value. m = mock; E = EnAd; 5 = Ad5. h p.i. = hours post-infection. Gy = radiation dose given in Gray.

Figure 3.9B shows there was no change in total 53BP1 levels in Ad5-infected cell lysates compared to mock, suggesting the fall in foci formation seen above is not secondary to a decrease in the total level of 53BP1. As anticipated, p53BP1 levels were decreased in irradiated, Ad5-infected cells. Interestingly, there was clear 53BP1 phosphorylation in EnAd-infected, non-irradiated cells. In addition, two smaller bands were detected by

antibody to p53BP1 in all EnAd-infected cells (Figure 3.9A). These findings were confirmed in HCT116 cells (Figure 3.10), indicating that the effect is not cell-line specific.

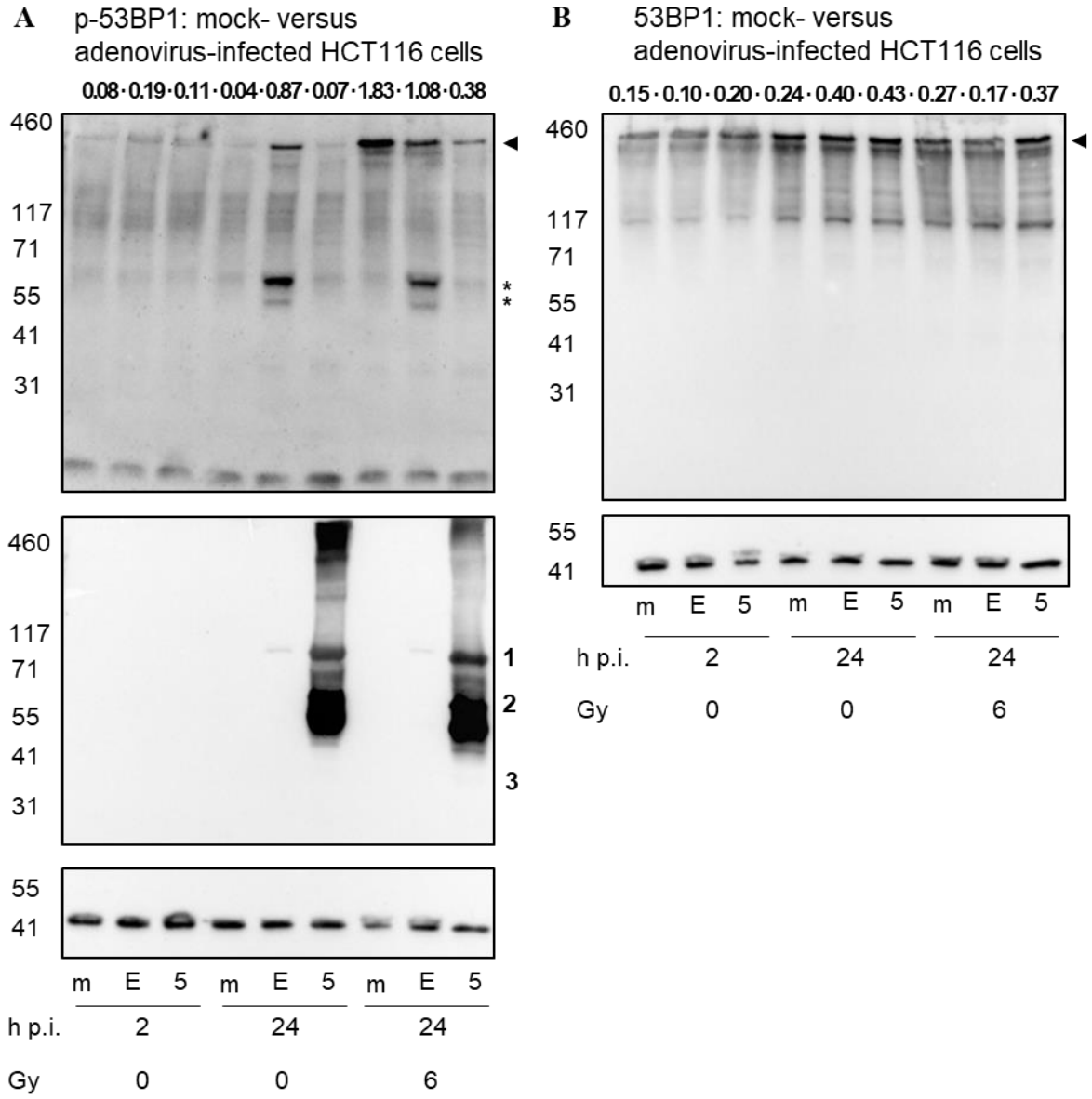


Figure 3.10 EnAd infection of HCT116 cells is associated with phosphorylation of 53BP1 in the absence of irradiation. HCT116 cells were seeded into 6-well plates and the next day mock-infected or infected with EnAd-SA-GFP or Ad5 at 100 MOI. Cell lysate was harvested 2 h p.i. and 24 h p.i. into RIPA buffer. Two hours prior to the 24 h time point, half of the samples were irradiated at 6 Gy and the other half mock-irradiated. Each lane contains 50 µg of protein. **(A)** Top panel shows results for antibody to 53BP1 phosphorylated at serine 1778 (labelled with arrow, non-specific bands labelled with *). Middle panel shows results for polyclonal antibody to late adenovirus structural proteins (labelled as 1, adenovirus hexon (105.3 kDa); 2, penton (62.3 kDa); and 3, fibre (36.1 kDa)). Bottom panel shows staining for β-actin. **(B)** Top panel shows staining for antibody to total 53BP1 (labelled with arrow) and bottom panel shows staining for β-actin. Density for each band is given above the corresponding lane as a β-actin-corrected value. Density analysis provided by Dr Sally Frost using Image Lab software. m = mock; E = EnAd; 5 = Ad5. h p.i. = hours post-infection. Gy = radiation dose given in Gray.

To investigate whether phosphorylation of 53BP1 in EnAd-infected cells was due to the lack of E4orf4 or due to a differing interaction between 53BP1 and group B or C adenoviruses, we also explored 53BP1 phosphorylation during infection with Ad11p, one of the group B viruses from which EnAd derives much of its genome. Ad11p contains full-length, functional *E4orf4*. The banding pattern, including 53BP1 phosphorylation and the smaller non-specific band, were identical for both group B viruses (Figure 3.11A), suggesting that the findings seen in EnAd-infected cells are not due to lack of E4orf4 but rather different interactions with this pathway between the different serotypes.

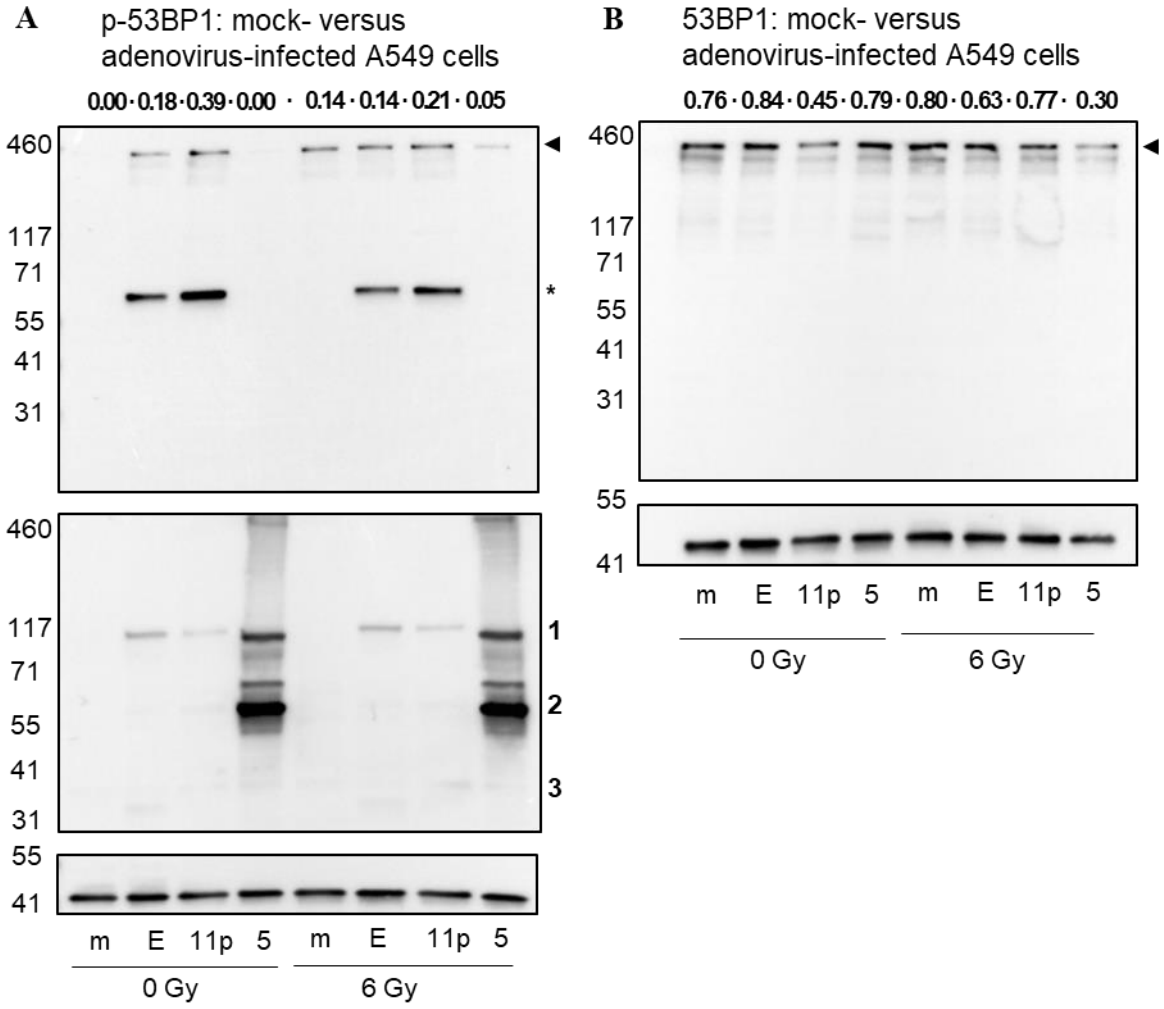


Figure 3.11 Ser1778 phosphorylation of 53BP1 in the absence of irradiation is conserved across two group B adenoviruses. A549 cells were seeded into 6-well plates and the next day mock-infected or infected with EnAd-SA-GFP, Ad11p, or Ad5 at 100 MOI. At 22 h p.i. half of all samples were irradiated at 6 Gy and the other half mock-irradiated. Cell lysate was harvested into RIPA buffer 24 h p.i. Each lane contains 20 µg of protein. **(A)** Top panel shows results for antibody to 53BP1 phosphorylated at serine 1778 (labelled with arrow, non-specific bands labelled with *). Middle panel shows results for polyclonal antibody to late adenovirus structural proteins (labelled as 1, adenovirus hexon (105.3 kDa); 2, penton (62.3 kDa); and 3, fibre (36.1 kDa)). Bottom panel shows staining for β-actin. **(B)** Top panel shows staining for antibody to total 53BP1 (labelled with arrow), and bottom panel shows staining for β-actin. Density for each band is given above the corresponding lane as a β-actin-corrected value. Density analysis provided by Dr Sally Frost using Image Lab software. m = mock; E = EnAd; 11p = Ad11p; 5 = Ad5. h p.i. = hours post-infection. Gy = radiation dose given in Gray.

Blotting for structural proteins in Figures 3.9-3.11 was used to confirm the presence of virus in the cell lysates. Despite infecting with equal MOI, structural protein levels were markedly different between different serotypes (Figures 3.9A, 3.10A, 3.11A). The antibody utilised is a polyclonal antibody developed using disrupted type 5 virions as the immunogen. It is therefore possible the variation in levels is due to differential binding of antibody depending on serotype, however the likeliest cause is variable infection kinetics between Ad5 and EnAd. The time point at which the cells were harvested would correspond to different points of the virus life cycle, one may therefore expect that different amounts of structural proteins have been produced. Of note, in Figure 3.11A the structural protein levels are similar between the two group B adenoviruses, but markedly different from the results seen using the group C virus Ad5. The time point of harvesting was such that all adenovirus serotypes would have undergone at least one cycle of replication, however, and thus any impact of both early and late gene production on p53BP1 and 53BP1 levels could be observed even in the context of differing structural protein levels.

3.2.5 Adenovirus infection reduces the formation of RAD51 foci following irradiation

RAD51 is a key member of the HR pathway [123], an alternative pathway to NHEJ involved in the repair of double-strand DNA breaks. As discussed above, the interaction between adenovirus infection and HR is less well established, however one may expect a compensatory increase in HR in cells where 53BP1 function is inhibited [125]. Nonetheless,

our preliminary experiments (Figures 3.4 and 3.5) are consistent with decreased irradiation-induced RAD51 foci formation in adenovirus-infected cells. We therefore wished to further explore this unexpected finding and the interaction between adenovirus infection and the HR pathway.

As before, A549 cells were mock-infected or infected with Ad5-CMV-GFP or EnAd-CMV-GFP at an MOI of 500 VP/cell. At 24 h p.i., plates were left non-irradiated or irradiated at 6 Gy and analysed at 0, 2, 6, and 24 h post-irradiation for RAD51, 53BP1, or γH2AX. Figure 3.12 shows representative images for RAD51 and DAPI staining 6 h post-irradiation, when RAD51 foci formation peaks (Figures 3.12A, C, E), and at the 24 h non-irradiated time point (Figures 3.12B, D, F). RAD51 foci are denoted in red in the merged image. Though multiple foci are present in uninfected irradiated cells (Figure 3.12A), they are virtually absent in GFP-positive cells in both irradiated and non-irradiated wells (Figures 3.12C-F), consistent with our previous findings of inhibited RAD51 foci formation in adenovirus-infected cells.

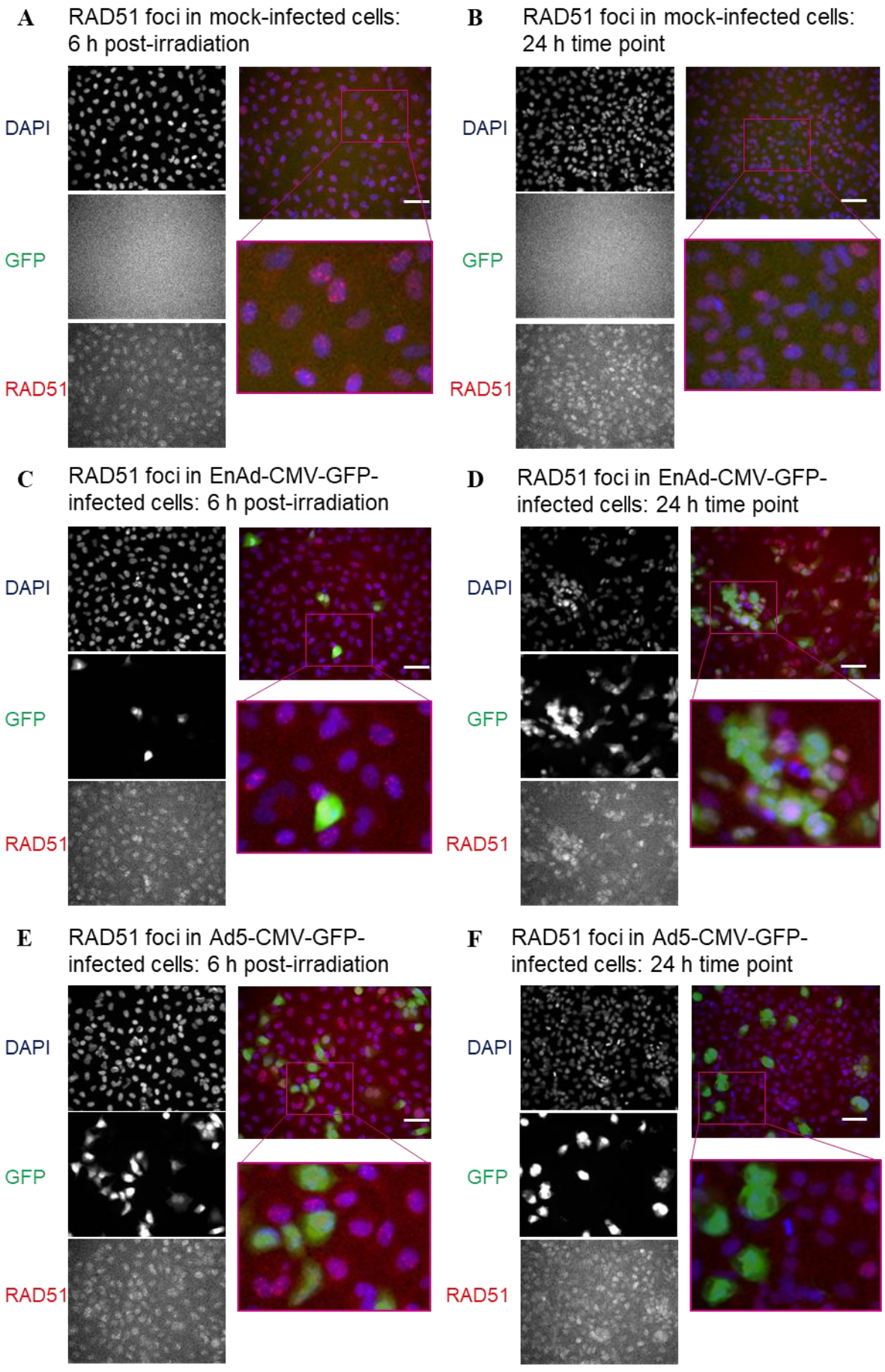
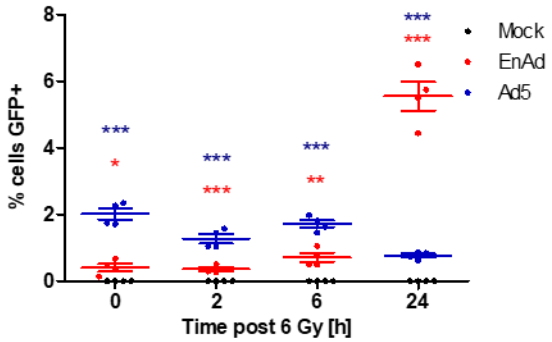

A
RAD51 foci in mock-infected cells: 6 h post-irradiation
B
RAD51 foci in mock-infected cells: 24 h time point
C
RAD51 foci in EnAd-CMV-GFP-infected cells: 6 h post-irradiation
D
RAD51 foci in EnAd-CMV-GFP-infected cells: 24 h time point
E
RAD51 foci in Ad5-CMV-GFP-infected cells: 6 h post-irradiation
F
RAD51 foci in Ad5-CMV-GFP-infected cells: 24 h time point
DAPI
GFP
RAD51

Figure 3.12 Adenovirus infection decreases irradiation-induced RAD51 foci formation. A549 cells were seeded into 96-well plates and the next day mock-infected **(A-B)** or infected with EnAd-CMV-GFP **(C-D)** or Ad5-CMV-GFP **(E-F)** at 500 VP/cell. At 24 h p.i. cells were either irradiated at 6 Gy **(A, C, E)** or left non-irradiated **(B, D, F**). Cells were fixed at different time points following irradiation and subsequently blocked and stained for DAPI and RAD51. Images demonstrate typical staining pattern seen in cells 6 h post-irradiation **(A, C, E)** or at the 24 h time point in non-irradiated plates (48 h post-infection) **(B, D, F).** Separate and merged images are shown, in merged image DAPI is represented by blue, GFP by green, and RAD51 by red. Scale bar = 50 μm.

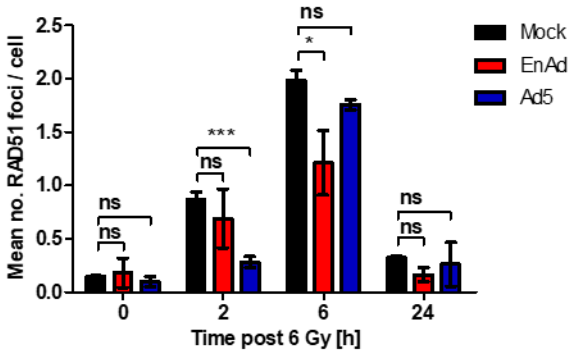
This is supported by data shown in Figure 3.13D, which demonstrates a significant decrease in the mean number of RAD51 foci/cell in irradiated, strongly GFP-positive adenovirus-infected cells when compared to mock-infected wells. There was likewise a trend towards decreased mean foci/cell formation in weakly GFP-positive adenovirus-infected cells at 2 h and 6 h post-irradiation (Figure 3.13B). This reached significance for Ad5-infected cells at 2 h post-irradiation and for weakly GFP-positive EnAd-infected cells at 6 h post-irradiation.

In non-irradiated samples, the mean number of RAD51 foci/cell was not significantly decreased in weakly or strongly GFP-positive cells compared to mock-infected cells (Figures 3.13F, H). There was a trend however towards decreased RAD51 mean foci/cell at the baseline time point in Ad5-infected, strongly GFP-positive cells, suggestive of some level of RAD51 foci inhibition even in the absence of irradiation. A decrease in mean RAD51 foci/cell in non-irradiated cells was also noted in the initial pilot experiment shown in Figure 3.4D.

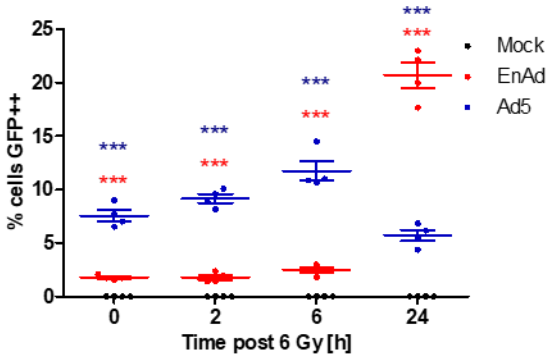
A Percentage weakly GFP-positive cells in irradiated sample



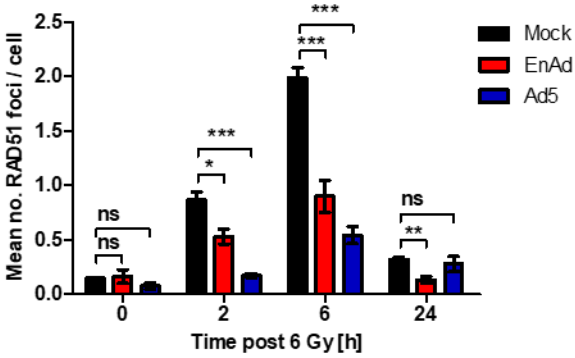
B Mean number RAD51 foci/cell in irradiated, weakly GFP-positive cells



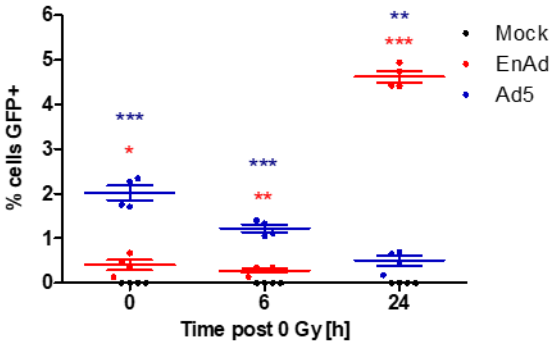
C Percentage strongly GFP-positive cells in irradiated sample



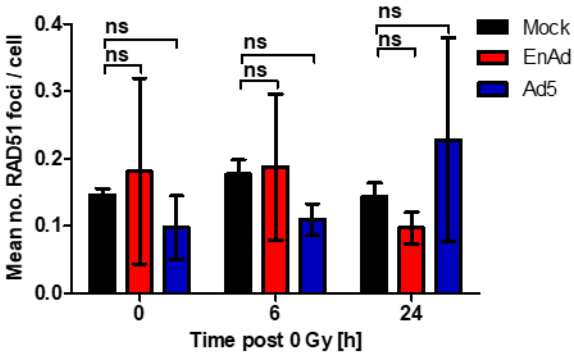
D Mean number RAD51 foci/cell in irradiated, strongly GFP-positive cells



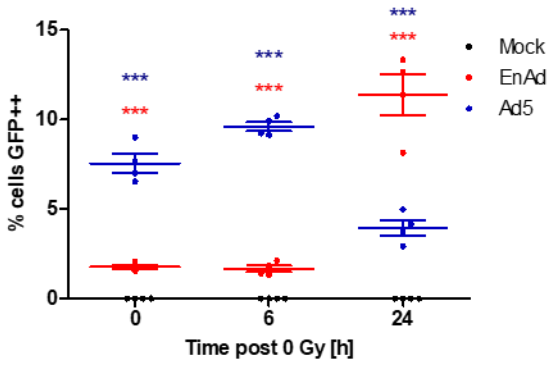
E Percentage weakly GFP-positive cells in non-irradiated sample



F Mean number RAD51 foci/cell in non-irradiated, weakly GFP-positive cells



G Percentage strongly GFP-positive cells in non-irradiated sample



H Mean number RAD51 foci/cell in non-irradiated, strongly GFP-positive cells

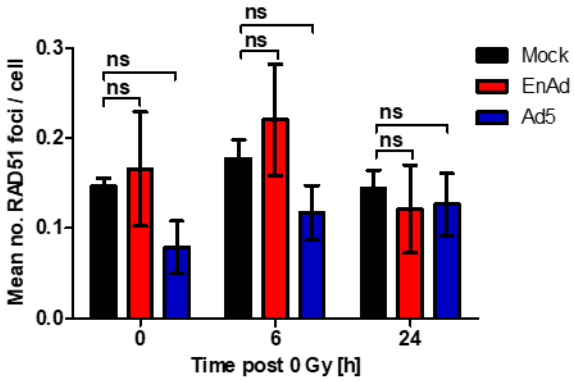


Figure 3.13 Adenovirus infection reduces the formation of RAD51 foci in irradiated cells. A549 cells were seeded into 96-well plates and the next day mock-infected or infected with EnAd-CMV-GFP or Ad5-CMV-GFP at 500 VP/cell. At 24 h p.i. cells were either irradiated at 6 Gy **(A-D)** or left non-irradiated **(E-H**). Cells were fixed at different time points following irradiation and subsequently blocked and stained for DAPI and RAD51. Data was acquired and analysed using IN Cell software to determine the percentage of weakly GFP-positive cells **(A, E),** and the percentage of strongly GFP-positive cells **(C, G)**. Gating allowed analysis of mean number of foci/cell specifically in weakly GFP-positive cells **(B, F)** and strongly GFP-positive cells **(D, H)**. Data shown is mean ± SEM of four biological replicates from a single experiment representative of three experiments. Significance was assessed using unpaired t-test against results for mock-infected cells. ns, not significant; $p < 0.05$, *; $p < 0.01$, **; $p < 0.001$, ***.

Overall, the results focusing specifically on GFP-expressing adenovirus-infected cells are consistent with virus-associated inhibition of RAD51 foci formation following IR. As there was also some trend towards decreasing foci formation in the absence of radiation in infected cells, adenovirus-infected cell lysates were probed for RAD51 by western blotting to assess if there was a decrease in total protein levels.

A549 (Figures 3.14A, C) or HCT116 cells (Figure 3.14B) were mock-infected or infected with EnAd-SA-GFP, Ad5, or Ad11p at an MOI of 100. Samples were harvested into RIPA buffer at 2 h and 24 h p.i. The intensity of the RAD51 bands did not decrease in infected versus mock-infected cells, suggestive of the fall in RAD51 foci/cell not being due to a decrease in total protein levels. A number of non-specific heavier bands were consistently seen in lysates from adenovirus-infected cells, though the weight of these appeared to vary between EnAd/Ad11p and Ad5 (Figure 3.14C). Blotting for structural proteins confirmed the presence of adenovirus in the cell lysate; once again levels were notably different between EnAd-Ad11p- and Ad5-infected samples (Figure 3.14C).

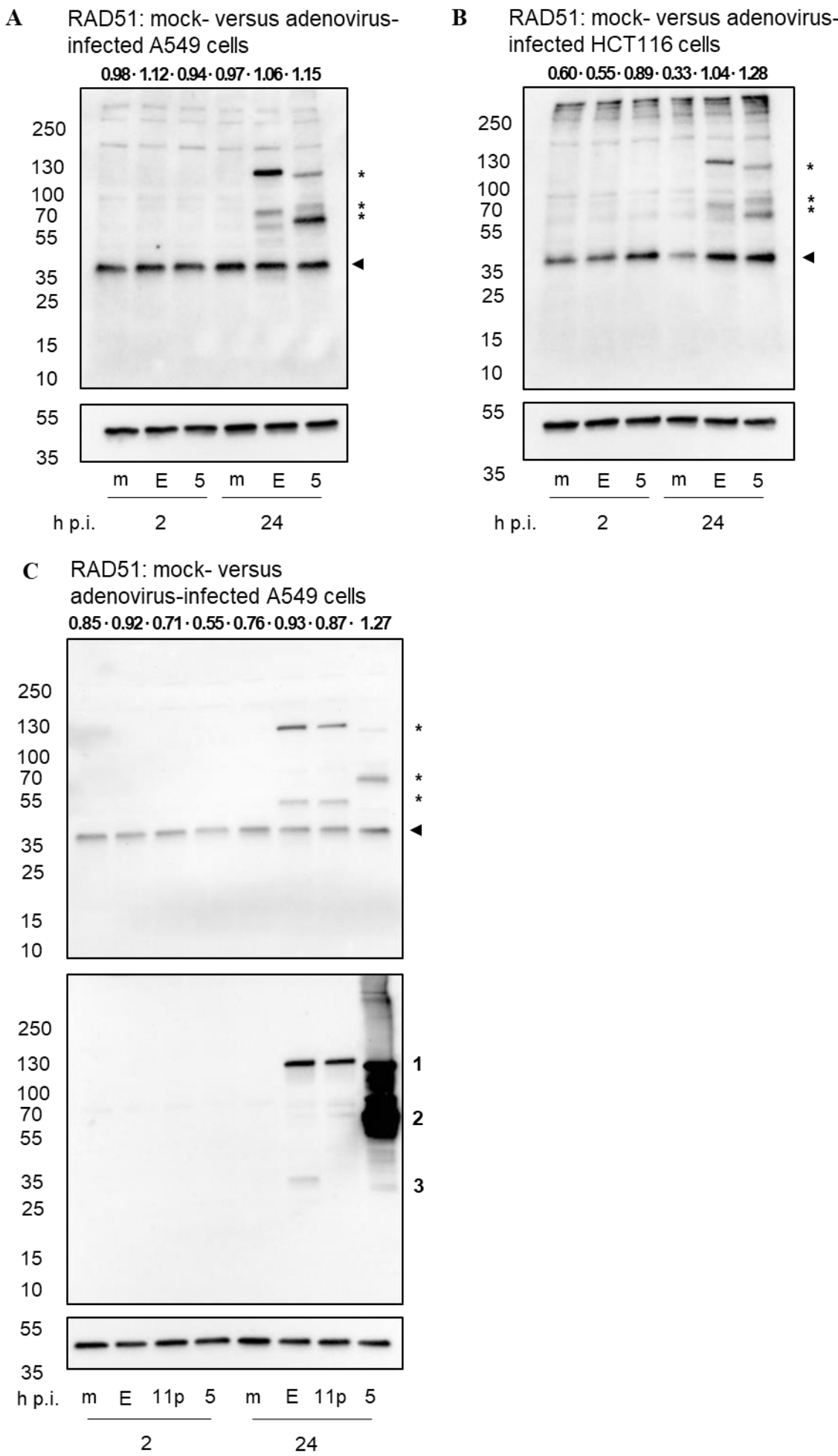

A
RAD51: mock- versus adenovirus-infected A549 cells
0.98 · 1.12 · 0.94 · 0.97 · 1.06 · 1.15
250
130
100
70
55
35
25
15
10
55
35
m E 5 m E 5
h p.i. 2 24
B
RAD51: mock- versus adenovirus-infected HCT116 cells
0.60 · 0.55 · 0.89 · 0.33 · 1.04 · 1.28
250
130
100
70
55
35
25
15
10
55
35
m E 5 m E 5
h p.i. 2 24
C
RAD51: mock- versus adenovirus-infected A549 cells
0.85 · 0.92 · 0.71 · 0.55 · 0.76 · 0.93 · 0.87 · 1.27
250
130
100
70
55
35
25
15
10
250
130
100
70
55
35
25
15
10
1
2
3
55
35
h p.i. m E 11p 5 m E 11p 5
2 24

Figure 3.14 Adenovirus infection is associated with non-specific heavy bands when staining for RAD51. A549 cells **(A, C)** or HCT116 cells **(B)** were seeded into 6-well plates and the next day mock-infected or infected with EnAd-SA-GFP or Ad5 **(A-C)** or Ad11p **(C)** at 100 MOI. Cell lysate was harvested into RIPA buffer 2 h p.i. and 24 h p.i. **(A-B)** Top panel shows results for antibody to RAD51 (labelled with arrow, non-specific bands denoted by *). Bottom panel shows staining for β-actin. Each lane contains 20 µg **(A)** or 30 µg **(B)** of protein. **(C)** Top panel shows results for antibody to RAD51 (labelled with arrow, non-specific bands denoted by *). Middle panel shows results for polyclonal antibody to late adenovirus structural proteins (labelled as 1, adenovirus hexon (105.3 kDa); 2, penton (62.3 kDa); and 3, fibre (36.1 kDa)). Bottom panel shows staining for β-actin. Each lane contains 15 µg of protein. Density for each band is given above the corresponding lane as a β-actin-corrected value. m = mock; E = EnAd; 11p = Ad11p; 5 = Ad5. h p.i. = hours post-infection.

To determine if these heavier bands represented modified RAD51 protein, *RAD51* expression was knocked down using siRNA-aided silencing. A549 cells were reverse transfected with either non-template control siRNA or siRNA against *RAD51*. At 48 h post-transfection, cells were either mock-infected or infected with EnAd-SA-GFP or Ad5 at an MOI of 100. At 24 h p.i., corresponding to 72 h post-transfection, samples were harvested for cell lysis and probed for RAD51 protein using western blotting. In cells transfected with siRNA to *RAD51*, a decrease in the RAD51-specific band was seen as expected, without a corresponding decrease in the intensity of the heavier, non-specific bands seen in adenovirus-infected cells (Figure 3.15). This indicates that the heavier bands detected by RAD51 antibody in the lysates of adenovirus-infected cells are not modified forms of RAD51.

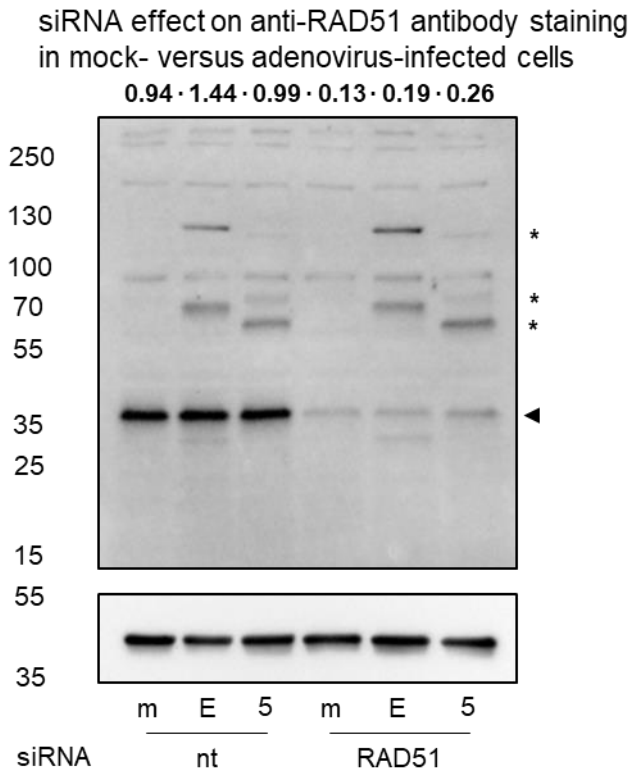


Figure 3.15 siRNA to *RAD51* does not affect adenovirus-associated non-specific western blot staining. A549 cells were seeded into 6-well plates, each well containing appropriate transfection reagents and siRNA either to *RAD51* or a non-template control. Medium was changed 6 h later. At 48 h post-transfection, cells were mock-infected or infected with EnAd-SA-GFP or Ad5 at MOI 100. Cell lysate was harvested into RIPA buffer 24 h later. Each lane contains 20 µg of protein. Top panel shows staining with RAD51 (labelled with arrow, non-specific bands denoted by *), bottom panel shows staining for β-actin. Density for each band is given above the corresponding lane as a β-actin-corrected value. m = mock; E = EnAd; 5 = Ad5. nt = non-template control.

3.2.6 Adenovirus infection is associated with decreased DNA ligase IV levels

All adenovirus serotypes investigated caused a decrease in DNA ligase IV levels following infection [58], we therefore sought to determine whether this also applies to EnAd. We first confirmed the specificity of the DNA ligase IV antibody by western blotting. A549 cells were reverse transfected with either a non-template control siRNA, siRNA to DNA ligase IV, or siRNA to PLK1, which acted as a positive control by inducing easily-observable apoptosis in transfected cells [126]. Cell lysates were harvested at 24 and 48 h post-transfection for probing with DNA ligase IV antibody. Figure 3.16 shows that the DNA

ligase IV antibody is specific for the protein, as no signal is present in samples in which DNA ligase IV expression was knocked down by siRNA.

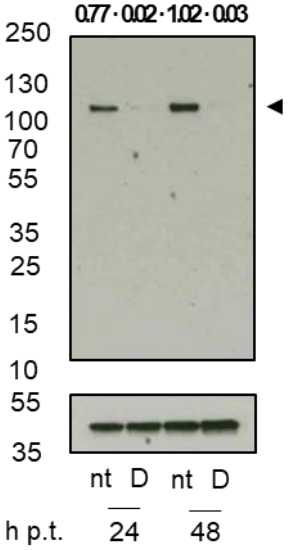


Figure 3.16 DNA ligase IV antibody is specific for protein of interest. A549 cells were seeded into 6-well plates, each well containing appropriate transfection reagents and siRNA either to DNA ligase IV, a non-template control or PLK1 (acting as a positive control for transfection). Medium was changed 16 h later and cell lysate harvested into RIPA buffer 24 and 48 h post-transfection (h p.t.). Each lane contains 25 µg of protein. Top panel shows staining with DNA ligase IV (arrow), bottom panel shows staining for β-actin. Density for each band is given above the corresponding lane as a β-actin-corrected value. nt = non-template control; D = DNA ligase IV siRNA.

We next tested the impact of infection with either Ad5 or EnAd on DNA ligase IV levels in three different cell lines (Figure 3.17). A549, HCT116 or HT-29 cells were infected at an MOI of 100 with Ad5 or EnAd-SA-GFP, or mock-infected. Lysates were harvested at 2 and 24 h p.i. and probed for DNA ligase IV expression by western blotting. DNA ligase IV levels in adenovirus-infected cells were markedly decreased in all three cell lines at 24 h p.i. This is consistent with previously published findings using a range of adenovirus serotypes [58] and suggests the impact of EnAd infection on DNA ligase IV levels parallels that of other adenoviruses.

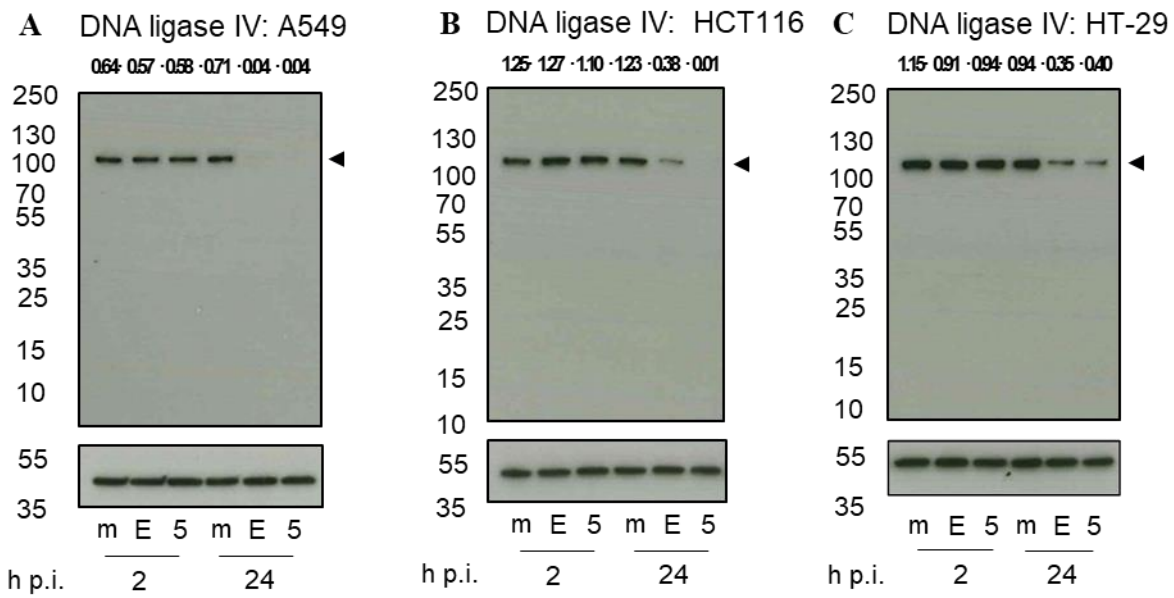


Figure 3.17 Adenovirus infection is associated with a decrease in DNA ligase IV levels. A549 **(A)**, HCT116 **(B)** or HT-29 **(C)** cells were seeded into 6-well plates and the subsequent day either mock-infected or infected with EnAd-SA-GFP or Ad5 at an MOI of 100. Cell lysate was harvested into RIPA buffer 2 h p.i. and 24 h p.i. Each lane contains 10 µg of protein. Western blot is representative of three repeats. Top panels denote staining with antibody to DNA ligase IV (arrow), bottom panel to β-actin. Density for each band is given above the corresponding lane as a β-actin-corrected value. m = mock; E = EnAd; 5 = Ad5. h p.i. = hours post-infection.

Published data has shown that the decrease in DNA ligase IV levels following infection is proteasomally-mediated in Ad5-infected cells [88]. We investigated whether this was also the case for EnAd. A549 cells were infected with EnAd-SA-GFP at 200 VP/cell (corresponding to approximately MOI 11), or mock-infected. At 2 h p.i. cells were treated with the proteasome inhibitor MG132 or DMSO vehicle control. Samples were harvested either immediately following addition of MG132/DMSO, or at 24 or 48 h p.i. Cell supernatant was harvested separately for assessment of $TCID_{50}$/mL. Whereas a fall in DNA ligase IV levels was seen 24 h p.i. in cells infected with MOI 100 (Figure 3.17), the decrease in DNA ligase IV at the lower level of infection used in this experiment only became apparent at 48 h p.i. and was less marked in cells also treated with MG132 (Figure 3.18A). This is in keeping with the EnAd-associated fall in DNA ligase IV levels being at least partially mediated by the proteasome.

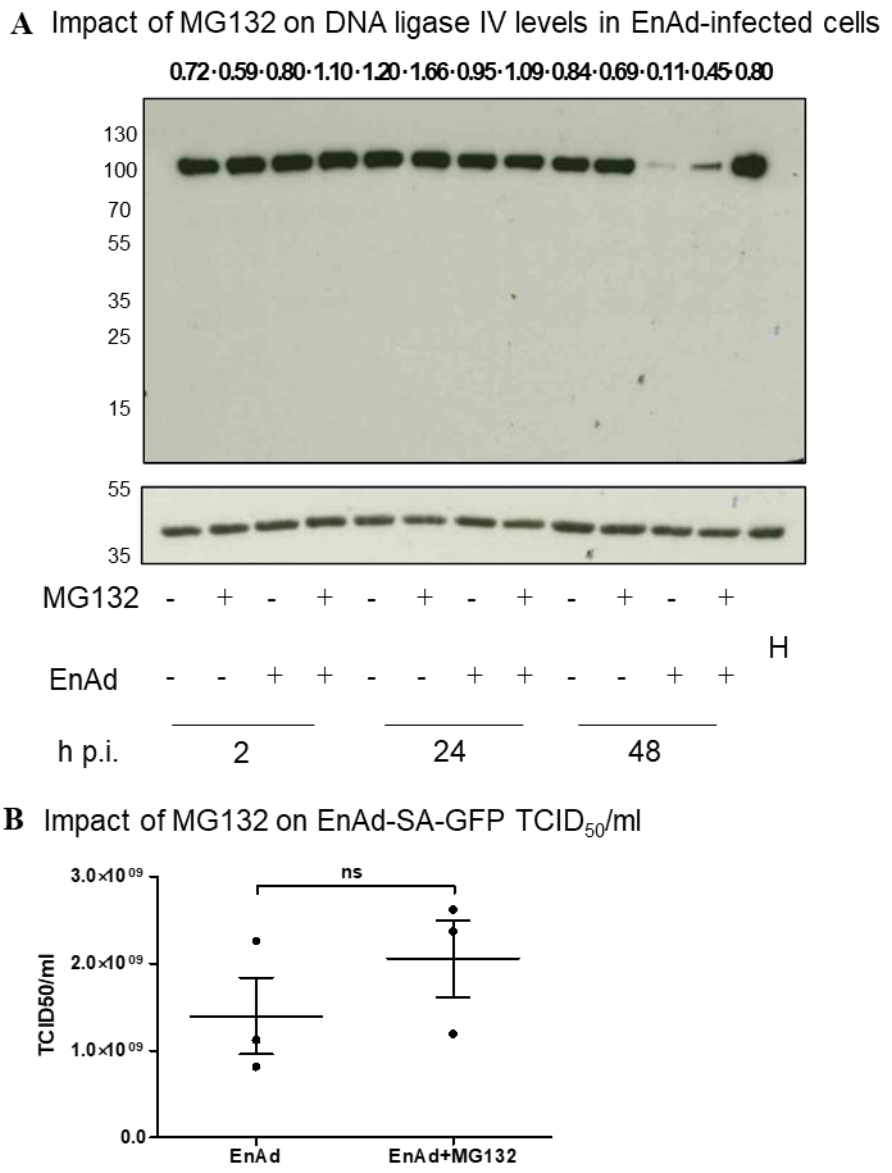


Figure 3.18 EnAd infection is associated with a partially proteasomally-mediated decrease in DNA ligase IV levels. A549 cells were seeded into 6-well plates and the next day infected with EnAd-SA-GFP at 200 VP/cell (corresponding to approximately MOI 11) or mock-infected. At 2 h p.i., medium was replaced with medium containing either 2 µl DMSO per well or 10 µM MG132 per well. **(A)** Cell lysate was harvested into RIPA buffer immediately post addition of MG132/DMSO, or 24 and 48 h p.i. HeLa cell lysate was used as a positive control for DNA ligase IV. Each lane contains 30 µg of protein. Top panel demonstrates staining for DNA ligase IV, bottom panel for β-actin. Density for each band is given above the corresponding lane as a β-actin-corrected value. Density analysis provided by Dr Sally Frost using Image Lab software. Western blot is representative of three repeats. **(B)** Cell supernatant was harvested 48 h p.i. and used to determine $TCID_{50}$/ml. Each data point represents the mean result of one experiment performed in triplicate. Graph shows mean ± SEM, significance was evaluated using unpaired t-test. H = HeLa lysate. h p.i. = hours post-infection.

One may predict that inhibiting DNA ligase IV degradation, a crucial step in the virus life cycle, may limit virus replication. We confirmed that there was no inhibition of infectious particle production in MG132- versus DMSO-treated cells (Figure 3.18B). Further, comparable levels of infectious virus particle production under both conditions suggest there is no impact of MG132 on virus replication. The reduced DNA ligase IV degradation at 48 h in proteasome inhibitor-treated, infected cells was therefore not due to MG132-mediated inhibition of EnAd reinfection.

3.3 Chapter main findings

In this chapter, we established a relatively elegant way of assessing the mean number of DDR foci/cell in adenovirus-infected cells. We utilised this to confirm an adenovirus-associated increase in γH2AX and further demonstrated reduced formation of 53BP1 and RAD51 foci in adenovirus- versus mock-infected cells following IR. Interestingly, we showed a significant increase in the formation of 53BP1 foci in adenovirus- versus mock-infected, non-irradiated cells. Using western blotting, we established that the changes seen in foci formation are not secondary to a decrease in total 53BP1 or RAD51 levels in infected cells, and that infection with group B adenovirus leads to phosphorylation at Ser1778 of 53BP1, even in the absence of irradiation. Finally, we confirmed that EnAd parallels previously published findings on adenovirus infection leading to a decrease in cellular DNA ligase IV levels and showed that this is partially proteasomally-mediated.

3.4 Chapter discussion

Previous groups have used IN Cell scanning and analysis of 53BP1 foci to investigate the effects of ionising radiation on the DDR pathway [127]. We refined this in the context of adenovirus infection to allow assessment of treatment effects within infected cells only, without potential interference from cells not yet infected by virus. The number of mean

foci/cell given for infected cells was therefore not influenced by the presence of non-infected cells in the well, but was an accurate representation of the intracellular environment in cells which had undergone early stages of infection. This being said, the expression of GFP following infection, even under control of the strong and constitutive CMV promoter, requires several hours. The results for mean foci/cell shown in this chapter would therefore not include cells in the very early stages of virus infection.

We differentiated between strongly and weakly GFP-positive cells during analysis of later experiments, to establish whether DDR foci formation followed a different pattern between the two. It was hypothesised that these weakly GFP-positive cells may represent an early stage of infection, or a lower level of infection (with regards to number of infecting particles). In fact, the number of weakly GFP-positive cells was found to be much lower than the number of strongly GFP-positive cells, and the results for mean foci/cell in these weakly GFP-positive cells showed, in the majority of cases, a less pronounced trend than that seen in strongly GFP-positive cells. The only exception to this was the formation of 53BP1 foci 2 h post-irradiation in Ad5-infected cells. This was significantly increased in weakly GFP-positive compared to mock-infected cells, but consistently significantly decreased at this time point in strongly GFP-positive Ad5-infected cells. A potential cause for this may be imperfect inhibition of this pathway, resulting in virus-induced pathway activation and foci formation in cells undergoing low or early stages of infection.

To investigate these findings further, the most straightforward follow up experiment would be to infect cells with Ad5 at a high MOI and fix at early time points after infection to assess whether an increase in mean 53BP1 foci/cell is seen at these conditions. An alternative approach which would provide information on foci formation at different stages of virus infection would be to develop and utilise an Ad5 viral construct which allows differentiation between early and late stages of infection. This is indeed already available for EnAd in the

form of a virus expressing UnaG and mCherry under E1A and MLP, respectively, thus allowing differentiation between cells infected by virus undergoing the early and late stage of infection [128]. Previous groups have used adenovirus DNA binding protein (DBP) as a marker for Ad5 infection [66] and replication [89]. This is an early region-encoded viral protein essential for virus replication [129] but would not identify very early stages of infection. Publications also describe using protein VII as a marker of incoming viral genome complexes [130].

The large number of known interactions between adenoviruses and the DDR pathway prompted us to include non-irradiated conditions in the experiment investigating foci formation. This led to the finding that 53BP1 foci formation appeared to be slightly but significantly higher in adenovirus-infected cells. One potential cause, the imperfect inhibition of this pathway in some infected cells, has already been briefly discussed. An alternative explanation is that adenoviral E1A has long been known to induce quiescent cell entry into S-phase (reviewed in Ben-Israel and Kleinberger [131]), and cells undergoing S-phase exhibit reorganisation of total 53BP1 from pan-nuclear to punctate [132]. It would therefore be interesting to perform an experiment using a marker for S-phase, such as 5-ethynyl-2'-deoxyuridine, to differentiate mean 53BP1 foci/cell in S-phase positive versus negative, weakly GFP-positive cells. Some co-localisation has previously been seen between 53BP1 phosphorylated at Ser1778 and viral DBP [66], therefore if an increase in 53BP1 foci formation is seen in infected cells regardless of cell cycle phase, this would lead to some interesting questions. One would have to query whether these 53BP1 foci are recruited by virus to aid in replication, as has previously been proposed for RAD51 and BRCA2 [89]. Alternatively, it is possible that the effects of adenovirus on DNA ligase IV levels and p53 function would make this increase in 53BP1 irrelevant to replication (as other parts of this pathway are also targeted). Finally, there is the hypothesis discussed above that

inhibition of 53BP1 foci formation is an important part of the virus life cycle but is imperfect/incomplete, which may partly explain why a more radical inhibition in 53BP1 foci formation is seen in strongly GFP-positive cells, and why some groups have found that irradiation is associated with an increase in virus production [100, 101]. If the latter were the case, one may predict that radiation would benefit virus function at low or early stages of infection by causing sequestration of DDR proteins away from VRCs and to double-strand DNA breaks.

Our foci experiments investigated the formation of 53BP1 and RAD51 foci but gave no information on the total levels of these proteins in the cell. Brestovitsky *et al.* demonstrated that infection with Ad5 lacking *E4orf4* led to phosphorylation of 53BP1 at Ser1778 [66]. We therefore investigated the total 53BP1 and p53BP1 levels in the presence and absence of adenovirus infection and irradiation. In keeping with published findings, p53BP1 was decreased in Ad5-infected cells. Interestingly, 53BP1 phosphorylation was detected in EnAd-infected, non-irradiated cells, as well as in irradiated cells. As EnAd is lacking functional *E4orf4* the experiment was repeated to include Ad11p, infection with which also resulted in 53BP1 phosphorylation at serine 1778. Serine 1778 is part of the 53BP1 section which is necessary and sufficient for p53 binding, however it does not directly interact with p53 [133]. It is not unreasonable to hypothesise that the differences seen in 53BP1 phosphorylation between the group B and C adenoviruses may be due to their distinct interactions with p53 [58]. Forrester *et al.* also demonstrated differing kinetics of ATM substrate phosphorylation between Ad5 and Ad11 [58], and Harding and Bristow found that phosphorylation at 53BP1 Ser1778 decreases following inhibition of ATM [132]. An alternative potential explanation for the contrasting results seen between Ad5 and EnAd/Ad11p may therefore be due to differing effects on ATM activity.

Overall, a decrease in the number of 53BP1 foci in adenovirus- versus mock-infected, irradiated cells may be due to a number of underlying mechanisms. We have demonstrated that there was no decrease in total 53BP1 levels to explain the results seen. A decrease in foci may be caused by enhancing foci resolution as opposed to inhibiting formation. However, Figure 3.8 demonstrates that, as opposed to a 53BP1 foci peak followed by a rapid drop-off as may be expected if this were the case, inhibition of foci was present at all time points. One may therefore hypothesise that adenovirus infection impacts on a part of the pathway which precedes 53BP1 foci formation, either at the level of DNA damage sensing or at the level of 53BP1 recruitment. Ad5 is already known to cause both degradation and relocalisation of members of the MRN complex, however Ad3 and Ad11 do not [94]. Thus, adenovirus infection likely leads to decreased 53BP1 foci formation by inhibiting the binding of oligomerised 53BP1 to flanking chromatin. This requires two histone modifications, the second of which is DDR-induced – $H4K20^{Me2}$ and $H2A(X)K15^{Ub}$ [134]. H2A ubiquitination is mediated by ATM-induced mediator of DNA damage checkpoint protein 1 (MDC1) recruitment of the E3 ubiquitin ligase RING finger (RNF)168 [25, 134], it is thus possible adenovirus infection may impact on one of these members of the DDR pathway.

53BP1 has a number of functions within the DDR [25]. Two of these relate directly to aspects already known to be inhibited by different adenovirus serotypes, namely c-NHEJ repair and ATM signalling. C-NHEJ in particular has been shown to be targeted by every adenovirus serotype studied [58]. We have argued that inhibition of 53BP1 foci formation by adenovirus is imperfect. Assuming c-NHEJ inhibition is crucial for the virus life cycle, multiple mechanisms of ensuring this occurs may be present to allow optimal viral replication.

Compared to NHEJ, much less is known about the interaction between adenoviruses and homologous recombination. We are the first group to show an adenovirus-associated decrease in HR foci formation following IR. The main publication on interactions between HR and adenovirus infection demonstrated no effect of HR status on cell sensitivity to infection by Ad11, but did demonstrate some striking interactions between Ad5 vectors and the HR pathway [89]. In fact, they showed colocalisation between VRCs and BRCA2/RAD51, increased sensitivity to Ad5 infection in HR-competent cells compared to matched HR-deficient cells, and no adenovirus-associated effect on HR efficiency. In light of this, our clear finding of decreased RAD51 foci formation in irradiated cells infected with Ad5 is unexpected. No increase in foci formation, potentially suggestive of colocalisation to VRCs, was seen in infected versus mock-infected, non-irradiated cells. Tookman *et al.* demonstrated colocalisation between VRCs and RAD51/BRCA2 in multiple cell lines, making it less likely that our finding was due to a difference in HR-Ad5 interaction between cell lines. The only obvious source of potential difference is the changes made to the Ad5 viruses used by the two groups. The results shown here are using Ad5 lacking E3 and with expression of GFP under control of the CMV promoter, whereas, apart from the initial results on cell sensitivity to Ad5 infection, the experiments in the paper by Tookman *et al.* are carried out with viral vectors deficient in E3B and/or E1A CR2. It is thus possible that these mutations may lead to a differing interaction between HR and the Ad5 vectors. Using immunoblotting, we found no change in total RAD51 levels in infected cells, in keeping with published results. We did however note consistent non-specific staining of heavier bands in lysates from adenovirus-infected cells. To investigate whether these bands may result from post-translational modification of RAD51, we knocked down *RAD51* expression using siRNA. Western blotting showed a decrease in the intensity of the expected RAD51 band but no change in the non-specific bands, suggesting these did not arise from

modification of RAD51. They may therefore be due to cross-reactivity of the antibody to viral proteins.

Similar to the results for 53BP1 foci, the findings of decreased RAD51 foci formation throughout the experimental time course, without an associated decrease in total RAD51 levels, would be in keeping with inhibited formation of RAD51 foci. As discussed in the introduction, a key aspect which favours HR over NHEJ repair is DNA end resection and processing into ssDNA overhangs. The next step in assessing which part of the pathway upstream of RAD51 foci formation may be inhibited by adenovirus infection would be to quantify RPA-ssDNA accumulation in adenovirus- versus mock-infected cells [135]. A decrease in RPA would be consistent with impaired function prior to this step in HR, such as DNA end resection. Alternatively, if the decreased RAD51 foci levels are due to impaired function of either BRCA2 or Rad52, one may expect to see no impact of adenovirus infection on RPA binding to ssDNA.

Finally, we investigated the effect of adenovirus infection on DNA ligase IV levels. Thus far, every serotype tested has been found to cause a decrease in the cellular levels of this DDR protein [58]. Accordingly, DNA ligase IV levels were decreased 24 h p.i. with Ad5 or EnAd at MOI 100 in three different cell lines. This decrease is proteasomally-mediated in Ad5 [88]; we investigated whether this was also the case in EnAd infection. The loss of DNA ligase IV following EnAd infection of A549 cells was partially, but not completely, abrogated by the addition of the proteasome inhibitor MG132. MG132 is a widely-utilised, reversible proteasome inhibitor and immunoblotting for p53 showed that this was increased at the time points and dose investigated in our experiments (results not shown), suggestive of successful proteasome inhibition. Our assessment of $TCID_{50}$/mL indicates this finding was not due to a simple decrease in the level of EnAd infection. These findings would suggest that, though proteasomal degradation is one of the mechanisms responsible for the

fall in DNA ligase IV levels following EnAd infection, other processes are also involved. Inhibition of the MRN complex is a key part of the Ad5 replication cycle and components of this complex are targeted both for degradation and relocalisation by different adenovirus proteins [94]. It is therefore not unreasonable to hypothesise that NHEJ inhibition by EnAd may likewise be mediated by a number of different pathways, as previously discussed. In particular, DNA ligase IV stability and half-life is altered by the presence of XRCC4 and DNA-PK – any effect of EnAd infection on these proteins may therefore impact on DNA ligase IV levels [136, 137] even in the context of adequate inhibition of the proteasome. The next logical experiment to conduct would be an assessment of DNA ligase ubiquitination in the presence and absence of EnAd, to evaluate whether this is affected by virus infection.

In summary, we show adenovirus-mediated inhibition at multiple levels of the DNA damage response pathway, and present the first report of an adenovirus-associated reduction in RAD51 foci formation following IR. One would expect the decrease in both 53BP1 and RAD51 foci formation, alongside total DNA ligase IV levels, to translate to inhibition of both HR and NHEJ activity in adenovirus-infected cells. Due to the rapid cytotoxicity seen in virus-infected cells, we were unable to successfully perform functional assays using HR- and NHEJ-reporter cell lines [138, 139]. The development of a non-replicating EnAd vector may be one way to formally assess this.

Given our findings, it would be interesting to investigate the effect of DDR inhibitors on adenovirus production. One might expect that, were inhibition of 53BP1 foci formation an important part of the virus life cycle, treatment with, for example, i53BP1 [125] may result in increased virus production, although it is difficult to predict the overall effect of the associated increase in HR. In the context of significantly decreased RAD51 foci formation suggestive of HR inhibition, combination treatment with a PARP inhibitor to assess for synthetic lethality would alternatively be a path of investigation with clear potential clinical

applications. Our results do support the use of these adenoviruses in combination with external beam radiation to augment IR-mediated cytotoxicity.

One repair pathway which was not directly investigated here is alt-NHEJ, including MMEJ. On the one hand, one may predict that inhibition of NHEJ and HR must result in an increase in alt-NHEJ as the only available mechanism left for repair of dsDNA breaks. On the other, the cell death seen following infection with these viruses *in vitro* is swift and complete. It is not inconceivable, therefore, that there is virus-mediated inhibition across all cellular dsDNA break repair pathways to counteract the detrimental impact of "repair" on the dsDNA virus genome.

Chapter 4: The impact of external beam radiation on virus production

4.1 Introduction: Hypothesis and chapter aims

An integral part of assessing the potential for synergy between oncolytic adenovirus therapy and radiotherapy involves investigating the effect of radiation on virus function and replication. As discussed in the previous chapter, radiation-induced cell death is primarily due to induction of dsDNA breaks. It would not be unreasonable to query whether dsDNA break induction in virus particles may interfere with their ability to spread and infect cells. Statistically, radiation is much less likely to affect viral DNA simply based on the relative size of the viral genome (approximately 36 kb) in comparison to the human genome (3×10^6 kb). The available evidence in fact supports *enhanced* adenovirus transgene expression and production when infection is combined with radiation treatment. As would be expected, this is not seen consistently for all cases, but appears to be dependent on the cell lines, MOI, radiation dose, and timing of treatment used.

Published data available on radiation-associated changes in viral uptake, transgene expression and/or production are predominantly based on replicating and non-replicating Ad5-based viral vectors, as Ad5 has been the prevalent adenovirus used in clinical trials to date. Zhang *et al.* demonstrated a radiation dose-sensitive, cell line-dependent increase in GFP expression from a non-replicating Ad5-CMV-GFP viral vector in pre-irradiated versus non-irradiated cells [140]. Interestingly, transgene expression *in vitro* was greatest when irradiation immediately preceded infection, whereas *in vivo* maximum increase was seen when infusion with an Ad5-CMV-β-galactosidase vector occurred 24 h post-irradiation. In both models greater radiation doses enhanced this effect. Confocal laser scanning was consistent with an increase in Cy3-labelled Ad5 vector uptake in pre-irradiated cells.

Chen *et al.* [100] and Dilley *et al.* [101] demonstrated an increase in infectious virus production *in vitro* when infecting LNCaP human prostate cancer cells with prostate tumour-targeted replication-competent Ad5 variants. Radiation occurred 24 h post-infection, at 10 Gy or 6 Gy respectively, in contrast to the Zhang *et al.* paper which demonstrated greatest viral transgene expression when infection occurred immediately after irradiation at 4 Gy. This increase in irradiated versus non-irradiated cells only became apparent at later time points. Interestingly, the radiation-induced increase in virus production was most prominent at lower MOIs, with fold-increases in PFU (plaque-forming units)/cell of 2.5, 16, and 317 for MOIs of 1, 0.1, and 0.01, respectively. *In vivo*, Dilley *et al.* also found an increased number of virus hexon-positive cells in irradiated versus non-irradiated LNCaP xenografts harvested 14 days post-treatment.

The enhanced response to radiation at lower MOIs and higher radiation doses discussed above was also observed by Hingorani *et al.* using non-replicating Ad5 vectors. The authors evaluated the expression of a range of transgenes under the control of various promoter sequences with the aim of defining how external beam radiation can best optimise sodium iodide symporter (NIS)-mediated Iodine-131 therapy [141]. Infection of HCT116 colorectal cancer cells with an Ad-CMV-NIS vector 24 h post-irradiation resulted in an increase in radioiodide uptake at lower, but not higher, MOI in irradiated cells; authors reported seeing similar results using the SIHN-58 (head and neck cancer) and H1299 (lung cancer) cell lines. This pattern was maintained when reversing treatment order and irradiating HCT116 cells 24 h p.i. with Ad-hTR-NIS. Infection of HCT116 cells with an Ad-CMV-GFP or Ad-CMV-lacZ vector 24 h post-irradiation showed transgene expression was higher in cells treated with greater radiation doses. *In vivo*, relative transgene expression of both GFP and luciferase was enhanced in irradiated versus non-irradiated xenografts when irradiation preceded infection by 24 h. There were exceptions to the pattern, for example relative

radioiodide uptake was reduced in irradiated cells infected with Ad-hTERT-NIS at MOI 0.01 and increased in irradiated cells infected at MOI 1. Irrespective of the promoter used, however, irradiation appeared to enhance transgene expression.

In contrast, Geoerger *et al.* found that pre-irradiation had no impact on luciferase activity in a panel of glioma cell lines infected with an adenoviral vector expressing luciferase under control of the CMV promoter [97]. Infections were carried out 48 h post-irradiation at 2 Gy or 5 Gy, at MOIs of 10 or 100. Furthermore, when IGRG121 tumour xenografts were injected with ONYX-015 7 h post-5 Gy of TBI *in vivo*, viral titres were slightly lower in irradiated versus non-irradiated tumours at 1, 3, and 6 days p.i. Ganesh *et al.* likewise detected no impact of radiation on infectious virus titres *in vivo* at the 14 day time point when RPMI2650 (head and neck cancer) xenografts were treated with either an Ad5-based replication competent construct (OV-5) or the chimeric oncolytic adenovirus OV-5T35H, and subsequently irradiated [99]. Mice received virus treatment (1×10^{10} VP) on days 1, 3, 5, and 7, and radiation (3.3 Gy per dose) on days 9, 11, and 13. A drop in infectious virus titre was observed at the day 28 time point in irradiated versus non-irradiated tumours, proposed to be due to radiation-induced cell death limiting viral spread.

The majority of published data therefore favour an enhanced effect of radiation on oncolytic virus production and/or transgene expression, though evidence suggests this is not consistent across different models and may be dependent on the virus and radiation dose utilised. We thus hypothesise that ionising radiation may potentiate Enadenotucirev (EnAd) replication, particularly at lower MOIs and higher radiation doses.

The primary aims of this chapter are:

1. To determine whether ionising radiation impacts on the production of EnAd virus particles.

2. If there is an impact, to establish whether this is radiation dose-dependent.

3. To explore the mechanisms underlying any radiation-mediated change in virus production.

4.2 Results

4.2.1 Irradiation causes an increase in EnAd viral genome production and infectious particle production in A549 cells in vitro

We initially assessed the impact of radiation on adenovirus genome production in infected A549 cells using qPCR. A549 cells were seeded into 12-well plates and the next day mock-infected or infected at an MOI of 0.1 with EnAd-SA-GFP, Ad5, or Ad11p in triplicate. At 24 h p.i., cells were mock-irradiated or irradiated at 10 Gy. At 72 h p.i. (corresponding to 48 h post-irradiation) cell supernatant and lysate were harvested separately. DNA extraction was performed and viral genome number quantified by qPCR using primers and probes specific for EnAd/Ad11p or Ad5 hexon or fibre, respectively. A clear increase in the number of EnAd particles was observed in the supernatants (Figures 4.1A, C), but not the lysates (Figures 4.1B, D), of irradiated A549 cells when compared to mock-irradiated controls. Though there was a trend towards an increased number of Ad11p particles in cell supernatants, this was not significant (Figures 4.2A, C). Conversely, there was a clear decrease in the number of Ad11p particles in the lysates of irradiated versus mock-irradiated cells (Figures 4.2B, D). This virus stock has been noted to result in rapid cell kill and this may partially explain the decreased number of virus particles detected, potentially due to premature cell lysis before maximum particle production was reached. There was no change in the number of Ad5 particles in the cell lysate of irradiated versus mock-irradiated cells, in keeping with results seen with EnAd (Figures 4.3B, D). Though there was some trend

towards an increased Ad5 particle number in the supernatant of irradiated cells, this was not significant (Figures 4.3A, C). This time point was chosen to allow sufficient effect from radiation while minimising virus-related cell death. Given that different virus serotypes can demonstrate variable growth characteristics depending on the cell line [142], however, further study may be required to assess whether similar results to EnAd are seen at different time points for Ad11p and Ad5, perhaps at a lower MOI to allow for assessment of any radiation effects which take longer to manifest.

It must be mentioned that cell lysates, but not supernatants, yielded very high viral genome counts which fell outside of the standard curve. All further experiments in which a high virus genome concentration was anticipated therefore included an extra step of diluting eluted DNA 1:1000 in DEPC-treated H_2O prior to performing qPCR.

A EnAd VP/well in A549 cell supernatant

	0 Gy (VP/well)	10 Gy (VP/well)	Ratio
Repeat 1	4.26×10^{9}	9.55×10^{9}	2.24
Repeat 2	8.38×10^{10}	3.02×10^{11}	3.61
Repeat 3	7.35×10^{10}	2.16×10^{11}	2.94
Mean ratio (95% CI)			**2.93 (1.23-4.62)**

B EnAd VP/well in A549 cell lysate

	0 Gy (VP/well)	10 Gy (VP/well)	Ratio
Repeat 1	3.35×10^{11}	3.17×10^{11}	0.95
Repeat 2	2.72×10^{12}	3.01×10^{12}	1.10
Repeat 3	6.55×10^{11}	1.21×10^{12}	1.85
Mean ratio (95% CI)			**1.30 (0.10-2.50)**

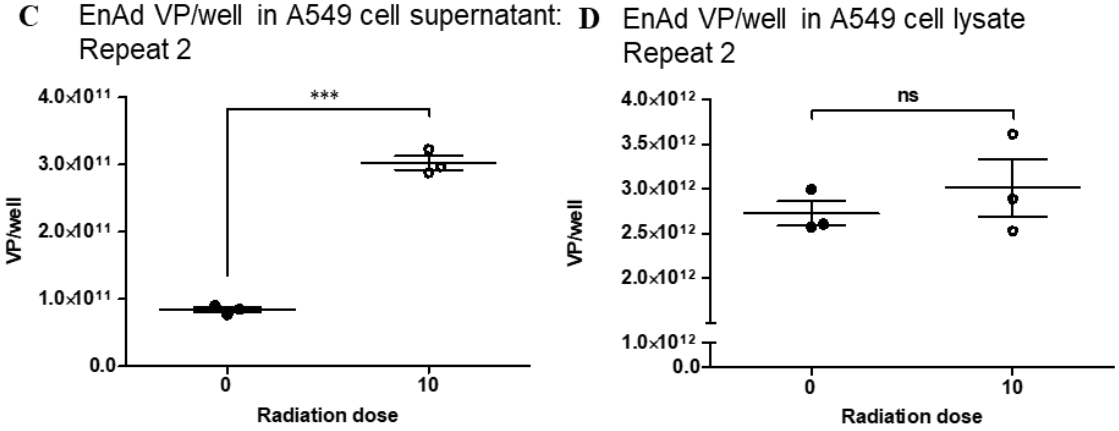


Figure 4.1 Irradiation of A549 cells increases supernatant Enadenotucirev (EnAd) virus particle number. A549 cells were seeded into 12-well plates one day prior to mock-infection or infection with EnAd-SA-GFP at an MOI of 0.1. At 24 hours post-infection (h p.i.) cells were either mock-irradiated or irradiated at 10 Gy. At 72 h p.i. supernatant and cell lysate were separately harvested. DNA extraction was carried out and viral genomes were measured using hexon-specific primers and probe. **(A-B)** Tables showing virus particle (VP)/well for the supernatant **(A)** and lysate **(B)** in irradiated versus non-irradiated wells (mean of three wells given). Ratio of VP/well after irradiation with 10 Gy/0 Gy was calculated for each repeat and 95% CI interval determined using Student's *t* distribution. **(C-D)** Data from repeat 2 illustrating distribution of data points seen within each individual experiment for supernatant **(C)** and lysate **(D)**. Each point corresponds to a biological replicate, overall mean ± SEM is shown. VP/well in mock wells is represented by a dashed line (too low to be seen on graphs). Significance was evaluated using unpaired t-test. ns, not significant; p <0.001, ***.

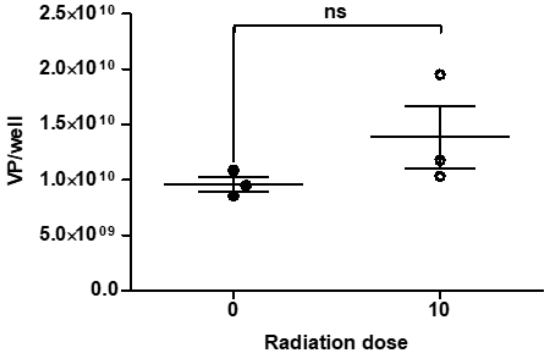
A Ad11p VP/well in A549 cell supernatant

	0 Gy (VP/well)	10 Gy (VP/well)	Ratio
Repeat 1	9.64×10^{9}	1.39×10^{10}	1.44
Repeat 2	3.37×10^{10}	1.24×10^{11}	3.68
Repeat 3	1.52×10^{11}	1.82×10^{11}	1.20
Mean ratio (95% CI)			**2.10 (-1.30-5.51)**

B Ad11p VP/well in A549 cell lysate

	0 Gy (VP/well)	10 Gy (VP/well)	Ratio
Repeat 1	3.74×10^{11}	1.69×10^{11}	0.45
Repeat 2	4.03×10^{11}	2.05×10^{11}	0.51
Repeat 3	5.35×10^{11}	3.14×10^{11}	0.59
Mean ratio (95% CI)			**0.52 (0.35-0.69)**

C Ad11p VP/well in A549 cell supernatant: Repeat 1



D Ad11p VP/well in A549 cell lysate Repeat 1

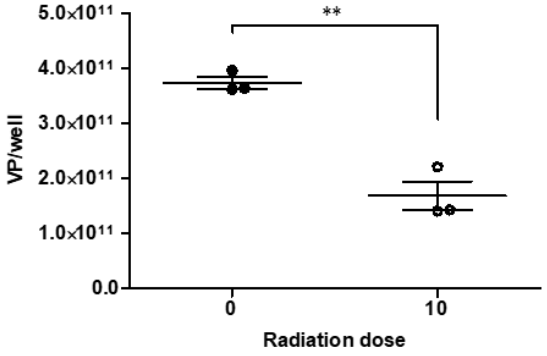


Figure 4.2 Irradiation of A549 cells decreases lysate adenovirus 11p (Ad11p) virus particle number. A549 cells were seeded into 12-well plates one day prior to mock-infection or infection with Ad11p at an MOI of 0.1. At 24 h p.i. cells were either mock-irradiated or irradiated at 10 Gy. At 72 h p.i. supernatant and cell lysate were separately harvested. DNA extraction was carried out and viral genomes were measured using hexon-specific primers and probe. **(A-B)** Tables showing VP/well for the supernatant **(A)** and lysate **(B)** in irradiated versus non-irradiated wells (mean of three wells given). Ratio of VP/well after irradiation with 10 Gy/0 Gy was calculated for each repeat and 95% CI interval determined using Student's *t* distribution. **(C-D)** Data from repeat 1 illustrating distribution of data points seen within each individual experiment for supernatant **(C)** and lysate **(D)**. Each point corresponds to a biological replicate, overall mean ± SEM is shown. VP/well in mock wells is represented by a dashed line (too low to be seen on graphs). Significance was evaluated using unpaired t-test. ns, not significant; p <0.01, **.

A Ad5 VP/well in A549 cell supernatant

	0 Gy (VP/well)	10 Gy (VP/well)	Ratio
Repeat 1	9.34×10^8	9.17×10^8	0.98
Repeat 2	6.56×10^9	9.7×10^9	1.48
Repeat 3	3.93×10^9	5.65×10^9	1.44
Mean ratio (95% CI)			**1.30 (0.61-1.99)**

B Ad5 VP/well in A549 cell lysate

	0 Gy (VP/well)	10 Gy (VP/well)	Ratio
Repeat 1	6.83×10^{10}	5.56×10^{10}	0.81
Repeat 2	3.97×10^{11}	6.26×10^{11}	1.57
Repeat 3	1.23×10^{12}	1.04×10^{12}	0.84
Mean ratio (95% CI)			**1.08 (0.01-2.15)**

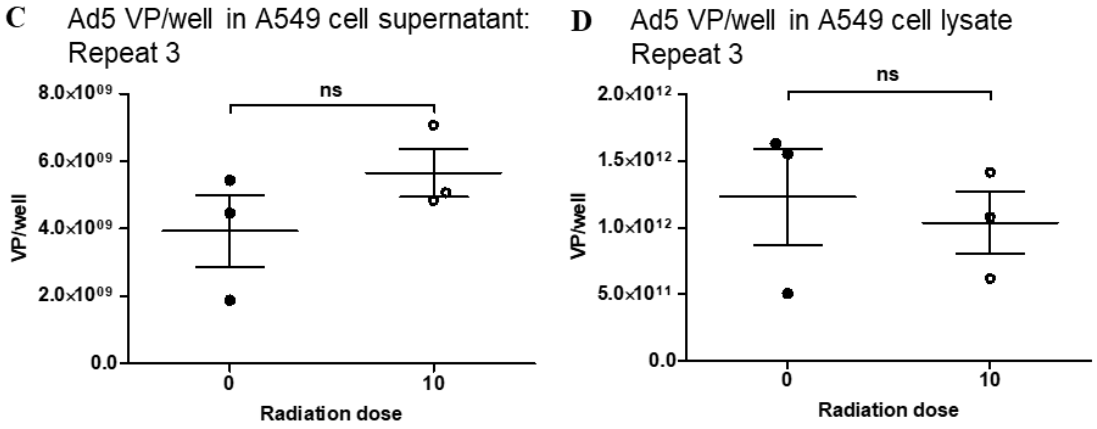


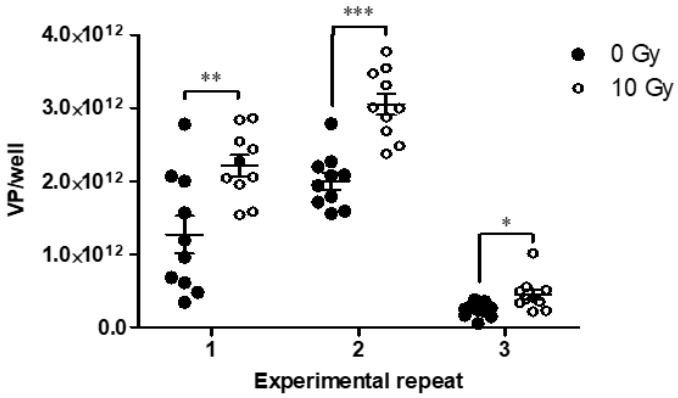
Figure 4.3 Irradiation of A549 cells has no effect on adenovirus 5 (Ad5) virus particle number. A549 cells were seeded into 12-well plates one day prior to mock-infection or infection with Ad5 at an MOI of 0.1. At 24 h p.i. cells were either mock-irradiated or irradiated at 10 Gy. At 72 h p.i. supernatant and cell lysate were separately harvested. DNA extraction was carried out and viral genomes were measured using fibre-specific primers and probe. **(A-B)** Tables showing VP/well for the supernatant **(A)** and lysate **(B)** in irradiated versus non-irradiated wells (mean of three wells given). Ratio of VP/well after irradiation with 10 Gy/0 Gy was calculated for each repeat and 95% CI interval determined using Student's *t* distribution. **(C-D)** Data from repeat 3 illustrating distribution of data points seen within each individual experiment for supernatant **(C)** and lysate **(D)**. Each point corresponds to a biological replicate, overall mean ± SEM is shown. VP/well in mock wells is represented by a dashed line (too low to be seen on graphs). Significance was evaluated using unpaired t-test. ns, not significant.

The data shown in Figure 4.1 would be consistent with increased viral burst size, seen previously in irradiated cells infected with Ad5-based viral constructs [100, 101]. This result could also arguably be seen due to earlier cell lysis, and therefore virus particle release, as a result of high dose radiation therapy. A follow up experiment was therefore performed to assess the whole well virus particle number. As before, 12-well plates were seeded with A549 cells. The subsequent day, wells were either mock-infected or infected with EnAd-SA-GFP at an MOI of 0.1. At 24 h p.i., plates were mock-irradiated or irradiated at 10 Gy. At 72 h p.i. (corresponding to 48 h post-irradiation), cells were dislodged from the growth surface and combined with supernatant for DNA extraction and virus particle quantification. There was an overall increase in VP number in irradiated versus non-irradiated wells (Figures 4.4A-B), in keeping with an increase in VP production as opposed to earlier particle release. The third repeat of this experiment included an intermediate dose of 4 Gy to assess for trend (Figure 4.4C). A test for linear regression returned a significant result for the relationship between VP number and radiation dose ($p = 0.0071$). This would be consistent with a linear relationship between radiation dose and virus particle production at this time point between 0 Gy and 10 Gy.

A Total EnAd VP/well

	0 Gy (VP/well)	10 Gy (VP/well)	Ratio
Repeat 1	1.267×10^{12}	2.213×10^{12}	1.75
Repeat 2	1.999×10^{12}	3.052×10^{12}	1.53
Repeat 3	2.348×10^{11}	4.492×10^{11}	1.91
Mean ratio (95% CI)			**1.73 (1.25-2.21)**

B Total EnAd VP/well: distribution of data



C Total EnAd VP/well: Repeat 3

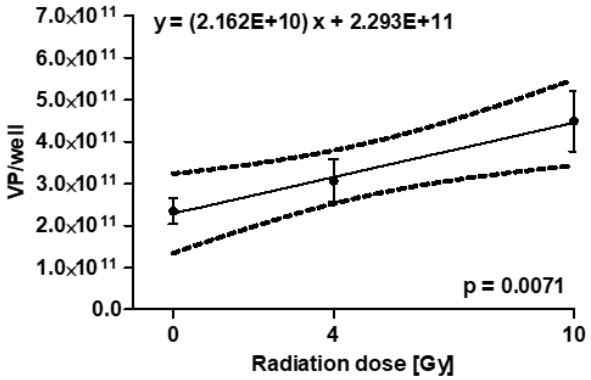


Figure 4.4 Irradiation of A549 cells increases total virus particle production. A549 cells were seeded into 12-well plates and the next day either mock-infected or infected with EnAd-SA-GFP at an MOI of 0.1. At 24 h p.i. cells were either mock-irradiated or irradiated at 10 Gy. The whole well was harvested at 72 h p.i. and viral genomes detected using hexon-specific primers and probe. **(A)** Table showing VP/well in irradiated versus non-irradiated wells (mean of ten wells given). Ratio of VP/well after irradiation with 10 Gy/0 Gy was calculated for each repeat and 95% CI interval determined using Student's *t* distribution. **(B)** Data showing the three individual experimental repeats from table above, illustrating distribution of data points seen within each individual experiment. Each point corresponds to a biological replicate, overall mean ± SEM is shown. VP/well in mock wells is represented by a dashed line (too low to be seen on graphs). Significance was evaluated using unpaired t-test. $p < 0.05$, *; $p < 0.01$, **; $p < 0.001$, ***. **(C)** Repeat 3 seen in table above included 4 Gy as an intermediate condition. Best-fit slope and mean ± SEM is shown, including equation of the best-fit line. VP/well in mock wells is represented by a dashed line (too low to be seen on graphs). Significance was evaluated using a test for linear regression.

This chapter introduction discussed the variable effect of radiation on adenovirus transgene expression and replication when using different MOIs, radiation doses, and timings between treatments. It would therefore be interesting to repeat the above experiment, exploring the impact on virus production of changing these variables. We may expect virus particle production to plateau at higher radiation doses if the radiation results in cell death that is too rapid to allow viral replication, or if changes in the cellular microenvironment do not support effective viral replication.

The results shown in Figures 4.1 and 4.4 demonstrate an increase in EnAd virus genome production in irradiated versus non-irradiated A549 cells, but do not provide information on the production of infectious virus particles. To investigate this, A549 cells were seeded into 96-well plates and mock-infected or infected with EnAd-SA-GFP (Figure 4.5C), Ad11p (Figure 4.5D), or Ad5 (Figure 4.5E) at an MOI of 0.1 the next day. At 24 h p.i., plates were either mock-irradiated or irradiated at 5, 10, or 20 Gy. $TCID_{50}$/mL was determined in cell supernatants harvested 5 days p.i. (corresponding to 4 days post-irradiation). As results did not appear to follow a normal distribution, significance was assessed using Kruskal-Wallis with Dunn's post-hoc test comparing irradiated conditions with 0 Gy. As shown in Figures 4.5C-E, a trend towards higher infectious particle concentration in the supernatants of irradiated versus non-irradiated cells was observed for all three viruses tested. However, in keeping with the results seen in Figures 4.1 to 4.3, the increase was significant only for EnAd at a radiation dose of 10 Gy (Figure 4.5C). Interestingly, all $TCID_{50}$/mL results were lower at 20 Gy than 10 Gy, further supporting the idea that the linear relationship seen in Figure 4.4C does not extend to very high radiation doses.

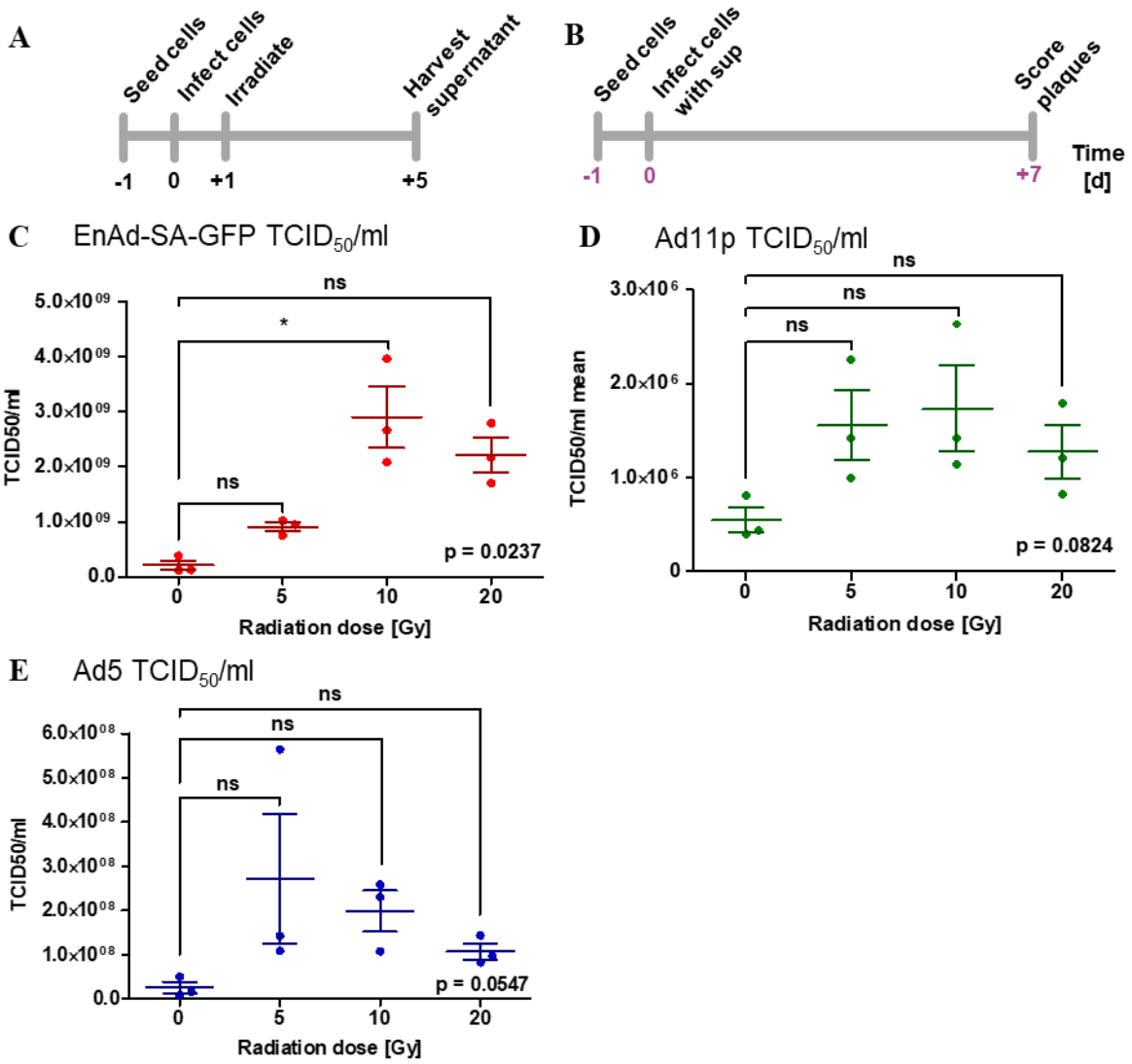


Figure 4.5 Irradiation of A549 cells increases infectious virus particle production. (A-B) Schematic illustrating experimental timeline. **(A)** A549 cells were seeded into 96-well plates one day prior to infection with adenovirus at an MOI of 0.1, or mock-infection, in triplicate. At 24 h p.i., cells were either mock-irradiated or irradiated at 5 Gy, 10 Gy, or 20 Gy. Cell supernatant was harvested 5 days p.i. **(B)** A549 cells were seeded into 96-well plates and used to calculate $TCID_{50}$ for supernatant harvested from cells infected with EnAd-SA-GFP **(C)**, Ad11p **(D)**, or Ad5 **(E)**. Graphs show mean ± SEM. Each point represents the mean of a single experiment carried out in triplicate. Significance was evaluated using Kruskal-Wallis test (p-value given bottom right corner) with Dunn's post-hoc testing (shown above data points). ns, not significant; p <0.05, *.

4.2.2 Irradiation leads to an increase in EnAd genome production and infectious particle production in vivo

A pilot *in vivo* experiment was designed to further evaluate the impact of radiation on EnAd production. EnAd is unable to replicate in murine cells; SCID mice were therefore chosen to allow implantation of human cell lines and maximise the potential for tumour growth. A colorectal carcinoma cell line, HCT116, was selected as this was the original tumour type on which EnAd was bioselected [110] and is the tumour type currently being targeted in the phase 1 CEDAR trial, assessing EnAd in combination with chemoradiotherapy. Further, the Phase 1 Mechanism of Action trial found that intravenous (i.v.) injection of EnAd resulted in successful delivery of virus to a range of tumour types, including colorectal [113].

Figure 4.6A summarises the experimental timeline. HCT116 cells (2 x 10^6/mouse) were injected subcutaneously (s.c.) into six SCID mice and the resulting tumours monitored until a predetermined volume of 50 mm^3 was reached. All mice were given three injections of 0.5 x 10^{10} VP of EnAd-SA-Fluc i.v. 48 h apart, a dosing schedule based on the clinical trial model [113]. Intravenous delivery was chosen over intratumoural to minimise the risk of tumour ulceration, which may occur following injection and irradiation of the same area. One day following the final virus dose, mice were randomised to receive either 10 Gy of irradiation to the tumour or to remain non-irradiated, in keeping with the dose and time point found to have a significant impact on virus production *in vitro* (Figures 4.4 and 4.5). At 6, 10, and 12 days post-first dose of EnAd-SA-Fluc (corresponding to 1, 5, and 7 days post-irradiation), mice received a s.c. dose of luciferin and underwent imaging using the IVIS to assess intratumoural luciferase expression. Tumours were harvested 12 days after the first dose of virus (corresponding to 7 days post-irradiation). Weight and tumour volume were regularly monitored throughout the experiment.

Tumour growth delay was seen in irradiated animals in two of the three pairs (Figures 4.6C, G). Unfortunately, there is no data for the final time point for pair one due to human error (Figure 4.6C). No animals reached the level of weight loss requiring sacrifice (>15% maintained for 24 h), though some weight loss was noted in all the mice and nutritional support in the form of mash was briefly required. Figures 4.6B, D, F show the data for mouse weights alongside all procedures performed. Minor weight loss was observed in all animals following the first virus injection; some stabilisation or loss was seen following the second injection; variable changes in weight were noted following the third. Marked weight loss occurred following irradiation and the first imaging session. Both irradiation and IVIS imaging were carried out under general anaesthesia, which may affect food intake. In addition, SCID mice are known to be particularly radiosensitive. Though shielding was utilised to limit irradiation to the tumour, a small area of mouse tissue will have received some radiation, potentially leading to exacerbated weight loss. It was decided that nude mice would be utilised in any future experiments assessing radiation and EnAd combination therapy.

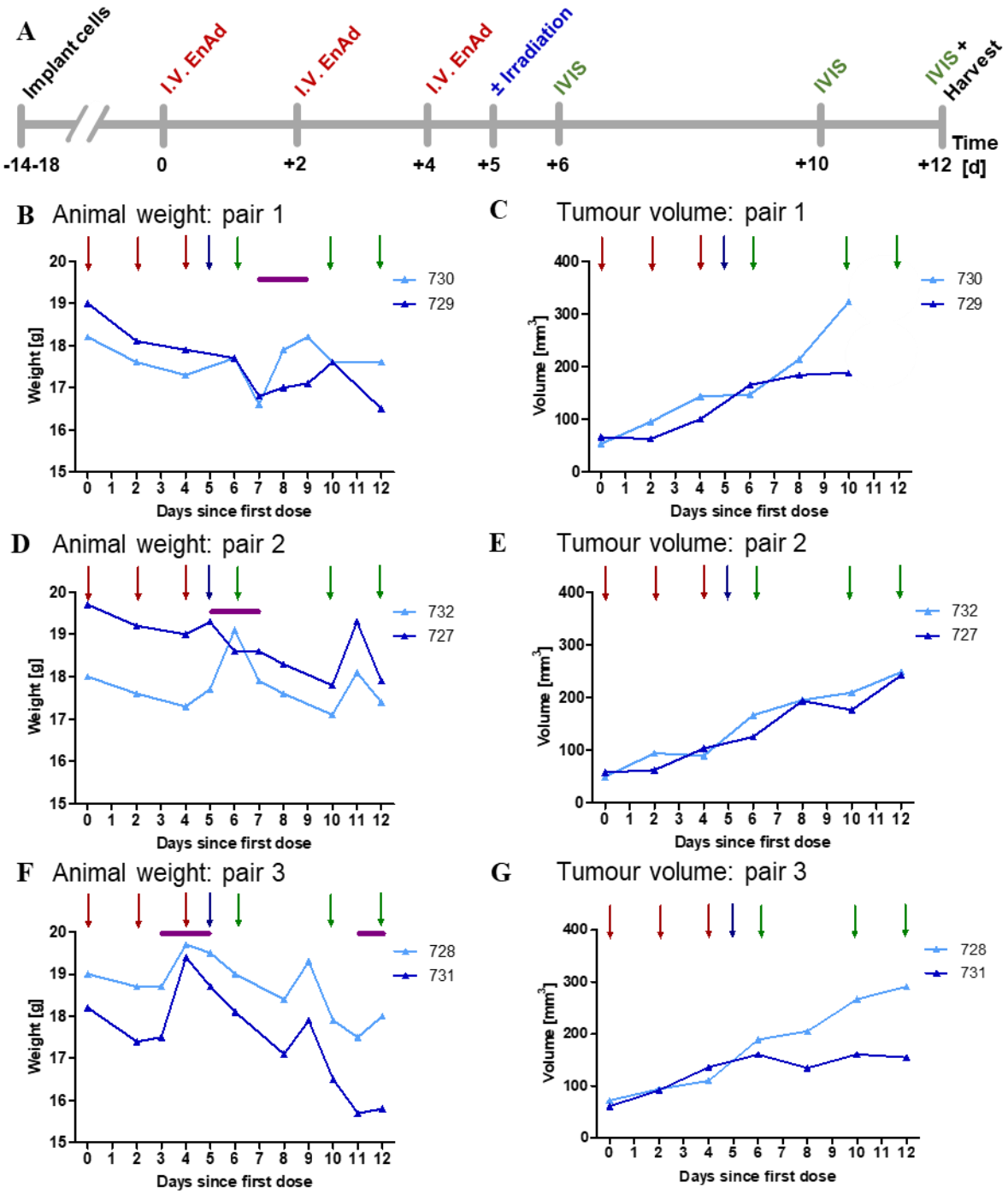


Figure 4.6 Establishing an *in vivo* tumour model to assess the effect of radiation on EnAd. (A) Schematic illustrating experimental timeline. HCT116 cells (2 x 10^6/mouse) were injected subcutaneously (s.c.) into six SCID mice. When tumours reached a volume of 50 mm^3, all mice were given three intravenous (i.v.) injections of 0.5 x 10^{10} VP of EnAd-SA-Firefly Luciferase (EnAd-SA-Fluc) 48 h apart. One day after the final dose, half of the animals were randomised to receive 10 Gy of radiation to the tumour. Over the next seven days, animal weight and tumour volume were monitored and three sessions were carried out on the In Vivo Imaging System (IVIS). Tumours were harvested 12 days after first virus dose. **(B-G)** Data showing results for paired experimental animals (light blue – no radiation; dark blue – 10 Gy). Arrows denote EnAd-SA-Fluc injections (red), radiation treatment (blue) and IVIS imaging sessions (green). Purple bar denotes mash given to animals to support through weight loss. **(B, D, F)** Changes in weight associated with treatment. **(C, E, G)** Tumour volumes from randomisation to harvesting.

Figures 4.7A-B show the technique used to assess peak luminescence. Following s.c. injection of luciferin, mice were scanned every minute. Scanning was discontinued when peak luminescence or the maximum time allowed for maintaining animals under general anaesthesia was reached, whichever was soonest. Tumour luminescence was determined by using Living Image Software to identify a "region of interest" over the tumour and a region representing "background fluorescence" over the head to allow calculation of total flux in the area of the tumour. As shown in Figure 4.7C, peak total flux was found to be elevated at later time points in two of three irradiated mice compared to non-irradiated animals. The third irradiated mouse (729, arrow), exhibited peak total flux approximating baseline levels at the final time point. This could be due to failure of luciferin delivery or to decreased virus replication and transgene expression in the tumour.

Fresh tumour tissues were harvested from these animals immediately post-sacrifice, and analysed for production of luciferase, infectious virions (as determined by $TCID_{50}$/mL), and viral genomes (Figures 4.7D-F). The data did not appear to be normally distributed, a finding frequently seen in this type of experiment. Normalisation was therefore carried out by taking natural logarithms, allowing statistical assessment through the use of unpaired t-test. Figure 4.7D shows results from the luciferase assay, in which a 10-fold increase was seen in luminescence/μg of protein in irradiated versus non-irradiated tissue. Interestingly, the highest luminesce value in this graph (arrow) corresponds to mouse 729, the animal demonstrating the lowest levels of luminescence at day 12 in Figure 4.7C. This would be consistent with the decreased peak total flux at this time point being secondary to a failure of luciferin delivery, as opposed to a true fall in virus levels. There was also a 9-fold increase in $TCID_{50}$/mL (Figure 4.7E), and a 19-fold increase in VP/mg of tissue (Figure 4.7F) in irradiated versus non-irradiated fresh tumour tissues, in keeping with the results seen *in vitro*. Figures 4.7G-H demonstrate the qPCR amplification curves.

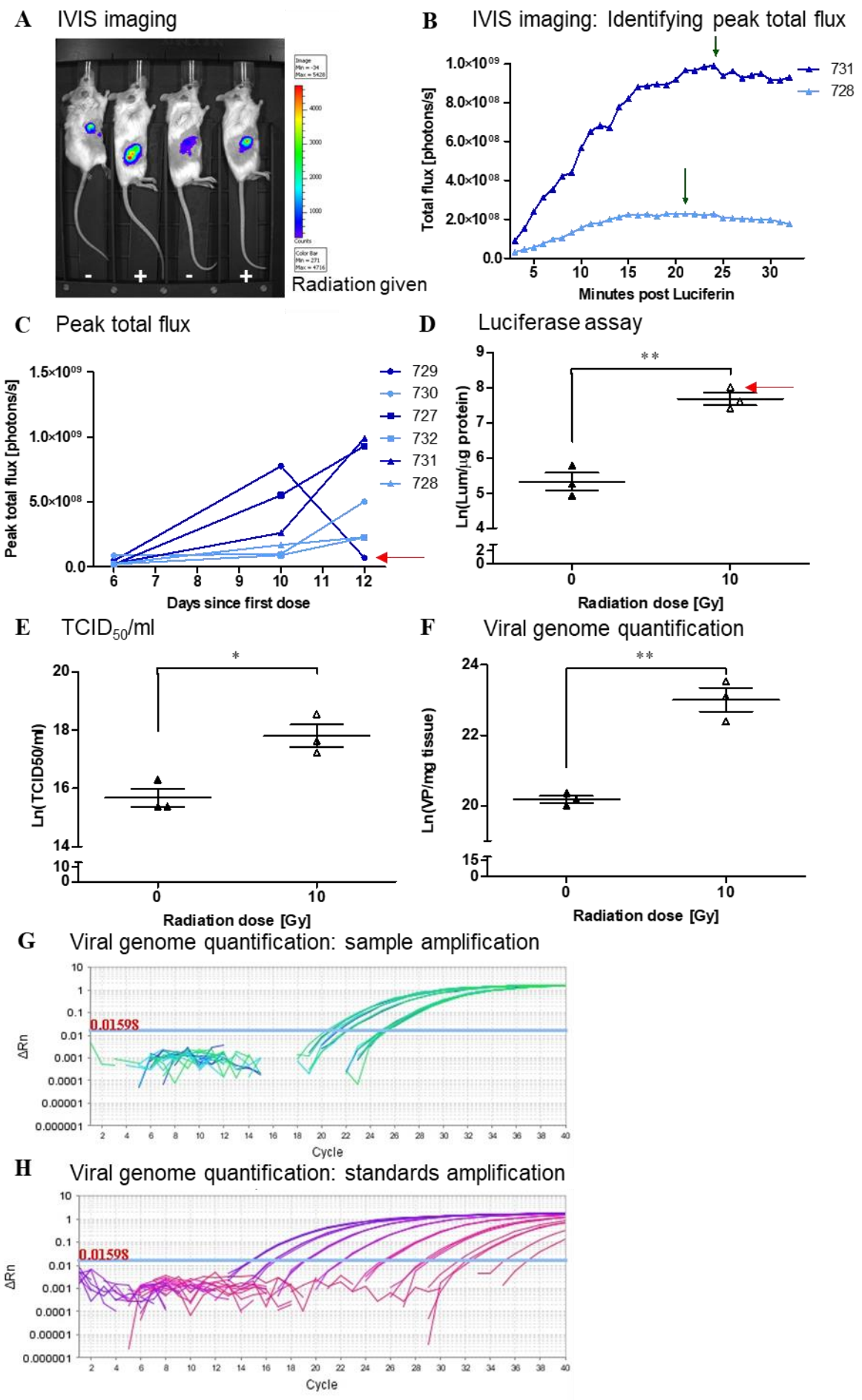

A IVIS imaging
- + - +
Radiation given
B IVIS imaging: Identifying peak total flux
Total flux [photons/s]
1.0×10^09
8.0×10^08
6.0×10^08
4.0×10^08
2.0×10^08
0.0
5 10 15 20 25 30
Minutes post Luciferin
731
728
C Peak total flux
Peak total flux [photons/s]
1.5×10^09
1.0×10^09
5.0×10^08
0.0
6 7 8 9 10 11 12
Days since first dose
729
730
727
732
731
728
D Luciferase assay
Ln(Lum/µg protein)
**
Radiation dose [Gy]
E TCID50/ml
Ln(TCID50/ml)
*
Radiation dose [Gy]
F Viral genome quantification
Ln(VP/mg tissue)
**
Radiation dose [Gy]
G Viral genome quantification: sample amplification
ΔRn
0.01598
Cycle
H Viral genome quantification: standards amplification
ΔRn
0.01598
Cycle

Figure 4.7 Irradiation of HCT116 cells *in vivo* is associated with increased EnAd production. HCT116 cells (2 x 10^6/mouse) were implanted s.c. into six SCID mice. Once tumours reached 50 mm^3, all mice were given three doses of 0.5 x 10^{10} VP of EnAd-SA-Fluc i.v. 48 hours apart. One day post final dose, three mice were randomised to receive a single fraction of 10 Gy to the tumour. Three IVIS imaging sessions were carried out and tumour volume and weight monitored for one week post irradiation, at which point tumours were harvested. **(A)** IVIS imaging session demonstrating luminescence at a single time point for two pairs of experimental animals. Irradiated mice are seven (second animal) or five (fourth animal) days post-irradiation. **(B)** Analysis of IVIS data was carried out by calculating tumour versus background flux for all images taken and identifying peak luminescence (green arrow). Dark blue denotes irradiated animal, light blue denotes non-irradiated. **(C)** Peak total flux for all pairs of animals. Imaging was carried out 6, 10, and 12 days post first EnAd-SA-Fluc injection. At the last session, tumours were harvested and half of each frozen for further homogenisation. Red arrow identifies mouse 729. **(D)** Luciferase assay was carried out on tissue homogenate and luminescence recorded using PolarStar plate reader. Red arrow identifies mouse 729. **(E)** $TCID_{50}$/ml of homogenate was evaluated on A549 cells. **(F-H)** DNA extraction was carried out on homogenate and viral genomes were measured using hexon-specific primers and probe. **(D-F)** Each point represents results from a single animal, graphs show mean ± SEM. Significance was evaluated by using logarithmic transformation to normalise data thus allowing use of unpaired t-test. $p < 0.05$, *; $p < 0.01$, **.

4.2.3 Irradiation leads to a cell line-dependent increase in EnAd receptor levels

Previously published data show that cellular receptors utilised by Ad5 increase after radiation in some cell lines [141] but not others [97, 143], and that irradiation is associated with a dynamin 2-mediated increase in Ad5 uptake [144]. An increase in EnAd replication seen in irradiated versus non-irradiated cells may therefore be due to an increase in EnAd receptor levels and subsequent virus uptake during a multi-step infection. In particular, the findings demonstrated in Figures 4.1 and 4.4 reflect low MOIs (0.1) and thus a multi-step infection process. Improved uptake during subsequent rounds of infection may be one explanation for the results seen.

We assessed expression of CD46 and DSG2, receptors utilised by group B adenoviruses [49, 50], in irradiated versus non-irradiated cells. A549, HCT116, and DLD1 cells (the latter highly susceptible to EnAd infection) were seeded into 12-well plates. One day later, cells were mock-infected or infected with EnAd-SA-GFP at an MOI of 0.1. At 24 h p.i., plates were mock-irradiated or irradiated at 10 Gy. At 24 h post-irradiation, supernatants and cells were collected to assess GFP, CD46 and DSG2 expression. This time point corresponds to

the time at which reinfection is likely to have occurred in the experiments shown in Figures 4.1 and 4.4.

Analysis was conducted as demonstrated in Figure 4.8; singlets were initially selected (Figure 4.8A), followed by gating to exclude cell debris (Figures 4.8B-C) and selection of live cells (Figure 4.8D). GFP positivity was assessed on this live cell population (Figure 4.8E), whereas PE positivity and median fluorescence (corresponding to CD46 or DSG2) was assessed on live cells after exclusion of low-level PE signal (Figures 4.8F-G). In the pilot experiment, it was noted GFP positivity was too low to allow comparison of CD46 or DSG2 levels between infected and non-infected cells. Experimental set-up was maintained, however, to assess whether the presence of this level of virus has any impact on these cellular receptors.

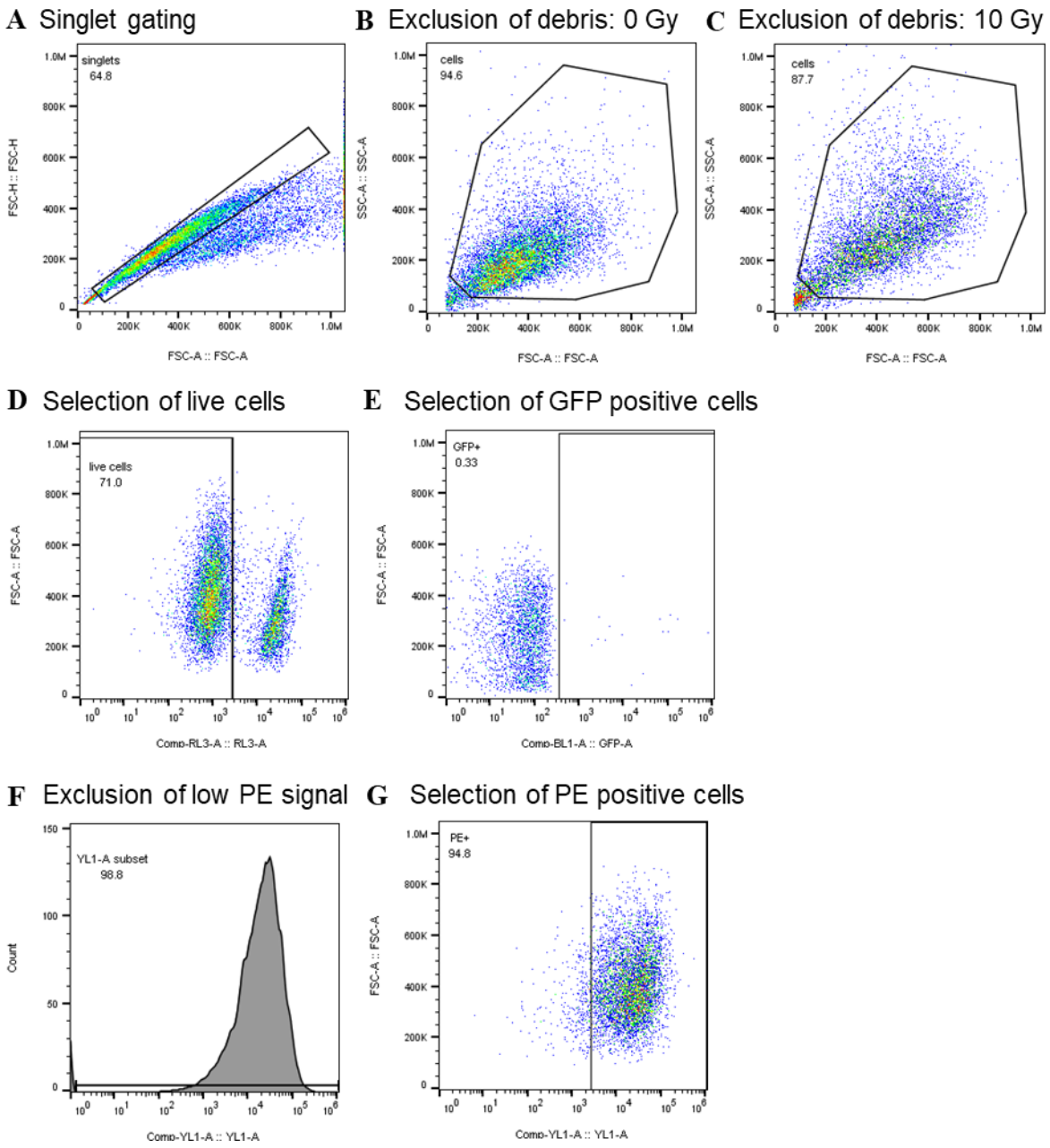


Figure 4.8 Flow cytometry analysis of CD46 and Desmoglein 2 (DSG2) receptor levels following irradiation, in the presence and absence of EnAd-SA-GFP. DLD1, HCT116, and A549 cells were seeded into 12-well plates. Cells were mock-infected or infected with EnAd-SA-GFP the next day at an MOI of 0.1. At 24 h p.i. cells were mock-irradiated or irradiated at 10 Gy. Supernatant and cells were harvested 48 h p.i. A549 cells are shown as a representative population. **(A)** Initial gating of singlets was carried out on forward scatter area (x-axis) versus forward scatter height (y-axis). Forward scatter area (x-axis) versus side scatter area (y-axis) was used to exclude debris, ensuring it encompassed cell distribution seen in both non-irradiated **(B)** and irradiated **(C)** cells. **(D)** Live cells were selected through gating on forward scatter area (y-axis) versus LIVE/DEAD fixable Near-IR Dead Cell stain (x-axis). Dead cells stain positive, gating was therefore carried out on the negative cell population. **(E)** GFP-positivity was assessed on live cells only by gating on forward scatter area (y-axis) versus BL-1 (used to detect GFP fluorescence) area (x-axis). **(F)** Very low level PE-positivity was excluded; median and percentage of PE positive cells **(G)** were calculated on the remaining population.

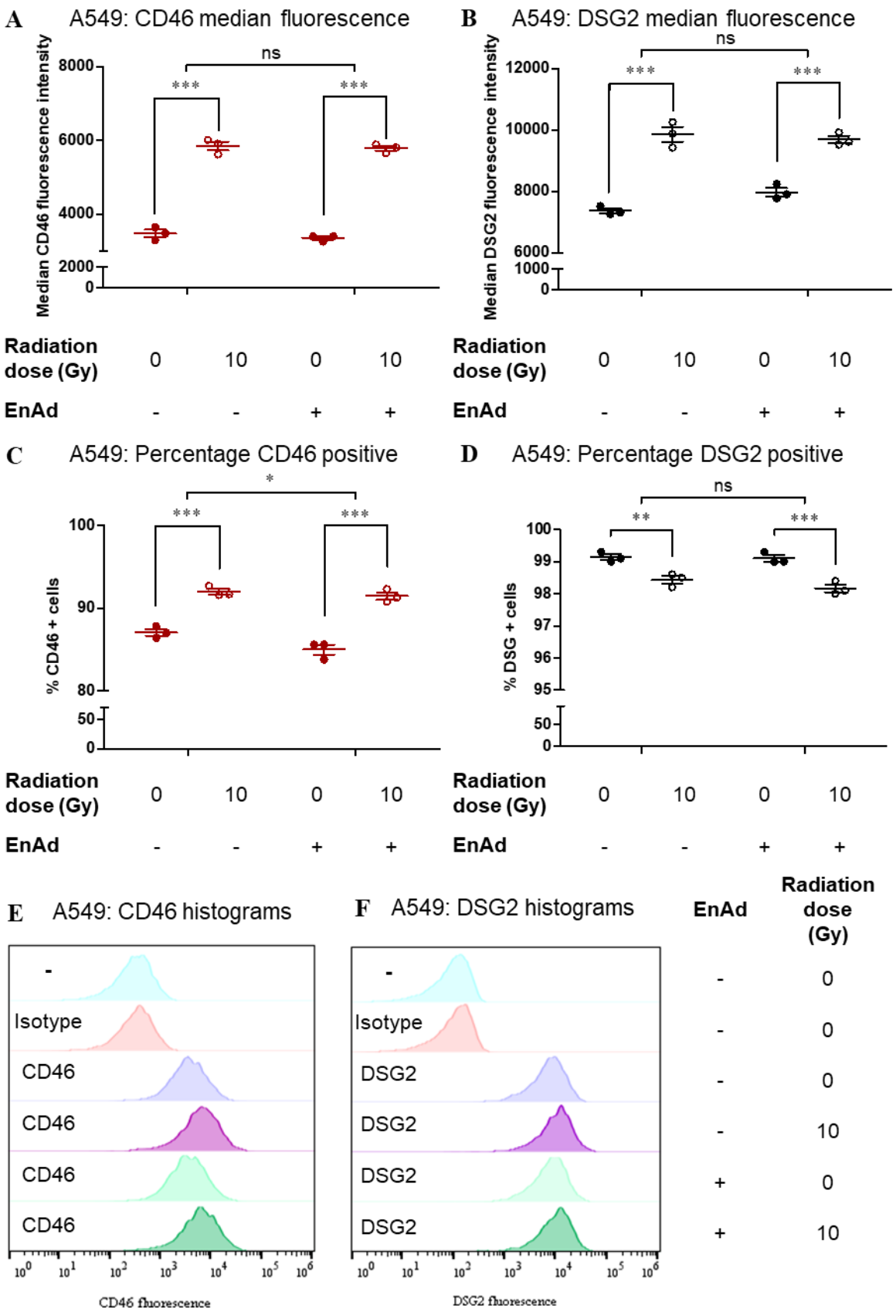

A
A549: CD46 median fluorescence
Median CD46 fluorescence intensity
8000
6000
4000
2000
0
ns
***
***
B
A549: DSG2 median fluorescence
Median DSG2 fluorescence intensity
12000
10000
8000
6000
1000
0
ns
***
***
Radiation dose (Gy) 0 10 0 10
EnAd - - + +
C
A549: Percentage CD46 positive
% CD46 + cells
100
90
80
50
0
*
***
***
D
A549: Percentage DSG2 positive
% DSG + cells
100
99
98
97
96
95
50
0
ns
**
***
E
A549: CD46 histograms
-
Isotype
CD46
CD46
CD46
CD46
CD46 fluorescence
F
A549: DSG2 histograms
-
Isotype
DSG2
DSG2
DSG2
DSG2
DSG2 fluorescence
EnAd
Radiation dose (Gy)
- 0
- 0
- 0
- 10
+ 0
+ 10

Figure 4.9 Irradiation of A549 cells causes an increase in EnAd receptor expression. A549 cells were seeded into 12-well plates. The next day cells were mock-infected or infected with EnAd-SA-GFP at an MOI of 0.1. At 24 h p.i. cells were mock-irradiated or irradiated at 10 Gy. Supernatant and cells were harvested together 48 h p.i. Median fluorescence **(A, B)**, percentage of positive cells **(C, D)**, and histograms (E, F) are shown for CD46 **(A, C, E)** and DSG2 **(B, D, F)**. Mean ± SEM of a single experiment representative of three experimental repeats is shown. Each point represents data for a single well. Significance was evaluated using 2-way ANOVA with Bonferroni post-test. ns, not significant; $p < 0.05$, *; $p < 0.01$; **; $p < 0.001$, ***.

There was a significant increase seen in median fluorescence in irradiated versus non-irradiated A549 cells for both CD46 (Figure 4.9A) and DSG2 (Figure 4.9B), consistent with an increase in receptor expression. This was not affected by the presence of virus. The percentage of CD46-positive cells also increased significantly in irradiated versus non-irradiated cells, irrespective of infection status (Figure 4.9C). Unexpectedly, the percentage of DSG2-positive cells decreased significantly in irradiated cells compared to non-irradiated cells (Figure 4.9D), despite an increase in DSG2 median fluorescence intensity. This raises the question of whether there is bifurcation of the cell population into strongly DSG2-positive cells and weakly DSG2-expressing cells. Again, this result appeared to be independent of infection status.

HCT116 cells showed a similar trend, though only two experimental repeats were analysed (Figure 4.10). CD46 and DSG2 median fluorescence intensity increased significantly in irradiated versus non-irradiated cells, and was unaffected by the addition of virus (Figures 4.10A-B). The percentage of CD46-positive cells likewise significantly increased in irradiated versus non-irradiated cells, however this was also marginally but significantly increased in cells to which EnAd-SA-GFP had been added (Figure 4.10C). These results would be consistent with a radiation-mediated increase in EnAd receptor levels, and putatively with enhanced CD46 expression in EnAd-infected HCT116 cells.

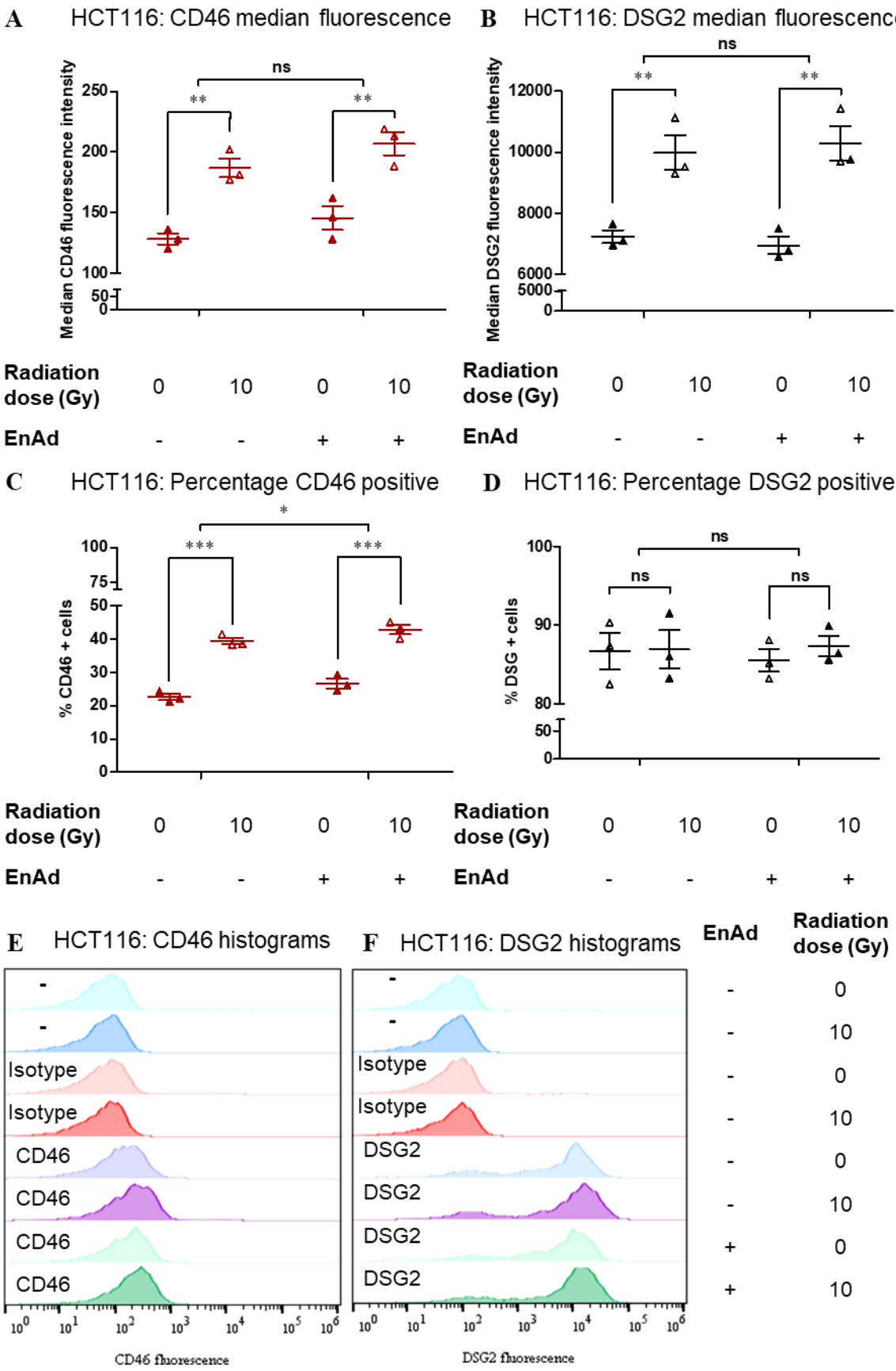

A
HCT116: CD46 median fluorescence
Median CD46 fluorescence intensity
250
200
150
100
50
0
ns
**
**
Radiation dose (Gy)
0
10
0
10
EnAd
-
-
+
+
B
HCT116: DSG2 median fluorescence
Median DSG2 fluorescence intensity
12000
10000
8000
6000
5000
0
ns
**
**
Radiation dose (Gy)
0
10
0
10
EnAd
-
-
+
+
C
HCT116: Percentage CD46 positive
% CD46 + cells
100
75
50
40
30
20
10
0
*
***
***
Radiation dose (Gy)
0
10
0
10
EnAd
-
-
+
+
D
HCT116: Percentage DSG2 positive
% DSG + cells
100
90
80
50
0
ns
ns
ns
Radiation dose (Gy)
0
10
0
10
EnAd
-
-
+
+
E
HCT116: CD46 histograms
-
-
Isotype
Isotype
CD46
CD46
CD46
CD46
CD46 fluorescence
F
HCT116: DSG2 histograms
-
-
Isotype
Isotype
DSG2
DSG2
DSG2
DSG2
DSG2 fluorescence
EnAd
Radiation dose (Gy)
-
0
-
10
-
0
-
10
-
0
-
10
+
0
+
10

Figure 4.10 Irradiation of HCT116 cells causes an increase in EnAd receptor expression. HCT116 cells were seeded into 12-well plates. The next day cells were mock-infected or infected with EnAd-SA-GFP at an MOI of 0.1. At 24 h p.i. cells were mock-irradiated or irradiated at 10 Gy. Supernatant and cells were harvested together 48 h p.i. Median fluorescence **(A, B)**, percentage of positive cells **(C, D)**, and histograms **(E, F)** are shown for CD46 **(A, C, E)** and DSG2 **(B, D, F)**. Mean ± SEM of a single experiment representative of two experimental repeats is shown. Each point represents data for a single well. Significance was evaluated using 2-way ANOVA with Bonferroni post-test. ns, not significant; $p < 0.05$, *; $p < 0.01$, **; $p < 0.001$, ***.

Surprisingly, DLD1 cells showed a clear deviation from the trends seen with A549 and HCT116 cells (Figure 4.11). Median CD46 and DSG2 fluorescence intensity (Figures 4.11A-B) and the percentage of positive cells (Figures 4.11C-D) decreased significantly in irradiated cells compared to non-irradiated cells. The histograms for CD46 and DSG2 fluorescence suggest the formation of two subpopulations, with a shift towards the population expressing lower levels of CD46 and DSG2 in irradiated wells (Figures 4.11E-F). The presence of EnAd lead to increased percentage of CD46-positive cells and median CD46 fluorescence intensity (Figures 4.11A, C), but had no effect on DSG2 levels (Figures 4.11B, D). Thus, though these findings are again suggestive of a potential increase in CD46 expression levels following EnAd infection, they also demonstrate that the effect of radiation on cellular EnAd receptors is cell line-dependent.

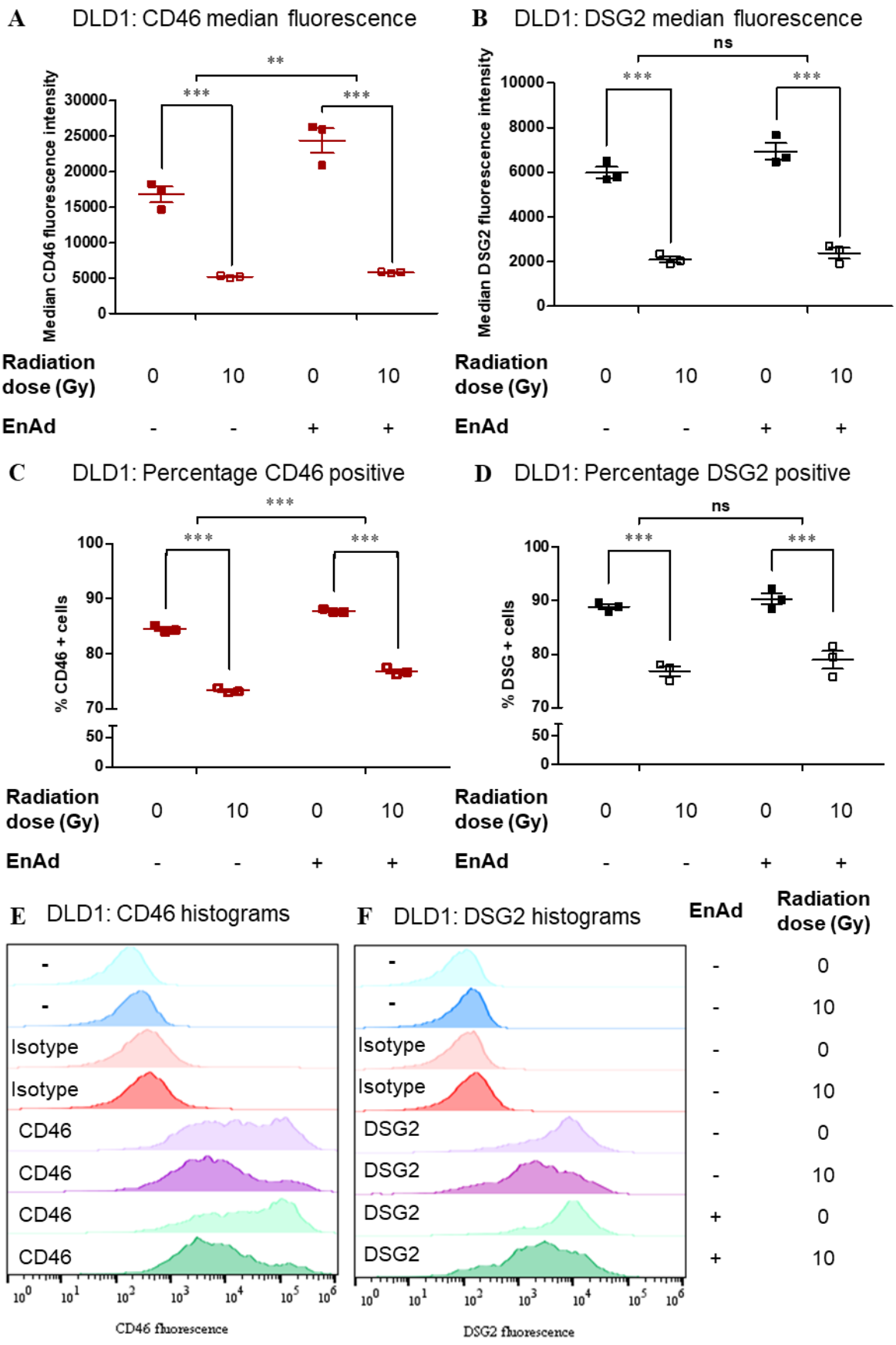

A
DLD1: CD46 median fluorescence
Median CD46 fluorescence intensity
30000
25000
20000
15000
10000
5000
0
**
***
***
Radiation dose (Gy)
0
10
0
10
EnAd
-
-
+
+
B
DLD1: DSG2 median fluorescence
Median DSG2 fluorescence intensity
10000
8000
6000
4000
2000
0
ns
***
***
Radiation dose (Gy)
0
10
0
10
EnAd
-
-
+
+
C
DLD1: Percentage CD46 positive
% CD46 + cells
100
90
80
70
50
0
***
***
***
Radiation dose (Gy)
0
10
0
10
EnAd
-
-
+
+
D
DLD1: Percentage DSG2 positive
% DSG + cells
100
90
80
70
50
0
ns
***
***
Radiation dose (Gy)
0
10
0
10
EnAd
-
-
+
+
E
DLD1: CD46 histograms
-
-
Isotype
Isotype
CD46
CD46
CD46
CD46
CD46 fluorescence
F
DLD1: DSG2 histograms
-
-
Isotype
Isotype
DSG2
DSG2
DSG2
DSG2
DSG2 fluorescence
EnAd
Radiation dose (Gy)
-
0
-
10
-
0
-
10
-
0
-
10
+
0
+
10

Figure 4.11 Irradiation of DLD1 cells causes a decrease in EnAd receptor expression. DLD1 cells were seeded into 12-well plates. The next day cells were mock-infected or infected with EnAd-SA-GFP at an MOI of 0.1. At 24 h p.i. cells were mock-irradiated or irradiated at 10 Gy. Supernatant and cells were harvested together 48 h p.i. Median fluorescence **(A, B)**, percentage of positive cells **(C, D)**, and histograms **(E, F)** are shown for CD46 **(A, C, E)** and DSG2 **(B, D, F)**. Mean ± SEM of a single experiment representative of three experimental repeats is shown. Each point represents data for a single well. Significance was evaluated using 2-way ANOVA with Bonferroni post-test. ns, not significant; p <0.05, *; p <0.01, **; p <0.001, ***.

Overall, of the two colorectal cell lines investigated, HCT116 cells, used in the *in vivo* experiment above (Figure 4.7), demonstrated a radiation-mediated increase in EnAd receptor expression, whilst a decrease was seen in DLD1 cells. Radiation-mediated enhanced receptor expression was further seen in A549 lung cancer cells, the cell line we have shown also demonstrates increased EnAd production *in vitro* following irradiation (Figures 4.4 and 4.5).

4.2.4 Irradiation does not lead to immediate or delayed increase in virus attachment and entry

Increased median DSG2 and CD46 expression in irradiated A549 cells may be one explanation for the observed enhanced virus production at low MOIs. Hypothetically, a higher number or density of EnAd receptors will increase the probability of virus binding and uptake, leading to downstream amplification in virus production during a multi-step infection. Zhang *et al.* have shown that there is a cell line-dependent increase in Ad5 vector uptake in pre-irradiated cells, which is greatest if infection takes place immediately following irradiation [140]; we therefore initially investigated whether EnAd infection likewise increased immediately following irradiation. Figure 4.12A illustrates the experimental timeline. A549 cells were seeded into 12-well plates and either mock-irradiated or irradiated at 10 Gy one day post-seeding. Cells were then immediately mock-infected (Figure 4.12B) or infected (Figure 4.12C) with EnAd-SA-GFP at an MOI of 0.1. At 2 h p.i., at which point uptake, but not replication, will have taken place [145], cell lysates

were harvested for DNA extraction and viral genome quantification. We found no significant difference in viral genome copy number between irradiated and non-irradiated cells (Figure 4.12C), in keeping with no effect of radiation on EnAd infection.

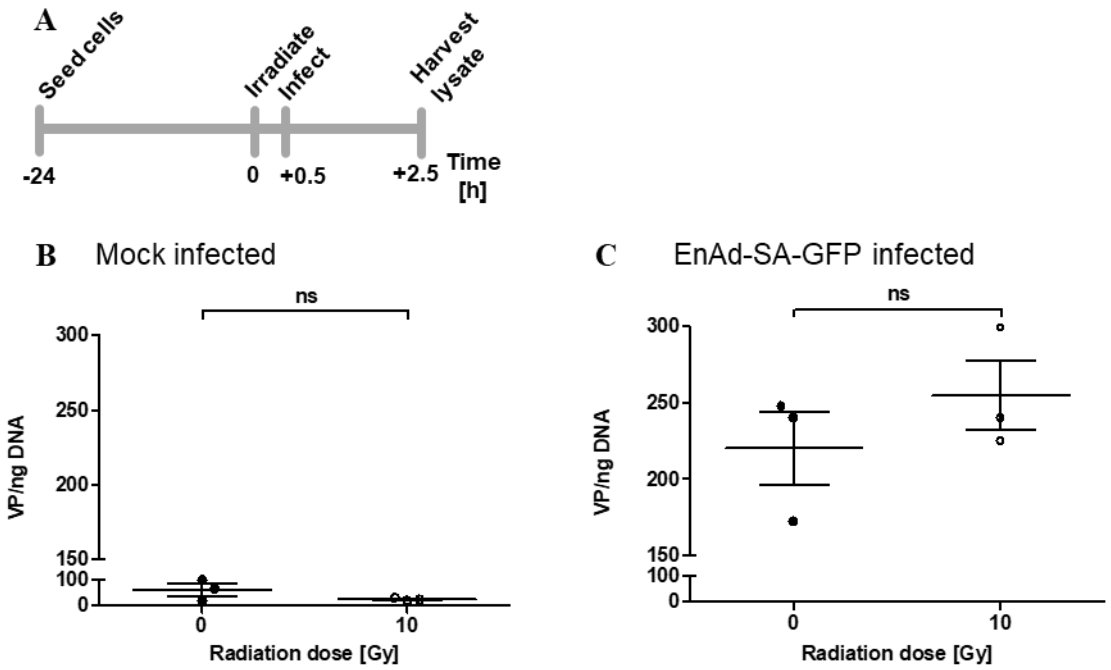


Figure 4.12 Irradiation of A549 cells has no immediate effect on EnAd infection. (A) Schematic illustrating experimental timeline. A549 cells were seeded into 12-well plates one day prior to mock-irradiation or irradiation at 10 Gy. Cells were immediately infected with EnAd-SA-GFP at an MOI of 0 **(B)**, or 0.1 **(C)**. At 2 h p.i., cells were washed twice with PBS and lysate was harvested. DNA extraction was carried out and viral genomes measured using hexon-specific primers and probe. **(B-C)** Viral genome copies per ng DNA. Data shown is mean ± SEM of a single experiment representative of four experimental repeats. Each data point corresponds to a single well. Significance was evaluated using unpaired t-test. ns, not significant.

Given that the observed increase in EnAd receptor expression by A549 cells occurred at 24 h post-irradiation (Figure 4.9), the experiment was adapted to assess virus infection at this time point. A549 cells were mock-irradiated or irradiated at 10 Gy in culture flasks. After 18 h, cells were seeded into 12-well plates and allowed to adhere for 6 h before mock-infection or infection with EnAd-SA-GFP (Figure 4.13A). This experimental timeline was formulated to minimise differences in cell numbers resulting from early radiation-associated cell death. Cell lysates were harvested for DNA extraction and virus particle quantification

by qPCR at 2 h p.i. A pilot experiment at MOIs of 0.1 and 1 showed no significant difference in irradiated versus non-irradiated cells at either dose (Figures 4.13C-D). Three further experimental repeats at MOIs of 0 or 0.1 also did not suggest any differences in virus infection (Figures 4.13E-F). The greater virus production in irradiated versus non-irradiated A549 cells is therefore not secondary to a magnification of this initial step of infection.

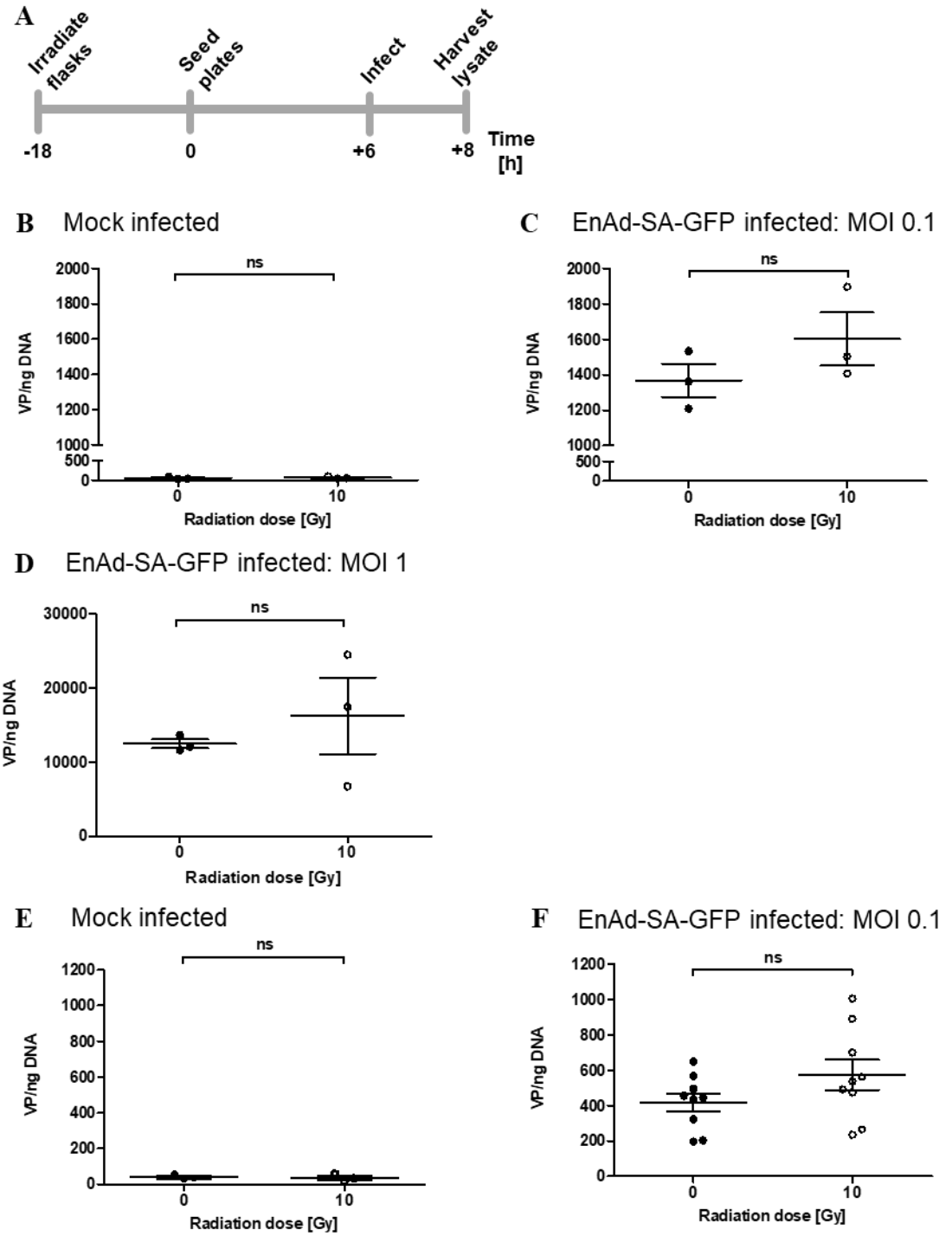


Figure 4.13 No impact on EnAd infection when cells are irradiated 24 hours prior to addition of virus (A) Schematic illustrating experimental timeline. A549 cells in cell culture flasks were irradiated at 10 Gy or mock-irradiated. Cells were seeded into 12-well plates 18 h later and allowed to adhere for 6 h, at which point they were mock-infected or infected with EnAd-SA-GFP at an MOI of 0.1 or 1. At 2 h p.i., cells were washed twice with PBS and lysate was harvested. DNA extraction was carried out and viral genomes were measured using hexon-specific primers and probe. **(B-D)** Results of a single pilot experiment showing mean ± SEM of VP/ng DNA in cells infected at an MOI of 0 **(B)**, 0.1 **(C**), or 1 **(D**). Each point corresponds to a single well. **(E-F)** Data showing mean ± SEM from a single experiment representative of three experimental repeats. Infection was carried out at an MOI of 0 **(E)** or 0.1 **(F)**. Each point corresponds to a single well. Significance was evaluated using unpaired t-test. ns, not significant.

4.2.5 Pre-irradiation leads to increased EnAd E1A expression

The finding that there is no increase in EnAd infection by irradiated cells despite greater receptor expression supports the hypothesis that enhanced virus production is due to an intracellular process. The earliest viral gene expressed is E1A, an early adenoviral transcriptional unit encoding two principal proteins which play roles in activating transcription and stimulating the cell to enter S-phase [39]. As commercial antibodies are only available against Ad2/5 E1A, we assessed EnAd E1A expression using EnAd-E1A-FLAGtag, which expresses E1A C-terminally tagged with the FLAG-tag octapeptide. Using this virus, we compared E1A expression in pre-irradiated versus non-irradiated cells. A549 cells in cell culture flasks were irradiated at 10 Gy or left non-irradiated, seeded into 6-well plates eight hours later, and allowed to adhere overnight. At 24 h post-irradiation, cells were mock-infected or infected with EnAd-E1A-FLAGtag at an MOI of 0.1, 1, or 10. Cell lysates were harvested after eight hours for analysis by western blotting. A marked increase in E1A expression was seen in pre-irradiated versus non-irradiated cells infected at an MOI of 10; the signal was below the limit of detection at lower MOIs (Figure 4.14A). In a similar experiment using HCT116 cells infected at MOIs of 0 or 10, a clear band corresponding to E1A-FLAGtag was seen in pre-irradiated, but not non-irradiated cells (Figure 4.14B). The experimental time course was extended to include harvesting of cells at both 8 and 12 h p.i.;

this confirmed greater E1A expression in pre-irradiated versus non-irradiated A549 cells at both time points (Figure 4.14C). Infecting HCT116 cells with MOIs of 0 or 20 and harvesting lysates at 8 and 12 h p.i. likewise showed marked E1A-FLAGtag expression in pre-irradiated cells, with only a faint band seen in non-irradiated cells (Figure 4.14D). These results suggest irradiation may enhance virus replication through an E1A-dependent mechanism.

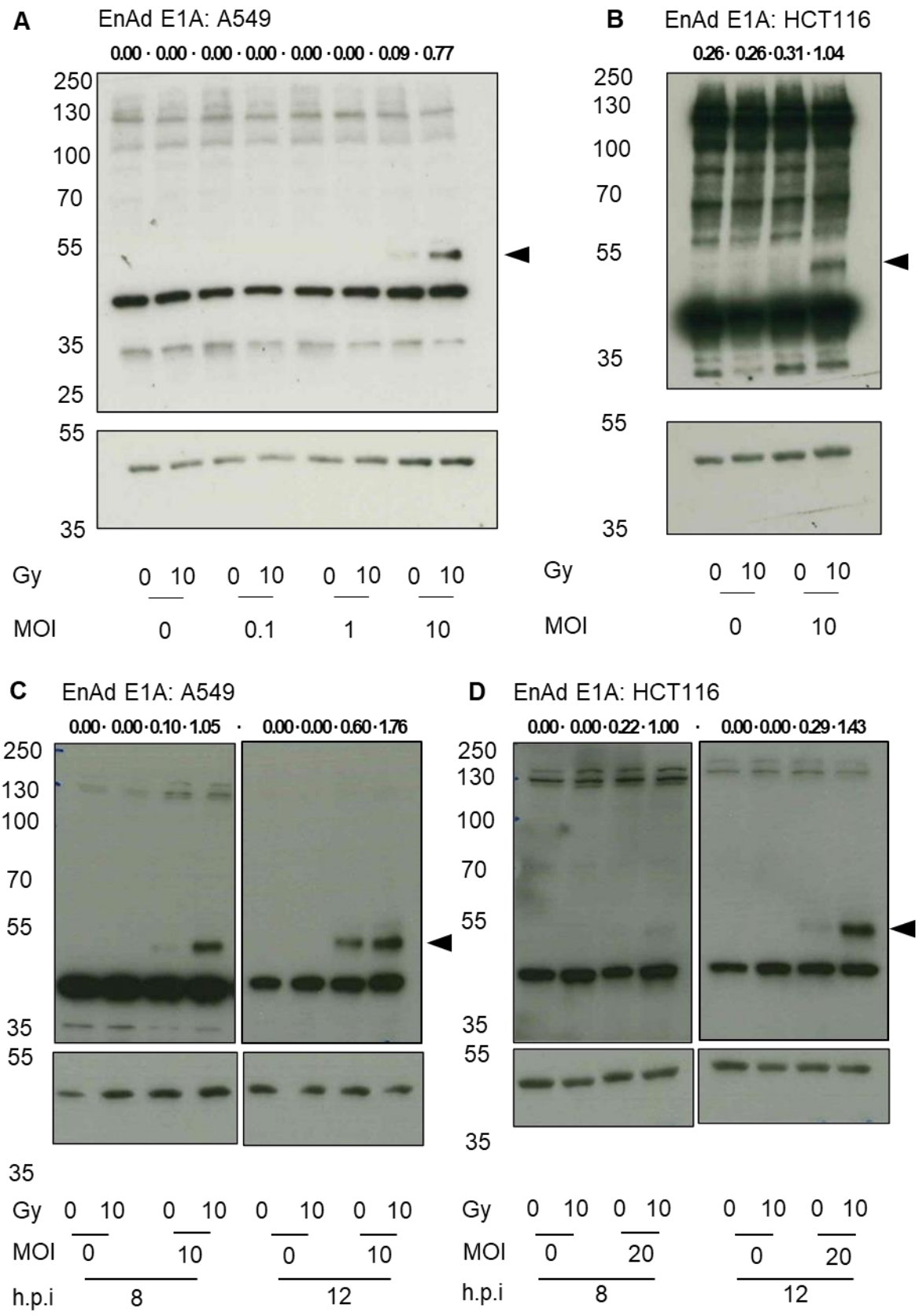

A
EnAd E1A: A549
0.00 · 0.00 · 0.00 · 0.00 · 0.00 · 0.00 · 0.09 · 0.77
250
130
100
70
55
35
25
55
35
Gy 0 10 0 10 0 10 0 10
MOI 0 0.1 1 10
B
EnAd E1A: HCT116
0.26 · 0.26 · 0.31 · 1.04
250
130
100
70
55
35
55
35
Gy 0 10 0 10
MOI 0 10
C
EnAd E1A: A549
0.00 · 0.00 · 0.10 · 1.05 · 0.00 · 0.00 · 0.60 · 1.76
250
130
100
70
55
35
55
35
Gy 0 10 0 10 0 10 0 10
MOI 0 10 0 10
h.p.i 8 12
D
EnAd E1A: HCT116
0.00 · 0.00 · 0.22 · 1.00 · 0.00 · 0.00 · 0.29 · 1.43
250
130
100
70
55
35
55
35
Gy 0 10 0 10 0 10 0 10
MOI 0 20 0 20
h.p.i 8 12

Figure 4.14 EnAd E1A expression is increased in pre-irradiated cells. (A, C) A549 or **(B, D)** HCT116 cells were irradiated at 10 Gy or left non-irradiated, and seeded after 8 h. Cells were infected with EnAd E1A-FLAGtag 24 h post-irradiation at an MOI of 0, 0.1, 1, or 10 **(A**), MOI 0 or 10 **(B, C**) or MOI 0 or 20 **(D)**. Cells were washed with PBS and harvested into RIPA 8 h p.i. **(A-B)** or 8 and 12 h p.i. **(C-D**). **(A-B)** Pilot experiments shown. A total of 30 μg **(A)** or 50 μg **(B)** of protein was loaded per lane. **(C-D)** 70 μg protein was loaded per lane. **(A-D)** Top panels show staining with anti-FLAGtag antibody (arrows indicate band of interest), bottom panels show staining with β-actin, used as a loading control. Density for each band was determined using ImageJ and is given above the corresponding lane as a β-actin-corrected value. Gy = radiation dose in Gray.

Interestingly, this pattern was not observed when cells were infected with Ad5 (Figure 4.15). A549 and HCT116 cells were pre-irradiated at 10 Gy or left non-irradiated as above, and infected with Ad5 at MOIs of 0 or 10, or 0 or 20, respectively. Probing for Ad5 E1A using western blotting demonstrated no increase in E1A expression in pre-irradiated versus non-irradiated A549 cells at 6, 8, 12, or 24 h p.i. (4.15A). Greater E1A expression was however noted in pre-irradiated versus non-irradiated HCT116 cells at 8 and 12 h p.i. (4.15B). Throughout this chapter we have observed differences between virus serotypes (Figures 4.1-4.3) and cell lines (Figures 4.9-4.11) in their response to radiation; it is therefore not surprising that this extends to the expression of this key viral protein.

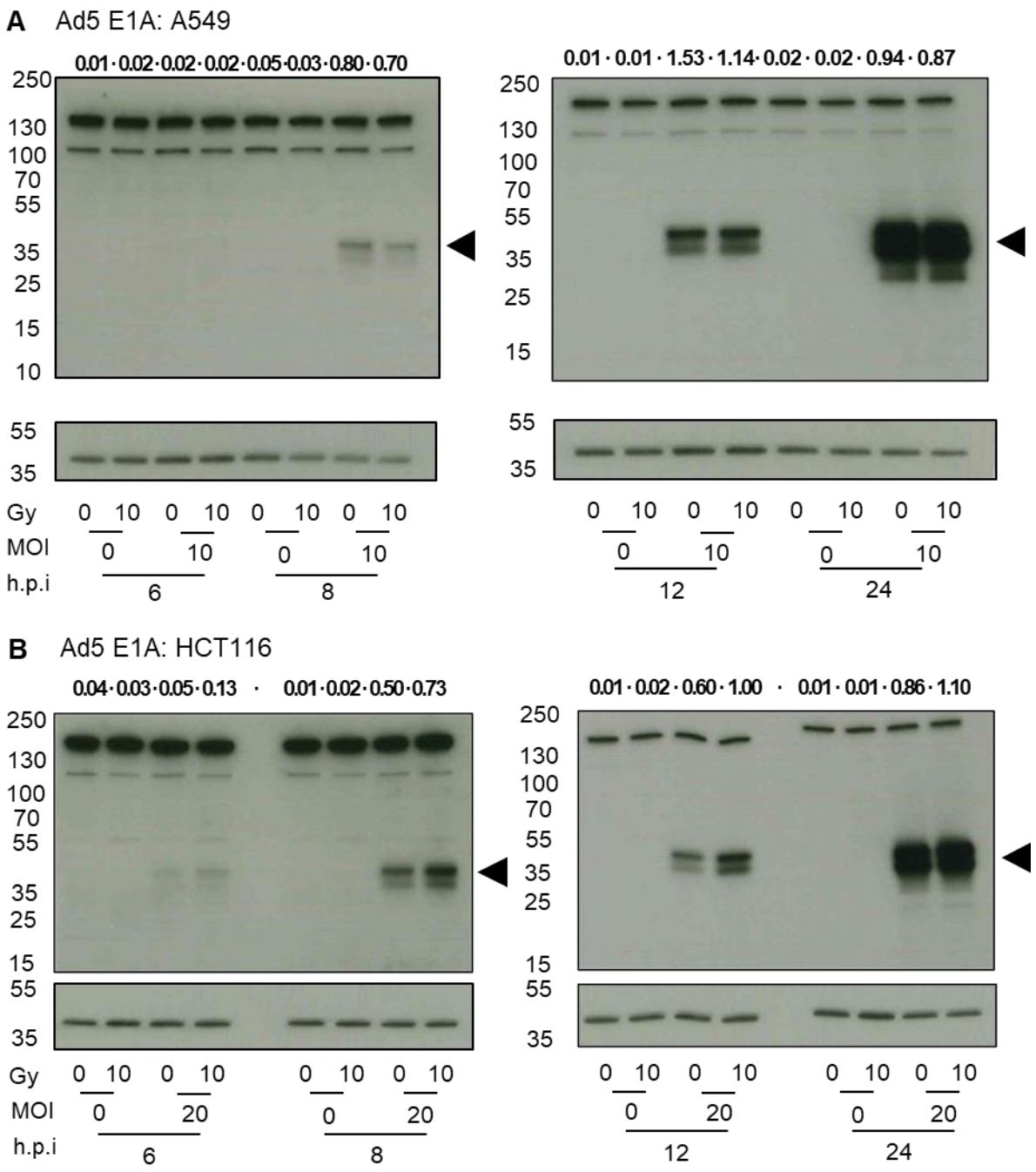


Figure 4.15 Pre-irradiation does not affect Ad5 E1A expression. (A) A549 or **(B)** HCT116 cells were irradiated at 10 Gy or left non-irradiated, and seeded after 8 h. Cells were infected with Ad5 24 h post-irradiation at an MOI of 0 or 10 **(A)**, or 0 or 20 **(B)**. Cells were washed with PBS and harvested into RIPA buffer at 6, 8, 12, and 24 h p.i. **(A-B)** A total of 30 μg protein was loaded per lane. Top panels show staining with anti-E1A antibody (arrows indicate band of interest), bottom panels show staining with β-actin, used as a loading control. Density for each band is given above the corresponding lane as a β-actin-corrected value. Density analysis provided by Dr Sally Frost using Image Lab software. Gy = radiation dose in Gray.

4.3 Chapter main findings

The results in this chapter demonstrate that there is a significant increase in total and infectious EnAd particle production from cells irradiated 24 h p.i. compared to non-irradiated cells, both *in vitro* and *in vivo*. At the time point studied, there is also a non-significant trend towards enhanced production of infectious Ad5 and Ad11p particles in the supernatant of A549 cells irradiated 24 h p.i.

The cell lines demonstrating radiation-associated virus increase also exhibited greater cell surface expression of CD46 and DSG2, the two receptors for EnAd, in irradiated versus non-irradiated cells. Nevertheless, this did not translate into improved virus infection. We did however show a marked increase in E1A expression in pre-irradiated versus non-irradiated, EnAd-infected A549 and HCT116 cells. This pattern did not extend to Ad5.

4.4 Chapter discussion

There is some conflicting evidence that irradiation can lead to augmented adenovirus production [97, 99-101]. This appears to be dependent on the cell line, radiation dose, and MOI used. As with the majority of publications concerning adenovirus, however, all the available evidence pertains to Ad5-based constructs. The results in this chapter show an increase in the production of virus particles in EnAd-infected A549 cells irradiated with 10 Gy 24 h p.i. at an MOI of 0.1. Low MOIs and high radiation doses were also associated with a radiation-mediated increase in transgene expression in the majority of non-replicating adenoviral constructs studied by Hingorani *et al.* [141]. Further, Chen *et al*. demonstrated increased infectious particle production in LNCaP prostate cancer cells treated with 10 Gy of radiation at 24 h p.i. with a prostate cancer-specific Ad5 construct at MOI 0.1, an experimental set-up similar to the one utilised in this thesis [100]. Interestingly however, in our study the trend toward increased Ad5 and Ad11p infectious particle production in

irradiated versus non-irradiated cells did not reach significance. These contrasting results may reflect variable growth characteristics of different virus serotypes in different cell lines, indeed the increase seen by Chen *et al.* was amplified at later time points.

Importantly, the increased production of EnAd observed *in vitro* also extended to an HCT116 xenograft *in vivo* model (Figure 4.7). Compared to non-irradiated controls, tissue from irradiated xenografts demonstrated a 9- to 19-fold increase in luciferase expression, viral genome copy number, and infectious particle concentration. These findings concur with the data presented by Dilley *et al.*, who showed that a single dose of 10 Gy given to xenografts 24 h p.i. with an Ad5-based prostate tumour-specific vector resulted in increased hexon staining 14 days p.i. [101].

Together, these results are consistent with a radiation-mediated increase in EnAd production at the time points, radiation doses, cell lines and MOI studied. Figure 4.4 showed a linear association between virus particle production and radiation across three doses. We anticipate a plateauing of the relationship at higher radiation doses if disruption of cell function and death reach a stage where effective viral replication cannot be supported. Indeed, Figure 4.5 suggests this is the case, as mean $TCID_{50}$/mL at 20 Gy appeared to be lower than 10 Gy for all three viruses. Further experiments to expand on the work in this chapter should investigate the production of EnAd in the presence and absence of radiation following infection at varying MOIs. The main obstacle we anticipate would be the identification of a time point at higher MOIs which allows enough time for the effects of radiation to come into play, which typically requires a number of cell cycles, but which is not so late that virus-induced cell death prevents spread.

A number of mechanisms are thought to contribute to radiation-associated virus increase, one of which is an effect on virus uptake. Some groups have reported that radiation increases

the cellular expression of receptors involved in the uptake of Ad5 [141], whereas others have found no effect [97, 143, 146]. There is less evidence on the effect of radiation on the group B adenovirus receptor CD46; some groups have reported this to increase [99], whereas others have determined no change [146, 147]. Qian *et al.* [144] and Egami *et al.* [148] linked an increased uptake of Ad5 vector in irradiated cells to higher expression of dynamin 2. Whilst there is limited information on the role of dynamin 2 in the uptake of group B adenoviruses, at least two members, Ad3 and Ad35, are known to undergo cell line-dependent use of dynamin-independent mechanisms to infect cells [149, 150].

We have found that CD46 and DSG2 expression levels are increased following irradiation in two cell lines, A549 and HCT116, but quite dramatically decreased in a third, DLD1. The percentage of CD46-positive, but not DSG2-positive, A549 and HCT116 cells also increased following irradiation. The results for CD46 in HCT116 and A549 cells are not unexpected; Ganesh *et al.* found increased CD46 levels following irradiation of RPMI2650, a head and neck cancer cell line [99], and discussed the potential that these changes may be cell line-dependent. The results in DLD1 cells are rather more surprising. Despite both cell lines being colorectal cancer cells, levels of both receptors increase in HCT116 but decrease in DLD1. The findings for DSG2 may relate to cell death, as it has been found to play a key role in apoptosis [151, 152]. Nava *et al.* have reported that DSG2 cleavage, albeit of the cytoplasmic domain, regulates early intestinal epithelial cell apoptosis. However, they also found this cleavage led to an early increase in total DSG2 levels, appearing to function in a positive feedback loop. Total DSG2 levels increased after three hours of camptothecin-induced apoptosis and peaked after six, decreasing 24 hours after apoptosis induction compared to baseline levels [151]. Cirillo *et al.* showed a progressive depletion over 24 hours in DSG2 levels in the colorectal tumour cell line HT-29 and the human keratinocyte cell line HaCaT following staurosporine-mediated induction of apoptosis [152]. Given that

DSG2 loss appears to be associated with the later stages of apoptosis, our findings may be due to a greater number of DLD1 cells reaching this stage by 24 hours post-irradiation with 10 Gy. An analysis of comparative radiosensitivity, however, suggests HCT116 cells are more radiosensitive than DLD1 cells [153]. In our experiments, DLD1 cells were more adherent, requiring stronger chemical and physical removal techniques, which may have impacted on cell health. Data analysis was carried out on live cells only, but this would not exclude cells undergoing apoptosis. Co-staining with Annexin V may be helpful in answering whether the decrease in DSG2 expression in irradiated DLD1 cells is associated with cell death, but this would require optimisation of the temporal relationship between DSG2 shedding and Annexin V expression. An experiment investigating the effect of lower doses of radiation on DLD1 cells may be the best first step in separating the effects of radiation on receptor expression in this cell line.

The progressive loss of DSG2 during apoptosis could explain why none of the three cell lines demonstrated an increase in the percentage of DSG2 positive cells following irradiation. Apoptosis in a small population of DSG2-negative cells may not necessarily be significantly reflected in median fluorescence intensity, but would affect the proportion of receptor-positive cells. The most interesting follow up experiment to conduct on the basis of these findings would be an assessment of virus production in irradiated versus non-irradiated DLD1 cells across a range of radiation doses.

In our experiment investigating the impact of radiation and/or EnAd on receptor expression, virus was added at a very low MOI. Our aim was not to explore the effect of infection on receptor expression in individual cells, but rather whether global changes in expression occur as a response to the levels of virus used in the *in vitro* experiments showing irradiation-associated virus increase. We found evidence of a small but significant EnAd-associated amplification in CD46 levels in two of the three cell lines studied. Ad35 vector-mediated

changes in CD46 cell surface expression have also previously been demonstrated, though infection predominantly led to downregulation of CD46 receptors. This was however cell line-dependent and expression was conversely increased in some cell lines [154]. Ad3 infection of A549 cells has been shown to lead to DSG2 shedding, with a marked decrease in membrane-associated DSG2 as detected by immunofluorescence 6 h p.i. [155]. We saw no such impact of EnAd on DSG2 expression in any of the cell lines studied.

Regardless of the above findings, the increase in CD46 and DSG2 expression in A549 cells did not translate into increased EnAd infection, even at time points and radiation doses at which a change in receptor levels was observed. One possible explanation is that, at low levels of adenovirus infection, receptor expression is not a limiting factor. This hypothesis could be tested by repeating this experiment at higher MOIs.

Interestingly, a marked increase in E1A expression was observed in EnAd-infected, pre-irradiated A549 and HCT116 cells. Though this was also the case in Ad5-infected HCT116 cells, no such increase was seen in Ad5-infected A549 cells. Expression of E1A by tumour cells is known to confer radiosensitisation [156, 157]; our findings therefore have interesting implications for a potential enhancement of cytotoxicity when EnAd is combined with radiation therapy, particularly in the clinical setting where fractionated dose regimes are utilised.

One of the mechanisms mediating enhanced EnAd production in irradiated A549 and HCT116 cells therefore appears to be an increase in the expression of the early viral transcription factor E1A. Nokisalmi *et al.* investigated potential mechanisms underlying radiation-mediated potentiation of adenovirus function, and found that the amount of double-strand DNA breaks appeared to correlate with non-replicating Ad5 vector transgene expression [146]. All experiments were conducted using viruses lacking in E1, however

enhanced transgene expression in irradiated versus non-irradiated cells was observed across a range of promoters and one may therefore propose that the mechanism underlying this relatively widespread change may also impact on E1A expression. Transgene expression in irradiated cells was further potentiated by treatment with a DNA-PK inhibitor or Irinotecan, a topoisomerase I inhibitor. Hingorani *et al.* have likewise shown that combining DNA damage repair inhibitors with radiation potentiates Ad5 vector transgene expression and provided evidence that this increase is mediated through the mitogen-activated protein kinase (MAPK)/extracellular signal-regulated kinase (ERK) pathway [158]. It would therefore be interesting to explore whether the radiation-mediated increase in E1A expression seen above is further enhanced by the addition of DDR pathway inhibitors and/or inhibited by inhibition of the MAPK/ERK signalling pathway.

To summarise, in this chapter we have demonstrated a radiation-mediated increase in EnAd production which is associated with greater E1A expression. Though we have explored some of the potential underlying mechanisms here, a full understanding is yet to be attained. Similar to Nokisalmi *et al.*, we would propose there is not one simple cause for these findings, but rather a number of complex interacting pathways [146].

Chapter 5: Synergistic cytotoxicity using combination treatment Enadenotucirev and radiation

5.1 Introduction: Hypothesis and chapter aims

Previous results in this thesis have shown that EnAd is able to inhibit the DDR pathway at multiple points. We have also demonstrated that radiation treatment enhances EnAd virus particle production, both total and infectious, *in vitro* as well as *in vivo*. The final step is thus evaluating whether cytotoxicity may be enhanced by combination treatment. This may occur through radiation-enhanced virus-mediated cytotoxicity, virus infection inhibiting the DDR and subsequent radiosensitisation, or a combination of both.

A substantial amount of evidence is currently available on the synergistic effect of radiation and adenovirus combination therapy on a range of tumour types *in vitro* and *in vivo*, almost all using Ad5-based constructs. The prostate-targeted replication-competent Ad5-based variant CV706 was shown to act synergistically, both *in vitro* and *in vivo*, on the human prostate carcinoma line LNCaP when combined with radiation post-infection [100]. *In vivo*, similar synergistic effects were seen in animals treated with a single 10 Gy dose 1 day post-infection (p.i.) and animals treated with 10 Gy/4 # on days 1, 3, 6, and 8. Dilley *et al*. likewise found the prostate-targeted Ad5-based oncolytic virus CG7870 acted synergistically with radiation therapy *in vitro* and *in vivo* [101]. Radiation treatment was delivered 24 h p.i., and the cell line used in both models was LNCaP.

Toth *et al.* utilised replication-competent Ad5-based constructs overexpressing E3-11.6K (adenovirus death protein) in combination with radiation therapy *in vitro* and *in vivo* [95]. A549 cells infected 24 h post-radiation with 6 Gy demonstrated an increase in virus-associated toxicity approximating 2-3 orders of magnitude compared to mock-irradiated

cells. Hep3B cells infected 24 h before or after 3 Gy of radiation gave similar results. *In vivo*, a combination of virus and radiation therapy lead to a significant tumour growth suppression compared to either treatment alone. Kawabe *et al.* also investigated the effect of combined radiation and virus treatment on lung cancer cells (A549 and H322), as well as normal lung fibroblasts (MRC-9 and CCD-16) [102]. The replication-deficient Ad5-based construct Ad5/CMV/p53 caused radiosensitisation in tumour, but not normal, cells *in vitro*. Combination treatment had a greater-than-additive effect on tumour growth compared to either treatment given on its own *in vivo*.

In head and neck tumour models, ONYX-015 (an E1B-55k-deleted group C-based replicating adenovirus) potentiated cytotoxicity when combined with radiation therapy in three anaplastic thyroid cell lines *in vitro* [96]. *In vivo*, combination treatment caused significant tumour growth delay in a human thyroid anaplastic carcinoma cell line xenograft, whereas no significant tumour growth delay compared to control was seen using single agent treatment. The chimeric oncolytic virus OV-5T35H likewise significantly delayed the growth of RPMI2650 head and neck tumour xenografts and significantly improved survival compared to monotherapy when given prior to fractionated radiation [99]. Combination radiation treatment with the Ad5-based replication-competent construct OV-5 was associated with delayed tumour growth compared to monotherapy, but not with a significant increase in survival time.

Other tumour types in which combination adenoviral and radiation therapy have been found to be beneficial in pre-clinical models include glioma and ovarian cancer cells. Emdad *et al.* demonstrated that replication-defective Ad5-based constructs expressing melanoma differentiation associated gene-7/MDA-7/IL-24 caused significantly more apoptosis and less colony formation in ovarian cancer cell lines when combined with low dose radiation

(2 Gy) than either treatment alone [103]. This effect was not apparent in normal human mesothelial cell lines. Geoerger *et al.* found a potentiating effect of ONYX-015 on two human malignant glioma xenografts derived from primary tumours [97]. This was reported to be additive in one of two xenografts, while a subtherapeutic virus dose resulted in significant tumour growth delay in the other xenograft when combined with 5 Gy of total body irradiation. Effects ranging from additive to supra-additive for a combination of adenovirus and radiation were also seen in glioma cell lines and primary cultures using the replication-competent Ad5 construct AdΔ24RGD, which carries a deletion in E1A and demonstrates αv integrin tropism [98]. *In vivo*, tumour regression was seen in all mice receiving combination treatment.

The literature therefore suggests that there may be a benefit of combining radiation and adenovirus treatment. We hypothesise that EnAd-associated cytotoxicity may be augmented by radiotherapy. Previous chapters have discussed the challenge of optimising *in vitro* experimental techniques to allow sufficient time to observe radiation-mediated cellular effects whilst avoiding excessive EnAd cytotoxicity. Other groups working with replication-competent oncolytic virus have in particular encountered the problem of replicating vector spread resulting in the destruction of colonies when conducting the clonogenic assay, the gold standard in assessing radiosensitisation [95]. Interestingly, despite the striking level of EnAd cytotoxicity noted *in vitro*, the evidence *in vivo* is consistent with a variable impact on tumour growth which appears to be dependent on model, cell type, virus dose and mode of delivery [110, 124, 159].

The primary aims of this chapter are therefore:

1. Develop an assay allowing assessment of EnAd and radiation combination treatment effect *in vitro*.

2. Explore potential synergies between EnAd and radiotherapy *in vitro*.

3. Develop an appropriate mouse model for evaluating potential synergies between EnAd and radiotherapy.

5.2 Results

5.2.1 Development of a modified plaque assay to monitor virus spread

We initially set out to develop an assay which would allow us to evaluate the impact of irradiation on EnAd-associated cytotoxicity, whilst circumventing the problem of vector spread causing generalised cell death encountered when using the clonogenic assay.

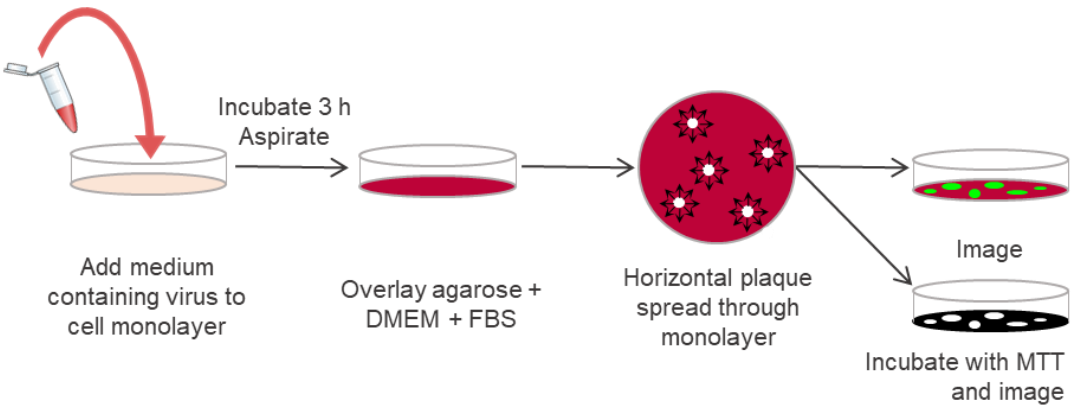
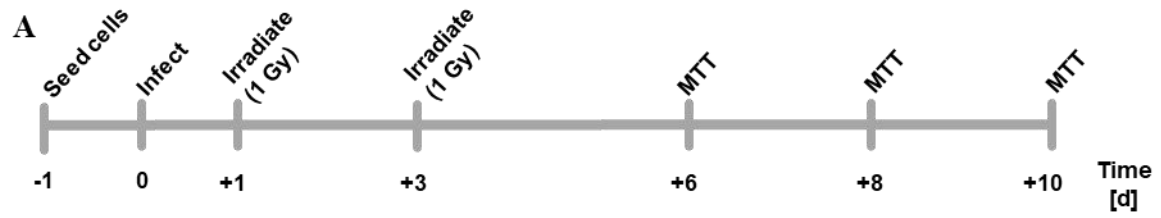


Figure 5.1 Summary of experimental setup for modified plaque assay. Cells are seeded into 6-well plates and subsequently incubated with 500 µL virus-containing medium, or mock-infected. At 3 hours post-infection (h p.i.) medium is aspirated and a 1% agarose + DMEM + 2% FBS mix is carefully layered onto cells. Plates are monitored and either imaged on the Celigo on alternate days or, when a pre-set endpoint is reached, incubated with MTT in a 1:10 dilution and imaged on a GelCount.

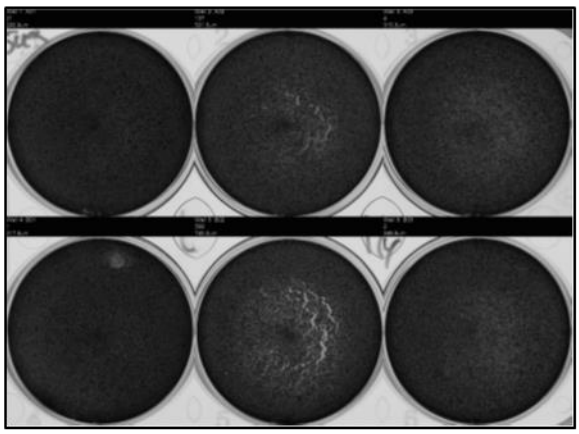
The plaque assay is a standard technique in virology used to assess the number of infectious virus particles in a sample. Following infection of a cell monolayer with different dilutions of the virus, an overlay of agarose and medium is added to limit viral spread to two dimensions (Figure 5.1). By serial monitoring of plaque size, we hypothesise that we can evaluate whether irradiation of cells changes virus spread behaviour in a cell monolayer.

Below, we describe two techniques to measure plaque size changes: monitoring plaque growth over a period of days using the Celigo cytometer, or serial staining of wells within a plate and subsequent scanning on a GelCount tumour colony counter (Figure 5.1).

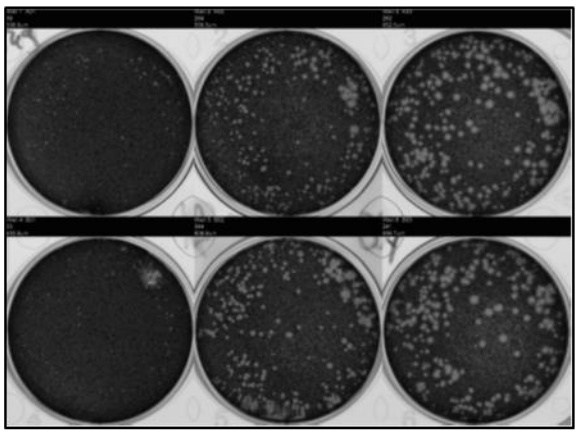
We initially utilised the method of serial staining to investigate whether virus spread through the monolayer is augmented by radiation in a dose-dependent manner. Figure 5.2A demonstrates the experimental timeline. A549 cells were seeded into four 6-well plates at a density of 1 x 10^6 cells/well and mock-infected (Figure 5.2B) or infected with 1 x 10^{-2} VP/cell the next day (Figures 5.2C-E). Medium containing virus was aspirated 3 h p.i. before overlaying cells with 3 mL DMEM + 2% FBS + 1% agarose. Two of the infected plates were irradiated at 1 Gy 24 h p.i. alongside the mock-infected plate. One of the infected plates received a second 1 Gy 72 h p.i., with the rest mock-irradiated. Two wells of each 6-well plate were then stained with MTT and imaged at 6 days p.i., two more were stained and imaged at 8 days p.i, and the final two at 10 days p.i., providing images of typical plaque size for each condition at these times (Figures 5.2B-E). Imaging and analysis were performed using a GelCount tumour colony counter and mean plaque area for each well was calculated. Figures 5.2F-H show the mean ± SEM plaque area for each well according to dose of radiation and infection, each graph representing a different time point. In infected wells, no significant difference was seen between the mock-irradiated and irradiated wells at 6 and 8 days p.i. (Figures 5.2F-G). However, at 10 days p.i. mean plaque area was significantly increased in infected wells irradiated at 2 Gy/2# compared to mock-irradiated wells (Figure 5.2H).



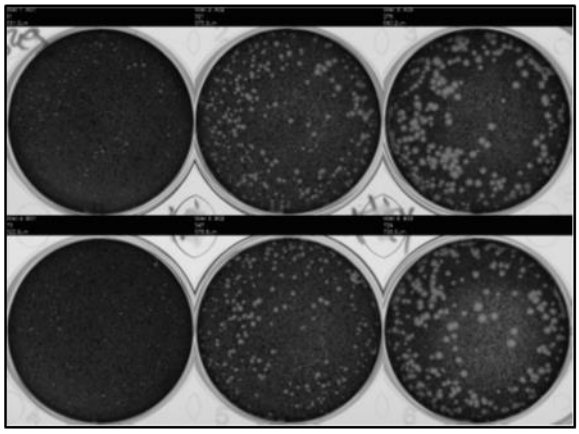
B Mock-infected / 1 Gy



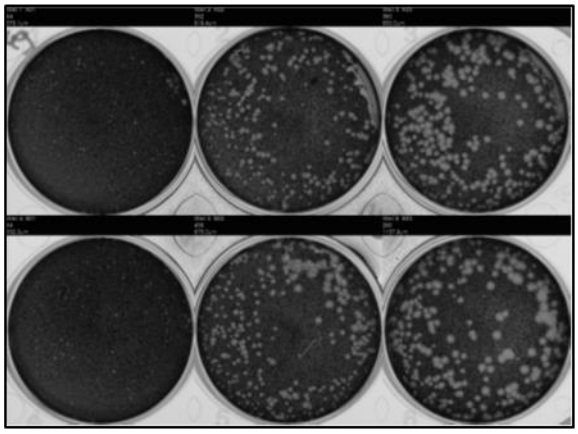
C Infected / 0 Gy



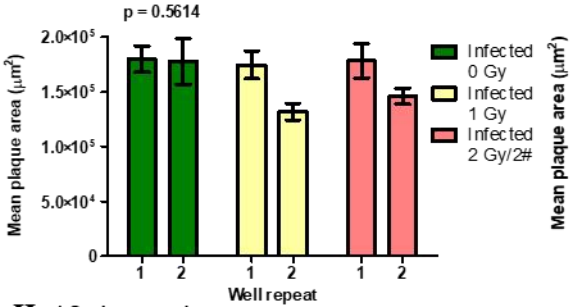
D Infected / 1 Gy



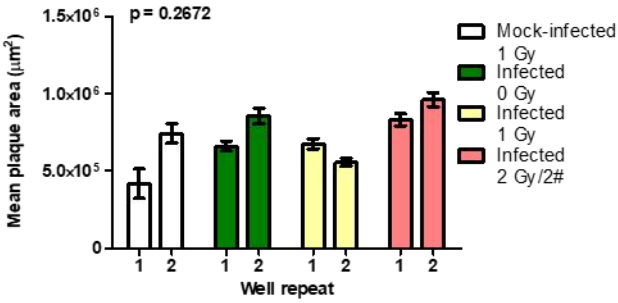
E Infected / 2 Gy



F 6 days p.i.



G 8 days p.i.



H 10 days p.i.

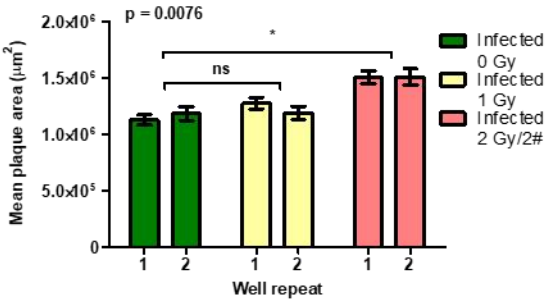


Figure 5.2 Plaque area in irradiated wells is increased at later time points. (A) Timeline of experiment. A549 cells were seeded into 6-well plates at a density of 1 x 10^6 cells/well. One day later cells were mock-infected **(B)** or infected with EnAd virus at 1 x 10^{-2} VP/cell **(C-E)**. At 3 h p.i. medium was aspirated and 3 mL of a 1% agarose + DMEM + 2% FBS mix carefully layered onto cells. At 24 h p.i. plates were mock-irradiated or irradiated at 1 Gy. The 2 Gy plate was given a further 1 Gy at 3 days p.i. MTT in a 1:10 dilution (300 μL) was added to wells A1 and B1 6 days p.i., wells A2 and B2 8 days p.i., and wells A3 and B3 10 days p.i. Plates were imaged on GelCount. **(B-E)** GelCount images of mock-infected / 1 Gy **(B)**, infected / 0 Gy **(C)**, infected / 1 Gy **(D)** and infected / 2 Gy plates **(E)**. **(F-G)** Plaque area given as mean ± SEM for two separate wells stained at each time point – 6 days p.i. **(F)**, 8 days p.i. **(G)** and 10 days p.i. **(H)**. Significance was evaluated using one-way ANOVA (p-value given in top left) with Bonferroni post-test (represented by ns or * in graph). ns, not significant; p <0.05, *.

Though this technique provided some encouraging results, further optimisation is still necessary. The main limitation is that continuous monitoring of a single culture and individual plaques over time is not possible, as the addition of MTT consumes the contents of the stained well and this therefore acts as an end-point assay.

One potential way of tracking plaque growth over a period of time is to use fluorescence imaging of a virus. EnAd-SA-GFP expresses GFP during the latter parts of the virus life cycle [110]. An experiment was thus conducted to establish a dilution of EnAd-SA-GFP resulting in easily discernible individual plaque formation. A549, HT-29 and DLD1 cells were seeded into 6-well plates at a density of 1 x 10^6 cells/well. One (A549 and DLD1) or two (HT-29) days later cells were infected with 1:10 serial dilutions ranging from 10 VP/cell to 1 x 10^{-13} VP/cell. Medium containing virus was aspirated 3 h p.i. before overlaying cells with 3 mL DMEM + 2% FBS + 1% agarose. Plates were monitored until plaques were easily discernible before adding MTT to wells containing identifiable individual plaques (Figure 5.3) for ease of visualisation and imaging. MTT was added to wells infected with 1 x 10^{-1} (DLD1 only), 1 x 10^{-2} and 1 x 10^{-3} VP/cell (all cell lines, images shown in Figure 5.3) at 6, 7, or 11 days p.i. for HT-29, A549, or DLD1 cells, respectively. Plates were scanned using a GelCount tumour colony counter. Infection at 1 x 10^{-3} VP/well appeared to result in easily discernible plaques under these conditions for all cell lines. A549 cells were selected for

further experiments as easily discernible plaques were seen within a relatively short time period (Figure 5.3A).

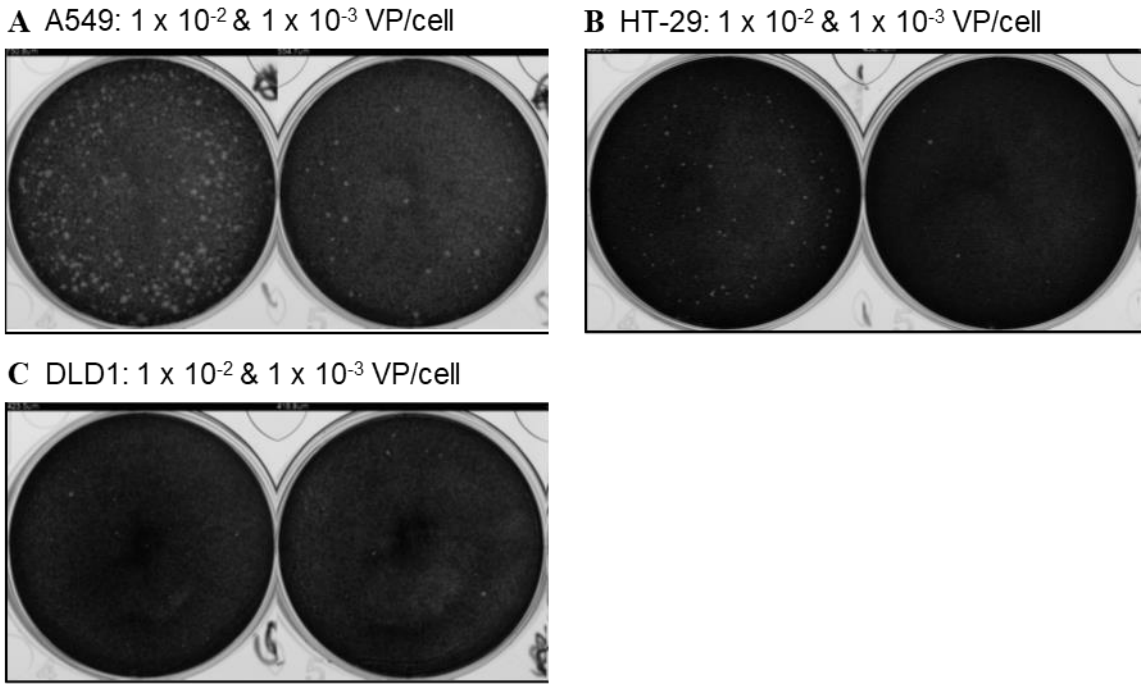


Figure 5.3 EnAd-SA-GFP infection at a dilution of 1 x 10^{-3} VP/cell allows visualisation of a sufficient number of individual virus plaques. (A-C) A549 **(A)**, HT-29 **(B)**, or DLD1 **(C)** cells were seeded into 6-well plates at a density of 1 x 10^{6} cells/well. One (A549 and DLD1) or two (HT-29) days later, EnAd-SA-GFP virus was added at 1:10 serial dilutions ranging from 10 VP/cell to 1 x 10^{-13} VP/cell, or cells were mock-infected. At 3 h p.i. medium was aspirated and 3 mL of a 1% agarose + DMEM + 2% FBS mix carefully layered onto cells. Wells were visually assessed until plaques were readily visible. Wells containing easily discernible plaques were incubated with 300 µL MTT and subsequently visualised on a GelCount. Results for wells infected with 1 x 10^{-2} VP/cell and 1 x 10^{-3} VP/cell shown above.

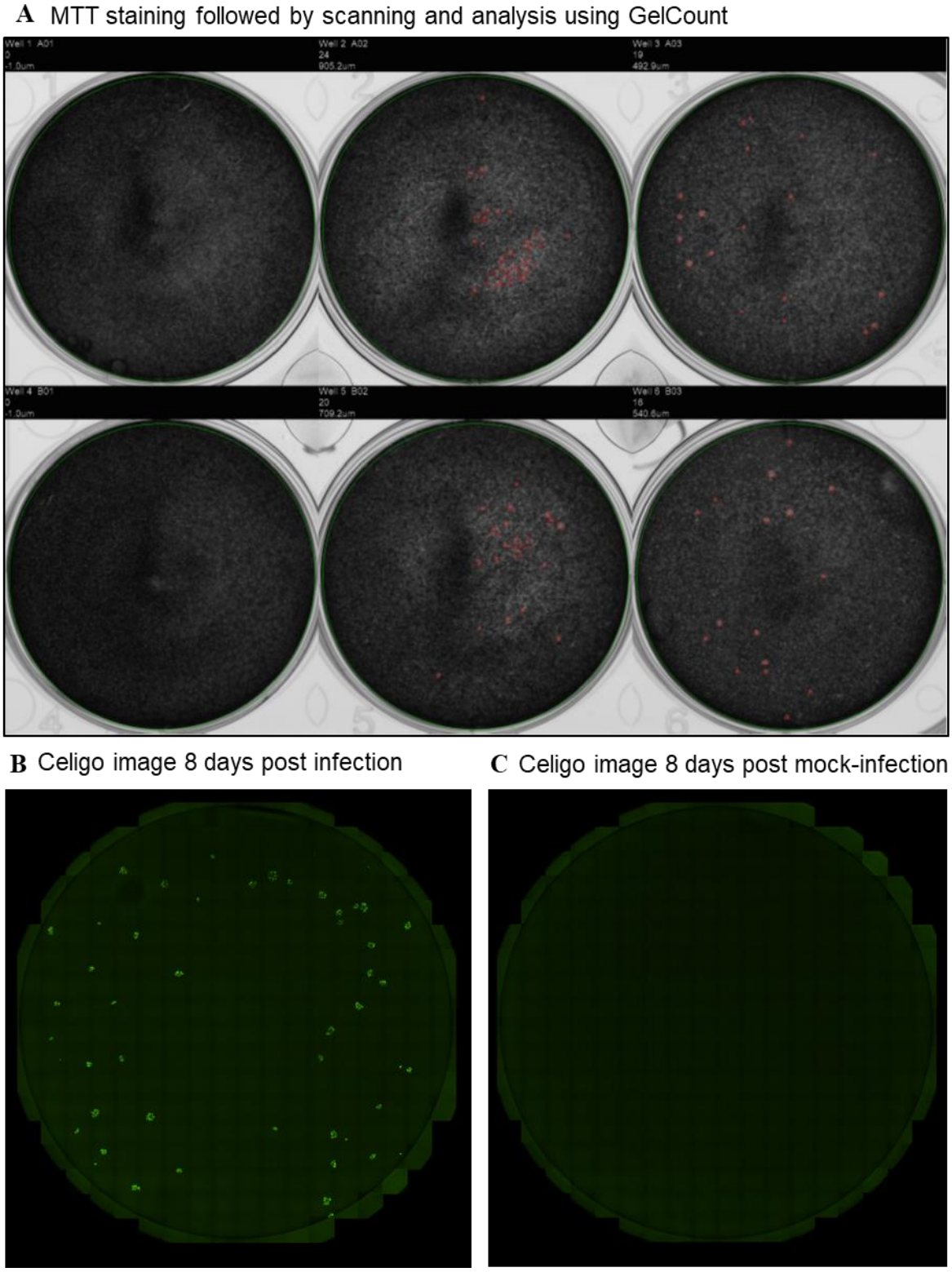


Figure 5.4 Celigo imaging allows improved visualisation of individual plaques and tracking over time. A549 cells were seeded into 6-well plates at a density of 1 x 10^6 cells/well. The next day cells were infected with EnAd-SA-GFP virus at 1 x 10^{-3} VP/cell **(A-B)** or mock-infected **(C)**. At 3 h p.i. medium was aspirated and 3 mL of a 1% agarose + DMEM + 2% FBS mix carefully layered onto cells. **(A)** 300 µL MTT was added to wells A1 and B1 6 days p.i., to wells A2 and B2 8 days p.i. and to wells A3 and B3 10 days p.i. Plate was scanned and plaques identified and analysed using a GelCount. **(B-C)** Plate was scanned daily on the Celigo 6-10 days p.i. – day 8 result shown above.

To establish whether a system allowing serial tracking of plaque area could be developed, we performed parallel experiments to compare plaque detection using MTT staining and GelCount imaging and analysis (Figure 5.4A), versus scanning on the Celigo (Figures 5.4B-C). A549 cells were seeded into 6-well plates at a density of 1 x 10^6 cells/well. The next day, cells were infected with EnAd at a dilution of 1 x 10^{-3} VP/cell, or mock-infected. Medium containing virus was aspirated 3 h p.i. before overlaying cells with 3 mL DMEM + 2% FBS + 1% agarose. As before, plates for GelCount assessment were stained with MTT at 6 days (first column), 8 days (second column) or 10 days (third column) p.i. (Figure 5.4A). In parallel, Celigo test wells were scanned daily from 6-10 days p.i. (Figures 5.4B-C show day 8 result). Detection of fluorescent plaques versus MTT staining allowed monitoring of a single well and individual plaque growth over time, and was less affected by non-plaque artefacts occurring during processing. Scanning on the Celigo was therefore deemed to be a superior technique for monitoring changes in virus plaque size over time compared to MTT staining and imaging using the GelCount tumour colony counter.

5.2.2 Pre-irradiation of cells increases EnAd spread through a cell monolayer

After establishing the optimal cell line, seeding density, virus type, infection dilution, and imaging technique for the modified plaque assay, we focused on identifying the radiation conditions with the greatest impact on plaque growth. A549 cells were seeded into 6-well plates at a density of 1 x 10^6 cells/well. The next day, cells were mock-infected or infected with EnAd-SA-GFP at a dilution of 1 x 10^{-3} VP/cell in triplicate. Medium containing virus was aspirated 3 h p.i. before overlaying cells with 3 mL DMEM + 2% FBS + 1% agarose. At 24 h p.i., plates were mock-irradiated or irradiated at 4 or 6 Gy. Plates were scanned on the Celigo 6, 8, and 10 days p.i. The acquisition settings were adjusted to slightly over-expose the image which allowed inclusion of the dead cells in the centre of the plaque in our total analysis. The percentage of GFP expression within the whole well and the change in

area between time points was calculated. Figure 5.5 shows summary results for three separate repeats, given as mean ± SEM. Though the percentage of GFP-positive area of the well in irradiated versus non-irradiated cells was consistently higher at all time points, this was not significant (Figure 5.5A). There was, however, a significantly lower increase in the percentage of GFP-positive area in the 6 Gy plate between days 6 and 8 compared to the 0 Gy plate (Figure 5.5B), potentially suggestive of decreased rate of plaque growth between these two days in irradiated cells.

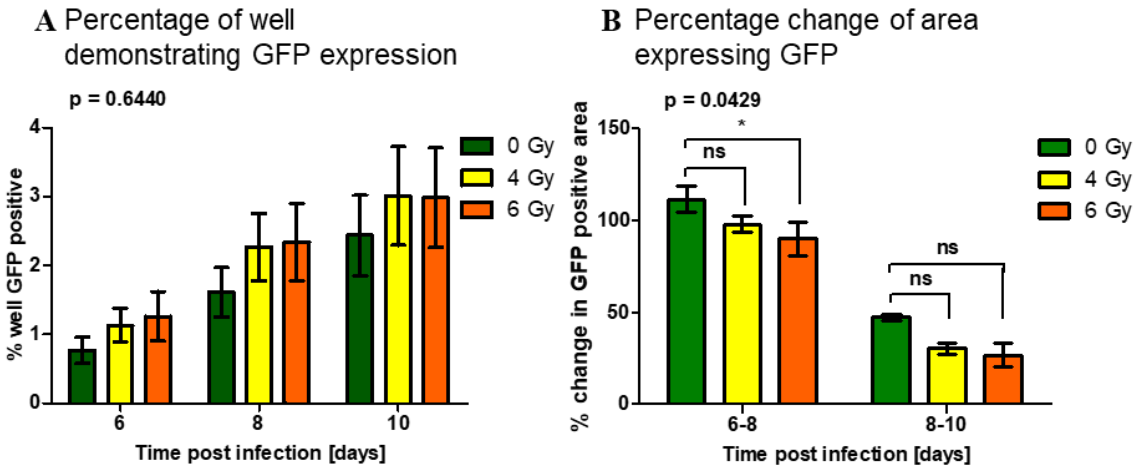


Figure 5.5 Irradiated wells demonstrate a decreased rate of GFP expansion and non-significantly increased GFP coverage compared to non-irradiated wells. A549 cells were seeded into 6-well plates at a density of 1 x 10^6 cells/well. The next day cells were infected with EnAd-SA-GFP virus at 1 x 10^{-3} VP/cell or mock-infected in triplicate. At 3 h p.i. medium was aspirated and 3 mL of a 1% agarose + DMEM + 2% FBS mix carefully layered onto cells. Plates were irradiated at 4 Gy or 6 Gy or mock-irradiated 24 h p.i and scanned 6, 8 and 10 days p.i. **(A)** Percentage of well demonstrating GFP expression. **(B)** Percentage change of area expressing GFP at D8 or D10 p.i, compared to previous image taken. Graphs show mean ± SEM of three separate experiments. Significance was evaluated using two-way ANOVA (p-value given in top left) with Bonferroni post-test (represented by ns or * in graph). ns, not significant; p <0.05, *.

We hypothesised that plaque growth may be maintained in irradiated cells by delivering radiation treatment in fractionated doses. Figure 5.6A demonstrates the resultant experimental timeline. A549 cells were seeded into three 6-well plates at a density of 1 x 10^6 cells/well and the subsequent day mock-infected or infected with 1 x 10^{-3} VP/cell of EnAd-SA-GFP in triplicate. At 3 h p.i. medium was aspirated and 3 mL of DMEM + 2% FBS + 1% agarose was carefully overlaid and allowed to dry. Plates were mock-irradiated or given 2 Gy at 1, 3, and 5 days p.i. (6 Gy/3#), or at 1, 3, 5, 7, and 9 days p.i. (10 Gy/5#). Scanning was carried out using the Celigo at 6, 8, and 10 days p.i. At 8 days p.i., the percentage of well demonstrating GFP expression was significantly higher in irradiated versus non-irradiated cells (Figure 5.7B). Figure 5.7D demonstrates that by 10 days p.i. the majority of plaques had fused together, precluding accurate analysis of plaque growth at this time point.

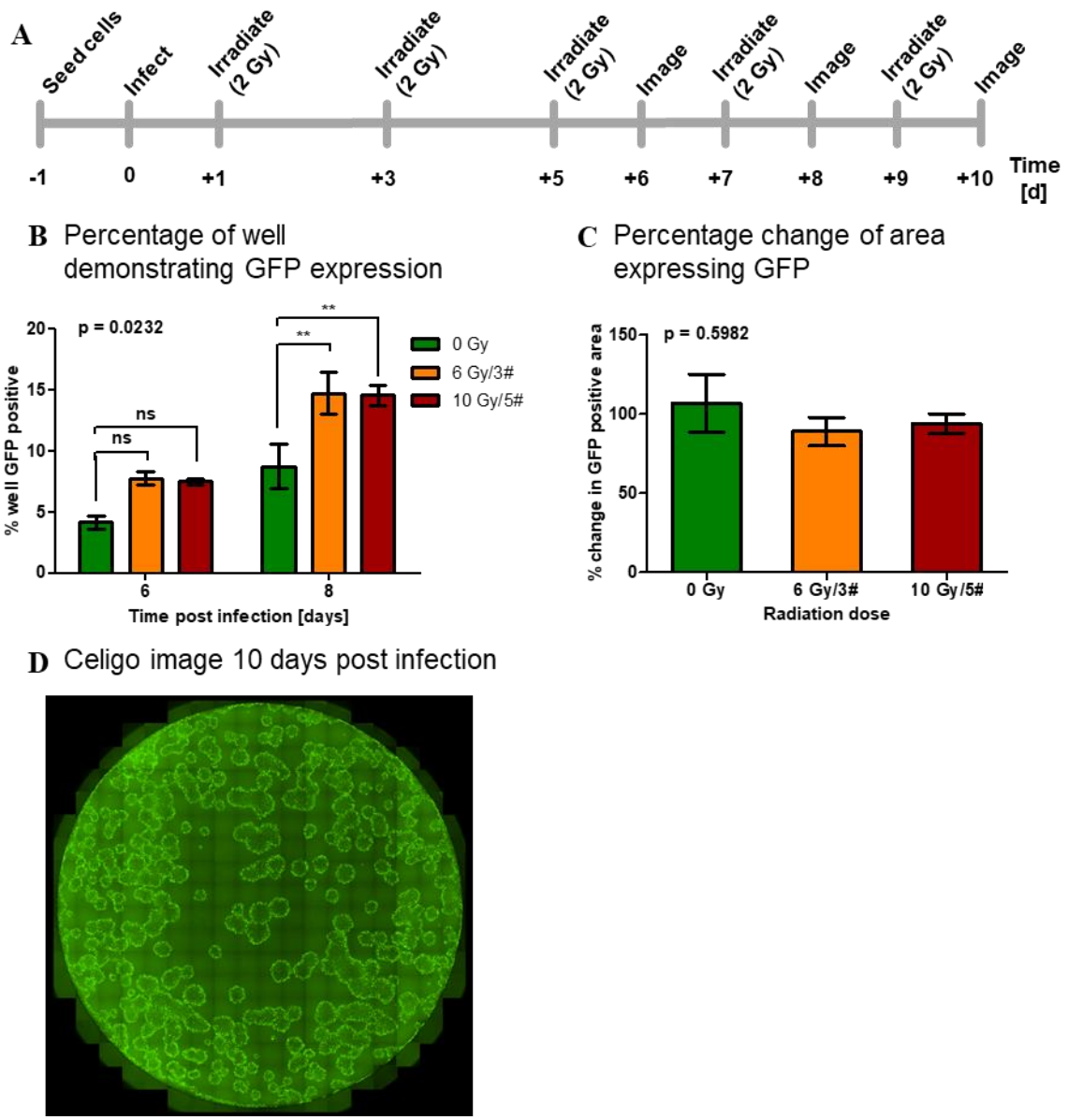


Figure 5.6 GFP coverage is increased in irradiated versus non-irradiated wells. (A) A549 cells were seeded into 6-well plates at a density of 1 x 10^6 cells/well. The next day cells were infected with EnAd-SA-GFP virus at 1 x 10^{-3} VP/cell or mock-infected in triplicate. At 3 h p.i. medium was aspirated and 3 mL of a 1% agarose + DMEM + 2% FBS mix carefully layered onto cells. Plates were mock-irradiated or irradiated at 2 Gy 1, 3, and 5 days p.i. (6 Gy/3#) or 1, 3, 5, 7, and 9 days p.i. (10 Gy/5#). Plates were scanned on the Celigo 6, 8, and 10 days p.i. Due to high plaque density, day 10 time point was unsuitable for analysis. **(B)** Percentage of well demonstrating GFP expression. Significance was evaluated using two-way ANOVA (p-value given in top left) with Bonferroni post-test (represented by ns or ** in graph). ns, not significant; p <0.01, **. **(C)** Percentage change of area expressing GFP at D8 p.i compared to previous image taken. Significance was evaluated using one-way ANOVA (p-value given in top left). Graphs show mean ± SEM of three wells within a single experiment. **(D)** Well representative of plaque density seen 10 days p.i. (10 Gy).

These findings support a model of increased viral spread in irradiated cells, however we hypothesised that the use of fewer virus particles per cell and manual spatial coordinate matching may enable more accurate assessment of radiation effects on plaque growth by tracking individual plaques over time. A549 cells were seeded into three 6-well plates at a density of 1 x 10^6 cells/well and infected with EnAd-SA-GFP at 1 x 10^{-4} VP/cell the next day. To minimise effects of nutrient depletion on plaque growth, wells were overlaid with 4 mL DMEM supplemented with 2% FBS and 1% agarose. Plates were again either mock-irradiated (0 Gy), given three doses of irradiation at 2 Gy/dose (6 Gy/3#), or given five doses at 2 Gy/dose (10 Gy/5#). Figure 5.7A shows image representative of well appearance 10 days p.i., with Figure 5.7B demonstrating the area detected as 'plaque' by the Celigo software. As well as plaque area, Celigo software analysis provided coordinates for each plaque, allowing use of manual spatial coordinate matching to track individual plaque growth over time. Only plaques trackable throughout the period of scanning were included in the analysis (white arrows in Figure 5.7B indicate non-plaque artefacts excluded from analysis). This allowed us to account for the impact of time on the differences seen between different radiation doses. We were also able to track individual plaque growth within this time period without interference from new, smaller plaques. As a trend towards increased plaque size in irradiated versus mock-irradiated cells had already been seen at 6 days p.i. in previous experiments (Figure 5.6A), scanning was commenced at 4 days p.i. to determine how early this trend first becomes apparent. Bonferroni post-test was consistent with a significant increase in mean plaque area in wells receiving 10 Gy/5# of irradiation compared to mock from 8 days p.i. onward. At 10 days p.i., mean plaque area was also significantly larger in wells receiving the lower dose of 6 Gy/3# compared to mock (Figure 5.7C).

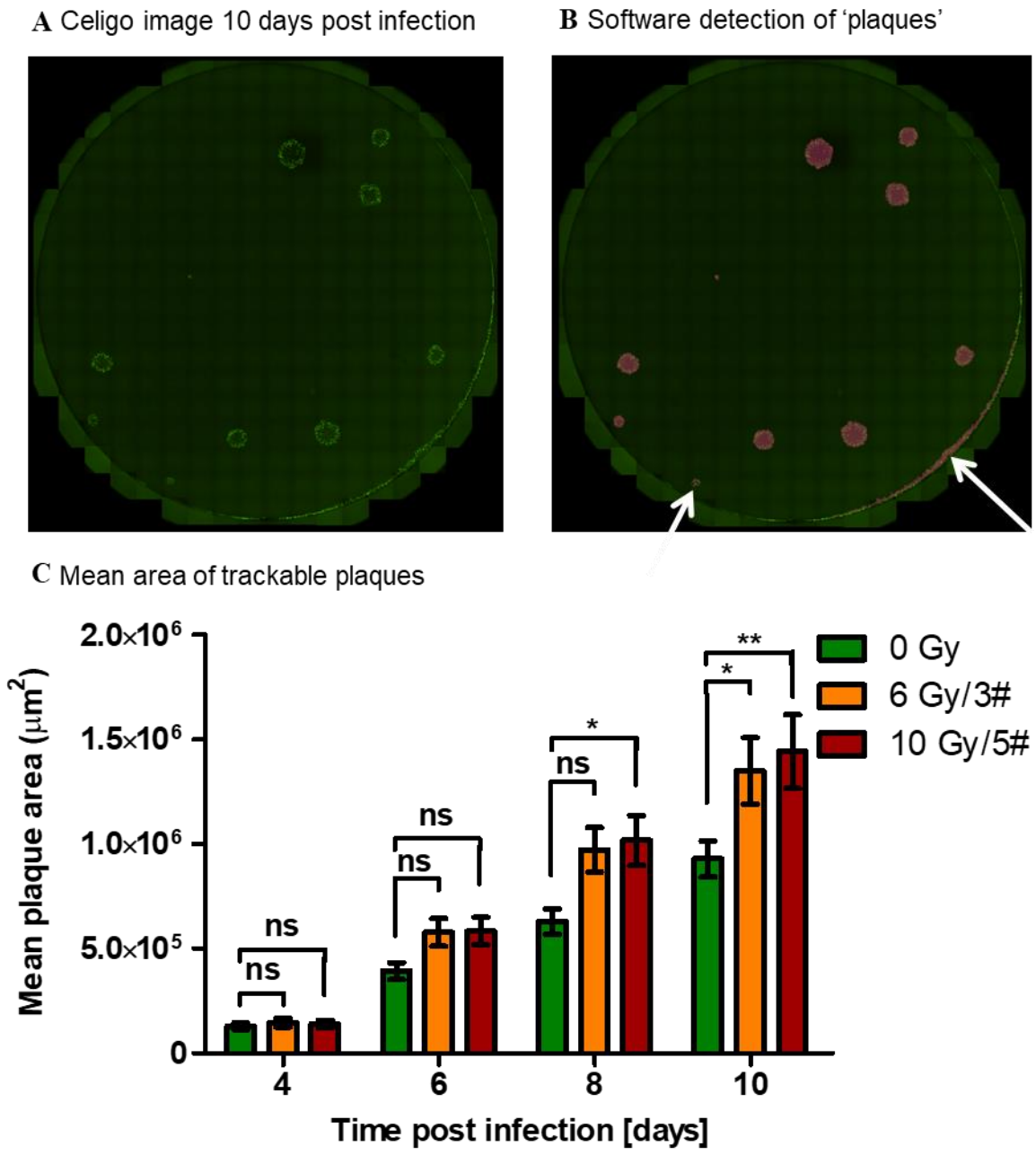


Figure 5.7 Mean plaque area is increased in irradiated versus non-irradiated wells. A549 cells were seeded into 6-well plates at a density of 1 x 10^6 cells/well. The next day cells were infected with EnAd-SA-GFP virus at 1 x 10^{-4} VP/cell or mock-infected in triplicate. At 3 h p.i. medium was aspirated and 4 mL of a 1% agarose + DMEM + 2% FBS mix carefully layered onto cells. Plates were mock-irradiated or irradiated at 2 Gy 1, 3, and 5 days p.i. (6 Gy/3#) or 1, 3, 5, 7, and 9 days p.i. (10 Gy/5#). Plates were scanned on the Celigo 4, 6, 8, and 10 days p.i. Analysis was carried out using Celigo software. **(A)** Well representative of plaques seen 10 days p.i. **(B)** Plaque area detected by Celigo software, non-plaque artefacts manually excluded from analysis highlighted by white arrows. **(C)** Area of all trackable plaques within a single experiment given as mean ± SEM. Significance was evaluated using two-way ANOVA with Bonferroni post-test. ns, not significant; p <0.05, *; p <0.01, **. As interaction between time and radiation dose was significant, post-test results only are shown.

As our results showed that fractionated radiation is associated with increased plaque size as infection progresses, we compared the impact of fractionated radiation versus a single high dose of radiation, given either before or after infection. Five 6-well plates were seeded with A549 cells at a density of 1 x 10^6 cells/well. After 6 h, one plate was irradiated at 10 Gy (10 Gy pre). At 24 h post-irradiation, cells were mock-infected or infected with EnAd-SA-GFP at 1 x 10^{-4} VP/cell in triplicate. At 3 h p.i., medium was aspirated and the monolayer was gently overlaid with 4 mL of DMEM containing 4% FBS and 1% agarose. The plate designated '10 Gy post' was given 10 Gy as a single fraction 24 h p.i. Plates receiving fractionated treatment were given either 2 Gy each at 1, 3, and 5 days p.i. (6 Gy/3#) or 1, 3, 5, 7, and 9 days p.i. (10 Gy/5#). Wells were scanned on the Celigo at 4, 6, 8, and 10 days p.i (Figure 5.8A) and analysed by manual spatial coordinate matching of plaques and two-way ANOVA with Bonferroni post-test. Mean plaque area in pre-irradiated versus non-irradiated cells was significantly larger after 6 days p.i (Figure 5.9B). A trend for increased mean plaque area was also seen in cells irradiated post-infection when compared to mock-irradiated cells.

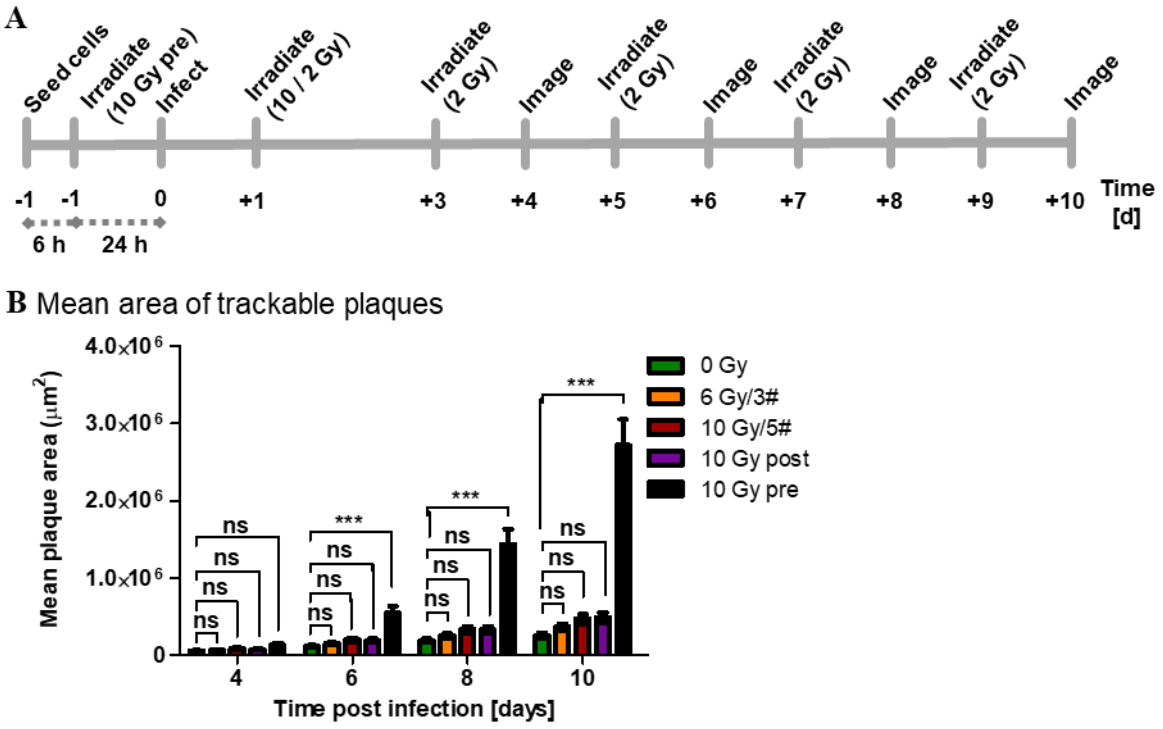


Figure 5.8 Mean plaque area is increased in pre-irradiated versus non-irradiated wells.
(A) Timeline of experiment. A549 cells were seeded into 6-well plates at a density of 1 x 10^6 cells/well. Six hours later one plate was irradiated at 10 Gy (10 Gy pre). At 24 hours post-irradiation cells were infected with EnAd-SA-GFP virus at 1 x 10^{-4} VP/cell or mock-infected in triplicate. At 3 h p.i. medium was aspirated and 4 mL of a 1% agarose + DMEM + 4% FBS mix carefully layered onto cells. At 24 h p.i. plates were mock-irradiated or irradiated at 2 Gy (10 Gy/5# and 6 Gy/3#) or 10 Gy (10 Gy post). Plates requiring fractionated treatment were further given 2 Gy on alternate days. All plates were scanned on the Celigo 4, 6, 8 and 10 days p.i. Analysis was carried out using Celigo software. **(B)** Area of all trackable plaques within a single experiment given as mean ± SEM. Significance was assessed using two-way ANOVA with Bonferroni post-test. ns, not significant; p <0.001, ***. As interaction between time and radiation dose was significant, post-test results only are shown.

During the above experiment we observed that pre-irradiated, infected wells demonstrated a media colour change suggestive of a higher pH compared to wells that were irradiated post-infection or mock-irradiated. Adenovirus has been shown to cause an increase in lactate production and consequent decrease in pH [160]. It is thus surprising that pre-irradiated wells, which demonstrate increased plaque size and therefore adenovirus production, instead displayed a higher pH. One possible explanation for this may be that there is an overall decreased number of cells in the well. If this allows more rapid spread of virus through the cell monolayer, this decreased cell density may also partly explain the larger plaque sizes at later time points. We hypothesised that early cell death after high doses of irradiation may

decrease the apparent seeding density at the time of virus infection and spread, which may partly explain why plaques in pre-irradiated wells increased more rapidly compared to the other conditions, and could account for a higher pH in these wells.

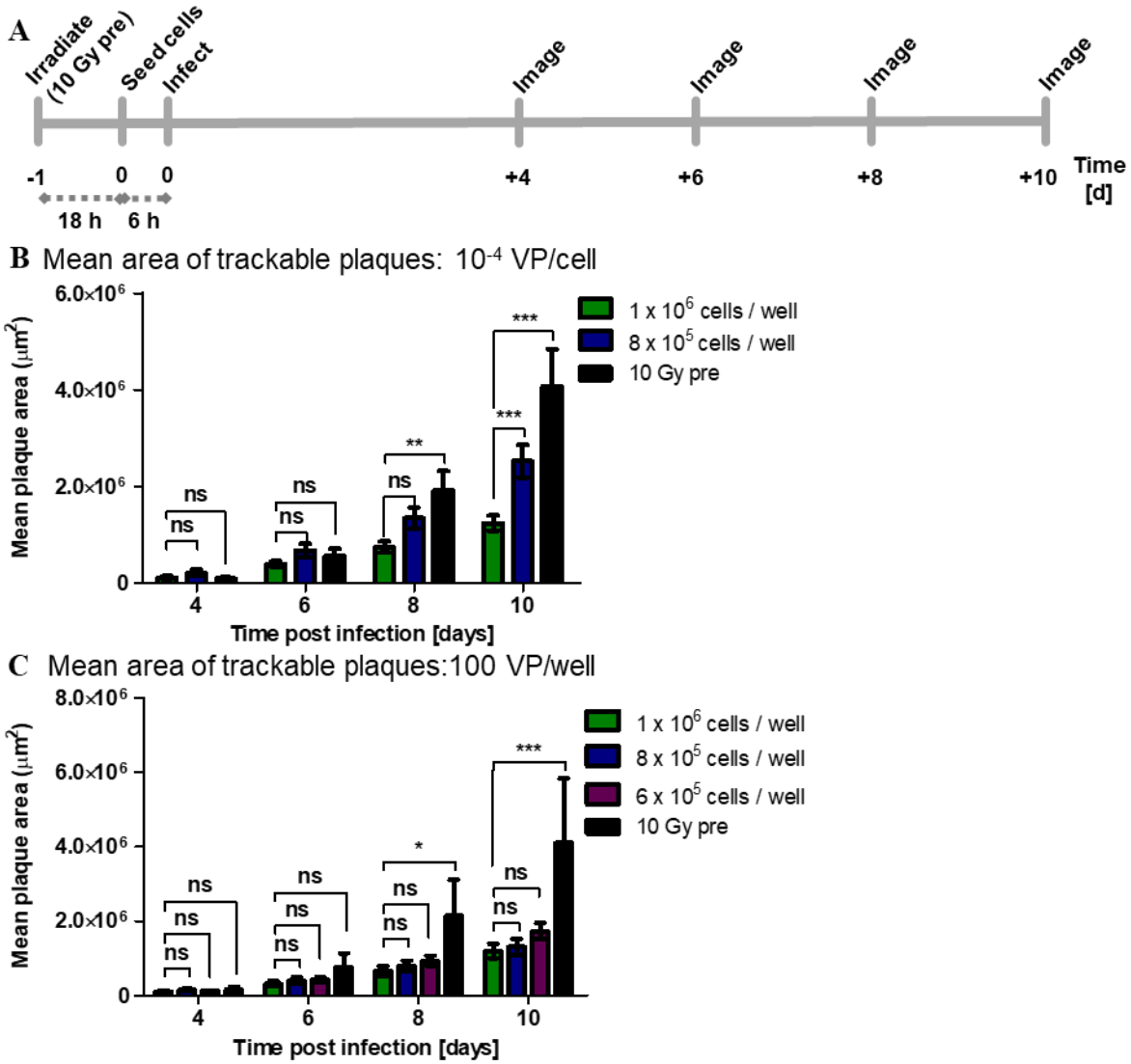


Figure 5.9 Mean plaque area is increased in lower density seeded wells. (A) Timeline of experiment. A549 cells were pre-irradiated at 10 Gy or non-irradiated. 18 hours later pre-irradiated cells were seeded into 6-well plates at a density of 1 x 10^6 cells/well. Non-irradiated cells were seeded at a density of 1 x 10^6 cells/well, 8 x 10^5 cells/well or 6 x 10^5 cells/well. Six hours later plates were infected with EnAd-SA-GFP virus or mock-infected in triplicate. At 3 h p.i. medium was aspirated and 4 mL of a 1% agarose + DMEM + 2% FBS mix carefully layered onto cells. All plates were scanned on the Celigo 4, 6, 8, and 10 days p.i. Analysis was carried out using Celigo software. **(B)** Infection was carried out at 10^{-4} VP/cell. Area of all trackable plaques is given as mean ± SEM from a single experiment. Too few plaques were seen in the 6 x 10^5 cells/well condition to allow analysis. **(C)** Infection was carried out at 100 VP/well (equivalent to 1 x 10^{-4} VP/cell for wells containing 1 x 10^6 cells). Area of all trackable plaques within a single experiment is given as mean ± SEM. Significance was assessed using two-way ANOVA with Bonferroni post-test. ns, not significant; p <0.05, *; p <0.01, **; p <0.001, ***. As interaction between time and radiation dose was significant, post-test results only are shown.

To assess whether the increased plaque size seen in pre-irradiated cells could partly be due to decreased cell density, an experiment was designed to investigate plaque growth at variable seeding densities (Figure 5.9). To minimise the potential effect of early cell death after high-dose radiation, A549 cells were either irradiated at 10 Gy or left non-irradiated before seeding into 6-well plates 18 h later at a density of 1 x 10^6 (irradiated and non-irradiated cells), 8 x 10^5 or 6 x 10^5 cells/well (non-irradiated cells only). Cell viability when counting was confirmed by trypan blue staining. Wells were assessed at 6 h post-seeding for adequate cell adhesion and infected with EnAd-SA-GFP or mock-infected in triplicate. At 3 h p.i., medium was aspirated and cells were overlaid with 4 mL of DMEM + 2% FBS + 1% agarose. Wells were imaged on the Celigo 4, 6, 8, and 10 days p.i. (Figure 5.9A) and analysed using Celigo software. Significance was assessed using two-way ANOVA with Bonferroni post-test, comparing mean plaque area in non-irradiated cells seeded at 1 x 10^6 cells/well ('standard seeding density') to all other conditions. A seeding density of 6 x 10^5 cells/well was too low to allow plaque detection at 4 days p.i with 10^{-4} VP/cell (Figure 5.9B). There was a significant increase in mean plaque area in pre-irradiated cells compared to non-irradiated cells at the standard seeding density, though this was seen only at 8 and 10 days p.i. Interestingly, mean plaque area also increased at 10 days p.i. in wells seeded at 8 x 10^5 cells/well compared to plaques at standard seeding density, suggesting the increase in mean plaque area seen in irradiated versus non-irradiated cells may partly be due to decreased density of the cell monolayer (Figure 5.9B).

To best mimic the conditions of our standard plaque assay, in which each well is assumed to contain 1 x 10^6 cells, a repeat was carried out using a virus amount equivalent to 1 x 10^{-4} VP/cell adjusted to standard seeding density (100 VP/well). At this level of infection, some plaques were visible in wells seeded at a density of 6 x 10^5 cells/well at 4 days p.i., allowing analysis of mean plaque growth (Figure 5.9C). A trend of larger mean plaque area at later

time points was seen in wells seeded at a lower density, supporting the hypothesis that this may partly explain the increase in mean plaque area seen in irradiated versus non-irradiated wells. Mean plaque area significantly increased at later time points in pre-irradiated cells compared to that seen in non-irradiated wells at standard seeding density.

To minimise the potential effect of high doses of radiation on early cell death, the experimental timeline was modified (Figure 5.10A). An optimised experiment was therefore conducted comparing plaque growth, as a model for virus spread, between cells receiving no irradiation, fractionated treatment, or a single high dose of radiation pre- or post-infection, to confirm the condition under which virus spread is optimally augmented. Flasks containing A549 cells were irradiated at 10 Gy (10 Gy pre) or left non-irradiated. At 18 h post-irradiation, cells were seeded into 6-well plates at a density of 1 x 10^6 cells/well. Six hours later, wells were assessed for cell adhesion and infected with EnAd-SA-GFP at 1 x 10^{-4} VP/cell in quadruplicate, with a single well in each plate mock-infected. At 3 h p.i., medium was aspirated and cells were overlaid with 4mL DMEM supplemented with 2% FBS and 1% agarose. Plates were subsequently treated with 10 Gy in a single fraction 24 h p.i. (10 Gy post); 2 Gy at 1, 3, and 5 days p.i. (6 Gy/3#); or 2 Gy at 1, 3, 5, 7, and 9 days p.i. (10 Gy/5#). One plate was mock-irradiated at 1, 3, 5, 7, and 9 days p.i (0 Gy). Plates were imaged at 4, 6, 8, and 10 days p.i. and analysed using Celigo software, manual spatial coordinate matching and two-way ANOVA with Bonferroni post-test. A significant increase was seen in the mean area of plaques in wells treated with 10 Gy compared to mock-irradiated wells at 8 and 10 days p.i. (Figure 5.10B), irrespective of the timing or mode of radiation. As above, the largest plaques were seen in pre-irradiated cells. These results are consistent with previous experiments and suggestive of maximal augmentation of EnAd plaque growth *in vitro* when radiation is given in a single high dose 24 h prior to infection.

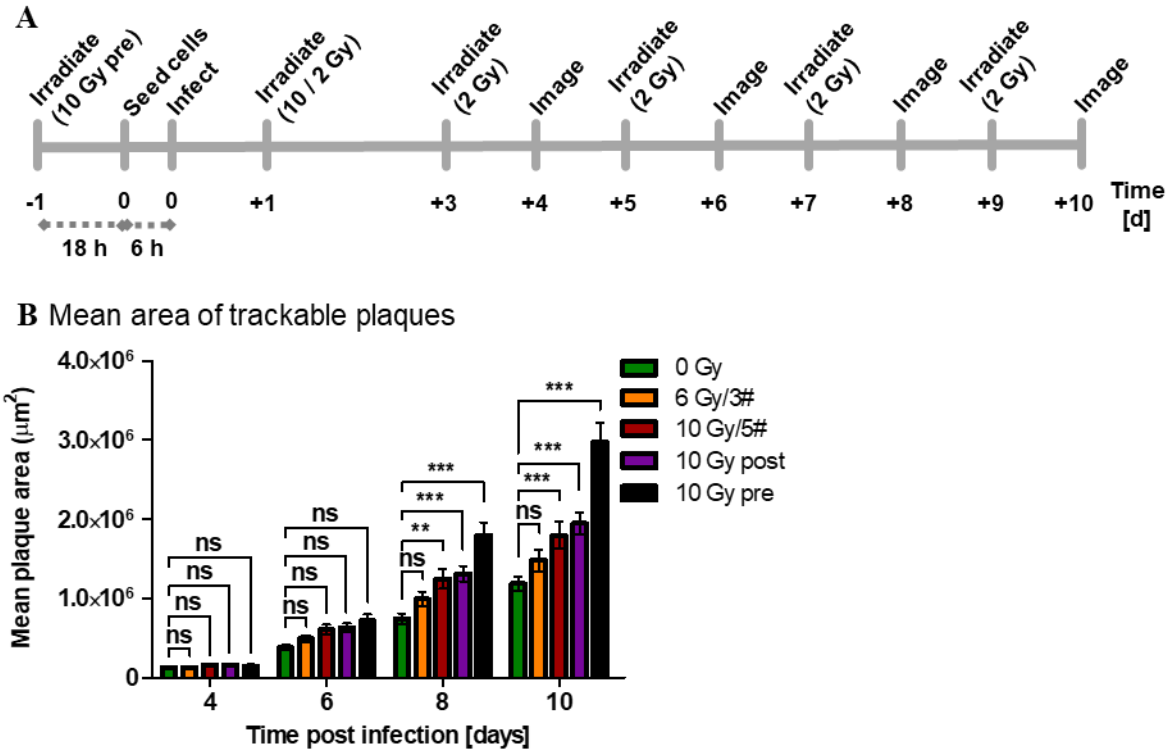


Figure 5.10 Mean plaque area is increased in irradiated versus non-irradiated wells.
(A) Timeline of experiment. A549 cells were pre-irradiated at 10 Gy or left non-irradiated and 18 hours later cells were seeded into 6-well plates at a density of 1 x 10^6 cells/well. Six hours later plates were infected with EnAd-SA-GFP virus at 1 x 10^{-4} VP/cell in quadruplicate. A single well in each plate was mock-infected. At 3 h p.i. medium was aspirated and 4 mL of a 1% agarose + DMEM + 2% FBS mix carefully layered onto cells. At 24 h p.i. plates were mock-irradiated or irradiated at 10 Gy (10 Gy post) or 2 Gy (10 Gy/5# and 6 Gy/3#). 10 Gy/5# and 6 Gy/3# were given a further 2 Gy at 3 and 5 days p.i., 10 Gy/5# was also irradiated at 2 Gy 7 and 9 days p.i. All plates were scanned on the Celigo 4, 6, 8, and 10 days p.i. Analysis was carried out using Celigo software. **(B)** Area of all plaques continuously available for analysis throughout scanning period given as mean ± SEM. Single experiment representative of two repeats is shown. Significance was assessed using two-way ANOVA with Bonferroni post-testing. ns, not significant; p <0.01, **; p <0.001, ***. As interaction between time and radiation dose was significant, post-test results only are shown.

5.2.3 In vitro cytotoxicity of EnAd and radiation combination treatment

Though the modified plaque assay allows us to study virus spread through a cell monolayer in irradiated versus non-irradiated cells, it cannot differentiate whether increased spread is a result of increased virus production or synergistic cytotoxicity. The xCELLigence real-time cell analysis system allows label-free measurement of electrical impedance as a proxy for cell attachment, proliferation and death. The base of the plate is coated with gold

microelectrodes and attachment of cells to the base masks these electrodes and impedes the flow of electricity through the well, giving a quantitative measure of relative cellular adherence.

A pilot experiment was designed to assess the rate of cytotoxicity in A549 cells treated with or without radiation or EnAd. Cells were irradiated at 10 Gy or mock-irradiated and seeded into xCELLigence wells 8 h later. At 24 h post-irradiation, cells were mock-infected or infected with EnAd-SA-GFP at an MOI of 0.1 in quadruplicate. Cell index was monitored for approximately 10 days from the start of the experiment. The maximum cell index for each experimental condition was determined to normalise readings as a fraction of the maximum and allow comparison between conditions (Figure 5.11). We observed accelerated cell death in infected, irradiated cells compared to all other conditions, indicating that the combination of infection and radiation does not impact negatively on cytotoxicity. However, we could not determine whether this was a synergistic or additive effect.

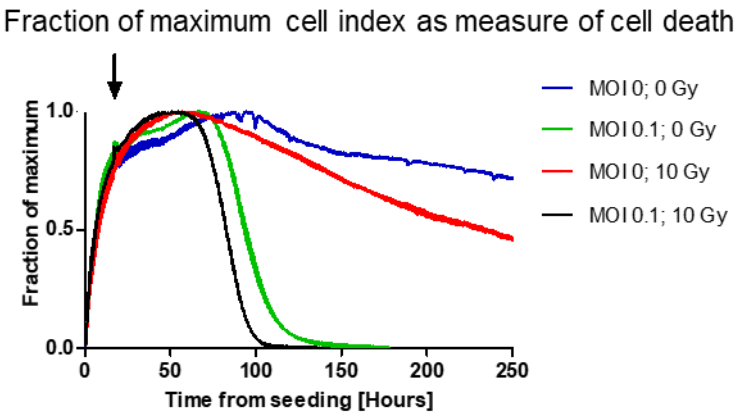


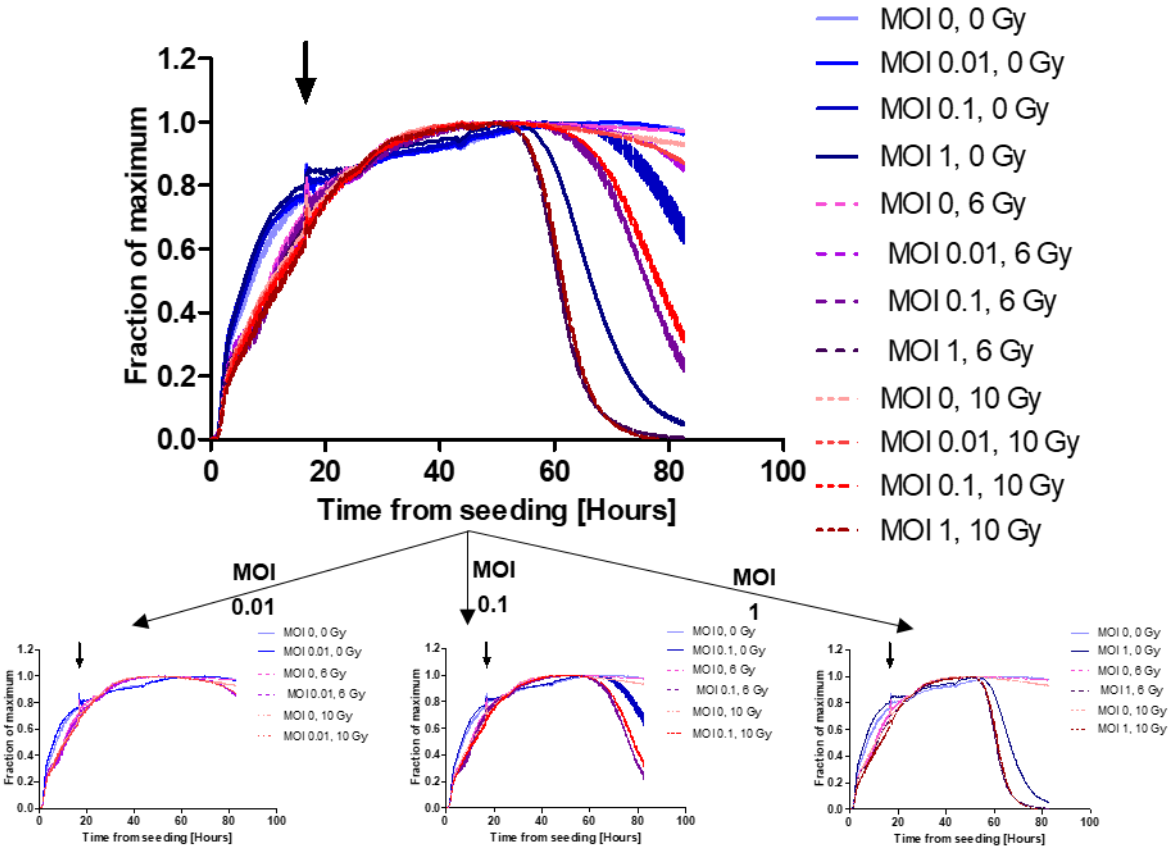
Figure 5.11 xCELLigence can be utilised to track cell death following irradiation ± EnAd infection. A549 cells were irradiated at 10 Gy or mock irradiated. Eight hours later eight wells of pre-irradiated and eight wells of non-irradiated cells were seeded at 2 x 10^4 cells/well. At 24 hours post-irradiation cells were either mock-infected or infected with EnAd-SA-GFP at an MOI of 0.1 (arrow). All conditions were plated in quadruplicate and electrical impendence measured as a model of cell death. Graph shows mean ± SEM of each recording given as a fraction of maximum cell index.

5.2.4 Early cytotoxicity in infected, irradiated cells in vitro suggests synergy between EnAd and radiation

To assess for potential synergy and evaluate the relationship between cytotoxicity, EnAd and radiation at different doses, a more extensive experimental set up was needed. A549 cells were mock-irradiated or irradiated at 6 or 10 Gy and seeded into xCELLigence wells 8 h post-irradiation. At 24 h post-irradiation, cells were mock-infected or infected with EnAd-SA-GFP at MOI 0.01, 0.1, or 1 in quadruplicate. Due to equipment failure, the experiment was terminated much earlier than planned (66 h p.i.). No appreciable difference was seen in virus-associated cytotoxicity between 6 and 10 Gy at this early time point (Figure 5.12A) and thus 2 and 6 Gy treatment was used in further experiments. Infected cells irradiated with 2 and 6 Gy showed increasing cytotoxicity with increasing radiation doses (Figure 5.12B). Cytotoxicity in infected cells irradiated at 6 Gy was greater than cytotoxicity in mock-irradiated cells infected with 10 x fewer infectious virus particles. Furthermore, during the time frame of this experiment there was a comparable level of cytotoxicity in mock-infected cells irradiated at 2 Gy or mock-irradiated. The addition of virus, however, lead to accelerated cytotoxicity in 2 Gy-irradiated versus mock-irradiated cells. This accelerated cytotoxicity of infected cells at near sub-therapeutic doses of radiation would be more suggestive of a synergistic, versus additive, effect on cell death.

To confirm this, Bliss independence analysis was conducted comparing observed and expected cytotoxicity of all dose combinations tested. Statistically significant Bliss synergy was seen at later time points in all treatment combinations. Synergistic cytotoxicity occurred at earlier time points when higher MOI and radiation doses were used.

A Fraction of maximum cell index as measure of cell death: 0 Gy, 6 Gy, 10 Gy



B Fraction of maximum cell index as measure of cell death: 0 Gy, 2 Gy, 6 Gy

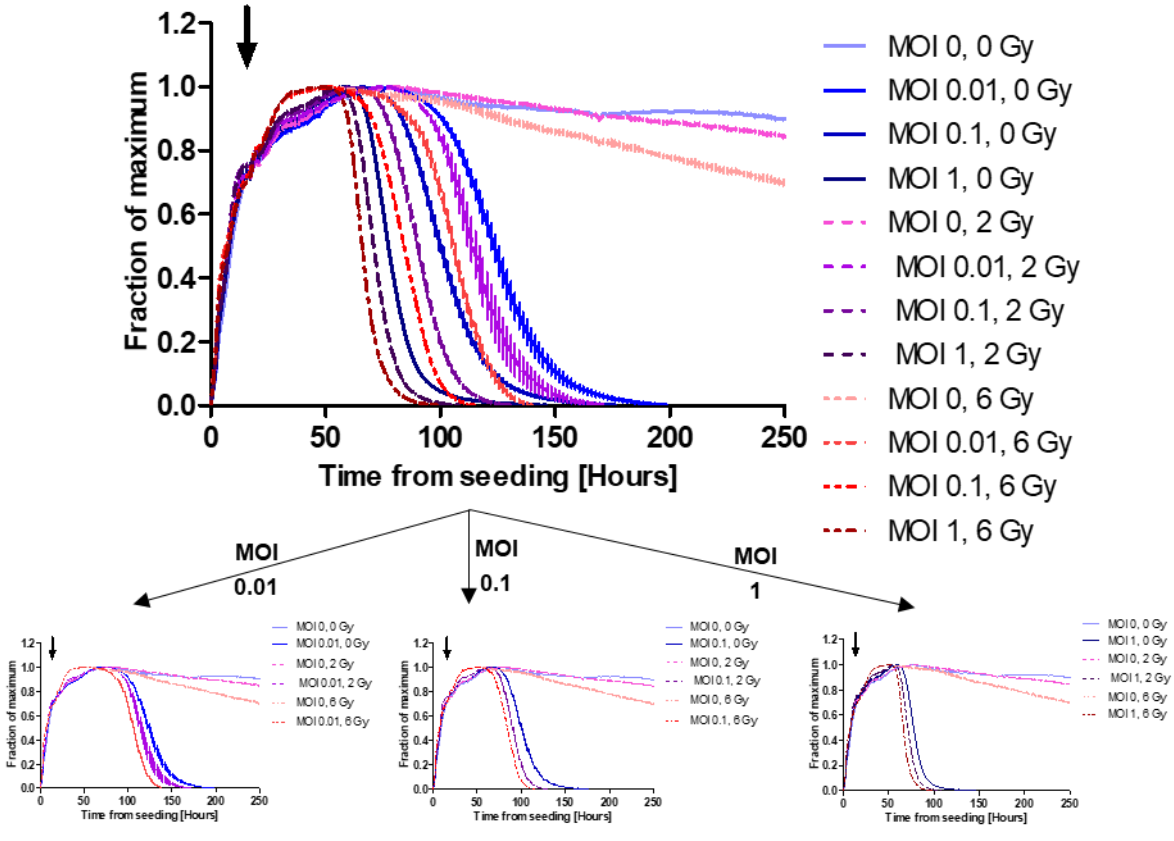


Figure 5.12 Radiation augments virus-induced cytotoxicity in a dose-dependent manner. (A-B) A549 cells were mock-irradiated or irradiated at 6 or 10 Gy **(A)**, or 2 or 6 Gy **(B)**. Eight hours later cells were seeded at 2 x 10^4 cells/well. At 24 hours post-irradiation cells were either mock-infected or infected with EnAd-SA-GFP at an MOI of 0.01, 0.1, or 1 (arrow). All conditions were plated in quadruplicate and electrical impendence measured as a model of cell death. Outer wells were excluded from analysis. Graphs show mean ± SEM of three wells given as a fraction of maximum cell index for all experimental conditions above and for individual dilutions and monotherapy below.

5.2.5 Intravenous Enadenotucirev administration results in tumour growth delay and increased survival in mice receiving a single dose of radiation

As discussed in the previous chapter, utilisation of SCID mice in a model investigating combination EnAd and radiation treatment resulted in early weight loss requiring nutritional support. A further pilot experiment was therefore required to establish the effect of these two treatments in a different mouse model prior to a larger tumour growth delay study. SCID mice are radiosensitive [161]; athymic nude mice were therefore chosen as an alternative immunosuppressed strain. HCT116 cells (2 x 10^6 cells/mouse) were injected subcutaneously into eight athymic nude mice and tumours monitored until they reached a pre-determined volume of 50 mm^3. At this stage, paired randomisation was conducted and mice given three intravenous injections of either 50 μL PBS or 0.5 x 10^{10} VP of EnAd-Fluc 48 h apart (Figure 5.13A). One day after the final injection, all animals received 10 Gy of radiation. The timeline of this treatment schedule was developed based on the clinical trial model and has been shown to lead to a significant increase in virus production both *in vitro* and *in vivo* (Chapter 4). Weight was closely monitored immediately following treatment. Unlike results seen with SCID mice, no concerning loss was seen with this mouse model (results not shown).Tumour volume and animal weight were monitored regularly until a tumour volume of 500 mm^3 was reached, at which point animals were sacrificed. Effective randomisation was achieved with regards to tumour starting size (Figure 5.13B) and days from tumour cell injection to first dose of treatment (Figure 5.13C). We therefore proceeded to survival analysis.

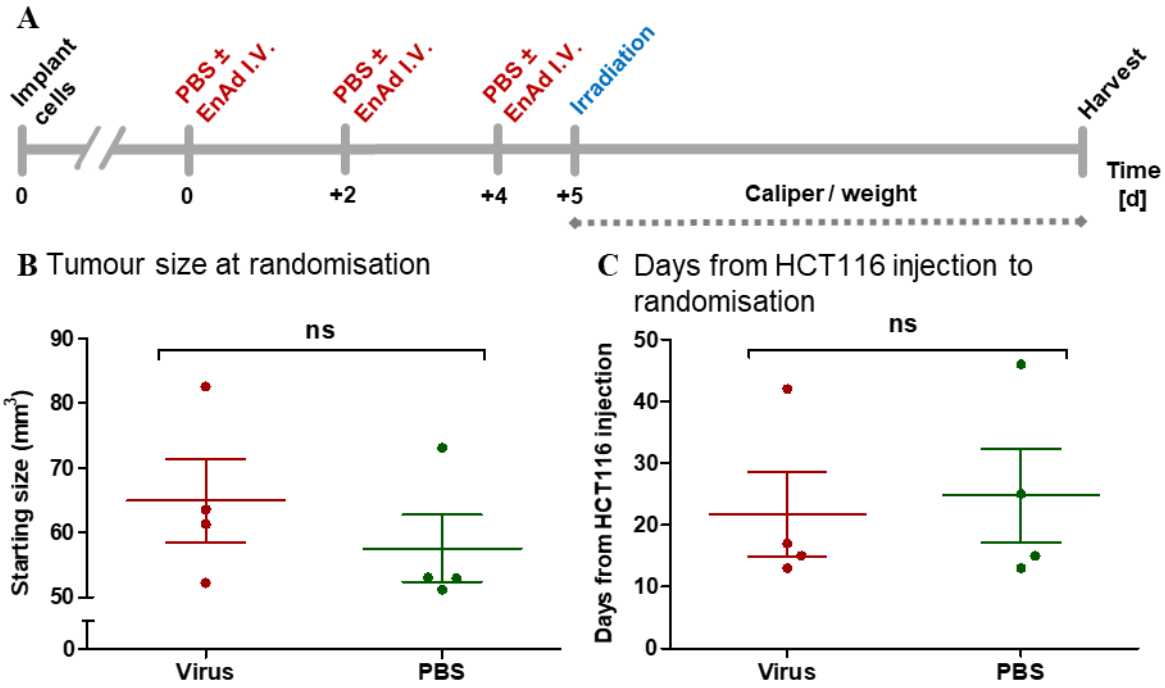


Figure 5.13 Effective randomisation was achieved in a pilot in vivo experiment.
(A) Schematic illustrating experimental timeline. HCT116 cells were injected s.c. into eight athymic nude mice (2 x 10^6 cells/mouse). Tumours were monitored until they reached a volume of 50 mm^3 at which point mice were randomised and four were given three i.v. injections of EnAd SA-Fluc (0.5 x 10^{10} VP/mouse) 48 hours apart, whereas four were given 50 µL PBS i.v. 48 hours apart. All animals received 10 Gy of radiation to the tumour 1 day post final dose. Animal weight and tumour volume was monitored until a tumour volume of 500 mm^3 was reached, at which point animals were sacrificed. **(B-C)** Starting tumour size **(B)** and days from HCT116 injection **(C)** were analysed in both groups to assess for effective randomisation. Graphs are shown as mean ± SEM. Significance was assessed using Mann-Whitney test.

Published data shows there is variable impact of EnAd monotherapy on DLD1, A549 or HT-29 tumour models [110, 124, 159]. A pilot experiment was therefore designed to see if any difference was seen in tumour growth delay in PBS- versus EnAd-treated, irradiated HCT116 xenografts. Only these two treatment conditions were utilised in the first instance to allow use of a small number of animals in this new model, and to provide guidance on whether a further, larger experiment was worth pursuing. A significant difference was seen between the group treated with PBS and radiation and the group treated with EnAd and radiation (Figure 5.14). This was assessed by calculating time from start of treatment to death (Figure 5.14A) and percent survival using log-rank test (Figure 5.14B). One animal

survived for markedly longer than the other mice in either treatment group. Even when this potential outlier was excluded from analysis, a significant difference between the two groups was maintained (results not shown). These results were consistent with a significant tumour growth delay in mice irradiated following treatment with EnAd versus PBS, when radiation was given as a single large dose 24 h after the final EnAd injection.

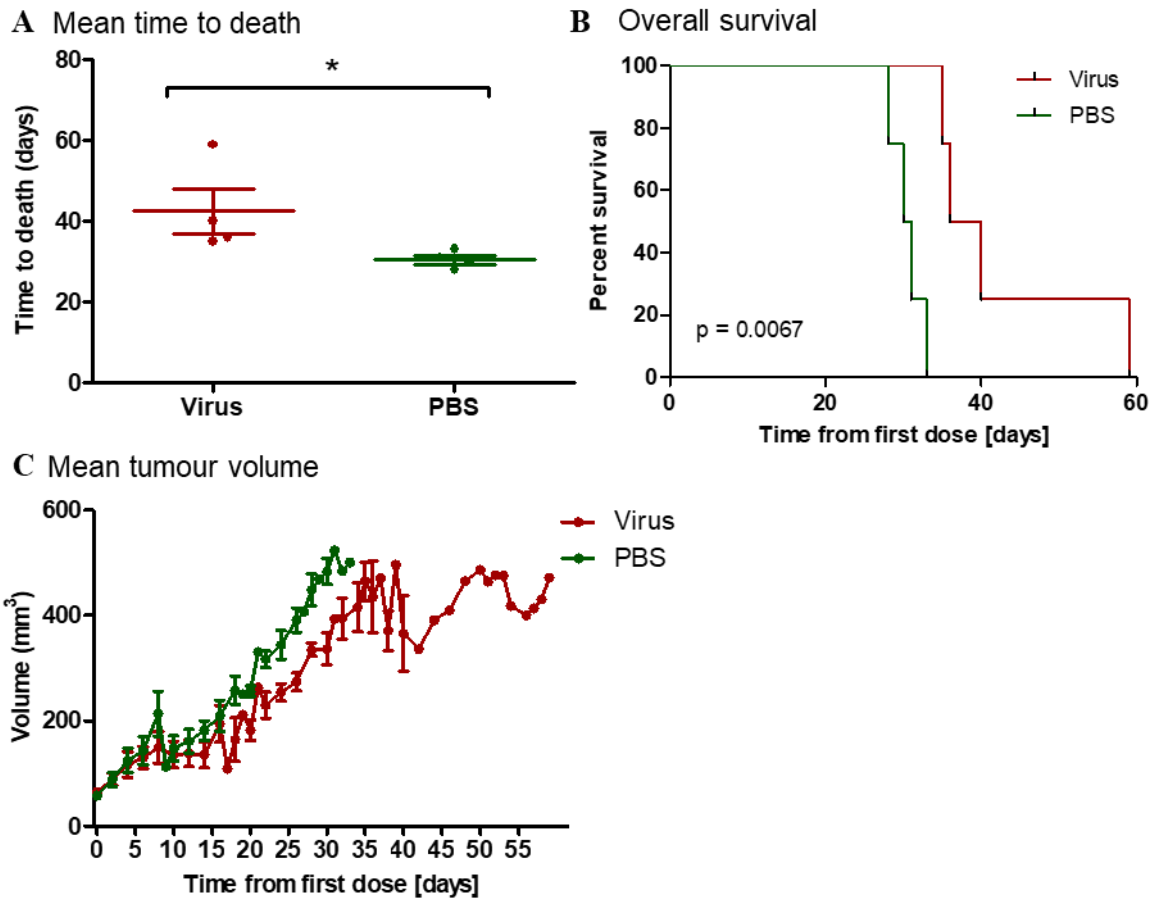


Figure 5.14 Pilot in vivo experiment is consistent with small but significant tumour growth delay. HCT116 cells were injected s.c. into eight athymic nude mice (2 x 10^6 cells/mouse). Tumours were monitored until they reached a volume of 50 mm^3 at which point mice were randomised and four were given three i.v. injections of EnAd SA-Fluc (0.5 x 10^{10} VP/mouse) 48 hours apart, whereas four were given 50 µL PBS i.v. 48 hours apart. One day post final dose, all animals received 10 Gy of radiation to the tumour. Animal weight and tumour volume was monitored until a tumour volume of 500 mm^3 was reached, at which point animals were sacrificed. **(A)** Time to death given as mean ± SEM. Significance was assessed using Mann-Whitney test. $p < 0.05$, *. **(B)** Survival curves showing survival of animals in both groups. Significance was assessed using log-rank test. **(C)** Raw data for tumour growth curve of both groups. Graph shows mean ± SEM for duration of experiment.

5.3 Chapter main findings

This chapter describes the development of an assay to assess the impact of radiation on virus spread. This is a modification of the standard plaque assay technique commonly used to quantify infectious virus particle concentration. Serial monitoring of fluorescent virus spread through a cell monolayer using Celigo was deemed to be the superior of two imaging techniques in assessing plaque size under different experimental conditions.

The results here presented are consistent with maximally augmented virus spread through a monolayer of A549 cells when these are irradiated at a dose of 10 Gy one day prior to infection. Furthermore, synergistic cytotoxicity was demonstrated in A549 cells infected one day post treatment with radiation. A pilot *in vivo* experiment was consistent with a significant increase in survival in mice treated with EnAd and 10 Gy of radiation versus radiation alone.

5.4 Chapter discussion

There are a number of challenges inherent in assessing for radiosensitisation or synergy using a replication-competent adenovirus which causes rapid *in vitro* cytotoxicity. The use of low MOIs, whilst allowing sufficient time to observe changes in radiosensitisation, may lead to these effects being missed as they would only be apparent in the small fraction of cells undergoing infection. Groups such as Toth *et al.* have acknowledged this limitation and developed alternative techniques to assess for treatment synergy, such as the 'vector spread assay', which determines cell death at different virus dilutions in the presence and absence of radiation [95]. We formed the hypothesis that, if a plaque assay is reliant on virus spread through a monolayer in two dimensions only, plaque growth could be tracked to assess the impact of different radiation doses on virus spread and cytotoxicity. Whilst this would not differentiate between additive and synergistic action, it would establish whether

radiation had a negative or positive impact on virus-induced cytotoxicity. In addition, it may allow determination of the radiotherapy dose/fractionation regime which demonstrates the greatest benefit in augmenting plaque spread.

This hypothesis was tested using two different imaging techniques: adding MTT to identify viable cells and scanning on a GelCount tumour colony counter, or serial scanning on a Celigo. Though both allowed assessment of mean plaque size at different times post infection, measurement with the Celigo allowed tracking of individual plaques throughout the experimental time course. However, the optimisation of analysis settings, manual serial coordinate matching and exclusion of non-plaque artefacts detected by the software were time-consuming. Though an algorithm can be developed to process this data, this may not exclude plaques which are limited in their growth by the well edge, or which appear to shrink due to central cell loss.

The benefit of lower, fractionated doses versus a single higher dose of radiation on virus spread and cytotoxicity was explored using the modified plaque assay. Multiple fractions of treatment on different days were anticipated to have a greater effect on plaque growth as the probability of an irradiated cell also being infected would be higher. Surprisingly, though plaque size in irradiated wells was consistently larger than in non-irradiated wells, particularly at later time points, a marginally greater effect was seen when cells were given a single high dose of radiation. Furthermore, the greatest effect was seen with radiation given 24 hours prior to infection.

The results seen in the last two chapters suggest the interaction between radiation and virus is dose-dependent. One of the potential reasons for a greater effect seen with a single dose of 10 Gy compared with 10 Gy/5# is that the former equates to a greater biologically effective dose. In addition, the impact of a ‘threshold’ dose of radiation on activation of three

prime repair exonuclease 1 (TREX1) and the cyclic GMP-AMP synthase/stimulator of IFN genes (cGAS/STING) pathway has now been determined [162]. It is therefore not unreasonable to hypothesise that 10 Gy may exceed another cellular pathway threshold favouring improved virus propagation and virus-induced cytotoxicity which is not reached by multiple individual doses of 2 Gy. It must be noted that the cGAS-STING pathway is also a major mediator of the cellular innate antivirus response in a number of cell lines [163]; however Lam and Falck-Pedersen have shown it is not activated in A549 cells by infection with group B adenoviruses [164].

Neither of these potential hypotheses explain why pre-irradiated cells demonstrate such a dramatic plaque size increase compared to cells irradiated post-infection. Chapter 4 shows that an increase in EnAd receptor expression in A549 cells has no impact on uptake. Pre-irradiation with 10 Gy, however, does markedly increase E1A expression compared to non-irradiated cells. Arguably, 10 Gy of irradiation given 24 hours prior to infection would lead to an intracellular environment more permissive of virus replication for one extra day (equivalent to one extra replication cycle) compared to the same dose given 24 hours post-infection. It would however be difficult to see how only one additional viral replication cycle would lead to such a dramatic effect on plaque size. Shah and Shea demonstrated that inducing cellular DNA breaks using etoposide or bleomycin led to sequestration of MRN at cellular DNA breaks and rescued genome replication of Ad5 ΔE1B 55k/ΔE4orf3 constructs [68]. If EnAd-induced DDR suppression is imperfect, as argued in Chapter 3, sequestration of the DDR proteins away from replicating viral genomes and to cellular dsDNA breaks during the initial cycle of replication may provide a greater-than-expected benefit to viral spread, especially at an early stage when MOI is very low.

The modified plaque assay demonstrates improved virus spread through a cell monolayer, but does not allow a direct measure of synergistic versus additive cytotoxicity. The xCELLigence system allows direct, ongoing estimation of cell cytotoxicity through measurement of electrical impedance in real-time. An initial pilot experiment suggested improved cytotoxicity in pre-irradiated, infected cells compared to monotherapy. A follow-up experiment demonstrated that, in the absence of virus infection, 2 Gy resulted in similar cytotoxicity to mock-irradiation during the experimental time period. The addition of EnAd however lead to a clear increase in cytotoxicity in 2 Gy- versus mock-irradiated cells, suggesting that there is synergy between radiation and EnAd infection. This was confirmed by Bliss independence analysis of the data normalised to a fraction of maximum cell index.

Ganesh *et al.* have previously argued that a delay in tumour growth seen with a combination of oncolytic virotherapy and radiation/cisplatin in their research was additive, not synergistic, as no increase in virus production was observed as would be expected in a synergistic relationship [99]. Certainly, an enhancement of virus production would be more likely to result in synergistic cytotoxicity, however this statement assumes that neither treatment negatively impacts on the cell death pathways activated by the other treatment. The results presented here demonstrate that EnAd particle production and spread increase in the presence of radiation, and that combined EnAd and radiation treatment lead to synergistic cytotoxicity *in vitro* in A549 cells. The next step in exploring this would be to validate this in other cell lines and virus doses.

Despite dramatic cytotoxicity results *in vitro*, EnAd has performed variably in *in vivo* models investigating tumour growth delay following infection. Tedcastle *et al.* found no significant difference in DLD1 xenograft tumour volume between mice treated with PBS and EnAd, though low doses were given to specifically mimic poor delivery [159]. Conversely, Kuhn

et al. demonstrated a significant dose-dependent decrease in tumour burden in EnAd-treated animals compared to animals treated with buffer, ONYX-015 or Ad11p in a liver metastasis xenograft model [110]. Survival was also significantly improved in EnAd-treated mice compared to untreated controls in subcutaneous and orthotopic A549 mouse models [124].

Strategies such as arming EnAd with matrix-degrading enzymes to improve viral spread have previously been explored as potential mechanisms to enhance cytotoxicity *in vivo* [159]. This chapter investigated whether radiation given post EnAd infection led to improved survival and tumour growth delay in an HCT116 mouse model when compared to radiation and PBS. There was a significant increase in survival and decrease in tumour growth using combination treatment compared to radiotherapy alone. However, as a small pilot study, only two treatment groups were included. A complete study should investigate differences in tumour growth delay between six groups: PBS only, EnAd only, PBS or EnAd followed by 10 Gy of radiation administered 24 h after the final dose of EnAd, and 10 Gy of treatment followed by PBS or EnAd. Furthermore, all treatments and measurements were conducted by a single researcher. Though measurements were periodically confirmed with a secondary, blinded investigator, the potential impact of subconscious bias cannot be excluded. A further study is therefore warranted to determine whether the effect of radiation on EnAd *in vivo* is additive or synergistic.

Chapter 6: Discussion

6.1 Summary of findings

We demonstrated a synergistic effect using EnAd and radiation combination therapy *in vitro*, and confirmed radiosensitisation when infection was followed by a single high dose of radiation *in vivo*. In exploring the underlying mechanisms, we showed that radiation 24 h p.i. lead to an increase in both total and infectious virus particle production, both *in vitro* and *in vivo*. Despite an increase in the expression of cellular receptors for group B adenoviruses, no associated increase in virus uptake was seen to account for our findings. Instead, pre-irradiation lead to a marked increase in the expression of the radiosensitising viral protein E1A, a key activator of early viral promoter transcription [39]. Radiosensitisation was likely further due to adenovirus-mediated inhibition of dsDNA damage repair, one of the radiobiological factors which determines tumour response to fractionated radiation treatment [5]. We showed that both EnAd and Ad5 infection resulted in reduced 53BP1 and RAD51 foci formation following IR, without an associated decrease in total protein levels. Finally, we refined a well-known technique for quantifying infectious VP to enable monitoring of viral spread through a cell monolayer.

6.2 General discussion and future directions

This thesis expands upon previous work in the field focusing primarily on Ad5-based viral vectors, and upon the work of Forrester *et al.* who showed that different serotypes interact differently with the DDR [58]. Experiments were generally structured to allow expression of all viral proteins prior to assessing impact on IR-mediated DDR pathways. Nevertheless we propose that EnAd-mediated DDR inhibition is likely due to early viral proteins, given this is the primary mechanism in Ad5 [94] and would act to inhibit repair pathways before the replicating dsDNA viral genome is exposed to cellular proteins.

Differing interactions between early virus proteins and the DDR, in particular the activation of MRN/53BP1/ATM, may partially explain the varying effects IR has on the replication of different serotypes. Further, an imperfect or incomplete inhibition of members of the MRN/53BP1/ATM complex would be consistent with a number of our findings, such as the significant increase in 53BP1 foci formation in non-irradiated, adenovirus-infected cells (Figures 3.8F, H). Incomplete inhibition of the DDR may further explain the finding of significantly increased 53BP1 foci formation in weakly GFP-positive, Ad5 infected cells at 2 h post-irradiation when strongly GFP-positive cells at this time demonstrated decreased foci formation (Figure 3.8B). Whilst E4orf4 is known to inhibit the phosphorylation of ATM substrates, including 53BP1, ATM deficiency nonetheless further improves virus replication compared to WT cells in samples infected with mutant Ad5 deficient in all E4 genes except E4orf4 [66]. This is suggestive of an imperfect inhibition of this aspect of the pathway by E4orf4 alone, which may become more pronounced at early or lower levels of virus infection.

One of the mechanisms by which IR enhances EnAd replication may be the sequestering of incompletely-inhibited DDR pathway members away from viral genomes and towards cellular dsDNA breaks. Indeed, sequestration of MRN away from viral genomes to sites of drug-induced DNA damage has been demonstrated by Shah *et al.*, who found this rescued replication of Ad5 vectors lacking E1B-55K and E4orf3 [68]. Of note, use of these drugs did not impact on WT Ad5 production in A549 cells, which is in keeping with our finding that irradiation had no significant effect on Ad5 production in this cell line. The authors linked the inhibited viral replication of these mutant Ad5 vectors to localised MRN-ATM activation. Forrester *et al.* have demonstrated that the impact of adenovirus infection on Mre11 varies between serotypes [58], whilst we showed that 53BP1, which interacts with both MRN and ATM [165], is phosphorylated following infection with the group B

adenoviruses EnAd and Ad11p, but not by Ad5 (Figures 3.9-3.11). 53BP1 acts to amplify the MRN-mediated activation of ATM in response to dsDNA breaks particularly in conditions where functional MRN is limited [165], such as would be the case in Ad5-infected cells. Inhibition of this complex is clearly a key part of the Ad5 replication cycle, as Ad5 also interacts with this part of the pathway through the E4orf4-mediated inhibition of the phosphorylation of a number of ATM/ATR substrates, including 53BP1, as discussed above [66]. The interaction between the MRN/53BP1/ATM complex and the group C serotype Ad5 therefore varies on a number of levels to that demonstrated with the group B adenoviruses EnAd and Ad11, and we propose this difference may be one of the mechanisms underlying the different impact IR has on virus function and replication.

To expand further on the findings that IR leads to increased EnAd VP production in A549 cells (Figure 4.4), our group recently published data comparing the impact of IR on Ad5, EnAd, and Ad11p in three different cell lines – A549, HCT116, and DLD1 [166]. This confirmed a significant increase in EnAd production in irradiated, versus mock-irradiated, A549 cells, but not in the other cell lines or with the other viruses. Rather, a significant decrease was observed in irradiated, Ad5-infected HCT116 cells, despite increased E1A expression in this cell line in pre-irradiated versus non-irradiated samples (Figure 4.15B). Further, no significant increase was seen in EnAd-infected irradiated HCT116 cells when compared to mock. This was a particularly unexpected finding, as pre-irradiated HCT116 cells demonstrated increased EnAd E1A expression compared to non-irradiated samples (Figures 4.14B, D), and *in vivo,* irradiation enhanced EnAd transgene expression, VP production and infectious particle production in HCT116 xenografts (Figure 4.7). This apparently conflicting result may be due to the differing radiobiological factors between cell culture and the 3D model, with the latter acting to amplify the effects of IR/EnAd combination treatment.

We propose above that the variable impact of IR on virus production may be due to differences in the interaction between DDR pathways and distinct adenovirus serotypes. We further hypothesise that the different effects of IR on adenovirus production in different tumour cell lines may be due to variation in the underlying DNA damage repair pathways, in particular mismatch repair [166]. The presence of microsatellite instability in HCT116 and DLD1 cells [167] may thus negate the benefit of enhanced E1A expression through an increase in the error rate of viral genome replication.

A link between DNA damage repair and virus activity following irradiation was also proposed by Hingorani *et* al., who connected this to an effect on the MAPK pathway [158]. The use of MAPK/ERK and PI3K inhibitors reduced the IR-mediated increase in transgene expression seen in cells infected with non-replicating Ad-CMV-GFP vectors. The paper does not give information on the mutation status of E1A in the non-replicating viral vectors, however this is commonly deleted in replication-deficient vectors [168]. Regardless, transfection with a reporter construct expressing GFP under control of the Egr-1 promoter gave similar results of DDR inhibitor-mediated enhancement of GFP expression in irradiated cells [158], this mechanism is therefore not reliant on E1A expression. Nonetheless, there is some overlap between E1A and the MAPK pathway which may partially account for the results seen by our group. *Egr1* transcription is activated through the interaction of ELK1, regulated by MAPK, and MED23 [169]. MED23 interaction with E1A conserved region 3 also acts to stimulate increased transcription [46]. Whilst the mechanisms driving increased E1A expression and upregulation of the MAPK pathway in response to IR remain unclear, both result in a cellular environment which favours a higher level of transcription, putatively leading to increased activation of viral promoters and increased viral activity.

EnAd was bioselected on a colorectal cancer cell line [110], and is currently undergoing phase 1 trials in patients with locally advanced rectal cancer to assess safety and tolerability when combined with chemoradiotherapy [115]. There are however a number of other tumour types in which radiotherapy is one of the standard treatment modalities, and in which treatment with a tumour-targeted radiosensitising agent may benefit patient outcomes. In particular, lung cancer, despite being one of the commonest types of malignancy, nevertheless remains a disease associated with a relatively low 5-year survival. In recent years, immunotherapy has become a standard treatment modality for non-small cell lung cancer. EnAd causes immunogenic cell death [114] and may therefore provide added benefit to treatment with radiation and/or checkpoint inhibitors in this tumour type. We have demonstrated cytotoxic synergy *in vitro* when the lung cancer cell line A549 is treated with IR and EnAd (Figure 5.12), and Marino *et al.* have shown a significant increase in survival in mice bearing subcutaneous and orthotopic A549 tumours treated with EnAd or transgene-expressing EnAd-based vectors when compared to untreated controls [124]. Of particular benefit is that EnAd can be administered intravenously to patients and does not rely on intratumoural administration to reach the tumour target, potentially allowing its use in the treatment of metastatic disease. The Mechanism of Action phase 1 study primarily focused on investigating EnAd delivery to colorectal tumours, however two patients with non-small cell lung cancer were included in the trial and tumour samples from both demonstrated EnAd DNA following intravenous administration [113].

There may also be some benefit in combining radiation with "armed" EnAd expressing transgenes, which can be locally enhanced by IR. Most recently, EnAd constructs modified to express bi- or tri-valent T-cell engagers targeted to the tumour microenvironment have shown promising results *in vitro* and *ex vivo* [91-93]. These have been specifically developed to deplete immunosuppressive tumour-associated fibroblasts [92] or macrophages [93], and

to stimulate an anti-tumour T cell-mediated response [91]. A fine balance exists between the immunostimulatory and immunoinhibitory impact of radiation [170]; combination treatment with these constructs may shift this away from the latter and promote a favourable anti-tumour immune response following radiotherapy.

Limitations of this study primarily relate to the sole use of A549 cells in many of the experiments presented. This cell line was specifically selected to provide a relatively radioresistant model [171] with which to assess for virus-mediated radiosensitisation. In addition, A549 cells formed an even monolayer and easily discernible virus plaques during the optimisation phase of the modified plaque assay (Figure 5.3). Variations in the impact of IR both on the expression of the early viral gene E1A (Figure 4.15) and on virus particle production [166] in different cell lines have been demonstrated, however. The interpretation of our findings must therefore be limited to the cell lines in which these experiments were conducted.

In vivo, a pilot experiment was designed to assess for potential radiosensitisation in HCT116 xenografts receiving combination EnAd and radiation treatment. Whilst radiosensitisation was confirmed, a larger experiment would be required as the next step to further assess for synergy. Further, the experimental timeline was designed to allow virus-mediated inhibition of the DDR prior to treatment with radiation, and to mirror virus dosing schedules in phase 1 clinical trials using EnAd [113, 172]. The greatest effect of radiation on EnAd plaque spread through a cell monolayer, however, was seen when a single high dose was given 24 h prior to infection (Figures 5.8 and 5.10). Irradiation of cells prior to EnAd infection was also shown to result in treatment synergy (Figure 5.12) and in enhanced expression of the radiosensitising virus protein E1A (Figure 4.14). Ideally, a follow up *in vivo* experiment would comprise six treatment groups to assess both for treatment synergy, and for the treatment order which results in greatest tumour growth delay – PBS only, EnAd only,

radiation followed by PBS, radiation followed by EnAd, PBS followed by radiation, and EnAd followed by radiation.

6.3 Concluding remarks

The Chemoradiation with Enadenotucirev as a Radiosensitiser in locally Advanced Rectal cancer (CEDAR) trial, a prospective phase 1 trial to assess the safety and tolerability of combination EnAd and chemoradiotherapy treatment in locally advanced rectal cancer, is currently recruiting patients [115]. The data here presented provide a mechanistic background to the effect that may be anticipated from EnAd/radiation combination treatment. Patients in the CEDAR trial will be treated with 50Gy in 25 fractions; we demonstrate synergy *in vitro* when EnAd is combined with 2 Gy of radiation (Figure 5.12), corresponding to the daily dose which will be given in the trial. Further, we show that pre-irradiation of HCT116 and A549 cells leads to increased expression of the radiosensitising viral protein E1A (Figures 4.14-4.15) [156, 157], and that a high single dose of radiation *in vivo* is associated with a radiosensitising effect of EnAd on HCT116 xenograft treatment (Figure 5.14). The results of this work therefore further justify the CEDAR trial and are also consistent with a potential benefit in the palliative setting, where the use of single high doses of radiation is common practice.

BIBLIOGRAPHY

1. Prise, K.M., et al., *New insights on cell death from radiation exposure.* Lancet Oncol, 2005. **6**(7): p. 520-8.
2. Joiner, M. and A. Van Der Kogel, *Basic clinical radiobiology*. 2009, London: Edward Arnold.
3. Hall, E.J. and A.J. Giaccia, *Radiobiology for the Radiologist*. 2011, Philadelphia, UNITED STATES: Wolters Kluwer Health.
4. Eriksson, D. and T. Stigbrand, *Radiation-induced cell death mechanisms.* Tumour Biol, 2010. **31**(4): p. 363-72.
5. Withers, H.R., *The Four R's of Radiotherapy*, in *Advances in Radiation Biology*, J.T. Lett and H. Adler, Editors. 1975, Elsevier. p. 241-271.
6. Steel, G.G., T.J. McMillan, and J.H. Peacock, *The 5Rs of Radiobiology.* International Journal of Radiation Biology, 1989. **56**(6): p. 1045-1048.
7. Moynahan, M.E. and M. Jasin, *Mitotic homologous recombination maintains genomic stability and suppresses tumorigenesis.* Nat Rev Mol Cell Biol, 2010. **11**(3): p. 196-207.
8. Lieber, M.R., *The mechanism of double-strand DNA break repair by the nonhomologous DNA end-joining pathway.* Annu Rev Biochem, 2010. **79**: p. 181-211.
9. McVey, M. and S.E. Lee, *MMEJ repair of double-strand breaks (director's cut): deleted sequences and alternative endings.* Trends Genet, 2008. **24**(11): p. 529-38.
10. Ciccia, A. and S.J. Elledge, *The DNA damage response: making it safe to play with knives.* Mol Cell, 2010. **40**(2): p. 179-204.
11. Aravind, L. and E.V. Koonin, *Prokaryotic homologs of the eukaryotic DNA-end-binding protein Ku, novel domains in the Ku protein and prediction of a prokaryotic double-strand break repair system.* Genome Res, 2001. **11**(8): p. 1365-74.
12. Gu, J. and M.R. Lieber, *Mechanistic flexibility as a conserved theme across 3 billion years of nonhomologous DNA end-joining.* Genes Dev, 2008. **22**(4): p. 411-5.
13. Doherty, A.J., S.P. Jackson, and G.R. Weller, *Identification of bacterial homologues of the Ku DNA repair proteins.* FEBS Lett, 2001. **500**(3): p. 186-8.
14. Connelly, J.C. and D.R. Leach, *Tethering on the brink: the evolutionarily conserved Mre11-Rad50 complex.* Trends Biochem Sci, 2002. **27**(8): p. 410-8.
15. Rocha, E.P., E. Cornet, and B. Michel, *Comparative and evolutionary analysis of the bacterial homologous recombination systems.* PLoS Genet, 2005. **1**(2): p. e15.
16. Shrivastav, M., L.P. De Haro, and J.A. Nickoloff, *Regulation of DNA double-strand break repair pathway choice.* Cell Research, 2008. **18**(1): p. 134-147.
17. Polo, S.E. and S.P. Jackson, *Dynamics of DNA damage response proteins at DNA breaks: a focus on protein modifications.* Genes Dev, 2011. **25**(5): p. 409-33.
18. Bernstein, K.A. and R. Rothstein, *At Loose Ends: Resecting a Double-Strand Break.* Cell, 2009. **137**(5): p. 807-810.
19. Branzei, D. and M. Foiani, *Regulation of DNA repair throughout the cell cycle.* Nat Rev Mol Cell Biol, 2008. **9**(4): p. 297-308.
20. Liu, J., et al., *Human BRCA2 protein promotes RAD51 filament formation on RPA-covered single-stranded DNA.* Nat Struct Mol Biol, 2010. **17**(10): p. 1260-2.
21. Zhang, F., et al., *PALB2 links BRCA1 and BRCA2 in the DNA-damage response.* Curr Biol, 2009. **19**(6): p. 524-9.
22. West, S.C., *Molecular views of recombination proteins and their control.* Nat Rev Mol Cell Biol, 2003. **4**(6): p. 435-45.
23. San Filippo, J., P. Sung, and H. Klein, *Mechanism of eukaryotic homologous recombination.* Annu Rev Biochem, 2008. **77**: p. 229-57.
24. Pannunzio, N.R., G. Watanabe, and M.R. Lieber, *Nonhomologous DNA end-joining for repair of DNA double-strand breaks.* J Biol Chem, 2018. **293**(27): p. 10512-10523.

25. Panier, S. and S.J. Boulton, *Double-strand break repair: 53BP1 comes into focus.* Nature Reviews Molecular Cell Biology, 2014. **15**(1): p. 7-18.
26. Chapman, J.R., et al., *RIF1 is essential for 53BP1-dependent nonhomologous end joining and suppression of DNA double-strand break resection.* Mol Cell, 2013. **49**(5): p. 858-71.
27. Chapman, J.R., et al., *BRCA1-associated exclusion of 53BP1 from DNA damage sites underlies temporal control of DNA repair.* J Cell Sci, 2012. **125**(Pt 15): p. 3529-34.
28. Isono, M., et al., *BRCA1 Directs the Repair Pathway to Homologous Recombination by Promoting 53BP1 Dephosphorylation.* Cell Reports, 2017. **18**(2): p. 520-532.
29. Chaurushiya, M.S. and M.D. Weitzman, *Viral manipulation of DNA repair and cell cycle checkpoints.* DNA Repair (Amst), 2009. **8**(9): p. 1166-76.
30. Chang, H.H.Y., et al., *Non-homologous DNA end joining and alternative pathways to double-strand break repair.* Nat Rev Mol Cell Biol, 2017. **18**(8): p. 495-506.
31. Pol, J., G. Kroemer, and L. Galluzzi, *First oncolytic virus approved for melanoma immunotherapy.* Oncoimmunology, 2016. **5**(1): p. e1115641.
32. Moore, A.E., *The destructive effect of the virus of Russian Far East encephalitis on the transplantable mouse sarcoma 180.* Cancer, 1949. **2**(3): p. 525-34.
33. Seymour, L.W. and K.D. Fisher, *Oncolytic viruses: finally delivering.* Br J Cancer, 2016. **114**(4): p. 357-61.
34. Kaufman, H.L., F.J. Kohlhapp, and A. Zloza, *Oncolytic viruses: a new class of immunotherapy drugs.* Nat Rev Drug Discov, 2015. **14**(9): p. 642-62.
35. Lilley, C.E., R.A. Schwartz, and M.D. Weitzman, *Using or abusing: viruses and the cellular DNA damage response.* Trends Microbiol, 2007. **15**(3): p. 119-26.
36. Weitzman, M.D., et al., *Interactions of viruses with the cellular DNA repair machinery.* DNA Repair (Amst), 2004. **3**(8-9): p. 1165-73.
37. Rowe, W.P., et al., *Isolation of a Cytopathogenic Agent from Human Adenoids Undergoing Spontaneous Degeneration in Tissue Culture.* Proceedings of the Society for Experimental Biology and Medicine, 1953. **84**(3): p. 570-573.
38. Hllleman, M.R. and J.H. Werner, *Recovery of New Agent from Patients with Acute Respiratory Illness.* Proceedings of the Society for Experimental Biology and Medicine, 1954. **85**(1): p. 183-188.
39. Fields, B.N., D.M. Knipe, and P.M. Howley, *Fields virology*. 5th ed. 2007, Philadelphia ; London: Wolters Kluwer Health / Lippincott Williams & Wilkins.
40. ROSEN, L., *A HEMAGGLUTINATION-INHIBITION TECHNIQUE FOR TYPING ADENOVIRUSES1.* American Journal of Epidemiology, 1960. **71**(1): p. 120-128.
41. Charman, M., C. Herrmann, and M.D. Weitzman, *Viral and cellular interactions during adenovirus DNA replication.* FEBS Lett, 2019. **593**(24): p. 3531-3550.
42. Ghebremedhin, B., *Human adenovirus: Viral pathogen with increasing importance.* Eur J Microbiol Immunol (Bp), 2014. **4**(1): p. 26-33.
43. Stewart, P.L., S.D. Fuller, and R.M. Burnett, *Difference imaging of adenovirus: bridging the resolution gap between X-ray crystallography and electron microscopy.* Embo j, 1993. **12**(7): p. 2589-99.
44. Russell, W.C., *Update on adenovirus and its vectors.* J Gen Virol, 2000. **81**(Pt 11): p. 2573-2604.
45. Berk, A.J., *Functions of adenovirus E1A.* Cancer Surv, 1986. **5**(2): p. 367-87.
46. Berk, A.J., *Recent lessons in gene expression, cell cycle control, and cell biology from adenovirus.* Oncogene, 2005. **24**(52): p. 7673-7685.
47. Bergelson, J.M., et al., *Isolation of a Common Receptor for Coxsackie B Viruses and Adenoviruses 2 and 5.* Science, 1997. **275**(5304): p. 1320-1323.
48. Roelvink, P.W., et al., *The coxsackievirus-adenovirus receptor protein can function as a cellular attachment protein for adenovirus serotypes from subgroups A, C, D, E, and F.* J Virol, 1998. **72**(10): p. 7909-15.

49. Gaggar, A., D.M. Shayakhmetov, and A. Lieber, *CD46 is a cellular receptor for group B adenoviruses.* Nat Med, 2003. **9**(11): p. 1408-12.
50. Wang, H., et al., *Desmoglein 2 is a receptor for adenovirus serotypes 3, 7, 11 and 14.* Nat Med, 2011. **17**(1): p. 96-104.
51. Kremer, E.J. and G.R. Nemerow, *Adenovirus Tales: From the Cell Surface to the Nuclear Pore Complex.* PLOS Pathogens, 2015. **11**(6): p. e1004821.
52. Kleinberger, T., *En Guard! The Interactions between Adenoviruses and the DNA Damage Response.* Viruses, 2020. **12**(9).
53. Hart, L.S., et al., *The adenovirus E4orf6 protein inhibits DNA double strand break repair and radiosensitizes human tumor cells in an E1B-55K-independent manner.* J Biol Chem, 2005. **280**(2): p. 1474-81.
54. Karen, K.A., et al., *Temporal regulation of the Mre11-Rad50-Nbs1 complex during adenovirus infection.* J Virol, 2009. **83**(9): p. 4565-73.
55. Weiden, M.D. and H.S. Ginsberg, *Deletion of the E4 region of the genome produces adenovirus DNA concatemers.* Proc Natl Acad Sci U S A, 1994. **91**(1): p. 153-7.
56. Stracker, T.H., C.T. Carson, and M.D. Weitzman, *Adenovirus oncoproteins inactivate the Mre11-Rad50-NBS1 DNA repair complex.* Nature, 2002. **418**(6895): p. 348-52.
57. Stracker, T.H., et al., *Serotype-specific reorganization of the Mre11 complex by adenoviral E4orf3 proteins.* J Virol, 2005. **79**(11): p. 6664-73.
58. Forrester, N.A., et al., *Serotype-specific inactivation of the cellular DNA damage response during adenovirus infection.* J Virol, 2011. **85**(5): p. 2201-11.
59. Pancholi, N.J. and M.D. Weitzman, *Serotype-specific restriction of wild-type adenoviruses by the cellular Mre11-Rad50-Nbs1 complex.* Virology, 2018. **518**: p. 221-231.
60. Evans, J.D. and P. Hearing, *Relocalization of the Mre11-Rad50-Nbs1 complex by the adenovirus E4 ORF3 protein is required for viral replication.* J Virol, 2005. **79**(10): p. 6207-15.
61. Carvalho, T., et al., *Targeting of adenovirus E1A and E4-ORF3 proteins to nuclear matrix-associated PML bodies.* J Cell Biol, 1995. **131**(1): p. 45-56.
62. Araujo, F.D., et al., *Adenovirus type 5 E4orf3 protein targets the Mre11 complex to cytoplasmic aggresomes.* J Virol, 2005. **79**(17): p. 11382-91.
63. Liu, Y., et al., *Adenovirus exploits the cellular aggresome response to accelerate inactivation of the MRN complex.* J Virol, 2005. **79**(22): p. 14004-16.
64. Johnston, J.A., C.L. Ward, and R.R. Kopito, *Aggresomes: a cellular response to misfolded proteins.* J Cell Biol, 1998. **143**(7): p. 1883-98.
65. Carrell, R.W. and D.A. Lomas, *Conformational disease.* Lancet, 1997. **350**(9071): p. 134-8.
66. Brestovitsky, A., et al., *The Adenovirus E4orf4 Protein Provides a Novel Mechanism for Inhibition of the DNA Damage Response.* PLoS Pathog, 2016. **12**(2): p. e1005420.
67. Gautam, D. and E. Bridge, *The kinase activity of ataxia-telangiectasia mutated interferes with adenovirus E4 mutant DNA replication.* J Virol, 2013. **87**(15): p. 8687-96.
68. Shah, G.A. and C.C. O'Shea, *Viral and Cellular Genomes Activate Distinct DNA Damage Responses.* Cell, 2015. **162**(5): p. 987-1002.
69. Zou, L. and S.J. Elledge, *Sensing DNA damage through ATRIP recognition of RPA-ssDNA complexes.* Science, 2003. **300**(5625): p. 1542-8.
70. Carson, C.T., et al., *Mislocalization of the MRN complex prevents ATR signaling during adenovirus infection.* Embo j, 2009. **28**(6): p. 652-62.
71. Blackford, A.N., et al., *Adenovirus 12 E4orf6 inhibits ATR activation by promoting TOPBP1 degradation.* Proc Natl Acad Sci U S A, 2010. **107**(27): p. 12251-6.
72. Nichols, G.J., J. Schaack, and D.A. Ornelles, *Widespread phosphorylation of histone H2AX by species C adenovirus infection requires viral DNA replication.* J Virol, 2009. **83**(12): p. 5987-98.

73. Cuconati, A., et al., *DNA damage response and MCL-1 destruction initiate apoptosis in adenovirus-infected cells.* Genes Dev, 2003. **17**(23): p. 2922-32.
74. Cimprich, K.A. and D. Cortez, *ATR: an essential regulator of genome integrity.* Nat Rev Mol Cell Biol, 2008. **9**(8): p. 616-27.
75. Flint, S.J., S.M. Berget, and P.A. Sharp, *Characterization of single-stranded viral DNA sequences present during replication of adenovirus types 2 and 5.* Cell, 1976. **9**(4 Pt 1): p. 559-71.
76. Gabler, S., et al., *E1B 55-kilodalton-associated protein: a cellular protein with RNA-binding activity implicated in nucleocytoplasmic transport of adenovirus and cellular mRNAs.* J Virol, 1998. **72**(10): p. 7960-71.
77. Blackford, A.N., et al., *A role for E1B-AP5 in ATR signaling pathways during adenovirus infection.* J Virol, 2008. **82**(15): p. 7640-52.
78. Fischer, M., *Census and evaluation of p53 target genes.* Oncogene, 2017.
79. Meek, D.W., *Tumour suppression by p53: a role for the DNA damage response?* Nat Rev Cancer, 2009. **9**(10): p. 714-23.
80. Querido, E., et al., *Regulation of p53 levels by the E1B 55-kilodalton protein and E4orf6 in adenovirus-infected cells.* J Virol, 1997. **71**(5): p. 3788-98.
81. Konig, C., J. Roth, and M. Dobbelstein, *Adenovirus type 5 E4orf3 protein relieves p53 inhibition by E1B-55-kilodalton protein.* J Virol, 1999. **73**(3): p. 2253-62.
82. Harada, J.N., et al., *Analysis of the adenovirus E1B-55K-anchored proteome reveals its link to ubiquitination machinery.* J Virol, 2002. **76**(18): p. 9194-206.
83. Lane, D.P., *Cancer. p53, guardian of the genome.* Nature, 1992. **358**: p. 15-16.
84. Toledo, F. and G.M. Wahl, *Regulating the p53 pathway: in vitro hypotheses, in vivo veritas.* Nat Rev Cancer, 2006. **6**(12): p. 909-23.
85. El-Deiry, W.S., *The role of p53 in chemosensitivity and radiosensitivity.* Oncogene, 2003. **22**(47): p. 7486-95.
86. Boyer, J., K. Rohleder, and G. Ketner, *Adenovirus E4 34k and E4 11k inhibit double strand break repair and are physically associated with the cellular DNA-dependent protein kinase.* Virology, 1999. **263**(2): p. 307-12.
87. Nebenzahl-Sharon, K., et al., *Biphasic Functional Interaction between the Adenovirus E4orf4 Protein and DNA-PK.* Journal of Virology, 2019. **93**(10): p. e01365-18.
88. Baker, A., et al., *Adenovirus E4 34k and E1b 55k oncoproteins target host DNA ligase IV for proteasomal degradation.* J Virol, 2007. **81**(13): p. 7034-40.
89. Tookman, L.A., et al., *RAD51 and BRCA2 Enhance Oncolytic Adenovirus Type 5 Activity in Ovarian Cancer.* Mol Cancer Res, 2016. **14**(1): p. 44-55.
90. McCormick, F., *Cancer gene therapy: fringe or cutting edge?* Nature Reviews Cancer, 2001. **1**(2): p. 130-141.
91. Freedman, J.D., et al., *Oncolytic adenovirus expressing bispecific antibody targets T-cell cytotoxicity in cancer biopsies.* EMBO Mol Med, 2017. **9**(8): p. 1067-1087.
92. Freedman, J.D., et al., *An Oncolytic Virus Expressing a T-cell Engager Simultaneously Targets Cancer and Immunosuppressive Stromal Cells.* Cancer Res, 2018. **78**(24): p. 6852-6865.
93. Scott, E.M., et al., *Bi- and tri-valent T cell engagers deplete tumour-associated macrophages in cancer patient samples.* Journal for ImmunoTherapy of Cancer, 2019. **7**(1): p. 320.
94. O'Cathail, S.M., et al., *Combining Oncolytic Adenovirus with Radiation-A Paradigm for the Future of Radiosensitization.* Front Oncol, 2017. **7**: p. 153.
95. Toth, K., et al., *Radiation increases the activity of oncolytic adenovirus cancer gene therapy vectors that overexpress the ADP (E3-11.6K) protein.* Cancer Gene Ther, 2003. **10**(3): p. 193-200.
96. Portella, G., et al., *ONYX-015 enhances radiation-induced death of human anaplastic thyroid carcinoma cells.* J Clin Endocrinol Metab, 2003. **88**(10): p. 5027-32.

97. Geoerger, B., et al., *Potentiation of radiation therapy by the oncolytic adenovirus dl1520 (ONYX-015) in human malignant glioma xenografts.* Br J Cancer, 2003. **89**(3): p. 577-84.
98. Lamfers, M.L., et al., *Potential of the conditionally replicative adenovirus Ad5-Delta24RGD in the treatment of malignant gliomas and its enhanced effect with radiotherapy.* Cancer Res, 2002. **62**(20): p. 5736-42.
99. Ganesh, S., et al., *Combination therapy with radiation or cisplatin enhances the potency of Ad5/35 chimeric oncolytic adenovirus in a preclinical model of head and neck cancer.* Cancer Gene Ther, 2009. **16**(5): p. 383-92.
100. Chen, Y., et al., *CV706, a prostate cancer-specific adenovirus variant, in combination with radiotherapy produces synergistic antitumor efficacy without increasing toxicity.* Cancer Res, 2001. **61**(14): p. 5453-60.
101. Dilley, J., et al., *Oncolytic adenovirus CG7870 in combination with radiation demonstrates synergistic enhancements of antitumor efficacy without loss of specificity.* Cancer Gene Ther, 2005. **12**(8): p. 715-22.
102. Kawabe, S., et al., *Adenovirus-mediated wild-type p53 gene expression radiosensitizes non-small cell lung cancer cells but not normal lung fibroblasts.* Int J Radiat Biol, 2001. **77**(2): p. 185-94.
103. Emdad, L., et al., *Ionizing radiation enhances adenoviral vector expressing mda-7/IL-24-mediated apoptosis in human ovarian cancer.* J Cell Physiol, 2006. **208**(2): p. 298-306.
104. Freytag, S.O., et al., *Prospective randomized phase 2 trial of intensity modulated radiation therapy with or without oncolytic adenovirus-mediated cytotoxic gene therapy in intermediate-risk prostate cancer.* Int J Radiat Oncol Biol Phys, 2014. **89**(2): p. 268-76.
105. Wheeler, L.A., et al., *Phase II multicenter study of gene-mediated cytotoxic immunotherapy as adjuvant to surgical resection for newly diagnosed malignant glioma.* Neuro Oncol, 2016. **18**(8): p. 1137-45.
106. Molnar-Kimber, K.L., et al., *Impact of preexisting and induced humoral and cellular immune responses in an adenovirus-based gene therapy phase I clinical trial for localized mesothelioma.* Hum Gene Ther, 1998. **9**(14): p. 2121-33.
107. Holterman, L., et al., *Novel replication-incompetent vector derived from adenovirus type 11 (Ad11) for vaccination and gene therapy: low seroprevalence and non-cross-reactivity with Ad5.* J Virol, 2004. **78**(23): p. 13207-15.
108. Vogels, R., et al., *Replication-deficient human adenovirus type 35 vectors for gene transfer and vaccination: efficient human cell infection and bypass of preexisting adenovirus immunity.* J Virol, 2003. **77**(15): p. 8263-71.
109. Abbink, P., et al., *Comparative seroprevalence and immunogenicity of six rare serotype recombinant adenovirus vaccine vectors from subgroups B and D.* J Virol, 2007. **81**(9): p. 4654-63.
110. Kuhn, I., et al., *Directed evolution generates a novel oncolytic virus for the treatment of colon cancer.* PLoS One, 2008. **3**(6): p. e2409.
111. Di, Y., L. Seymour, and K. Fisher, *Activity of a group B oncolytic adenovirus (ColoAd1) in whole human blood.* Gene Ther, 2014. **21**(4): p. 440-3.
112. Boni, V., et al., *1068PA PHASE 1 MECHANISM OF ACTION STUDY OF INTRA-TUMOURAL (IT) OR INTRAVENOUS (IV) ADMINISTRATION OF ENADENOTUCIREV, AN ONCOLYTIC AD11/AD3 CHIMERIC GROUP B ADENOVIRUS IN COLON CANCER PATIENTS UNDERGOING RESECTION OF PRIMARY TUMOUR.* Annals of Oncology, 2014. **25**(suppl_4): p. iv368-iv368.
113. Garcia-Carbonero, R., et al., *Phase 1 study of intravenous administration of the chimeric adenovirus enadenotucirev in patients undergoing primary tumor resection.* J Immunother Cancer, 2017. **5**(1): p. 71.
114. Dyer, A., et al., *Oncolytic Group B Adenovirus Enadenotucirev Mediates Non-apoptotic Cell Death with Membrane Disruption and Release of Inflammatory Mediators.* Mol Ther Oncolytics, 2017. **4**: p. 18-30.

115. O'Cathail, S.M., et al., *A phase 1 trial of the safety, tolerability and biological effects of intravenous Enadenotucirev, a novel oncolytic virus, in combination with chemoradiotherapy in locally advanced rectal cancer (CEDAR).* Radiation Oncology, 2020. **15**(1): p. 151.
116. Singer, V.L., et al., *Characterization of PicoGreen reagent and development of a fluorescence-based solution assay for double-stranded DNA quantitation.* Anal Biochem, 1997. **249**(2): p. 228-38.
117. Murakami, P. and M.T. McCaman, *Quantitation of adenovirus DNA and virus particles with the PicoGreen fluorescent Dye.* Anal Biochem, 1999. **274**(2): p. 283-8.
118. Kärber, G., *Beitrag zur kollektiven Behandlung pharmakologischer Reihenversuche.* Naunyn-Schmiedebergs Archiv für experimentelle Pathologie und Pharmakologie, 1931. **162**(4): p. 480-483.
119. BLISS, C.I., *THE TOXICITY OF POISONS APPLIED JOINTLY1.* Annals of Applied Biology, 1939. **26**(3): p. 585-615.
120. Joiner, M.C. and A. van der Kogel, *Basic Clinical Radiobiology Fourth Edition*. 2009, London, UNKNOWN: CRC Press.
121. Royds, J.A., et al., *p53 promotes adenoviral replication and increases late viral gene expression.* Oncogene, 2006. **25**(10): p. 1509-20.
122. Schultz, L.B., et al., *p53 binding protein 1 (53BP1) is an early participant in the cellular response to DNA double-strand breaks.* J Cell Biol, 2000. **151**(7): p. 1381-90.
123. Baumann, P. and S.C. West, *Role of the human RAD51 protein in homologous recombination and double-stranded-break repair.* Trends Biochem Sci, 1998. **23**(7): p. 247-51.
124. Marino, N., et al., *Development of a versatile oncolytic virus platform for local intra-tumoural expression of therapeutic transgenes.* PLoS One, 2017. **12**(5): p. e0177810.
125. Canny, M.D., et al., *Inhibition of 53BP1 favors homology-dependent DNA repair and increases CRISPR-Cas9 genome-editing efficiency.* Nat Biotechnol, 2018. **36**(1): p. 95-102.
126. Spänkuch-Schmitt, B., et al., *Effect of RNA silencing of polo-like kinase-1 (PLK1) on apoptosis and spindle formation in human cancer cells.* J Natl Cancer Inst, 2002. **94**(24): p. 1863-77.
127. Feng, J., et al., *A novel automatic quantification method for high-content screening analysis of DNA double strand-break response.* Sci Rep, 2017. **7**(1): p. 9581.
128. Yousaf, I., et al., *Attenuation of the Hypoxia Inducible Factor Pathway after Oncolytic Adenovirus Infection Coincides with Decreased Vessel Perfusion.* Cancers (Basel), 2020. **12**(4).
129. Stillman, B.W., *The replication of adenovirus DNA with purified proteins.* Cell, 1983. **35**(1): p. 7-9.
130. Komatsu, T., K. Nagata, and H. Wodrich, *An Adenovirus DNA Replication Factor, but Not Incoming Genome Complexes, Targets PML Nuclear Bodies.* J Virol, 2016. **90**(3): p. 1657-67.
131. Ben-Israel, H. and T. Kleinberger, *Adenovirus and cell cycle control.* Front Biosci, 2002. **7**: p. d1369-95.
132. Harding, S.M. and R.G. Bristow, *Discordance between phosphorylation and recruitment of 53BP1 in response to DNA double-strand breaks.* Cell Cycle, 2012. **11**(7): p. 1432-44.
133. Joo, W.S., et al., *Structure of the 53BP1 BRCT region bound to p53 and its comparison to the Brca1 BRCT structure.* Genes Dev, 2002. **16**(5): p. 583-93.
134. Zimmermann, M. and T. de Lange, *53BP1: pro choice in DNA repair.* Trends in Cell Biology, 2014. **24**(2): p. 108-117.
135. Forment, J.V., R.V. Walker, and S.P. Jackson, *A high-throughput, flow cytometry-based method to quantify DNA-end resection in mammalian cells.* Cytometry. Part A : the journal of the International Society for Analytical Cytology, 2012. **81**(10): p. 922-928.
136. Bryans, M., M.C. Valenzano, and T.D. Stamato, *Absence of DNA ligase IV protein in XR-1 cells: evidence for stabilization by XRCC4.* Mutat Res, 1999. **433**(1): p. 53-8.

137. Wang, Y.-G., et al., *Phosphorylation and Regulation of DNA Ligase IV Stability by DNA-dependent Protein Kinase.* Journal of Biological Chemistry, 2004. **279**(36): p. 37282-37290.
138. Pierce, A.J., et al., *XRCC3 promotes homology-directed repair of DNA damage in mammalian cells.* Genes Dev, 1999. **13**(20): p. 2633-8.
139. Ogiwara, H., et al., *Histone acetylation by CBP and p300 at double-strand break sites facilitates SWI/SNF chromatin remodeling and the recruitment of non-homologous end joining factors.* Oncogene, 2011. **30**(18): p. 2135-2146.
140. Zhang, M., et al., *Ionizing radiation increases adenovirus uptake and improves transgene expression in intrahepatic colon cancer xenografts.* Mol Ther, 2003. **8**(1): p. 21-8.
141. Hingorani, M., et al., *Radiation-mediated up-regulation of gene expression from replication-defective adenoviral vectors: implications for sodium iodide symporter gene therapy.* Clin Cancer Res, 2008. **14**(15): p. 4915-24.
142. Shashkova, E.V., S.M. May, and M.A. Barry, *Characterization of human adenovirus serotypes 5, 6, 11, and 35 as anticancer agents.* Virology, 2009. **394**(2): p. 311-20.
143. Bieler, A., et al., *Impact of radiation therapy on the oncolytic adenovirus dl520: implications on the treatment of glioblastoma.* Radiother Oncol, 2008. **86**(3): p. 419-27.
144. Qian, J., et al., *Ionizing radiation-induced adenovirus infection is mediated by Dynamin 2.* Cancer Res, 2005. **65**(13): p. 5493-7.
145. Pied, N. and H. Wodrich, *Imaging the adenovirus infection cycle.* FEBS Lett, 2019. **593**(24): p. 3419-3448.
146. Nokisalmi, P., et al., *Radiation-induced upregulation of gene expression from adenoviral vectors mediated by DNA damage repair and regulation.* Int J Radiat Oncol Biol Phys, 2012. **83**(1): p. 376-84.
147. Liu, C., et al., *Combination of measles virus virotherapy and radiation therapy has synergistic activity in the treatment of glioblastoma multiforme.* Clin Cancer Res, 2007. **13**(23): p. 7155-65.
148. Egami, T., et al., *Radiation enhances adenoviral gene therapy in pancreatic cancer via activation of cytomegalovirus promoter and increased adenovirus uptake.* Clin Cancer Res, 2008. **14**(6): p. 1859-67.
149. Amstutz, B., et al., *Subversion of CtBP1-controlled macropinocytosis by human adenovirus serotype 3.* Embo j, 2008. **27**(7): p. 956-69.
150. Kalin, S., et al., *Macropinocytotic uptake and infection of human epithelial cells with species B2 adenovirus type 35.* J Virol, 2010. **84**(10): p. 5336-50.
151. Nava, P., et al., *Desmoglein-2: a novel regulator of apoptosis in the intestinal epithelium.* Mol Biol Cell, 2007. **18**(11): p. 4565-78.
152. Cirillo, N., et al., *The most widespread desmosomal cadherin, desmoglein 2, is a novel target of caspase 3-mediated apoptotic machinery.* J Cell Biochem, 2008. **103**(2): p. 598-606.
153. Williams, J.R., et al., *Human tumor cells segregate into radiosensitivity groups that associate with ATM and TP53 status.* Acta Oncol, 2007. **46**(5): p. 628-38.
154. Sakurai, F., et al., *Downregulation of human CD46 by adenovirus serotype 35 vectors.* Gene Ther, 2007. **14**(11): p. 912-9.
155. Wang, H., et al., *Intracellular Signaling and Desmoglein 2 Shedding Triggered by Human Adenoviruses Ad3, Ad14, and Ad14P1.* J Virol, 2015. **89**(21): p. 10841-59.
156. Sánchez-Prieto, R., et al., *Carcinoma cell lines become sensitive to DNA-damaging agents by the expression of the adenovirus E1A gene.* Oncogene, 1996. **13**(5): p. 1083-92.
157. Martin-Duque, P., et al., *In vivo radiosensitizing effect of the adenovirus E1A gene in murine and human malignant tumors.* Int J Oncol, 1999. **15**(6): p. 1163-8.
158. Hingorani, M., et al., *Inhibition of repair of radiation-induced DNA damage enhances gene expression from replication-defective adenoviral vectors.* Cancer Res, 2008. **68**(23): p. 9771-8.

159. Tedcastle, A., et al., *Actin-resistant DNAse I Expression From Oncolytic Adenovirus Enadenotucirev Enhances Its Intratumoral Spread and Reduces Tumor Growth.* Mol Ther, 2016. **24**(4): p. 796-804.
160. Thai, M., et al., *Adenovirus E4ORF1-induced MYC activation promotes host cell anabolic glucose metabolism and virus replication.* Cell Metab, 2014. **19**(4): p. 694-701.
161. Biedermann, K.A., et al., *scid mutation in mice confers hypersensitivity to ionizing radiation and a deficiency in DNA double-strand break repair.* Proc Natl Acad Sci U S A, 1991. **88**(4): p. 1394-7.
162. Vanpouille-Box, C., et al., *DNA exonuclease Trex1 regulates radiotherapy-induced tumour immunogenicity.* Nat Commun, 2017. **8**: p. 15618.
163. Lam, E., S. Stein, and E. Falck-Pedersen, *Adenovirus detection by the cGAS/STING/TBK1 DNA sensing cascade.* J Virol, 2014. **88**(2): p. 974-81.
164. Lam, E. and E. Falck-Pedersen, *Unabated adenovirus replication following activation of the cGAS/STING-dependent antiviral response in human cells.* J Virol, 2014. **88**(24): p. 14426-39.
165. Lee, J.H., et al., *53BP1 promotes ATM activity through direct interactions with the MRN complex.* Embo j, 2010. **29**(3): p. 574-85.
166. Pokrovska, T.D., et al., *External Beam Radiation Therapy and Enadenotucirev: Inhibition of the DDR and Mechanisms of Radiation-Mediated Virus Increase.* Cancers (Basel), 2020. **12**(4).
167. Ahmed, D., et al., *Epigenetic and genetic features of 24 colon cancer cell lines.* Oncogenesis, 2013. **2**(9): p. e71.
168. Danthinne, X. and M.J. Imperiale, *Production of first generation adenovirus vectors: a review.* Gene Therapy, 2000. **7**(20): p. 1707-1714.
169. Wang, G., et al., *Mediator requirement for both recruitment and postrecruitment steps in transcription initiation.* Mol Cell, 2005. **17**(5): p. 683-94.
170. Weichselbaum, R.R., et al., *Radiotherapy and immunotherapy: a beneficial liaison?* Nat Rev Clin Oncol, 2017.
171. Das, A.K., et al., *Non–Small Cell Lung Cancers with Kinase Domain Mutations in the Epidermal Growth Factor Receptor Are Sensitive to Ionizing Radiation.* Cancer Research, 2006. **66**(19): p. 9601-9608.
172. Machiels, J.-P., et al., *A phase 1 dose escalation study of the oncolytic adenovirus enadenotucirev, administered intravenously to patients with epithelial solid tumors (EVOLVE).* Journal for ImmunoTherapy of Cancer, 2019. **7**(1): p. 20.